SOLID STATE NANOSTRUCTURES AS PLATFORMS FOR EMERGING QUANTUM TECHNOLOGIES

by

Dale Scerri

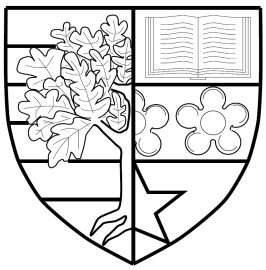

Submitted for the degree of
Doctor of Philosophy

Institute of Photonics and Quantum Sciences
School of Engineering and Physical Sciences
Heriot-Watt University

May 2019

Sometimes science is more

art than science, Morty.

Lot of people don't get that.

RICK SANCHEZ

Abstract

In this thesis, we investigate the use of solid state nanostructures in quantum metrology, information and computation. In the first chapter, we introduce the polaron master equation which accurately captures the non-Markovian dynamics resulting from the strong interaction between the nanostructure and its vibrational environment. In the next two chapters, we give the technical background required for subsequent chapters.

In the next two chapters, we focus on applications of self-assembled quantum dots. We investigate the modified emission properties of such a nanostructure close to a metal surface, followed by an extension of our model to a sample of $N > 1$ quantum dots. In the next chapter, we propose a novel cluster state generation scheme, using a hole-spin in a quantum dot to generate strings of frequency-entangled photons. Inspired by the results in this chapter, we then propose a new approach to reconstruct the quantum state of a system which has accumulated random errors which are only characterised post-measurement.

Turning our attention to negatively charged nitrogen-vacancy centres, we then investigate a new technique of increasing the coherence time of an electron spin by adaptively gaining information about the state of its dilute environment.

Acknowledgements

There are several people who have contributed in making my PhD experience a thrilling ride. First of all I'd like to thank my supervisor Erik Gauger for coping with all my questions with quintessentially British politeness. Thank you to my fellow QTT members[1] (in no particular order): Will Brown, David Reichmuth, Dominic Rouse, Berke Ricketti, Romane Moulin, Alexandre Coates and Scott Davidson. Special thanks to Will, my (unofficial) art marketing manager and Alexandre for proofreading parts of this thesis and suggesting I should "acknowledge Alex iz kool". Despite not being officially part of the group, I wouldn't have made it through those lonely empty office days if it wasn't for the company of my rubber duck collection, especially Count Quackula and Dr. Allam.

I'm deeply indebted to our experimental collaborators of Heriot-Watt Quantum Photonics Lab, especially Brian Gerardot for keeping us theorists grounded, and Cristian Bonato for helping me with my (previously non-existent) Python coding practices. I would also like to thank Ted Santana for our collaborations, despite having joined warmer pastures in Brazil.

I'm grateful for my friends back in Malta, mostly for dealing with my awful taste in memes during my many breakdowns, as well as the Thirlestane gang, who have introduced me to Dungeons and Dragons, thus finalising my transcendence to geekdom. Special thanks to the best bestie ever, Michelle, for all the care packages we sent each other in times of need!

To my parents, Odette and Albert, and brother, Gary: Saying that I wouldn't be here without you is an understatement. I will be forever indebted for your constant support and affection, especially to my mum (and best friend). I would also like to thank Buddy and Tasha, but I doubt they'll ever be able to read this, so give them lots of hugs and treats, I'm sure they'd appreciate that more!

Finally, thank you Barbara (and Leia of course!), for accepting me for who I am and for always being there when I need you the most. May we have many adventures with Tilly (once we figure out what kind of fuel she takes).

[1] especially for making me realise how much I hate hiking.

ACADEMIC REGISTRY

Research Thesis Submission

Please note this form should be bound into the submitted thesis.

Name*:*	Dale Scerri		
School:	EPS		
Version: *(i.e. First, Resubmission, Final)*	Final	Degree Sought:	Doctor of Philosophy

Declaration

In accordance with the appropriate regulations I hereby submit my thesis and I declare that:

1. The thesis embodies the results of my own work and has been composed by myself
2. Where appropriate, I have made acknowledgement of the work of others
3. Where the thesis contains published outputs under Regulation 6 (9.1.2) these are accompanied by a critical review which accurately describes my contribution to the research and, for multi-author outputs, a signed declaration indicating the contribution of each author (complete Inclusion of Published Works Form – see below)
4. The thesis is the correct version for submission and is the same version as any electronic versions submitted*.
5. My thesis for the award referred to, deposited in the Heriot-Watt University Library, should be made available for loan or photocopying and be available via the Institutional Repository, subject to such conditions as the Librarian may require
6. I understand that as a student of the University I am required to abide by the Regulations of the University and to conform to its discipline.
7. Inclusion of published outputs under Regulation 6 (9.1.2) shall not constitute plagiarism.
8. I confirm that the thesis has been verified against plagiarism via an approved plagiarism detection application e.g. Turnitin.

* *Please note that it is the responsibility of the candidate to ensure that the correct version of the thesis is submitted.*

Signature of Candidate*:*		Date:	

Submission

Submitted By *(name in capitals):*	DALE SCERRI
Signature of Individual Submitting:	
Date Submitted:	

For Completion in the Student Service Centre (SSC)

Received in the SSC by *(name in capitals):*			
Method of Submission *(Handed in to SSC; posted through internal/external mail):*			
*E-thesis Submitted (**mandatory for final theses**)*			
Signature:		Date:	

ACADEMIC REGISTRY

Inclusion of Published Works

Declaration

This thesis contains one or more multi-author published works. In accordance with Regulation 6 (9.1.2) I hereby declare that the contributions of each author to these publications is as follows:

Citation details	D. Scerri, T. S. Santana, B. D. Gerardot, and E. M. Gauger, “Method of images applied to driven solid-state emitters", Phys. Rev. B, vol. 95, p. 165403, Apr. 2017.
D. Scerri	Performed analysis, wrote paper
T. S. Santana	Edited paper, contributed to analysis discussion
B. D. Gerardot	Conceived project, contributed to analysis discussion, edited paper
E. M. Gauger	Conceived project, contributed to analysis discussion, edited paper, supervised project
Signature:	
Date:	

Citation details	D. Scerri, R. N. E. Malein, B. D. Gerardot, and E. M. Gauger, “Frequency encoded linear cluster states with coherent Raman photons", Phys. Rev. A, vol. 98, p. 022318, Aug. 2018.
D. Scerri	Performed analysis, wrote paper
R. N. E. Malein	Edited paper, contributed to analysis discussion
B. D. Gerardot	Conceived project, contributed to analysis discussion, edited paper
E. M. Gauger	Conceived project, contributed to analysis discussion, edited paper, supervised project
Signature:	
Date:	

ACADEMIC REGISTRY

Citation details	D. Scerri, E. Gauger, and G. Knee, “Coarse-graining in retrodictive quantum state tomography", Journal of Physics Communications, 2019.
D. Scerri	Performed analysis, wrote paper
E. Gauger	Edited paper, contributed to analysis discussion, supervised project
G. Knee	Contributed to analysis discussion, edited paper, supervised project
Signature:	
Date:	

Contents

List of publications

This thesis is based on the following publications:

- **Chapter 5**:
  - D. Scerri, T. S. Santana, B. D. Gerardot, and E. M. Gauger, "Method of images applied to driven solid-state emitters," *Phys. Rev. B*, vol. 95, p. 165403, Apr. 2017.
  - D. Scerri, and E. M. Gauger, "Super- and subradiance from driven solid state emitters near reflective boundaries." (manuscript in preparation)
- **Chapter 6**: D. Scerri, R. N. E. Malein, B. D. Gerardot, and E. M. Gauger, "Frequency-encoded linear cluster states with coherent Raman photons," *Phys. Rev. A*, vol. 98, p. 022318, Aug. 2018.
- **Chapter 7**: D. Scerri, E. M. Gauger, and G. C. Knee, "Coarse-graining in retrodictive quantum state tomography," *Journal of Physics Communications*, 2019.
- **Chapter 8**: D. Scerri, and E. M. Gauger, and C. Bonato, "Spin bath narrowing using adaptive Bayesian algorithms." (manuscript in preparation)

The following two manuscripts (both in preparation) are related, and their work has been carried out during the doctoral training period, but are not included in this thesis:

- Z. X. Koong, D. Scerri, M. Rambach, E. M. Gauger, and B. D. Gerardot "Coherent and incoherent scattering from resonantly driven quantum dots."

- S. Kumar, A. Branny, R. Proux, D. Scerri, E. M. Gauger, and B. D. Gerardot "Exciton-phonon interaction and decay-dynamics of localized excitons in monolayer WSe_2."

Chapter 1

Introduction and outline

1.1 Introduction

Over the last few decades, it has become increasingly evident that quantum mechanics is indeed the most accurate description of the fundamental building blocks of our universe. Experimental evidence has been steadily increasing, consistently proving what theory had claimed before, and, more importantly, showing new results which shed light on the gaps in our knowledge of this field. Harnessing quantum phenomena in the lab is becoming a reality more and more each day, extending our ability to build quantum devices, such as single photon sources emitting single light quanta at the push of a button, or artificial light absorbers inspired by the work Nature has been carrying out for millions of years.

Technologies dating back to the 20^{th} century already harness some aspects of quantum mechanics; from the importance of electronic band structures in semiconductor-based manufacturing, to nuclear magnetic resonance in magnetic resonance imaging. However, in order to construct next level technologies, we need to make use of properties which are only available on a nanoscale level, at which the environment plays an important, often detrimental, role on the system's dynamics. It is thus of utmost importance to have theoretical models which take into account the environmental interactions for such nano-devices, serving as blueprints not only for extending our understanding about how these devices should work, but also how to build them in realistic experimental conditions.

The main aim of this thesis is to discuss novel theoretical proposals for solid state nanostructure-based applications, ranging from improving single photon sources, to applications of these systems in quantum computing. As we shall see, the environments of these structures play a non-trivial role in the latter's dynamics, and thus we aim to model these interactions accurately in order to better understand how future technologies can be improved and implemented in the lab.

1.2 Outline

We start this thesis by discussing some technical background which underpins the subsequent chapters. In Chapter 2, we shall go over the density matrix approach of describing quantum states, and, more importantly introduce the master equation formalism of describing the interaction of a system with its environment. In light of the solid state theme of this thesis, we shall discuss interactions with the electromagnetic and vibrational environment of the system, and introduce the polaron picture for strong system-vibrational couplings. Finally, we shall briefly discuss collective behaviour induced by these interactions.

Having discussed the mathematical background of a general solid state nanostructure and its environment, in Chapter 3 we introduce self-assembled quantum dots and nitrogen-vacancy centres as examples of such structures, giving their corresponding energy level structures as well as the optical and, in the case of nitrogen-vacancy centres, microwave selection rules for these systems.

We finish the introductory part of the thesis by introducing the measurement-based quantum computation paradigm and the multi-qubit highly-entangled states required for this framework in Chapter 4. We conclude this chapter by discussing the use of solid state emitters to generate photonic versions of these entangled states used for quantum computation.

In the next half of the thesis, we focus on novel work building up on the fundamentals discussed in the first half. In Chapter 5, the 'image dipole' approach, developed for atomic structures close to reflective surfaces, is applied to a driven self-assembled quantum dot near a metal surface, for which we include interactions

with its vibrational environment by deriving the polaron master equation. Motivated by the agreement between the image approach and the half-sided cavity which we include for comparison, we extend our results to more than a single emitter, observing enhanced emitted intensity due to the presence of the surface.

In Chapter 6 we propose an application of quantum dots as single emitters in the field of measurement-based quantum computation, discussed in Chapter 4. More precisely, we develop a novel cluster state generation scheme using hole-spins in quantum dots to generate a string of frequency-entangled Raman photons. We demonstrate that our scheme has a number of advantages over rival schemes, and propose an extension to mitigate the probabilistic aspect of our scheme, which stems from the randomness of the scattering events.

Inspired by the probabilistic nature of the scheme presented in Chapter 6, we develop and benchmark protocols for quantum state tomography based on retrodicting random errors which are only characterised post-measurement. We show how several state-of-the-art quantum information schemes relying on solid state emitters can benefit from this approach, as it allows for the mitigation of uncertainty in the emission time. We also develop a coarse-grained approach and show that we can gain a significant reduction in computation time for a small sacrifice in reconstruction fidelity.

Finally, in Chapter 8 we discuss how to increase the coherence time of an electron spin in a negatively charged nitrogen-vacancy centre by estimating the interaction with its spin bath environment. We introduce an adaptation of the Bayesian adaptive sensing scheme, which has been successfully used to estimate unknown magnetic fields by applying a series of Ramsey measurements on the electron spin of a negatively charged nitrogen-vacancy centre. By adaptively choosing the measurement parameters for each Ramsey sequence, we show that we can get an improved estimate the interaction strength between the electron spin and its environment with each measurement sequence, resulting in a significant improvement of the electron spin's coherence time.

As every chapter has its own concluding remarks, we shall briefly summarise the

results and structure of the thesis in the Chapter 9.

Chapter 2

Open Quantum Systems

Solid state quantum systems typically interact with larger surrounding environments to various extents. It is thus imperative to model these interactions, and their effects on the nanostructure's dynamics, in order to assess the feasibility of using such a structure as a quantum technology platform. The *open quantum system* formalism is thus more adequate to describe the evolution of solid state nanostructures in the presence of multiple environments. In this section, after briefly outlining the evolution of closed systems, we describe how the dynamics of a solid state open quantum system can be modelled via a *master equation*, which we shall then be using, in various forms, throughout the rest of this thesis.

2.1 Density Matrix formalism

An isolated quantum system can be described by a *state vector* $|\psi(t)\rangle$, whose time evolution is governed by the Schrödinger equation, which, for a general, time-dependent Hamiltonian, is given by

$$i\hbar\frac{\mathrm{d}}{\mathrm{d}t}|\psi(t)\rangle = H(t)\,|\psi(t)\rangle \ , \tag{2.1}$$

where $H(t)$ is the system Hamiltonian (in most cases, we will set the reduced Planck's constant to unity). Whilst in most cases we shall be dealing with time-independent Hamiltonians, we will keep the time-dependent notation for generality for the time being. The solution to the above equation can be written using a *time evolution*

operator $U(t, t_0)$ which evolves the state vector $\psi(t_0)$ at an initial time t_0 to $\psi(t)$ at time t, that is

$$|\psi(t)\rangle = U(t, t_0)\,|\psi(t_0)\rangle \ , \tag{2.2}$$

and hence

$$i\hbar\frac{\partial}{\partial t}U(t, t_0) = H(t)U(t, t_0) \ , \tag{2.3}$$

where $U(t_0, t_0) = I$. It can also be seen that $U(t, t_0)$ is a unitary operator. For time independent Hamiltonians, we can easily integrate equation (2.3) and obtain a very simple form for the time evolution operator

$$U(t, t_0) = \exp\left[-\frac{i}{\hbar}H(t - t_0)\right] \ . \tag{2.4}$$

However, if the system is closed, but not isolated (e.g. driving the system by means of an external force), then the system Hamiltonian is not necessarily time-independent. In such case, the time evolution operator takes the more general form

$$U(t, t_0) = T_{\leftarrow}\exp\left[-\frac{i}{\hbar}\int_{t_0}^{t}\mathrm{d}s H(s)\right] \ , \tag{2.5}$$

where $T_{\leftarrow}$ is the *chronological time-ordering operator*.

This pure state representation fails, however, when the system can be found in any number of states $|\psi_i(t)\rangle$ (with probability, say p_i) of an ensemble $\{|\psi_i(t)\rangle\}$, each of which evolves according to the Schrödinger equation (2.1). A representation of such a *mixed state* is captured by the *density operator* formalism, in which such a state can be written as

$$\rho(t) = \sum_i p_i\,|\psi_i(t)\rangle\,\langle\psi_i(t)| \ , \tag{2.6}$$

where $\{|\psi_i(t)\rangle\}$ is a set of normalised (but not necessarily orthogonal) Hilbert space vectors spanning the system space $\mathcal{H}_S$. The density operator satisfies a number of properties, namely:

- *Hermiticity*: $\rho^\dagger(t) = \rho(t)$;
- *Positivity*: $\langle\phi(t)|\,\rho(t)\,|\phi(t)\rangle \geq 0,\ \forall\,|\phi(t)\rangle \in \mathcal{H}_S$;
- *Normalisation*: $\mathrm{tr}(\rho(t)) = 1$, that is, $\sum_i p_i = 1$.

If we consider the system at an initial time t_0, the density operator at time t can be then written in terms of the time evolution operator and the density operator at this initial time as

$$\rho(t) = U(t, t_0)\rho(t_0)U^\dagger(t, t_0)\ . \tag{2.7}$$

After differentiating with respect to time, gives an equation of motion for the density operator

$$\frac{\mathrm{d}}{\mathrm{d}t}\rho(t) = -\frac{i}{\hbar}[H(t), \rho(t)]\ , \tag{2.8}$$

which is the celebrated *Liouville–von Neumann equation*, describing the unitary time evolution of a quantum system $\rho(t)$.

Another useful property of the density matrix formalism is related to the expectation value of an operator A, which, for a pure state $|\psi\rangle$, simply evaluates to $\langle\psi|\,A\,|\psi\rangle$. Extending this representation to density matrix formalism, we obtain:

$$\langle A\rangle = \mathrm{tr}(\rho A) = \sum_i p_i\,\langle\psi_i|\,A\,|\psi_i\rangle\ , \tag{2.9}$$

where we have dropped the time notation for brevity.

So far we have limited ourselves to single systems. More often than not, however, we deal with composite systems; for example, consider a system S which is composed of the two systems $S^{(1)}$ and $S^{(2)}$, with Hilbert spaces $\mathcal{H}^{(1)}$ and $\mathcal{H}^{(2)}$ respectively. Then the Hilbert space of the composite system is given by $\mathcal{H} = \mathcal{H}^{(1)} \otimes \mathcal{H}^{(2)}$, where $\otimes$ denotes the tensor product. Furthermore, if $\{|\psi_i^{(1)}\rangle\}$ and $\{|\psi_i^{(2)}\rangle\}$ are two orthonormal bases for the two systems comprising S, then any state in $\mathcal{H}$ can be

written as

$$|\Psi\rangle = \sum_{i,j} a_{ij} |\psi_i^{(1)}\rangle \otimes |\psi_j^{(2)}\rangle \ , \tag{2.10}$$

meaning that $\{|\psi_i^{(1)}\rangle \otimes |\psi_j^{(2)}\rangle\}$ forms a new basis for the composite Hilbert space. Moreover, if $O^{(1)}$ and $O^{(2)}$ are operators acting on the Hilbert spaces $\mathcal{H}^{(1)}$ and $\mathcal{H}^{(2)}$ respectively, then $O^{(1)} \otimes O^{(2)}$ is an operator acting on $\mathcal{H}$ whose action is defined by

$$(O^{(1)} \otimes O^{(2)})(|\psi_i^{(1)}\rangle \otimes |\psi_i^{(2)}\rangle) \coloneqq (O^{(1)}|\psi_i^{(1)}\rangle) \otimes (O^{(2)}|\psi_i^{(2)}\rangle). \tag{2.11}$$

This also means that we can write the operators $O^{(1)}$ and $O^{(2)}$ as operators acting on $\mathcal{H}$ as $O^{(1)} \otimes I^{(2)}$ and $I^{(1)} \otimes O^{(2)}$ respectively, where $I^{(i)}$ is the identity operator for the i^{th} system. The same decomposition holds for the density matrix ρ of the composite system if the two subsystems are uncorrelated, that is $\rho = \rho^{(1)} \otimes \rho^{(2)}$. This then implies that that $\langle O^{(1)} \otimes O^{(2)} \rangle = \langle O^{(1)} \rangle \langle O^{(2)} \rangle$, using Eq. (2.9). This of course doesn't hold true when the two systems are *entangled*, in which case $\rho \neq \rho^{(1)} \otimes \rho^{(2)}$, meaning that the expectation value cannot be represented by this trivial decomposition.

In most cases, we are interested in studying only a subsystem of the composite one. Suppose, for example, that the two subsystems consist of the system S we are studying and the environment E with which it interacts, illustrated in Fig. 2.1. In this case, starting from the combined density operator ρ, we can arrive at the *reduced density operator* ρ_S of the system:

$$\rho_S = \text{tr}_E(\rho) \ , \tag{2.12}$$

where tr_E denotes the *partial trace* over the environment subsystem, defined by

$$\text{tr}_E(|\psi_i^{(S)}\rangle\langle\psi_j^{(S)}| \otimes |\psi_k^{(E)}\rangle\langle\psi_l^{(E)}|) = |\psi_i^{(S)}\rangle\langle\psi_j^{(S)}| \ \text{tr}(|\psi_k^{(E)}\rangle\langle\psi_l^{(E)}|) \ . \tag{2.13}$$

Having obtained the reduced density operator for the system, we now turn our attention towards the latter's time evolution. Keeping track of both system and envi-

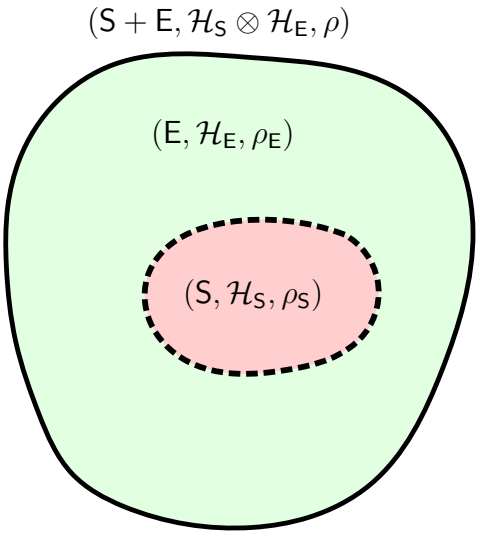

Figure 2.1: Typically, we are interested in the dynamics of a smaller system S (red), interacting with an environment E (green). Whilst the combined $S + E$ is usually closed (solid boundary), this system-environment interaction means that the dynamics of the system S cannot be described by unitary evolution.

ronment dynamics, however, can be mathematically and computationally expensive. In order to avoid this, we avoid keeping track of the environment's evolution explicitly, but instead focus on the evolution of the system and how it is influenced by the environment.

2.2 Master Equation formalism

In order to come up with the effective master equation detailing the evolution of the system, we follow closely the steps in Ref. [1]. Consider a Hamiltonian H acting on the composite system ρ in the Hilbert space $\mathcal{H}_S \otimes \mathcal{H}_E$, illustrated in Fig. 2.1. Then H can be written as $H = H_S + H_E + H_I$, where H_S and H_E are the Hamiltonians governing the free evolution of the system and environment respectively, whilst H_I is the Hamiltonian describing the interaction of the two subsystems. We will assume that H does not have an explicit time-dependence, so that we can write the interaction Hamiltonian in the interaction picture as

$$H_I(t) = U^\dagger(t) H_I U(t) \ , \tag{2.14}$$

where $U(t) = \exp\left(-\frac{i}{\hbar}(H_S + H_E)t\right)$ is the time evolution operator (assuming H does not depend explicitly on time). We can then make use of the interaction picture von Neumann equation (c.f. (2.8)) and integrate it once to obtain

$$\rho(t) = \rho(0) - \frac{i}{\hbar}\int_0^t \mathrm{d}s\ [H_I(s), \rho(s)]\ . \tag{2.15}$$

Then, after inserting the above back into the von Neumann equation and tracing over the environment (assuming that $\mathrm{tr}_E[H_I(t), \rho(0)] = 0$ with an adequate form of H_I), we find that

$$\frac{\mathrm{d}}{\mathrm{d}t}\rho_S(t) = -\frac{1}{\hbar^2}\int_0^t \mathrm{d}s\ \mathrm{tr}_E[H_I(t), [H_I(s), \rho(s)]]\ . \tag{2.16}$$

The above differential equation is still exact, and still contains the density matrix for the composite system. In order to eliminate this and obtain an equation which can be solved easily, we need to make a number of careful approximations, the first being the *Born approximation*, which essentially states that the effect of the system on the bath is small (i.e. weak-coupling approximation), which then allows us to write $\rho(t)$ as

$$\rho(t) \approx \rho_S(t) \otimes \rho_E\ , \tag{2.17}$$

where ρ_S and ρ_E are the system and environment density matrices, respectively. The second approximation we then take is known as the *Markov approximation*, which allows us to substitute $\rho_S(s)$ with $\rho_S(t)$ in the integrand. This approximation means that the state of the system at time t depends only on the state $\rho_S(t)$ at this time, effectively meaning that the system is 'memoryless'. This brings us to the Redfield equation:

$$\frac{\mathrm{d}}{\mathrm{d}t}\rho_S(t) = -\frac{1}{\hbar^2}\int_0^t \mathrm{d}s\ \mathrm{tr}_E[H_I(t), [H_I(s), \rho_S(t) \otimes \rho_E]]\ . \tag{2.18}$$

which, despite being time-local (i.e. ρ_S at time t depends only on $\rho_S(t)$), the system's time evolution still depends on our choice for the initial state. Thus, despite the

above being a *Born–Markov* master equation, we can still perform one additional simplification which will give us the master equation in the desired form, which removes the explicit dependence of the reduced density operator on our choice for $\rho_S(0)$ in the above integral. Indeed, we can avoid this initial time-dependence by substituting s with $t - s$ in the integrand and take the limit as the integral upper limit goes to infinity. This is justified as long as the integrand vanishes rapidly for s much larger than the timescale τ_E over which the bath correlation functions decay. We finally obtain a master equation which is time-local and in Born–Markov form, given by

$$\frac{\mathrm{d}}{\mathrm{d}t}\rho_S(t) = -\frac{1}{\hbar^2}\int_0^\infty \mathrm{d}s\ \mathrm{tr}_E[H_I(t), [H_I(t-s), \rho_S(t)\otimes\rho_E]]\ . \tag{2.19}$$

In order to simplify our master equation, we decompose the Schrödinger picture interaction $H_I \in \mathcal{H}_S \otimes \mathcal{H}_E$ as

$$H_I = \sum_\alpha A_\alpha \otimes B_\alpha\ , \tag{2.20}$$

where A_α and B_α act on $\mathcal{H}_S$ and $\mathcal{H}_E$, respectively, $A_\alpha^\dagger = A_\alpha$ and $B_\alpha^\dagger = B_\alpha$. Assuming that the spectrum of H_S is discrete, we can further decompose H_I into eigenoperators of the system Hamiltonian. This can be done by defining the new operators

$$A_\alpha(\omega) \coloneqq \sum_{\epsilon'-\epsilon=\hbar\omega} \Pi(\epsilon)A_\alpha\Pi(\epsilon')\ , \tag{2.21}$$

where $\Pi(\epsilon)$ is the projection operator for the eigenspace corresponding to ϵ, and the sum is all possible values of ϵ and ϵ' such that the difference between the two is $\hbar\omega$. It can be easily shown that these operators are indeed eigenoperators of the system Hamiltonian

$$[H_S, A_\alpha(\omega)] = -\hbar\omega A_\alpha(\omega)\ , \tag{2.22}$$

$$[H_S, A_\alpha^\dagger(\omega)] = \hbar\omega A_\alpha^\dagger(\omega)\ , \tag{2.23}$$

and that $A_\alpha^\dagger(\omega) = A_\alpha(-\omega)$ and hence in the interaction picture, we get that

$$e^{\frac{i}{\hbar}H_S t} A_\alpha(\omega) e^{-\frac{i}{\hbar}H_S t} = e^{-i\omega t} A_\alpha(\omega) \ , \tag{2.24}$$

$$e^{\frac{i}{\hbar}H_S t} A_\alpha^\dagger(\omega) e^{-\frac{i}{\hbar}H_S t} = e^{i\omega t} A_\alpha^\dagger(\omega) \ . \tag{2.25}$$

By summing over all possible energy differences and making use of the completeness relation we also get a relation between A_α and $A_\alpha(\omega)$:

$$\sum_\omega A_\alpha(\omega) = \sum_\omega A_\alpha^\dagger(\omega) = A_\alpha \ . \tag{2.26}$$

Hence, using (2.20), (2.24) and (2.26), we get a simple form for the interaction picture interaction Hamiltonian

$$H_I(t) = \sum_{\alpha,\omega} e^{-i\omega t} A_\alpha(\omega) \otimes B_\alpha(t) = \sum_{\alpha,\omega} e^{i\omega t} A_\alpha^\dagger(\omega) \otimes B_\alpha^\dagger(t) \ , \tag{2.27}$$

where $B_\alpha(t) = e^{\frac{i}{\hbar}H_B t} B_\alpha e^{-\frac{i}{\hbar}H_B t}$. We also note that, using the fact that $\mathrm{tr}_E[H_I(t), \rho(0)] = 0$, the average of the bath operators B_α vanishes, that is

$$\langle B_\alpha(t) \rangle \coloneqq \mathrm{tr}(B_\alpha(t)\rho_E) = 0 \ . \tag{2.28}$$

Now that we have an expanded form of the interaction Hamiltonian, we insert it back into our Born–Markov master equation (2.19) to obtain

$$\frac{\mathrm{d}}{\mathrm{d}t}\rho_S(t) = \frac{1}{\hbar^2} \int_0^\infty \mathrm{d}s \ \mathrm{tr}_E\{H_I(t-s)\rho_S(t)\rho_E H_I(t) - H_I(t)H_I(t-s)\rho_S(t)\rho_B\} + \mathrm{H.c.} \tag{2.29}$$

$$= \sum_{\omega,\omega'} \sum_{\alpha,\beta} e^{(\omega'-\omega)t} \Gamma_{\alpha\beta}(\omega) \left(A_\beta(\omega)\rho_S(t) A_\alpha^\dagger(\omega') - A_\alpha^\dagger(\omega') A_\beta(\omega)\rho_S(t) \right) + \mathrm{H.c.} \ , \tag{2.30}$$

where H.c. denotes the Hermitian conjugate, and

$$\Gamma_{\alpha\beta}(\omega) \coloneqq \frac{1}{\hbar^2}\int_0^\infty \mathrm{d}s e^{i\omega s}\langle B_\alpha^\dagger B_\beta(t-s)\rangle \tag{2.31}$$

is the *spectral correlation tensor* of the reservoir correlation functions defined by $\langle B_\alpha^\dagger(t)B_\beta(t-s)\rangle \coloneqq \mathrm{tr}_E\left(B_\alpha^\dagger(t)B_\beta(t-s)\rho_E\right)$. In most of the cases we shall consider, the environment state will be taken to be stationary, i.e. $[H_B, \rho_E] = 0$ (for example, a thermal state). This then means the correlation functions above are time homogeneous, that is

$$\langle B_\alpha^\dagger(t)B_\beta(t-s)\rangle = \langle B_\alpha^\dagger(s)B_\beta(0)\rangle \ , \tag{2.32}$$

which in turn implies that the spectral correlation tensor is time-independent. It should be noted that the Markov approximation is only valid as long as the environment correlation functions decay timescale τ_E is relatively small when compared to the timescale of the system relaxation time τ_R.

We are now able to make a final approximation, which allows us to discard any non-secular terms from our master equation; that is, terms involving $\omega' \neq \omega$. This is valid as long as the timescale of the system evolution (which is defined by the difference $|\omega - \omega'|,\ \omega \neq \omega'$) is considerably smaller than the system relaxation time τ_R, since this implies that the non-secular term oscillate very rapidly and hence can be ignored. This means that our master equation simplifies to

$$\frac{\mathrm{d}}{\mathrm{d}t}\rho_S(t) = \sum_\omega \sum_{\alpha,\beta} \Gamma_{\alpha\beta}(\omega)\left(A_\beta(\omega)\rho_S(t)A_\alpha^\dagger(\omega) - A_\alpha^\dagger(\omega)A_\beta(\omega)\rho_S(t)\right) + \mathrm{H.c.} \tag{2.33}$$

Transforming back to the Schrödinger picture involves simply adding the unitary evolution term appearing in the von Neumann equation to the RHS of the above. After rearranging Eq. (2.33) above, we obtain the final form of the Lindblad master

equation, given by

$$\frac{\mathrm{d}}{\mathrm{d}t}\rho_S = -\frac{i}{\hbar}[H_S+H_C,\rho_S]+\sum_{\omega}\sum_{\alpha,\beta}\gamma_{\alpha\beta}(\omega)\left(A_\beta(\omega)\rho_S A_\alpha^\dagger(\omega) - \frac{1}{2}\{A_\alpha^\dagger(\omega)A_\beta(\omega),\rho_S\}\right) , \tag{2.34}$$

where $\gamma_{\alpha\beta}(\omega) = \mathrm{Re}\left[\Gamma_{\alpha\beta}(\omega)\right]$, and H_C includes the additional energy shifts, that is

$$H_C = \sum_{\omega}\sum_{\alpha,\beta} S_{\alpha\beta}(\omega)A_\alpha^\dagger(\omega)A_\beta(\omega) , \tag{2.35}$$

with $S_{\alpha\beta}(\omega) = \mathrm{Im}\left[\Gamma_{\alpha\beta}(\omega)\right]$. Eq. (2.34) thus describes the evolution of the system in the presence of a dissipative environment, whose effects on the system are captured by the *dissipator*, which is given by the second term of the RHS.

2.2.1 Multiple environments

Having briefly outlined the formalism of master equations, we now turn our attention towards the two main environments with which a solid state system interacts, which are the electromagnetic and vibrational environment. We will first discuss briefly these two environments, and will then show how these give rise to the master equation describing the evolution of such solid state spins.

2.2.2 Light-matter interaction

Now that we have briefly introduced system-environment interactions, we can focus on one of the most fundamental interactions for solid state nanostructures, that is light-matter interactions involving a charged particle and free-space electromagnetic fields. We can describe a generic electromagnetic field by a vector potential $\mathbf{A}(\mathbf{r},t)$, $\mathbf{r}$ and t denoting the position and time-dependence of this potential, respectively, satisfying the homogenous wave equation:

$$\nabla^2\mathbf{A}(\mathbf{r},t) - \frac{1}{c^2}\frac{\partial^2}{\partial t^2}\mathbf{A}(\mathbf{r},t) = 0 . \tag{2.36}$$

In order to account for this electromagnetic field, we need to modify the Schrödinger equation in order to solve for the evolution of the charged particle, namely by adding an additional term to the momentum operator $-i\hbar\nabla \rightarrow -i\hbar\nabla + e\mathbf{A}(\mathbf{r},t)$ describing the effect of the electromagnetic field on the system. The time-dependent Schrödinger equation then reads

$$\left[-\frac{\hbar^2}{2m}\nabla^2 + \frac{\partial}{\partial t}\mathbf{r}\cdot e\mathbf{A}(\mathbf{r},t) + V(\mathbf{r})\right]\psi(\mathbf{r},t) = H\psi(\mathbf{r},t)\ , \tag{2.37}$$

where m and $V(\mathbf{r})$ are the effective mass of and the potential experienced by the charged particle, respectively. After substituting for $\mathbf{A}(\mathbf{r},t) = \frac{1}{2}\mathbf{B}(t)\times\mathbf{r}$, and making the dipole approximation (that is $\mathbf{A}(\mathbf{r},t) = \mathbf{A}(\mathbf{r}_d,t) \coloneqq \mathbf{A}(t)$ across the particle's region, whose location is given by $\mathbf{r}_d$), we obtain the final form of the time-dependent Schrödinger equation, given by

$$\left[-\frac{\hbar^2}{2m}\nabla^2 + e\mathbf{r}\cdot\mathbf{E}(t) + V(\mathbf{r})\right]\psi(\mathbf{r},t) = H\psi(\mathbf{r},t)\ . \tag{2.38}$$

Having simplified the Schrödinger equation, we can now compare it to the equation governing the dynamics for a non-interacting charged particle and obtain the term representing the matter-light interaction, which is the second term on the LHS of Eq. (2.38), that is

$$H_d = e\mathbf{r}\cdot\mathbf{E}(t) \coloneqq -\mathbf{D}\cdot\mathbf{E}(t)\ , \tag{2.39}$$

where, for a two-level system (TLS) with ground state $|0\rangle$ and excited state $|X\rangle$, the electron dipole operator $\mathbf{D}$ is given by $\mathbf{D} \coloneqq -e\mathbf{r} = \mathbf{d}_{0X}\,|0\rangle\langle X| + \mathbf{d}_{X0}\,|X\rangle\langle 0|$, with $\mathbf{d}_{X0} = \mathbf{d}_{0X}^*$ and zero diagonal terms due to the odd parity of the operator $\mathbf{r}$.

Suppose that our TLS interacts with a (classical) oscillating electric field given by

$$\mathbf{E}(t) = E_l(\mathbf{e}\mathrm{e}^{-i\omega_l t} + \mathbf{e}^*\mathrm{e}^{+i\omega_l t})\ , \tag{2.40}$$

where E_l is the amplitude of the electric field, $\mathbf{e}$ is the field's polarisation, and ω_l its

frequency. The time-dependent Hamiltonian for this system is then given by

$$H_S = \frac{1}{2}\hbar\omega_0\sigma_z + H_L \ , \tag{2.41}$$

where the first term represents the energy splitting between the two states of the TLS (σ_z being the usual Pauli operator), with transition frequency ω_0, whilst the second term is the interaction Hamiltonian of the TLS with this field, which, from Eq. (2.39), is then given by

$$H_L = -E_l(|0\rangle\langle X| + |X\rangle\langle 0|)\left[\mathbf{d}_{0X}\cdot(\mathbf{e}\mathrm{e}^{-i\omega_l t} + \mathbf{e}^*\mathrm{e}^{+i\omega_l t})\right] \ , \tag{2.42}$$

where we have assumed that the dipole moment $\mathbf{d}_{0X}$ is real for simplicity. The Hamiltonian in matrix form then reads

$$H = \begin{pmatrix} \hbar\omega_0/2 & -E_l\mathbf{d}_{0X}\cdot(\mathbf{e}\mathrm{e}^{-i\omega_l t} + \mathbf{e}^*\mathrm{e}^{+i\omega_l t}) \\ -E_l\mathbf{d}_{0X}\cdot(\mathbf{e}\mathrm{e}^{-i\omega_l t} + \mathbf{e}^*\mathrm{e}^{+i\omega_l t}) & -\hbar\omega_0/2 \end{pmatrix} \ . \tag{2.43}$$

Despite the innocuous form of (2.43), solving the Schrödinger equation is somewhat tedious due to the time-dependence of this Hamiltonian. In order to circumvent this issue, we will first move to a *rotating frame*, that is, we apply the unitary transformation

$$U(t) = \cos\left(\frac{\omega_l t}{2}\right)\mathbb{I}_2 + i\sin\left(\frac{\omega_l t}{2}\right)\sigma_z = \begin{pmatrix} \mathrm{e}^{i\omega_l t/2} & 0 \\ 0 & \mathrm{e}^{-i\omega_l t/2} \end{pmatrix} \ , \tag{2.44}$$

which moves us to a frame rotating with the frequency ω_l of the driving field. Transforming $|\psi(t)\rangle \to |\psi'(t)\rangle \coloneqq U(t)\,|\psi(t)\rangle$, Eq. (2.1) now becomes

$$i\hbar\frac{\mathrm{d}U^\dagger(t)}{\mathrm{d}t}\,|\psi'(t)\rangle + i\hbar\, U^\dagger(t)\frac{\mathrm{d}\,|\psi'(t)\rangle}{\mathrm{d}t} = HU^\dagger(t)\,|\psi'(t)\rangle \ , \tag{2.45}$$

which, after multiplying to the left by $U(t)$ and rearranging the terms, simplifies to

$$i\hbar\frac{\mathrm{d}\,|\psi'(t)\rangle}{\mathrm{d}t} = H'\,|\psi'(t)\rangle \ , \tag{2.46}$$

where the new Hamiltonian in the rotating frame, H', is given by

$$\begin{aligned} H' &= U(t)HU^\dagger(t) - i\hbar\, U(t)\frac{\mathrm{d}U^\dagger(t)}{\mathrm{d}t} \\ &= \begin{pmatrix} \hbar(\omega_0-\omega_l)/2 & -E_l\mathbf{d}_{0X}\cdot(\mathbf{e}+\mathbf{e}^*\mathrm{e}^{+2i\omega_l t}) \\ -E_l\mathbf{d}_{0X}\cdot(\mathbf{e}\mathrm{e}^{-2i\omega_l t}+\mathbf{e}^*) & -\hbar(\omega_0-\omega_l)/2 \end{pmatrix} , \end{aligned} \tag{2.47}$$

where the time-dependence of the transformed Hamiltonian is thus only due to the $\mathrm{e}^{\pm 2i\omega_l t}$ terms on the off-diagonal entries, double the frequency of the time-dependent parts in the lab frame Hamiltonian (2.43). We typically work at, or close to, *resonance*, that is, when the driving frequency ω_l is close to the TLS's transition frequency, such that $|\omega_l - \omega_0| \ll \omega_0$. In this regime, as long as $|E_l\mathbf{d}_{0X}| \ll \omega_0$, the rapidly oscillating terms on the off-diagonal entries do not affect the system dynamics appreciably, and can thus be dropped, resulting in the time-independent *rotating wave approximation* (RWA) Hamiltonian, given by

$$H = \frac{1}{2}\hbar\delta\sigma_z - \frac{1}{2}\hbar(\Omega\sigma_+ + \Omega^*\sigma_-) , \tag{2.48}$$

where $\delta = \omega_0 - \omega_l$ is the detuning, the *Rabi frequency* is given by $\Omega = \frac{2}{\hbar}E_l\mathbf{d}_{0X}\cdot\mathbf{e}$, and $\sigma_\pm$ are the raising and lowering operators for the TLS.

2.2.3 Lattice-matter interaction

Having described the interaction between an electric dipole and an electromagnetic field, we now briefly derive the Hamiltonian describing the interaction between a dipole and the surrounding lattice ions, although a much more detailed account can be found in Ref. [2]. These interactions play a significant role in the dynamics of solid state nanostructures, such as quantum dots or nitrogen vacancy centres in diamond, due to the inevitable solid state matrix surrounding the electron (these nanostructures are discussed in more detail in Chapter 3). The displacement of the lattice ions from their equilibrium position can be described by phonons, which are quantised vibrational excitations of the lattice. Since electronic excitations modify

the crystal lattice potential, which in turn determines the ionic equilibrium positions, the electron strongly interacts with the phonons in the crystal lattice, giving rise to the phonon-dressed electronic state, or *polaron*.

The lattice-matter interaction Hamiltonian can be obtained by integrating the unscreened electron-atom potential $V_{ep}(\mathbf{r})$ over the charge density $\rho(\mathbf{r})$ of the solid [2], that is

$$H_I^{pn} = \int d^3r \ \rho(\mathbf{r}) V_{ep}(\mathbf{r}) \tag{2.49}$$

Following the steps in Ref. [2], we arrive at the Hamiltonian

$$H_I^{pn} = \sum_{\mathbf{k},\mathbf{G}} M_{\mathbf{k}+\mathbf{G}} \varrho(\mathbf{k}+\mathbf{G})(b_{\mathbf{k}} + b_{-\mathbf{k}}^{\dagger}) \ , \tag{2.50}$$

where $\mathbf{k}$ and $\mathbf{G}$ denote momentum and reciprocal lattice vectors, respectively, $\varrho(\mathbf{k}+\mathbf{G})$ is the particle density operator, and $b_{\mathbf{k}}$ ($b_{\mathbf{k}}^{\dagger}$) is the $\mathbf{k}$-mode phonon annihilation (creation) operator. The coupling matrix element $M_{\mathbf{k}+\mathbf{G}}$ is given by

$$M_{\mathbf{k}+\mathbf{G}} = -V_{ei}(\mathbf{k}+\mathbf{G})(\mathbf{k}+\mathbf{G})\xi_{\mathbf{k}} \left(\frac{\hbar}{2\rho\nu\omega_{\mathbf{k}}} \right)^{1/2} \ , \tag{2.51}$$

with V_{ei} being the electron-ion potential, $\xi_{\mathbf{k}}$ the $\mathbf{k}$-mode phonon polarisation vector, ρ the mass density of the solid, and ν the lattice volume.

The excited states in semiconductors tend to be at a low energy; in fact, in thermal equilibrium, the former are at an energy band minimum, usually near an edge or centre. Thus, electrons do not interact with short-wavelength phonons and can as such be ignored to a good approximation. This means that we can retain only the $\mathbf{G} = 0$ term in the sum (2.50), as terms involving $G \neq 0$ correspond to short-wavelengths. In these materials, most interactions with long-wavelength phonons fall within two main categories. *Deformation potential coupling* to acoustic phonons is essentially the long-wavelength approximation of (2.51). This means that we may take the electron-ion potential to be constant $V_{eq}(\mathbf{k}) \xrightarrow[\mathbf{k}\to 0]{} D_c$ or $V_{eq}(\mathbf{k}) \xrightarrow[\mathbf{k}\to 0]{} D_v$, depending on whether the electron is in the conduction or valence band, respectively. In this limit, we also have that $\xi_{\mathbf{k}} \to \hat{\mathbf{k}}$, obtaining the deformation potential coupling

Hamiltonian

$$H_I^{pn,DP} = D \sum_{\mathbf{k}} \left(\frac{\hbar}{2\rho\nu\omega_{\mathbf{k}}} \right)^{1/2} |\mathbf{k}| \varrho(\mathbf{k}) (b_{\mathbf{k}} + b_{-\mathbf{k}}^{\dagger}) \ , \tag{2.52}$$

with the summation going only over longitudinal acoustic phonon modes, and $D \in \{D_c, D_v\}$. The second type of electron-acoustic phonon coupling is the *piezoelectric coupling*, with the corresponding interaction Hamiltonian given by

$$H_I^{pn,PZ} = i \sum_{\mathbf{k}} \left(\frac{\hbar}{2\rho\nu\omega_{\mathbf{k}}} \right)^{1/2} M_{\lambda}(\hat{k}) \varrho(\mathbf{k}) (b_{\mathbf{k}} + b_{-\mathbf{k}}^{\dagger}) \ , \tag{2.53}$$

where the coupling matrix element $M_{\lambda}(\hat{k})$ is independent of the magnitude of $\mathbf{k}$, but highly dependent on the latter's direction and the polarisation λ of the acoustic phonons, with different values obtained for *transverse acoustic* (TA) and *longitudinal acoustic* (LA) phonons.

Electron-acoustic phonon interactions may involve both types of interactions discussed here. Due to the fact that these two different processes are out of phase (deformation potential is real, whilst piezolectric interaction is imaginary [2]), the joint interaction Hamiltonian may be simply written down as

$$\begin{aligned} H_I^{pn} &= \sum_{\mathbf{k}} \left(\frac{\hbar}{2\rho\nu\omega_{\mathbf{k}}} \right)^{1/2} \tilde{M}(\mathbf{k}) \rho(\mathbf{k}) (b_{\mathbf{k}} + b_{-\mathbf{k}}^{\dagger}) \ ; \\ \tilde{M}(\mathbf{k}) &= D|\mathbf{k}| + iM_{\lambda}(\hat{k}) \ , \end{aligned} \tag{2.54}$$

and hence, $|\tilde{M}(\mathbf{k})|^2 = D^2|\mathbf{k}|^2 + |M_{\lambda}(\hat{k})|^2$, so that the two processes do not interfere (and hence may be treated separately) up to second order.

Furthermore, Eq. (2.54) can be further simplified if we consider a TLS: Defining the wavefunctions of the two states $|0\rangle$ and $|X\rangle$ as $\psi_0(\mathbf{r})$ and $\psi_X(\mathbf{r})$, respectively, we can define the corresponding *form-factors* as $\varrho_{00}(\mathbf{k}) \coloneqq \int d\mathbf{r} |\psi_0(\mathbf{r})|^2 \exp(i\mathbf{k} \cdot \mathbf{r})$ and $\varrho_{XX}(\mathbf{k}) \coloneqq \int d\mathbf{r} |\psi_X(\mathbf{r})|^2 \exp(i\mathbf{k} \cdot \mathbf{r})$ for the electron in the valence and conduction band, respectively. Assuming that the energy splitting between the ground and excited state is much larger than the phonon energies considered, the off-diagonal terms in the interaction (2.54) can be ignored due to negligible overlap between

the ground and excited state wavefunctions [3], and hence, after subtracting a term proportional to the identity, we arrive at the final, simplified interaction term

$$H_I^{pn} = |X\rangle\langle X| \sum_{\mathbf{q}} g_{\mathbf{k}}(b_{\mathbf{k}} + b_{-\mathbf{k}}^\dagger) \ , \tag{2.55}$$

where the coupling constant $g_{\mathbf{k}}$ is defined as

$$g_{\mathbf{k}} = \left(\frac{\hbar}{2\rho\nu\omega_{\mathbf{k}}}\right)^{1/2} \left[\tilde{M}_X(\mathbf{k})\varrho_{XX}(\mathbf{k}) - \tilde{M}_0(\mathbf{k})\varrho_{00}(\mathbf{k})\right] \ , \tag{2.56}$$

where, as defined in Eq. (2.54), $\tilde{M}_X(\mathbf{k}) = D_c|\mathbf{k}| + iM_\lambda(\hat{k})$ and $\tilde{M}_0(\mathbf{k}) = D_v|\mathbf{k}| + iM_\lambda(\hat{k})$.

Despite the already simplified phonon interaction Hamiltonian (2.55), the coupling constant still requires explicit evaluation, which is considerably hard to calculate unless we make assumptions about the geometry of the wavefunction. One such approximation is the *envelope function approximation* (also known as the $\mathbf{k}\cdot\mathbf{p}$ method), which states that it suffices to study the behaviour of the slowly varying function enveloping TLS wavefunction which varies more rapidly. For typical solid state systems, such as GaAs quantum dots, we can us the approximation of a spherically symmetric parabolic potential for both the valence and conduction bands, leading to the explicit form of the form factors $\varrho_{ii}(\mathbf{k}) = \exp(-d_i^2|\mathbf{k}|^2/4) \ ; i \in \{0, X\}$. This finally leads to the electron-phonon coupling constants

$$g_{\mathbf{k}} = \left(\frac{\hbar}{2\rho\nu\omega_{\mathbf{k}}}\right)^{1/2} \left[\tilde{M}_X(\mathbf{k})\mathrm{e}^{-d_X^2|\mathbf{k}|^2/4} - \tilde{M}_0(\mathbf{k})\mathrm{e}^{-d_0^2|\mathbf{k}|^2/4}\right] \tag{2.57}$$

which include both deformation and piezolelectric couplings between the TLS and $\mathbf{k}-$momentum acoustic phonons

2.2.4 Polaron frame multiple-environment master equation

Having defined both light- and lattice-matter interactions, we can derive the master equation for an electron (or hole) interacting with both the electromagnetic and vibrational environments. We are typically interested in weak optical driving of the electron, and hence the light-matter coupling can be treated perturbatively

[1], leading to a quasi-Lindblad optical dissipative term in the master equation (c.f. Eq. (2.34)). In solid state systems, the coupling to the vibrational environment cannot be treated in the same manner, however, as the weak-coupling treatment is, as the name suggests, only valid for weak vibrational coupling and/or low temperatures, which is not always the case for solid state systems such as quantum dots [3]. However, it should be noted that despite the limited regimes of validity, this weak-coupling treatment has been applied successfully to experimental data showing the effects of phonons on Rabi oscillations of a solid state exciton [4, 5].

As discussed at the beginning of Sec. 2.2.3, the electron-phonon interactions lead to the formation of the polaron quasiparticle, and hence, for strong couplings, it makes sense to move to a frame in which we consider the polaron dynamics instead. Moving to such a frame would then allow us to treat any weak 'leftover' phonon-interactions perturbatively. This then leads us to the formulation of the *polaron master equation* [6, 7, 8, 9, 10] which, provided interactions with the optical environment are weak enough, adequately captures the electron dynamics due to interactions with both environments [3].

2.2.4.1 Hamiltonian

We start this section by first introducing the Hamiltonian describing the system and environment ($S + E$) Hamiltonians (taking $\hbar = 1$):

$$\begin{aligned} H_S &= \delta \left|X\right\rangle \left\langle X\right| + \frac{\Omega}{2}\left(\left|0\right\rangle \left\langle X\right| + \left|X\right\rangle \left\langle 0\right|\right) \ , \\ H_E^{pt} &= \sum_{\mathbf{q},\,\lambda} \nu_{\mathbf{q}} a^\dagger_{\mathbf{q}\lambda} a_{\mathbf{q}\lambda} \ , \\ H_E^{pn} &= \sum_{\mathbf{k}} \omega_{\mathbf{k}} b^\dagger_{\mathbf{k}} b_{\mathbf{k}} \ , \end{aligned} \tag{2.58}$$

where, for ease of notation, we have added a term proportional to the identity to the energy splitting term, *pt* and *pn* denote terms involving the optical and vibrational environments, respectively, and $a^\dagger_{\mathbf{q}\lambda}$ ($a_{\mathbf{q}\lambda}$) is the $\mathbf{q}\lambda$-photon creation (annihilation) operator, with λ being the mode polarisation index. Recall that, in the dipole

approximation, the photon interaction Hamiltonian (Eq. (2.39)) is given by

$$H_I^{pt} = -\mathbf{d} \cdot \mathbf{E}(\mathbf{r}_d)(|0\rangle \langle X| + |X\rangle \langle 0|) \ , \tag{2.59}$$

with $\mathbf{E}(\mathbf{r})$ being the Schrödinger picture electric field in free space [11],

$$\mathbf{E}(\mathbf{r}) = i \sum_{\mathbf{q},\lambda} \left[\mathbf{u}_{\mathbf{q}\lambda}(\mathbf{r}) a_{\mathbf{q}\lambda} - \text{H.c.}\right] \ . \tag{2.60}$$

The spatial mode functions $\mathbf{u}_{\mathbf{q}\lambda}(\mathbf{r})$ for free space are given by

$$\mathbf{u}_{\mathbf{q}\lambda}(\mathbf{r}) = \sqrt{\frac{\omega_{\mathbf{q}\lambda}}{2\epsilon\nu}} \mathbf{e}_{\mathbf{q}\lambda} \mathrm{e}^{i\mathbf{q}r} \ , \tag{2.61}$$

where $\omega_{\mathbf{q}\lambda}$ and $\mathbf{e}_{\mathbf{q}\lambda}$ are the frequency and polarisation of the $\mathbf{q}\lambda$ electromagnetic field mode and ϵ is the electric permittivity. Finally, as discussed in Sec. 2.2.3, the interaction with the phonon bath can be represented by the Hamiltonian given by Eq. (2.55)

$$H_I^{pn} = |X\rangle \langle X| \sum_{\mathbf{k}} g_{\mathbf{k}} (b_{\mathbf{k}}^\dagger + b_{\mathbf{k}}) \ , \tag{2.62}$$

where, since $g_{\mathbf{k}}$ does not depend on the sign of $\mathbf{k}$ (cf. Eq. (2.57)), we have rearranged the terms in Eq. (2.55) to group $\pm\mathbf{k}$ terms together (instead of $b_{-\mathbf{k}}^\dagger$ and $b_{\mathbf{k}}$). Thus the total Hamiltonian is given by $H = H_S + H_E^{pt} + H_E^{pn} + H_I^{pt} + H_I^{pn}$.

Having defined all the relevant terms in the Hamiltonian, we are now able to move to the polaron frame by using the standard Lang–Firsov-type transformation $U = e^S$, with $S = |X\rangle \langle X| \sum_{\mathbf{k}} (g_{\mathbf{k}}/\omega_{\mathbf{k}})(b_{\mathbf{k}}^\dagger - b_{\mathbf{k}})$, obtaining the following transformed system Hamiltonian:

$$H_{SP} = \delta' |X\rangle \langle X| + \frac{\Omega}{2} \left(|0\rangle \langle X| B_- + |X\rangle \langle 0| B_+\right) \ , \tag{2.63}$$

where $\delta' = \delta - \sum_{\mathbf{k}} g_{\mathbf{k}}^2/\omega_{\mathbf{k}}$, and the phonon bath operators $B_\pm$ are defined as $B_\pm = \Pi_{\mathbf{k}} D_{\mathbf{k}}(g_{\mathbf{k}}/\omega_{\mathbf{k}})$, with $D_{\mathbf{k}}(\pm\alpha) = \exp\left[\pm(\alpha b_{\mathbf{k}}^\dagger - \alpha^* b_{\mathbf{k}})\right]$ being the $\mathbf{k}$th mode displacement operator. We define the *phonon spectral density* as $J_{pn}(\omega) = \sum_{\mathbf{k}} g_{\mathbf{k}}^2 \delta(\omega_{\mathbf{k}} - \omega)$, which is a useful measure of the electron-phonon coupling $g(\omega)$ in the continuum

limit. We use a superohmic exciton-phonon spectral density $J_{pn}(\omega)$ with exponential cut-off at frequency ω_c that is typically appropriate for self-assembled III-V quantum dots [12, 5]:

$$J_{pn}(\omega) = \alpha\omega^3 \mathrm{e}^{-\frac{\omega^2}{\omega_c^2}} \ . \tag{2.64}$$

In the polaron frame, the detuning is then given by $\delta' \to \delta - \int_0^\infty J_{pn}(\omega)/\omega$, and the light-matter interaction Hamiltonian Eq. (2.59) becomes

$$\begin{aligned} H_{IP}^{pt} =& i \left|0\right\rangle \left\langle X\right| B_- \sum_{\mathbf{q},\lambda} \mathbf{d}\cdot\mathbf{u}^*_{\mathbf{q}\lambda}(\mathbf{r}_d) a^\dagger_{\mathbf{q}\lambda} \\ & -i \left|X\right\rangle \left\langle 0\right| B_+ \sum_{\mathbf{q},\lambda} \mathbf{d}\cdot\mathbf{u}_{\mathbf{q}\lambda}(\mathbf{r}_d) a_{\mathbf{q}\lambda} \ . \end{aligned} \tag{2.65}$$

With the definitions $A_1^{pt} = \left|0\right\rangle\left\langle X\right|$, $A_2^{pt} = A_1^{pt\dagger}$, $B_1^{pt} = B_-$, $B_2^{pt} = B_1^{pt\dagger}$, $C_1 = i\sum_{\mathbf{q},\lambda} \mathbf{d}\cdot\mathbf{u}^*_{\mathbf{q}\lambda}(\mathbf{r}_d) a^\dagger_{\mathbf{q}\lambda}$, and $C_2 = C_1^\dagger$, we can compactly write the above Hamiltonian as

$$H_{IP}^{pt} = \sum_{i=1}^{2} A_i^{pt} \otimes B_i^{pt} \otimes C_i \ . \tag{2.66}$$

Since the second term in Eq. (2.63) contains system and environment operators, we identify this as our new exciton-phonon interaction term [3]. This new interaction term possesses a non-zero expectation value with respect to the thermal equilibrium bath state ρ_E^{pn}; tracing out the phonon bath degrees of freedom, we thus obtain

$$\begin{aligned} & \mathrm{Tr}_E^{pn}\left[\frac{\Omega}{2}\left(\left|0\right\rangle\left\langle X\right| B_- + \left|X\right\rangle\left\langle 0\right| B_+\right)\rho_E^{pn}\right] \\ & \quad = \frac{\Omega}{2}\left(\left\langle B\right\rangle \left|0\right\rangle\left\langle X\right| + \left\langle B\right\rangle \left|X\right\rangle\left\langle 0\right|\right) \ , \end{aligned} \tag{2.67}$$

where

$$\left\langle B\right\rangle = \exp\left[-\frac{1}{2}\int_0^\infty \mathrm{d}\omega \frac{J_{pn}(\omega)}{\omega^2}\coth(\beta\omega/2)\right] \ . \tag{2.68}$$

In order to be able to expand perturbatively, we therefore define the system-bath interaction with respect to this value. To this end, we add the expectation value by defining $\mathcal{B}_\pm = B_\pm - \left\langle B\right\rangle$ and $\Omega^{pn} = \left\langle B\right\rangle\Omega$ and regrouping our system and interaction

Hamiltonian terms, obtaining:

$$H_{SP} = \delta' \left|X\right\rangle \left\langle X\right| + \frac{\Omega^{pn}}{2} \left(\left|0\right\rangle \left\langle X\right| + \left|X\right\rangle \left\langle 0\right|\right) \ , \tag{2.69}$$

$$H_{IP}^{pn} = \frac{\Omega}{2} \left(\left|0\right\rangle \left\langle X\right| \mathcal{B}_- + \left|X\right\rangle \left\langle 0\right| \mathcal{B}_+\right) \ . \tag{2.70}$$

As in the case of Eq. (5.15), we introduce the operator labels $B_{1/2}^{pn} = \mathcal{B}_{\mp}$, $A_1^{pn} = \frac{\Omega}{2} \left|0\right\rangle \left\langle X\right|$ and $A_2^{pn} = A_1^{pn\dagger}$, allowing us to recast the above interaction Hamiltonian into the compact form

$$H_{IP}^{pn} = \sum_{i=1}^{2} A_i^{pn} \otimes B_i^{pn} \ , \tag{2.71}$$

which will prove useful for the derivation of the master equation.

2.2.4.2 Master Equation

Having obtained our Hamiltonian in the polaron frame and partitioned it into system, interaction and environment parts, we can make use of the generically derived microscopic coupling form of the second-order Born-Markov master equations of Ref. [1] (Eqn. 3.118). The interaction terms Eqs. (5.15) and (5.19) are of the required form underlying this derivation, and the resultant ME (in the interaction picture) reads:

$$\begin{aligned} \frac{\mathrm{d}}{\mathrm{d}t}\rho_{SP}(t) = & \\ & - \int_0^\infty \mathrm{d}\tau \ \mathrm{Tr}_E[H_{IP}(t), [H_{IP}(t-\tau), \rho_{SP}(t) \otimes \rho_E(0)]] \ , \end{aligned} \tag{2.72}$$

where $H_{IP}(t) = H_{IP}^{pn}(t) + H_{IP}^{pt}(t)$, and Tr_E denotes the trace over both environments [1]. It can be easily shown [3] that the right-handside (RHS) of the above equation can be split into two parts:

$$\begin{aligned} \frac{\mathrm{d}}{\mathrm{d}t}\rho_{SP}(t) = & \\ & - \int_0^\infty \mathrm{d}\tau \mathrm{Tr}_E^{pn}[H_{IP}^{pn}(t), [H_{IP}^{pn}(t-\tau), \rho_{SP}(t) \otimes \rho_E^{pn}(0)]] \\ & - \int_0^\infty \mathrm{d}\tau \mathrm{Tr}_E[H_{IP}^{pt}(t), [H_{IP}^{pt}(t-\tau), \rho_{SP}(t) \otimes \rho_E(0)]] \ . \end{aligned} \tag{2.73}$$

Since we assume that the (initial) environmental state is thermal, $\rho_E(0)$ factorises: $\rho_E(0) = \rho_E^{pn}(0) \otimes \rho_E^{pt}(0)$.

2.2.4.3 Phonon bath correlations

We proceed by analysing the first term on the RHS of Eq. (5.21) which captures the influence of phonons on the TLS dynamics with scattering rates determined by phonon correlation functions [8, 9, 10]. In the ME formalism, the rate $\gamma(\omega)$ of a dissipative process is given by $\gamma(\omega) = 2\mathrm{Re}\left[\int_0^\infty \mathrm{d}s K(s)\right]$, where $K(s)$ is the relevant correlation function. For our phonon dissipator, these functions are given by

$$\begin{aligned} C_{ii}^{pn}(\tau) &= \mathrm{Tr}_E^{pn}\left[\mathcal{B}_\pm^\dagger(\tau)\mathcal{B}_\pm(0)\rho_E^{pn}(0)\right] \\ &= \langle B\rangle^2(\mathrm{e}^{\phi(\tau)} - 1)\ , \end{aligned} \tag{2.74}$$

$$\begin{aligned} C_{ij}^{pn}(\tau) &= \mathrm{Tr}_E^{pn}\left[\mathcal{B}_\pm^\dagger(\tau)\mathcal{B}_\mp(0)\rho_E^{pn}(0)\right] \\ &= \langle B\rangle^2(\mathrm{e}^{-\phi(\tau)} - 1)\ , \end{aligned} \tag{2.75}$$

where $i, j \in \{1, 2\}$, $i \neq j$. After some algebra, we obtain a (non-secular) phonon dissipator of the form

$$\begin{aligned} &\gamma^{pn}(\omega')\mathcal{L}[\sigma_-] + \gamma^{pn}(-\omega')\mathcal{L}[\sigma_+] \\ &- \gamma_{cd}^{pn}(\omega')\mathcal{L}_{cd}[\sigma_-] - \gamma_{cd}^{pn}(-\omega')\mathcal{L}_{cd}[\sigma_+]\ , \end{aligned} \tag{2.76}$$

where $\mathcal{L}[C] = C\rho_{SP}C^\dagger - \frac{1}{2}\{C^\dagger C, \rho_{SP}\}$ and $\mathcal{L}_{cd}[C] = C\rho_{SP}C - \frac{1}{2}\{C^2, \rho_{SP}\}$. The rates $\gamma^{pn}(\pm\omega')$ and γ_{cd}^{pn} are calculated to be

$$\gamma^{pn}(\pm\omega') = \frac{(\Omega^{pn})^2}{4}\int_{-\infty}^{\infty}\mathrm{d}\tau\ \mathrm{e}^{\pm i\omega'\tau}\left(\mathrm{e}^{\phi(\tau)} - 1\right)\ , \tag{2.77}$$

$$\gamma_{cd}^{pn}(\omega') = \frac{(\Omega^{pn})^2}{4}\int_{-\infty}^{\infty}\mathrm{d}\tau\ \cos(\omega'\tau)\left(1 - \mathrm{e}^{-\phi(\tau)}\right)\ , \tag{2.78}$$

$$\gamma_{cd}^{pn}(-\omega') = \frac{(\Omega^{pn})^2}{4}\int_{-\infty}^{\infty}\mathrm{d}\tau\ \cos(\omega'\tau)\left(1 - \mathrm{e}^{-\phi(\tau)}\right)\ , \tag{2.79}$$

where $\phi(\tau) = \int_0^\infty \mathrm{d}\omega \frac{J_{pn}(\omega)}{\omega^2}[\coth(\beta\omega/2)\cos(\omega\tau) - i\sin(\omega\tau)]$. The rates $\gamma^{pn}(\omega')$ and $\gamma^{pn}(-\omega')$ correspond to enhanced radiative decay and incoherent excitation of the

TLS, respectively, whilst $\gamma_{cd}^{pn}(\pm\omega')$ constitute cross-dephasing rates corresponding to the non-secular terms of the form $\mathcal{L}_{cd}[C]$ in Eq. (2.76) which only affect off-diagonal terms of the optical Bloch equations [10].

2.2.4.4 Electromagnetic bath correlations

Having arrived at the Lindblad form of the phonon dissipator, we now turn our attention to the second term of the RHS of Eq. (2.73). As in the previous section, we begin by writing the explicit forms of the correlation functions obtained from Eq. (5.21):

$$\begin{aligned} & C_{ij}^{pt}(\tau) \\ & = \mathrm{Tr}_E\left[\left(B_i^{pt\dagger}(\tau)\otimes C_i^{\dagger}(\tau)\right)\left(B_j^{pt}(0)\otimes C_j(0)\right)\rho_E(0)\right] \ , \\ & = \mathrm{Tr}_E^{pn}\left[B_i^{pt\dagger}(\tau)B_j^{pt}(0)\rho_E^{pn}(0)\right]\mathrm{Tr}_E^{pt}\left[C_i^{\dagger}(\tau)C_j(0)\rho_E^{pt}(0)\right] \ , \end{aligned} \tag{2.80}$$

where $i,j\in\{1,2\}$. After substituting for the bath operators, we make use of the following relations

$$\begin{aligned} \mathrm{Tr}_E^{pt}\left[a_{\mathbf{q}\lambda}a_{\mathbf{q}'\lambda'}\rho_E^{pt}(0)\right] &= \mathrm{Tr}_E^{pt}\left[a_{\mathbf{q}\lambda}^{\dagger}a_{\mathbf{q}'\lambda'}^{\dagger}\rho_E^{pt}(0)\right] = \ 0 \ , \\ \mathrm{Tr}_E^{pt}\left[a_{\mathbf{q}\lambda}a_{\mathbf{q}'\lambda'}^{\dagger}\rho_E^{pt}(0)\right] &= \delta_{\mathbf{q}\mathbf{q}'}\delta_{\lambda\lambda'}(1+N(\nu_{\mathbf{q}})) \approx \ \delta_{\mathbf{q}\mathbf{q}'}\delta_{\lambda\lambda'} \ , \\ \mathrm{Tr}_E^{pt}\left[a_{\mathbf{q}\lambda}^{\dagger}a_{\mathbf{q}'\lambda'}\rho_E^{pt}(0)\right] &= \delta_{\mathbf{q}\mathbf{q}'}\delta_{\lambda\lambda'}N(\nu_{\mathbf{q}}) \approx \ 0 \ , \end{aligned} \tag{2.81}$$

where we have assumed that $\forall\omega > 0$, the Planck distribution $N(\omega) = [\exp(\beta\hbar\omega)-1]^{-1} \approx 0$. This means that we only have a single non-vanishing correlation function $C_{11}^{pt}(\tau)$. Following Ref. [3], we consider well-separated photon and phonon correlation times (appropriate for an unstructured photonic environment), so that $C_{11}^{pt}(\tau)$ reduces to the photon bath correlation function in the absence of a phonon bath. From Eq. (5.24), this correlation function is given by

$$C_{11}^{pt}(\tau) = \frac{|\mathbf{d}|^2}{6\pi^2\epsilon c^3}\int_0^{\infty}\mathrm{d}\nu\ \nu^3\ \mathrm{Tr}_E^{pn}\left[B_+^{pt}(\tau)B_-^{pt}(0)\rho_E^{pn}(0)\right] \ , \tag{2.82}$$

and hence, the spontaneous emission rate can be calculated from the Fourier transform of the correlation function

$$\begin{aligned}\Gamma_{11}^{pt}(\omega) &= \frac{|\mathbf{d}|^2}{6\pi^2\epsilon c^3}\int_0^\infty\int_0^\infty \mathrm{d}\tau\ \mathrm{d}\nu\ \nu^3 \mathrm{Tr}_E^{pn}\left[B_+^{pt}(\tau)B_-^{pt}(0)\rho_E^{pn}(0)\right]\mathrm{e}^{-i(\nu-\omega)\tau} \\ &= \frac{|\mathbf{d}|^2}{6\pi^2\epsilon c^3}\int_0^\infty \mathrm{d}\tau\ \langle B\rangle^2\,\mathrm{e}^{\phi(\tau)}\int_0^\infty \mathrm{d}\nu\ \nu^3\mathrm{e}^{-i(\nu-\omega)\tau}\ .\end{aligned} \tag{2.83}$$

In order to simplify Eq. (2.83), we make the assumptions that we are only interested in frequencies close to resonance (i.e. close to ω), and that the effective photon spectral density in free space is flat [3], which means that $\int_0^\infty \mathrm{d}\nu_{\mathbf{q}}\ \nu^3 \approx \int_{-\infty}^\infty \mathrm{d}\nu\ \nu^3$. Hence we can reduce further Eq. (2.83):

$$\begin{aligned}\Gamma_{11}^{pt}(\omega) &\approx \frac{|\mathbf{d}|^2\omega^3}{6\pi^2\epsilon c^3}\langle B\rangle^2\int_0^\infty \mathrm{d}\tau\ \mathrm{e}^{\phi(\tau)}\int_{-\infty}^\infty \mathrm{d}\nu\ \mathrm{e}^{-i(\nu-\omega)\tau} \\ &= \frac{|\mathbf{d}|^2\omega^3}{6\pi\epsilon c^3}\langle B\rangle^2\int_0^\infty \mathrm{d}\tau\ \mathrm{e}^{\phi(\tau)}\delta(\tau) \\ &= \frac{|\mathbf{d}|^2\omega^3}{6\pi\epsilon c^3}\langle B\rangle^2\,\mathrm{e}^{\phi(0)} \\ &= \frac{|\mathbf{d}|^2\omega^3}{6\pi\epsilon c^3} \\ &= \frac{1}{2}\gamma(\omega)\ ,\end{aligned} \tag{2.84}$$

where we have made use of the fact that $\mathrm{e}^{\phi(0)} = \langle B\rangle^{-2}$. Hence, with the above approximations, the spontaneous emission rate remains unaffected by the electron-phonon interactions, that is $\gamma(\omega) = |\mathbf{d}|^2\omega^3/3\pi\epsilon c^3$.

2.3 Collective effects in atomic and solid state systems

Collective behaviour in atomic system has been the subject of several studies of the last few decades [13, 14, 15] and is still a highly active field of research [16, 17, 18]. For atomic systems, the vibrational environment does not play an important role, and thus most research focussed mainly on the electromagnetic environment. For

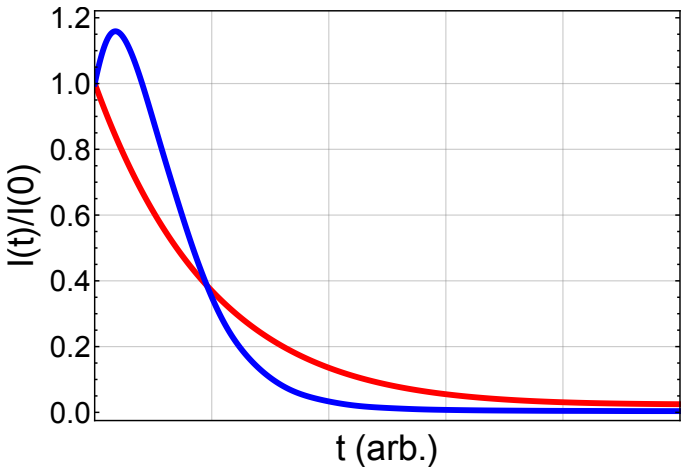

Figure 2.2: Spontaneous emission intensity against time for an ensemble of emitters. For an independent ensemble (red), the decay follows a simple exponential law. On the other hand, collective effects for separations much lower than the emission wavelength drastically change the decay dynamics of the sample (blue), showing the two key features of superradiance; the intensity increasing above the initial value, followed by a faster decay.

solid state systems, however, these environmental interactions can play a key role in the emitter's dynamics [19, 3, 20, 21, 22], as we have already seen in Section. 2.2.4. In this section, whilst we will still focus mainly on the optical collective behaviour of an ensemble of emitters, whilst a brief prelude to the collective vibrational effects will also be given.

2.3.1 Collective radiative emission

When a sparse ensemble of emitters (such as atoms or quantum dots) is prepared in the (joint) excited state, the emitters spontaneously emit photons and follow an exponential decay law, with the decay constant given by the spontaneous emission rate (c.f. Eq. 2.84). Thus, the emitters interact independently with the optical environment. This simple decay law cannot describe, however, the dynamics of a dense ensemble of emitters. In such case, the collective system decays much more quickly and stronger than the independent case, giving rise to the *superradiance* phenomenon [1, 13, 14]. More specifically, if the emitters interact with a common electromagentic field having wavelength much larger than the separation between emitters, the sample is permutationally invariant with respect to the location of the emitters. Thus, the latter interact coherently with the surrounding electromagentic

field and emit a strong burst of light, with the intensity proportional to the square of the number of emitters, as shown in Fig. 2.2.

Consider a sample of N identical TLSs, with transition frequency ω, located at positions $\mathbf{r}_j;\ j \in \{1, 2, ..., N\}$. The system Hamiltonian is then be given by

$$H_S = \frac{1}{2}\hbar\omega \sum_{i=1}^{N} \sigma_z^{(i)} \ . \tag{2.85}$$

Moreover, if the sample is interacting with an electromagnetic field given by Eq. (2.60), the interaction Hamiltonian (c.f. Eq. (2.59)) is given by

$$H_I^{pt} = -\sum_{i=1}^{N} \mathbf{d_i} \cdot \mathbf{E}(\mathbf{r}_i)(|0_i\rangle \langle X_i| + |X_i\rangle \langle 0_i|) \ , \tag{2.86}$$

where $\mathbf{d_j}$, $|0_j\rangle$ and $|X_j\rangle$ are the dipole moment, ground and excited states of the j^{th} TLS, respectively (for simplicity, we shall assume $\mathbf{d}_j = \mathbf{d},\ \forall j$ unless otherwise stated). The weak coupling collective master equation is found to be [1, 11]

$$\frac{\mathrm{d}}{\mathrm{d}t}\rho_N(t) = -\frac{i}{\hbar}[H_S + H_C, \rho_N] + \sum_{i,j=1}^{N} \gamma_{ij} \left(\sigma_-^{(j)} \rho_N \sigma_+^{(i)} - \frac{1}{2}\{\sigma_+^{(i)}\sigma_-^{(j)}, \rho_N\} \right) \ , \tag{2.87}$$

where, ignoring the self Lamb shift term, we obtain a similar form to Eq. (2.34), with H_C being the off-diagonal Lamb shift term which also corresponds to a *Förster Hamiltonian* giving rise to coherent, distant-dependent interactions between the different TLSs in the sample. More specifically, assuming parallel dipoles for simplicity, H_C and γ_{ij} are given by

$$\begin{aligned} H_{C,ij} &= (1 - \delta_{ij})\frac{1}{2}\mathcal{G}(q_0 r_{ij})\gamma_0 \ , \\ \gamma_{ij} &= (1 + \mathcal{F}(q_0 r_{ij}))\gamma_0 \ , \end{aligned} \tag{2.88}$$

where r_{ij} is the distance between the i^{th} and j^{th} dipoles, $q_0 = 2\pi/\lambda_0$, with λ_0 being the emission wavelength, and $\mathcal{G}(x)$ and $\mathcal{F}(x)$ are geometrical factors [11, 1, 23] given by:

$$\begin{aligned}\mathcal{G}(x) &= \frac{3}{2}\left(\frac{\sin(2x)}{(2x)^2} + \frac{\cos(2x)}{(2x)^3} - \frac{\cos(2x)}{2x}\right) \ , \\ \mathcal{F}(x) &= \frac{3}{2}\left(\frac{\sin(2x)}{2x} + \frac{\cos(2x)}{(2x)^2} - \frac{\sin(2x)}{(2x)^3}\right) \ .\end{aligned} \tag{2.89}$$

Hence, in the limit of $r_{ij} \to \infty$ we get that $H_{C,ij}, \gamma_{ij} \to 0$. Indeed these collective effects become negligible at separations exceeding the emission wavelength of the emitter [24]. It should be noted that whilst optical driving has been omitted from our brief calculation, a more thorough analysis involving a classical driving fields leads to the same collective results, as can be seen from Ref. [11].

2.3.2 Collective vibrational effects

We now turn our attention to vibrational collective behaviour in solid-state nanostructure ensembles. For simplicity, we take $N = 2$ dipoles, although the results can be easily extended to any number of TLS. We start from the Hamiltonian Eq. (2.58) for two driven TLSs, that is

$$\begin{aligned}H_S =& \delta_1 \left|X_1\right\rangle \left\langle X_1\right| + \frac{\Omega_1}{2}\left(\left|0_1\right\rangle \left\langle X_1\right| + \left|X_1\right\rangle \left\langle 0_1\right|\right) \\ &+ \delta_2 \left|X_2\right\rangle \left\langle X_2\right| + \frac{\Omega_2}{2}\left(\left|0_2\right\rangle \left\langle X_2\right| + \left|X_2\right\rangle \left\langle 0_2\right|\right) \ , \\ H_E^{pt} =& \sum_{\mathbf{q},\,\lambda} \nu_{\mathbf{q}} a^\dagger_{\mathbf{q}\lambda} a_{\mathbf{q}\lambda} \ , \\ H_E^{pn} =& \sum_{\mathbf{k}} \omega_{\mathbf{k}} b^\dagger_{\mathbf{k}} b_{\mathbf{k}} \ ,\end{aligned} \tag{2.90}$$

where $|0_j\rangle$ and $|X_j\rangle$ denote the ground and excited states of the j^{th} state, and we have defined the position dependent phonon couplings as $g^{(j)}_{\mathbf{k}} = |g_{\mathbf{k}}| e^{i\mathbf{k}\cdot\mathbf{r}_j}$ [25]. For fully collective effects, $g^{(1)}_{\mathbf{k}} = g^{(2)}_{\mathbf{k}} \neq 0, \ \forall k$, whereas, for partial collective behaviour, $g^{(1)}_{\mathbf{k}}$ and $g^{(2)}_{\mathbf{k}}$ are non-zero for some common phonon modes (albeit not $\forall k$). For completely disjoint baths, and hence no collective effects, the two emitters are then coupled to mutually exclusive sets of phonon modes. In this section, we take the general case of partial collective behaviour, which includes the full and partial collective

behaviours as its limits.

Following the steps of Sec. 2.2.4, we derive the first few steps of the polaron master equation in order to obtain the 'collective parameter', which, as we shall see, determines how strong the collective effects induced from common vibrational bath modes are. To this end, we define a more general polaron transformation for two TLS (taking into account any common bath modes):

$$\begin{aligned} \mathrm{e}^{S} &\coloneqq \exp\left(\left|X_1\right\rangle\left\langle X_1\right| P_1 + \left|X_2\right\rangle\left\langle X_2\right| P_2\right) \ , \\ P_j &= \sum_{\mathbf{k}} \left(\frac{g_{\mathbf{k}}^{(j)}}{\omega_{\mathbf{k}}} b_{\mathbf{k}}^{\dagger} - \frac{g_{\mathbf{k}}^{(j)*}}{\omega_{\mathbf{k}}} b_{\mathbf{k}} \right) \ , \end{aligned} \tag{2.91}$$

The polaron transformation (2.91) can then be separated using Baker–Campbell–Hausdorff formula as

$$\begin{aligned} U = \mathrm{e}^{S} &= \mathrm{e}^{S_1}\mathrm{e}^{S_2} \exp\left(-\frac{1}{2} \left|X_1\right\rangle\left\langle X_1\right| \left|X_2\right\rangle\left\langle X_2\right| \left[P_1, P_2\right] \right) \\ &= U_1 U_2 \exp\left(-\mathcal{C} \left|X_1\right\rangle\left\langle X_1\right| \left|X_2\right\rangle\left\langle X_2\right|\right) \ , \end{aligned} \tag{2.92}$$

where $U_j \coloneqq \exp(S_j) = \exp(\left|X_j\right\rangle\left\langle X_j\right| P_j)$, and $\mathcal{C} \coloneqq \frac{1}{2}[P_1, P_2]$.The transformed lowering operators for the two TLSs are then found to be

$$\begin{aligned} U\sigma_{-}^{(1)}U^{\dagger} &= \sigma_{-}^{(1)}\mathrm{e}^{-P_1} \exp\left(\mathcal{C}^* \left|X_2\right\rangle\left\langle X_2\right|\right) \ , \\ U\sigma_{-}^{(2)}U^{\dagger} &= \sigma_{-}^{(2)}\mathrm{e}^{-P_2} \exp\left(\mathcal{C} \left|X_1\right\rangle\left\langle X_1\right|\right) \ , \end{aligned} \tag{2.93}$$

from which we can see how the quantity $\mathcal{C}$ determines the degree of collective behaviour. Indeed, if the two systems are interacting equally with the same vibrational modes (equivalent to setting $\mathbf{\Delta r} = 0$ and $K_{sub}^{(1)} = K_{sub}^{(2)}$), we get that $U = U_1 U_2$ since $P_1 = P_2$. The same limit can be obtained for the other extreme, that is, $\mathbf{\Delta r} \to \infty$. In this case, the two systems are independent. One can easily show that this factor

can be simplified to

$$\mathcal{C} = i \sum_{\mathbf{k}} \frac{|g_{\mathbf{k}}|^2}{\omega_{\mathbf{k}}^2} \sin(\mathbf{k} \cdot \boldsymbol{\Delta}\mathbf{r}) \ , \tag{2.94}$$

where $\boldsymbol{\Delta}\mathbf{r} \coloneqq \mathbf{r}_2 - \mathbf{r}_1$. In the continuum limit, we get that

$$\mathcal{C} \to \int_0^\infty \frac{J_{pn}(\omega)}{\omega^2} f(\boldsymbol{\Delta}\mathbf{r}, \omega) \tag{2.95}$$

For 1D phonons, which we consider in this section for simplicity, the geometrical factor $f(\boldsymbol{\Delta}\mathbf{r}, \omega) = \sin(\omega|\boldsymbol{\Delta}\mathbf{r}|/c)$, and hence this gives rise to a rapidly oscillating term if $|\boldsymbol{\Delta}\mathbf{r}| \gg \lambda_{pn}$, where λ_{pn} is the phonon wavelength. Thus, for large separations, the phonon environment does not give rise to any collective behaviour as exponential terms involving $\mathcal{C}$ average out, resulting in independent phonon baths.

Chapter 3

Solid State Systems

Having given an overview of the vibrational and electromagnetic environments, and their effects on a general TLS, we shall now briefly discuss specific examples of solid state nanostructures, whose dynamics are heavily influenced by these environments. As we shall see, such systems tend to have rich Hilbert spaces, and thus allow us to identify effective subspaces which we can use for various quantum metrology and information applications.

3.1 Quantum dots

In this section, a brief introduction to *self-assembled* quantum dots shall be given, starting from their fabrication process. We then discuss some approximations which allow us to treat a quantum dot as a simple TLS. Finally, we give a brief description of the dipole selection rules, which give rise to the several optical transitions available for these nanostructures.

3.1.1 Fabrication of self-assembled quantum dots

Quantum dots are semiconductor heterostructures embedded or deposited in a higher band gap environment. In our case, we shall be considering self-assembled quantum dots, which are commonly fabricated using techniques such as Molecular Beam Epitaxy (MBE) and Metal Organic Chemical Vapour Deposition (MOCVD). A semiconducting layer is grown on a substrate with a higher constant, and, after a

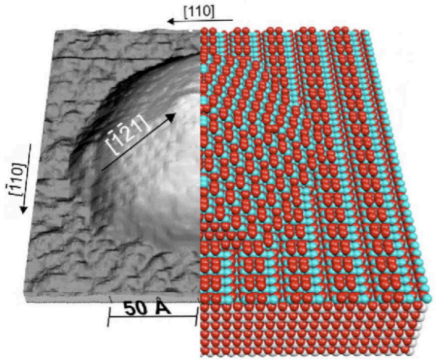

Figure 3.1: A self-assembled InAs quantum dot grown on GaAs substrate. The left part shows a high resolution STM image and the right is a numerical model based on DFT [26]. Picture courtesy of Dr. Thomas Hammerschmidt.

certain thickness of grown material is obtained (determined by the latter's chemical potential and lattice constant mismatch between the two layers), nucleation of randomly shaped islands occurs (c.f. Fig. 3.1). These islands are then overgrown by the substrate, 'capping' off the grown layer and embedding these regions in substrate material. This growth process is known as Stranski–Krastanov growth. Although the grown islands are fairly random in shape and position, several layers of material can be stacked on top of each other, resulting in the lining up of these islands due to strain minimization.

The difference in band gap allows the charge carriers of the dot to be trapped in a three-dimensional spatial confinement potential, resulting in discrete energy levels similar to the ones of a particle-in-a-box model. This means that most of the single atom experiments can be reproduced using quantum dots (such as Rabi oscillations [27] and anti-bunching [28]), earning quantum dots the title of 'artificial atoms'.

3.1.2 Quantum dots as two-level systems

When an electron is excited to the conduction band, it leaves a hole behind, forming an electron-hole pair known as an *exciton*[1]. The energy required to create an exciton is less than the bulk semiconductor band gap, and hence the excitons are trapped in the quantum dot. As a result of the overlap between the wavefunctions

[1]This is known as a *charge-neutral exciton* (X^0 transition). Negative (Positive) charged excitons, or *trions* (X^- (X^+) transition) are created when there are two electrons (holes) involved in the transition.

of the fixed electron and hole, the exciton has an associated transition dipole and, moreover, an associated lifetime corresponding to the electron-hole recombination time.

Despite their seemingly small size, quantum dots are extremely hard to model from a many-body perspective. Colloidal quantum dots can contain anywhere from 10^2 to 10^5 atoms, the electrons of which mutually interact via long range Coulomb force. However, a number of approximations have been devised over the years to reduce this complex system to, effectively, a single TLS. Doing so would mean that the many-body problem would be reduced to solving a single Schrödinger equation. The first approximation employed is known as the *effective mass approximation*, in which the electrons are treated as free particles with a modified, or effective, mass, after accounting for the interaction with the crystal lattice (effectively treating a bound particle as free, but with a modified mass). The second approximation is the envelope function approximation, discussed in Sec. 2.2.3. Although these two approximations seem rather simplistic, they have been found to work well in practice.

In addition to the above approximations, infinite square wells and harmonic potentials in the growth and lateral directions, respectively, are often assumed, which is considered to be a simple yet realistic approach. However, more advanced treatments can be employed instead, such as the *empirical pseudopotential method* (EPM) [29] or *Density functional theory* (DFT) [30], which we shall not go into since they are not important for this thesis. These approximations result in the confinement potential having non-equidistant energy levels. Hence, it is possible to drive one transition by carefully choosing the appropriate driving frequency, meaning that the quantum dot behaves, effectively, like a simple TLS.

3.1.3 Selection rules

Let us consider the dipole moment of the exciton, which depends on the overlap of the electron and hole wavefunctions, and is defined as

$$\mathbf{d} = e \int \psi_e^*(\mathbf{r}) \mathbf{r} \psi_h(\mathbf{r}) \, \mathrm{d}\mathbf{r} \ , \tag{3.1}$$

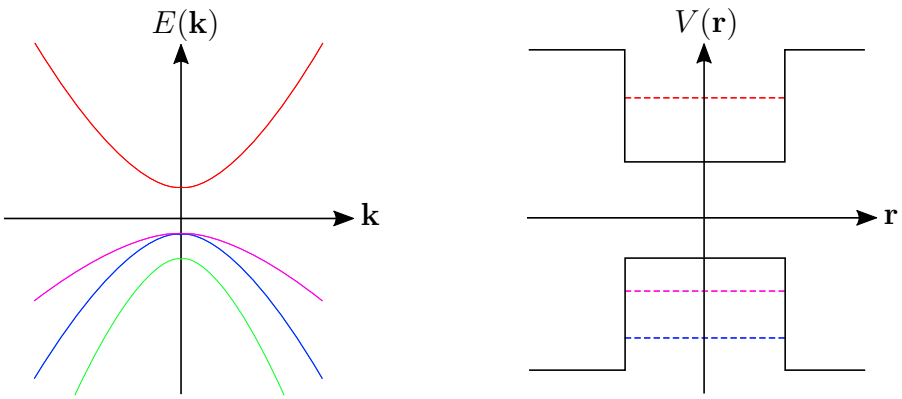

Figure 3.2: (Left) Dispersion relation of the electrons and holes near the band edge, showing the presence of electrons (red), heavy (pink), light (blue) and split-off (green) holes. (Right) The discrete energy level structure for electrons and holes due to the dot's spatial confinement, showing the lifting of the degeneracy of the light and heavy holes due to their different effective masses.

where $\psi_e(\mathbf{r})$ and $\psi_h(\mathbf{r})$ are the electron and hole wavefunctions, respectively. This integral, under the approximations mentioned above, can be split up into two integrals, one describing the overlap of the electron and hole wavefunctions, whilst the other contains the relevant Bloch functions. In order to study the selection rules for a quantum dot, we need to analyze these Bloch functions for the symmetry features of the wavefunctions. The conduction band has s-like orbital wavefunction symmetry, with total (orbital) angular momentum $J = \frac{1}{2}$ ($L = 0$), whilst the valence band has two bands due to the p-like symmetry, one with total (orbital) angular momentum $J = \frac{1}{2}$ ($L = 0$) and another with total (orbital) angular momentum $J = \frac{3}{2}$ ($L = 1$). The states of the valence $J = \frac{1}{2}$ band are known as split-off holes, due to the band's shift caused by spin-orbit coupling, whilst the $J = \frac{3}{2}$ band is further divided into $J_z = \pm\frac{3}{2}$ "heavy" holes and $J_z = \pm\frac{1}{2}$ "light" holes. The dispersion relation for the electrons and holes, as well as the respective discrete energy levels, is depicted in Fig. 3.2.

In this configuration, one can easily see that there are only four dipole allowed transitions for single photon processes. Electrons in the $J_z = \frac{3}{2}$ and $J_z = \frac{1}{2}$ valence states can be excited to the $J_z = \frac{1}{2}$ and $J_z = -\frac{1}{2}$ conduction states, respectively, by σ^- photons propagating in the z direction, orthogonal to the quantum dot's plane. Similarly, electrons in the $J_z = -\frac{3}{2}$ and $J_z = -\frac{1}{2}$ valence states can be excited to the

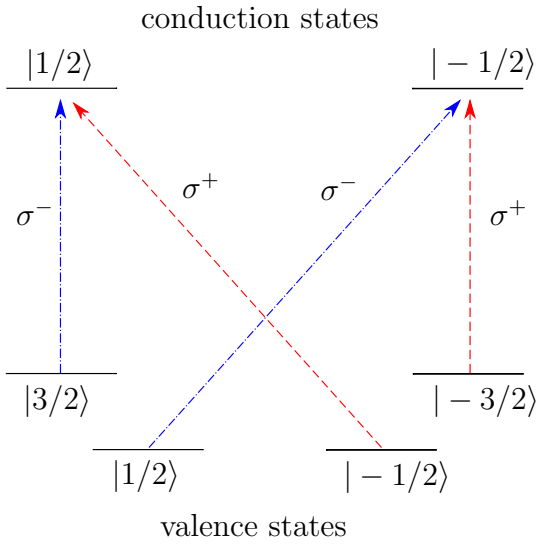

Figure 3.3: Selection rules for transitions between the lower conduction and valence band states, where the state $|m_j\rangle$ denotes the state with $J_z = m_j$.

$J_z = -\frac{1}{2}$ and $J_z = \frac{1}{2}$ conduction states, respectively, by σ^+ photons propagating in the z direction. A schematic of these dipole-allowed transitions is given in Fig. 3.3, showing how different optical polarisations can target different pairs of valence and conduction band states, forming a basic TLS.

3.2 Nitrogen Vacancy centres

Nitrogen vacancy (NV) centres are a central system in many quantum metrological protocols [31, 32, 33, 34, 35, 36] mainly due to their microwave addressability and the ability of reading out the spin optically. In this section, we will briefly describe the properties that define neutral (NV^0) and charged ($NV^{\pm}$) states of an NV centre, as well as the fabrication process of these diamond defects.

3.2.1 Charge properties and control of NV centres

NV centres are a type of point defect in the diamond lattice. As the name suggests, these point defects are formed by substituting a nitrogen atom and a carbon vacancy in the lattice structure, both of which define the charge properties of the resulting defect. In the nitrogen atom, three out of five of its valence electrons form covalent bonds with the surrounding carbon atoms, leaving two unpaired electrons.

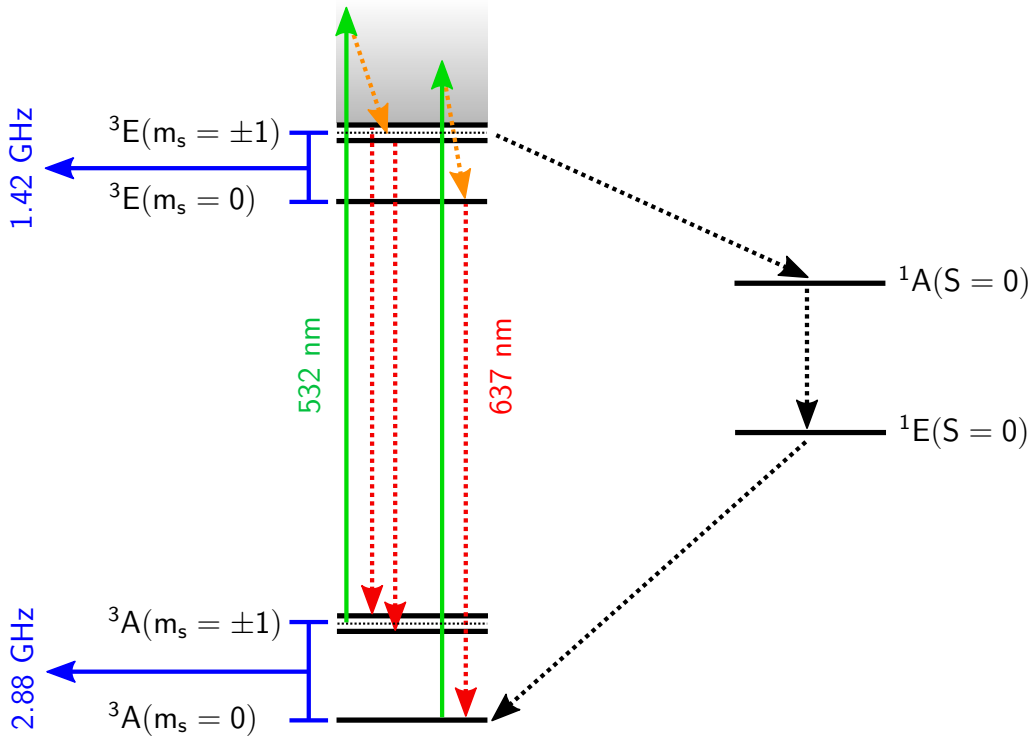

Figure 3.4: Energy level diagram of an NV centre. The preferential non-spin-preserving transition through the (metastable) singlet states ^1A and ^1E (black dotted arrows) allows the spin to be read out optically. The green arrows indicate excitation into the phonon sideband (grey), the red lines indicate the spin-preserving radiative transitions, and the orange lines represent vibrational, non-radiative, relaxation to the excited state manifold.

The vacancy, on the other hand, has three unpaired electrons, two of which form a quasi-covalent bond, thus effectively leaving only one available electron from the lattice vacancy. The resulting atomic system then consists of the nitrogen and vacancy along the axis of the NV centre, and three carbon atoms at the base of the axis, forming a triangular pyramidal structure having C_{3v} symmetry, that is, with 120° rotational symmetry about the NV axis, as well as three vertical plane symmetries (each plane containing the axis and a carbon atom). This is the basic structure of the neutral NV^0 centre, which, however, cannot be addressed optically or magnetically.

Luckily, NV centres can trap electrons from the nitrogen donors in the lattice, resulting in the net negative charge of the NV^- centre which is typically done by applying external voltage to a doped diamond p-n junction [37]. This trapped electron then may form a spin pair with the unpaired vacancy electron, resulting in an $S = 1$ spin system. Unlike its neutral counterpart, the negatively charged state

of the NV centre is magneto-optically active, making it an excellent platform for photoluminescence experiments. Furthermore, the ability to manipulate the electron spin magnetically is especially useful to lift the degeneracy of the $m_s = \pm 1$ sublevels in the ground and excited state. However, possibly the most desirable feature of NV^- centres is the ability to address them both using microwave radiation and optically. In fact, the transition energy separation of the $m_s = 0$ and $m_s = \pm 1$ states is within the microwave region, thus allowing control over the $m_s = 0$ and $m_s = \pm 1$ populations. Moreover, it is also possible to optically control the population of certain sublevels of the ground and excited states [38], as we briefly discuss in Sec. 3.2.3.

3.2.2 Fabrication

Having discussed the basic properties of the different charge states of NV centres, we can now very briefly discuss fabrication of these point defects by means of ion irradiation and annealing [39]. By using high energy ion irradiation, several kinds of defects are created in the sample, one type of which being Frenkel pairs, which are defects created when a lattice ion is displaced from its lattice position to an interstitial site. Annealing then allows these defects to move around, with some pairs separating and creating the individual vacancy sites (which then form part of the NV centre), with the mobile interstitials aiding nitrogen diffusion and aggregation. The annealing treatment also serves to remove any additional defects which deplete the photoluminescence of the sample. During this heat treatment (at around $600 - 800°C$), most of the NV centres form due to mobilisation of the substitutional nitrogen and vacancy sites, with the former trapping the latter due to strain caused on the lattice by the implanted nitrogen atoms (although other processes can cause additional nitrogen vacancy pairs to develop, such as divacancies consisting of vacancies trapped by N_2 defects [39].).

3.2.3 NV centres as two level systems

We now discuss the level structure of an NV centre[2], and how we can find a suitable two level subspace which allows for optical and microwave control. The level structure is shown in Fig. 3.4, with ^3A and ^3E being the ground and excited states, having the spin sublevels $m_s = -1, 0, 1$ (due to the NV centre having spin S=1). Due to the NV centre's C_{3v} symmetry, the $m_s = \pm 1$ states are degenerate for both the ground and excited states, although this degeneracy can be lifted by applying an external magnetic field.

An attractive feature of the NV defects is the large dipole moments of the allowed transitions, meaning that these transitions can be optically detected. Furthermore, optical manipulation is possible due to the allowed, non-radiative transition from the excited $m_s = \pm 1$ state to the $m_s = 0$ ground state. Due to this additional non-spin-preserving, and thus non-radiative, transition from the excited $m_s = \pm 1$ states to the ground $m_s = 0$ state via the metastable states (Fig. 3.4), it is possible to read out the spin state via the (unbalanced) fluorescence signal. More specifically, as the excited $m_s = \pm 1$ spin population is shelved in the metastable singlet states, whereas the population of the excited $m_s = 0$ state decays radiatively to the ground $m_s = 0$ state, the average fluorescence signal for the $m_s = \pm 1$ transiton is lower than the signal for the $m_s = 0$ transition [40]. Thus, optical spin readout is also possible due to the heavy dependence of the fluorescence signal on the electron spin state [41].

[2]We shall be referring to the negative NV centre state NV^- simply as NV, unless otherwise stated.

Chapter 4

An introduction to Measurement-based quantum computation

Quantum computation is a by now mature [42, 43], but highly active area of research [44, 45, 46], yet it suffers several outstanding questions regarding the nature and requirements for a system to be considered as a 'quantum computer'; even the advantages of quantum computers over their classical counterparts are still not yet fully classified. Several models have been developed to describe quantum computation, including the measurement-based quantum computation (MBQC) [47, 48, 49, 50], quantum circuit [43, 51] and adiabatic quantum computation models [52], although this is far from a comprehensive list of the models developed over the last few decades. While every model has its own set of advantages and experimental challenges, the MBQC model offers solutions to some of the major downfalls of the 'traditional' circuit model.

In this chapter, we shall in fact focus on the MBQC model, which will serve us as a brief introduction to the concepts behind Chapter 6, which involves making use of the four-level structure of a quantum dot and the corresponding selection rules in order to generate *cluster states*.

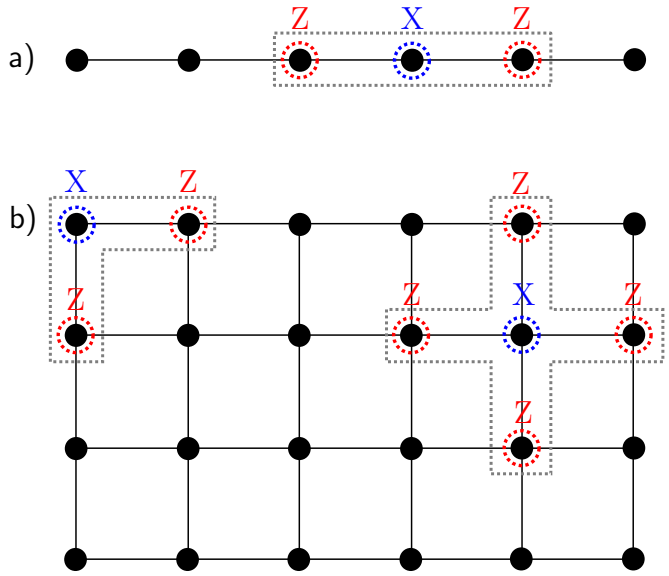

Figure 4.1: **a)** 1D (linear) cluster state. **b)** 2D cluster state, required as a resource for universal quantum computation in the measurement-based computation model.

4.1 Cluster states and MBQC

Cluster states are part of a family of multi-particle, highly-entangled states called *graph states*. The name of the latter stems from their ability to be parametrised by graphs, that is, a set $G = (V, E)$ of $|V|$ vertices and edges $E \subseteq [V]^2$ connecting any pairs of vertices. To every graph G we can then associate a quantum graph state $|G\rangle$. A cluster state can then be seen as a realisation of a graph state, in which the corresponding graph is a connected subset of some d-dimensional lattice. Physically, this graph-state correspondence can be realised by associating a qubit in the $|+\rangle = \frac{1}{\sqrt{2}}(|0\rangle + |1\rangle)$ state to each vertex of the graph, and applying a controlled Z-gate $C_Z = diag(1, 1, 1, -1)$ to every pair of vertices connected by an edge. The resulting state $|G\rangle$ can then be written as $|G\rangle = \prod_{(a,b)\in E} C_Z^{\{a,b\}} |+\rangle^{\otimes V}$, where $C_Z^{\{a,b\}}$ is the controlled gate applied to the pair $(a, b) \in E$.

An alternative description, which is perhaps easier to depict visually, is the following: Define an operator $K^{(a)} = \sigma_x^{(a)} \bigotimes_{b\in N(a)} \sigma_z^{(b)}$ for each vertex a, where the tensor product runs over vertices b in the neigbourhood $N(a)$ of a. The corresponding graph state $|G\rangle$ is then defined as the *simultaneous* $+1$ eigenstate of the $|V|$ operators $\{K^{(a)};\ a \in V\}$, that is $K^{(a)} |G\rangle = |G\rangle\,,\ \forall a \in V$. A schematic of the graph state $|G\rangle$ is given in Fig. 4.1, where we show some elements from the set

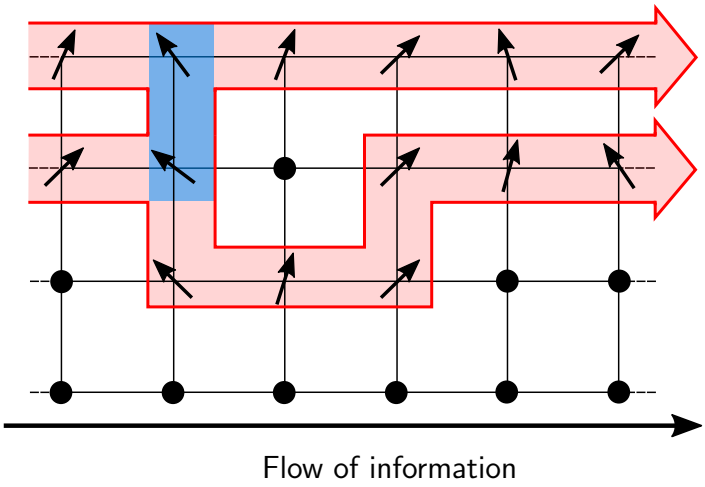

Figure 4.2: Schematic of how the MBQC model uses entanglement as a computational resource, with the computation being performed from left to right. The blue shaded area represents a two-qubit gate (being orthogonal to the 'computational direction').

$\{K^{(a)};\ a \in V\}$ for a 2D and 1D cluster state.

Having prepared such a highly-entangled 2D state, any quantum computation can then be implemented by means of single qubit measurements [47, 48, 49]. In Fig. 4.2 we show how such a computation can be visualised. Moving from left to right, single qubit measurements in different bases are performed sequentially, with previous measurement results inferring which basis should be used next, consuming entanglement between qubits as a resource in order to carry out the computation. The computation result is then encoded in the states of the final qubits which can be read out in the computational basis (i.e. $\{|0\rangle, |1\rangle\}$). Thus, this model is not bound by two-qubit gates, unlike the quantum circuit model. Furthermore, since MBQC relies on single qubit measurements, failing to perform a measurement at any point during the computation would only affect neighbouring entangled qubits, leaving the remaining ones in an intact cluster state. In the quantum circuit model, however, gate failures would affect the coherence of the state thus disturbing the entire calculation.

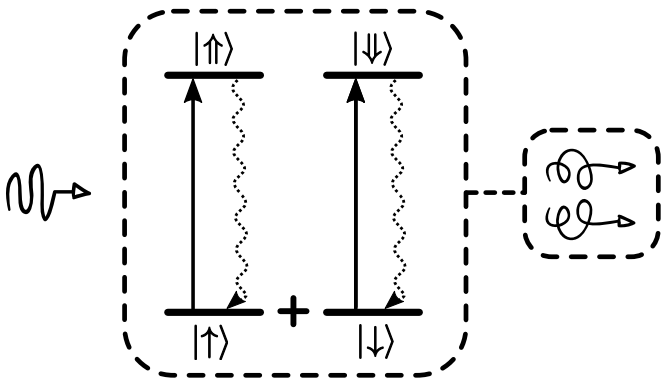

Figure 4.3: Schematic of the Lindner and Rudolph scheme for generating linear cluster states [53]. After preparing the quantum dot in a superposition of the two ground states ($|\uparrow\rangle, |\downarrow\rangle$), a timed x-polarised excitation pulse couples to both allowed transitions to the trion states ($|\Uparrow\rangle, |\Downarrow\rangle$). Upon relaxation, the emitted photon's polarisation degree of freedom is entangled with the quantum dot's spin degree of freedom.

4.1.1 Solid state implementations

Despite matter qubits being an intuitive candidate for cluster state generation, the former suffer from several experimental challenges. As discussed in Chapters 2 and 3, matter qubits suffer from considerable interaction with their environment, which depletes the quality of these matter-qubit cluster states significantly. An alternative candidate would be using photonic degrees of freedom as the qubit components for these states. Photons, unlike matter qubits, barely interact with their environment, which would result in cluster states of much higher quality. Furthermore, by using combinations of half- and quarter-waveplates, these can be easily measured in any desired basis.

To obtain these photonic cluster states, however, we need a source to generate photons in the first place. The goal would then be to use the emitter as both the photon and the entanglement generator. Several platforms for generating photonic cluster states have been proposed over the past few years, varying from solid state emitters such as quantum dots [53, 54, 55, 56, 57, 58] and crystal defects [56, 59] to parametric downconversion [60, 61], all presenting their own sets of advantages and challenges. The experimental challenges of obtaining two (and indeed higher) dimensional cluster states generated from any of these sources can be significantly reduced by using linear cluster states as a resource and applying probabilistic fusion

gates between qubits from adjacent linear states [62, 54, 63], or 'glueing' together micro-clusters [64]. In their seminal paper, Lindnder and Rudolph proposed using a quantum dot to generate a photonic linear cluster state. The scheme uses the quantum dot to generate entanglement between the nanostructure's spin and photons' polarisation degrees of freedom, respectively (Fig. 4.3). By using carefully timed pulsed excitations, they were able to show that it was possible, in theory, to generate 12-photon cluster state in realistic experimental conditions [53].

Most solid state-based protocols, like the Lindner and Rudloph scheme, rely on pulsed excitations to drive optical transitions in a matter qubit to entangle the emitter's spin and emitted photons' polarisation degrees of freedom, respectively. We shall be discussing a novel approach using hole spins in quantum dots in Chapter 6 (which is inspired by the Lindner and Rudolph protocol [53]) as well as discussing the drawbacks of some of the current proposed schemes.

Chapter 5

Method of images applied to driven solid-state emitters

5.1 Motivation

Increasing the collection efficiency from solid-state emitters is an important step towards achieving robust single photon sources, as well as optically connecting different nodes of quantum hardware. Furthermore, the efficiency of several solid state based MBQC schemes rely on the emitter's ability to generate photons deterministically, as we shall see in Chapter 6. It is thus imperative to minimise photon loss which can have drastic effects on the fidelity of the resulting photonic state.

The most basic, and perhaps intuitive, method to improve the collection efficiency from quantum dots is simply adding a metallic substrate [65, 66, 67] effectively acting as a mirror, which was shown to give efficiency increases of up to 50% [65]. Mirrors have widespread use for directing light from sources that emit across a extended solid angle, for example in the form parabolic reflectors in everyday light sources. On the nanoscale, precise guiding of photons into particular optical modes is of paramount importance for quantum information processing and communication, where on demand single photons are required [68, 69, 70, 71]. Although micron-sized spherical mirrors for open access microcavities [72] have recently enabled the investigation of quantum dot–cavity systems in the strong coupling regime [73, 74], the use of sophisticated mirrors remains a challenge for solid-state quantum

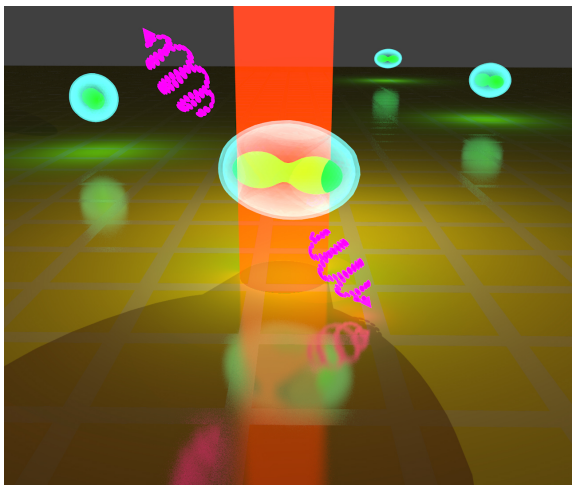

Figure 5.1: Artistic rendition of a driven quantum dot, depicted as a cyan spheroid, in the proximity of a golden metallic surface. The corresponding 'image dot' is shown blurred on the other side 'below' of the semiconductor-gold interface. The optical dipoles are depicted as 'dumbbells' within the quantum dots. The vertical red beam represents the laser driving, and the magenta spiralling arrows indicate scattered photons.

emitters that are often embedded in heterogenous layers of substrates with varying refractive indices. This motivates the more straightforward alternative of increasing the photon collection efficiency by placing the emitter above a planar mirroring interface [75, 76, 77].

Seminal work [78] by Drexhage in 1970 first demonstrated that a reflective interface modifies the intrinsic properties of the emitter, influencing both the emission frequency [79, 80] and the emitter's excited lifetime [80, 81, 82, 15, 11, 83]. In recent years, progress in the synthesis and control of solid-state emitters has enabled experimental investigation of these modified properties of condensed-state emitters including quantum dots [84, 65] as well as perovskite [85] and transition metal dichalcogenide monolayers [86] deposited on reflective surfaces. Circuit QED analogues of an atom and a variable mirror have also been successfully implemented [87, 88]; these offer the advantage of increased control over the artificial atom's interaction with the mirror. With improved atom-mirror coupling, Hoi *et al.* managed to collect over 99% of the radiation by coupling a transmon microwave emitter to a 1D superconducting waveguide [87].

Several theoretical investigations [79, 80, 81, 11] have shown that an atomic two-level system (TLS) near a reflective surface can be modelled as a pair of emit-

ters: the real one as well as an identical emitter that is placed equidistant from, but on the opposite side of, the interface (see Figs. 5.1 and 5.2). The basic idea follows that of the electrostatics concept of an image charge to capture the surface charge distribution that ensures meeting the electric field boundary conditions [89]. In the optical case, the 'method of images' relies on considering the emission from the combined dipole-image system. This yields the same expression for the modified spontaneous emission (SE) rate which one obtains from a full QED treatment (employing surface-dependent response functions to arrive at the modifications to the emitter's lifetime and transition frequency [90]). The image dipole treatment has also been applied to model the surface-induced modifications of more complex structures such as molecules [91, 92], multiple dipole emitters [93, 94, 16], and solid state-emitters [84, 85]. To date, however, the latter have largely ignored the vibrational solid state environment and the excitation step or the continuous wave (cw) laser driving typical of a resonance fluorescence (RF) setting.

Motivated by these successes, we here present a full image dipole multipolar gauge polaron master equation (ME) treatment of a driven solid state TLS (such as, e.g., a quantum dot) in the proximity of a metal surface (see Fig. 5.1), based on our recent work in Ref. [24]. Our calculations extend previous image dipole studies as follows: (i) we consider driven systems, showing how to incorporate a laser driving term into the dipole and image Hamiltonian; (ii) we discuss the need for introducing an additional 'selection rule' to prevent unphysical double excitation; (iii) we generalise this selection rule for multiple emitters close to the interface; (iv) we demonstrate how a solid-state phonon environment can be accounted for – via a single bosonic bath that is perfectly correlated across the real emitter and its image.

We will show that the resulting master equation model remains highly intuitive and possesses appealing simplicity. We establish the correctness of this model by comparing the single emitter results to those obtained from an alternative calculation which does not involve fictitious entities or rely on ad-hoc assumptions: the half-sided cavity model. This agreement gives us confidence that the model can, indeed, be extended to the case of multiple solid-state emitters near a reflective surface,

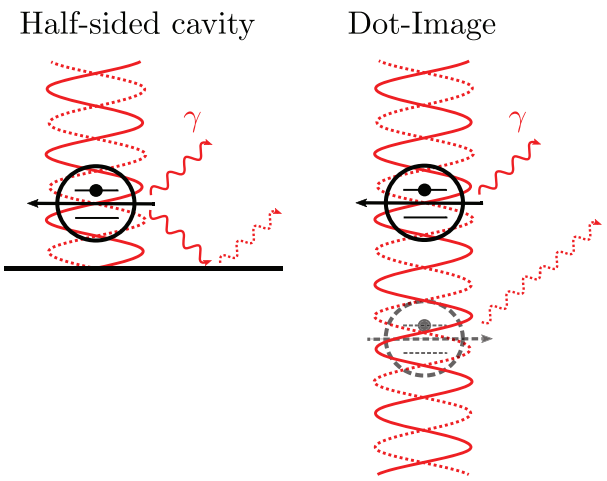

Figure 5.2: Two equivalent descriptions of an emitter near a perfect metallic mirror. **Left:** schematic of the Green's function and half-sided cavity approaches. **Right:** the emitter supplemented with a fictitious image dipole. The solid (dashed) red arrows indicate emitted (reflected) photons whereas the solid (dashed) red curve indicates the incident (reflected) driving beam.

laying the groundwork for the investigation of collective effects in this setting, where we believe that an image approach is easier to deploy than both the Green's function and the half-sided cavity approach. Indeed we find that the superradiant behaviour of a collection of emitters is modified by the presence of the surface, depending on the emitter–surface separation.

5.2 Green's function approach: Brief summary

We begin by summarising the main results of the Green's function approach for modelling the optical environment of a dipole emitter. This can be applied to obtain the spontaneous emission rate of an emitter in free space [95] as well as in the presence of a metallic surface [95, 96, 82]. Whilst this approach gives a closed analytical solution for the case of a single dipole, a numerical route has to be taken to model a system comprised of a larger number of emitters [16, 95], even in the absence of a driving field and phonon-environments. Therefore, we here limit the discussion to a single 'bare' emitter as an independent reference point for the spontaneous emission rate (and energy shift) in that idealised configuration.

Let the dipole be situated at position $\mathbf{r}_s$, where $\mathbf{r}_s$ is perpendicular to a metal surface containing the origin of the coordinate system. In the Green's function

approach, the emitter is usually modelled as a classical dipole oscillating harmonically with amplitude $\mathbf{x}$ at frequency ω_0 about $\mathbf{r}_s$ [16]. In vacuum, the spontaneous emission rate can be calculated as

$$\gamma_0^{pt}(\omega_0) = \frac{4\omega_0^2}{\pi\epsilon_0\hbar c^2}\left[\hat{\mathbf{d}}\cdot\mathrm{Im}\{\mathbf{G}(\mathbf{r}_s,\mathbf{r}_s;\omega_0)\}\cdot\hat{\mathbf{d}}\right] , \tag{5.1}$$

where ϵ_0 is the electric permittivity of vacuum, c is the speed of light, $\hat{\mathbf{d}}$ is a unit vector indicating the direction of the emitter's dipole moment, and $\mathbf{G}(\mathbf{r}_s,\mathbf{r}_s;\omega_0)$ is the Fourier transform of the dyadic Green's function at the emitter's position [95]. In Ref. [16], Choquette *et al.* studied the the collective decay rate of N such classical emitters near a planar interface, arriving at a diagonal Green's function matrix, so that Eq. (5.1) allows one to find the spontaneous emission rate for arbitrary dipole orientations.

To obtain the spontaneous emission rate in a dielectric environment, we consider the following expression for the normalised dissipated power:

$$\frac{P}{P_0} = 1 + \frac{6\pi\epsilon_0\epsilon_r}{|\mathbf{d}|^2k^3}\mathrm{Im}\{\mathbf{d}^*\cdot\mathbf{E}_s(\mathbf{r}_s)\} , \tag{5.2}$$

where P_0 is rate of energy dissipation in free space, ϵ_r and k are the relative permittivity and wave vector magnitude in the dielectric surrounding the emitter, respectively, $\mathbf{d}$ is the dipole moment, and $\mathbf{E}_s(\mathbf{r}_s)$ is the scattered electric field at the dipole's position (which, for a single dipole near the surface, corresponds to the reflected field) [95]. The connection between the Green's function and the decay rate of the dipole emitter is established via the relationship

$$\frac{P}{P_0} = \frac{\gamma^{pt}(\omega_0)}{\gamma_0^{pt}(\omega_0)} . \tag{5.3}$$

Rearranging the above then yields an integral expression for the desired spontaneous emission rate $\gamma^{pt}(\omega_0)$.

In the Green's function approach, care must be taken when considering the limit of a perfect conductor, as assuming perfect reflectivity for all frequencies entails a violation of the sum rule for the emission rates derived using the restirctions imposed

on the environment-modified Green's function [97, 98]. However, additional insight gained from the method of images can in fact resolve this apparent violation [98].

We note that the Green's function method is not limited to ideal metallic interfaces but can also be applied straightforwardly to reflective dielectric interfaces, simply by substituting appropriate dielectric constants into the above relevant expressions [95]. In this case, one obtains qualitatively very similar results for a dielectric mirror, especially at larger separations [95]. Whilst our discussion of the method of images focuses on the special case of a perfectly conducting surface, this approach can be easily extended to the problem of dielectric interfaces as well [89]. Further, under certain conditions, the method of images applies to more complex reflective structures, such as distributed Bragg mirrors[1].

5.3 Half-sided Cavity Model

In the previous section, we discussed how to determine the spontaneous emission rate for an undriven emitter interacting only with a photonic environment. However, in order to fully model a solid-state emitter such as a quantum dot, we need to include interactions between the emitter and its phonon environment [100, 101]. Now we shall derive the polaron ME for a TLS near a metal surface, by modelling the latter as a half-sided Fabry–Pérot cavity positioned at $z = 0$ lying in the xy plane, and the quantum dot positioned at $z = r_s \geq 0$, where $r_s = |\mathbf{r}_s|$. Our calculation follows the general cavity model from Refs. [102, 11] as well as Sec. 2.2.4, taking the appropriate limits for the reflectivity and transmittivity of the two mirrors to obtain, effectively, only a single perfectly reflecting surface (see Fig. 5.3). In this Chapter, we will not go through the entire derivation of the ME as in Sec. 2.2.4, but focus only on the main points which differ from the derivation given in Sec. 2.2.4 to avoid repetition.

[1] In the case of distributed Bragg mirrors (DBMs), the reflectivity only reduces to that of a hard reflector for particular geometries, such as for plane waves normal to the surface and with frequencies falling into the stop-band of the DBM. See Ref. [99] for more details.

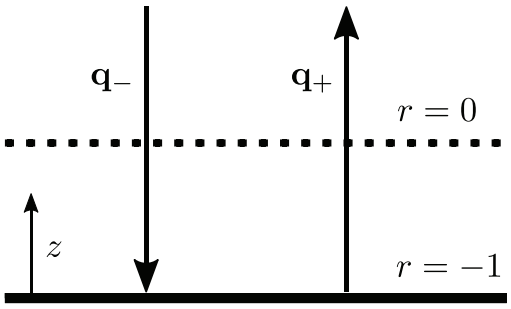

Figure 5.3: The limiting case of the Fabry–Pérot cavity, effectively reducing to a single perfectly reflecting surface. The arrows indicate the wavevectors in (5.5) and (5.10), and r denotes the surface reflection coefficient [102, 11].

5.3.1 Hamiltonian

We consider a driven TLS with ground state $|0\rangle$ and excited state $|X\rangle$, which is governed by the following Hamiltonian in a rotating frame and after the usual rotating wave approximation ($\hbar = 1$)

$$H_S = \delta \, |X\rangle \langle X| + \frac{\Omega_{cav}^*}{2} \, |0\rangle \langle X| + \text{H.c.} \ , \tag{5.4}$$

where H.c. denotes the Hermitian conjugate and $\delta = \omega_0 - \omega_l$ is the detuning between the TLS transition frequency ω_0 and the laser frequency ω_l. Treating the driving electromagnetic wave as a classical field (cf. Chapter 2), the effective Rabi frequency Ω_{cav} in the presence of the metal surface is given by

$$\Omega_{cav} = 2\sqrt{\frac{\omega_l}{2\epsilon V}} \, \mathbf{d} \cdot \left(\mathbf{e}_{l_-} \mathrm{e}^{-i\mathbf{q}_l r} - \mathbf{e}_{l_+} \mathrm{e}^{i\mathbf{q}_l r} \right) \ , \tag{5.5}$$

where $\mathbf{d}$ is the dipole moment, and $\mathbf{q}_l$ is the laser field wavevector, with polarisation $\mathbf{e}_{l_-}$ ($\mathbf{e}_{l_+}$ after reflection), as shown in Fig. 5.3 for the case of the laser beam being perpendicular to the surface. Photon and phonon environments are modelled by the Hamiltonians

$$H_E^{pt} = \sum_{\mathbf{q},\,\lambda} \nu_{\mathbf{q}} a_{\mathbf{q}\lambda}^\dagger a_{\mathbf{q}\lambda} \ , \tag{5.6}$$

$$H_E^{pn} = \sum_{\mathbf{k}} \omega_{\mathbf{k}} b_{\mathbf{k}}^\dagger b_{\mathbf{k}} \ , \tag{5.7}$$

where $b_{\mathbf{k}}^\dagger$ and $a_{\mathbf{q}\lambda}^\dagger$ ($b_{\mathbf{k}}$ and $a_{\mathbf{q}\lambda}$) are the $\mathbf{k}$-phonon and $\mathbf{q}\lambda$-photon creation (annihilation) operators, respectively. In the dipole approximation, the photon interaction Hamiltonian is of the form

$$H_I^{pt} = -\mathbf{d}\cdot\mathbf{E}(\mathbf{r}_s)(|0\rangle\langle X| + |X\rangle\langle 0|) \tag{5.8}$$

with $\mathbf{E}(\mathbf{r})$ being the Schrödinger picture electric field for the half-sided cavity [11, 102],

$$\mathbf{E}(\mathbf{r}) = i\sum_{\mathbf{q},\lambda}\left[\mathbf{u}_{\mathbf{q}\lambda}(\mathbf{r})a_{\mathbf{q}\lambda} - \text{H.c.}\right] \ . \tag{5.9}$$

The spatial mode functions $\mathbf{u}_{\mathbf{q}\lambda}(\mathbf{r})$ for an ideal half-sided cavity (of perfect reflectivity) are given by

$$\mathbf{u}_{\mathbf{q}\lambda}(\mathbf{r}) = \sqrt{\frac{\omega_{\mathbf{q}\lambda}}{2\epsilon V}}\left(\mathbf{e}_{\mathbf{q}_-\lambda}\mathrm{e}^{i\mathbf{q}_- r} - \mathbf{e}_{\mathbf{q}_+\lambda}\mathrm{e}^{i\mathbf{q}_+ r}\right) \ . \tag{5.10}$$

Here, $\mathbf{q}_-$ ($\mathbf{q}_+$) is the incident (reflected) wavevector, with corresponding polarisation $\mathbf{e}_{\mathbf{q}_-\lambda}$ ($\mathbf{e}_{\mathbf{q}_+\lambda}$). For simplicity, we have assumed that the dipole moment $\mathbf{d}$ of the TLS is real.

Recall that interaction with the phonon bath can be described by Eq. (2.55):

$$H_I^{pn} = |X\rangle\langle X|\sum_{\mathbf{k}} g_{\mathbf{k}}(b_{\mathbf{k}}^\dagger + b_{\mathbf{k}}) \ , \tag{5.11}$$

where $g_{\mathbf{k}}$ is the coupling strength of the TLS's excited electronic configuration with phonon mode $\mathbf{k}$. We move to the polaron frame by employing the standard polaron transformation $U = e^S$, $S = |X\rangle\langle X|\sum_{\mathbf{k}}(g_{\mathbf{k}}/\omega_{\mathbf{k}})(b_{\mathbf{k}}^\dagger - b_{\mathbf{k}})$, obtaining the following transformed system Hamiltonian:

$$H_{SP} = \delta'|X\rangle\langle X| + \frac{\Omega_{cav}^*}{2}|0\rangle\langle X|B_- + \frac{\Omega_{cav}}{2}|X\rangle\langle 0|B_+ \ , \tag{5.12}$$

where (we recall from Sec. 2.2.4) $\delta' = \delta - \sum_{\mathbf{k}} g_{\mathbf{k}}^2/\omega_{\mathbf{k}}$ (becoming $\delta - \int_0^\infty J_{pn}(\omega)/\omega$ in the continuum limit), and the phonon bath operators $B_\pm$ are defined as $B_\pm = \Pi_{\mathbf{k}} D_{\mathbf{k}}(g_{\mathbf{k}}/\omega_{\mathbf{k}})$. Once again, we shall be using the superohmic exciton–phonon spec-

tral density given by Eq. (2.64):

$$J_{pn}(\omega) = \alpha\omega^3 \mathrm{e}^{-\frac{\omega^2}{\omega_c^2}} \ . \tag{5.13}$$

In the polaron frame the light-matter interaction Hamiltonian Eq. (5.8) then becomes

$$H_{IP}^{pt} = i\left|0\right\rangle\left\langle X\right| B_- \sum_{\mathbf{q},\lambda} \mathbf{d}\cdot\mathbf{u}^*_{\mathbf{q}\lambda}(\mathbf{r}_s) a^\dagger_{\mathbf{q}\lambda} - i\left|X\right\rangle\left\langle 0\right| B_+ \sum_{\mathbf{q},\lambda} \mathbf{d}\cdot\mathbf{u}_{\mathbf{q}\lambda}(\mathbf{r}_s) a_{\mathbf{q}\lambda} \ . \tag{5.14}$$

Borrowing the notation from Sec. 2.2.4, $A_1^{pt} = \left|0\right\rangle\left\langle X\right|$, $A_2^{pt} = A_1^{pt\dagger}$, $B_{1/2}^{pt} \equiv B_\mp$, $C_1 = i\sum_{\mathbf{q},\lambda} \mathbf{d}\cdot\mathbf{u}^*_{\mathbf{q}\lambda}(\mathbf{r}_s) a^\dagger_{\mathbf{q}\lambda}$, and $C_2 = C_1^\dagger$, we can rewrite the above Hamiltonian as

$$H_{IP}^{pt} = \sum_{i=1}^{2} A_i^{pt} \otimes B_i^{pt} \otimes C_i \ . \tag{5.15}$$

Following the steps outlined in Chapter 2, we obtain the new phonon interaction term from the second term in Eq. (5.12); tracing out the phonon bath degrees of freedom, we thus obtain

$$\begin{aligned} &\mathrm{Tr}_E^{pn}\left[\left(\frac{\Omega^*_{cav}}{2}\left|0\right\rangle\left\langle X\right| B_- + \frac{\Omega_{cav}}{2}\left|X\right\rangle\left\langle 0\right| B_+\right)\rho_E^{pn}\right] \\ &\qquad = \frac{\Omega^*_{cav}}{2}\langle B\rangle\left|0\right\rangle\left\langle X\right| + \frac{\Omega_{cav}}{2}\langle B\rangle\left|X\right\rangle\left\langle 0\right| \ , \end{aligned} \tag{5.16}$$

where $\langle B\rangle$ is defined in Eq. (2.68). In order to expand perturbatively, we therefore define the system-bath interaction with respect to this value. To this end, we add the expectation value by defining $\mathcal{B}_\pm = B_\pm - \langle B\rangle$ and $\Omega_{cav}^{pn} = \langle B\rangle\Omega_{cav}$ and regrouping our system and interaction Hamiltonian terms, obtaining:

$$H_{SP} = \delta'\left|X\right\rangle\left\langle X\right| + \frac{\Omega^{pn*}_{cav}}{2}\left|0\right\rangle\left\langle X\right| + \frac{\Omega^{pn}_{cav}}{2}\left|X\right\rangle\left\langle 0\right| \ , \tag{5.17}$$

$$H_{IP}^{pn} = \frac{\Omega^*_{cav}}{2}\left|0\right\rangle\left\langle X\right|\mathcal{B}_- + \frac{\Omega_{cav}}{2}\left|X\right\rangle\left\langle 0\right|\mathcal{B}_+ \ . \tag{5.18}$$

As for Eq. (5.15), we introduce operator labels $B_{1/2}^{pn} = \mathcal{B}_\mp$, $A_1^{pn} = \Omega^*_{cav}/2\left|0\right\rangle\left\langle X\right|$

and $A_2^{pn} = A_1^{pn\dagger}$ to recast the above interaction Hamiltonian into the compact form

$$H_{IP}^{pn} = \sum_{i=1}^{2} A_i^{pn} \otimes B_i^{pn} \tag{5.19}$$

which will prove useful for the derivation of the master equation.

5.3.2 Master Equation

Following the steps in Sec. 2.2.4, we are now able to write down a second-order Borm–Markov ME, given by

$$\begin{aligned} \frac{\mathrm{d}}{\mathrm{d}t}\rho_{SP}(t) = & \\ & - \int_0^\infty \mathrm{d}\tau \ \mathrm{Tr}_E[H_{IP}(t), [H_{IP}(t-\tau), \rho_{SP}(t) \otimes \rho_E(0)]] \ , \end{aligned} \tag{5.20}$$

where $H_{IP}(t) = H_{IP}^{pn}(t) + H_{IP}^{pt}(t)$, and Tr_E denotes the trace over both environments [1]. As discussed in Sec. 2.2.4, the ME can be separated into two parts:

$$\begin{aligned} \frac{\mathrm{d}}{\mathrm{d}t}\rho_{SP}(t) = & \\ & - \int_0^\infty \mathrm{d}\tau \mathrm{Tr}_E^{pn}[H_{IP}^{pn}(t), [H_{IP}^{pn}(t-\tau), \rho_{SP}(t) \otimes \rho_E^{pn}(0)]] \\ & - \int_0^\infty \mathrm{d}\tau \mathrm{Tr}_E[H_{IP}^{pt}(t), [H_{IP}^{pt}(t-\tau), \rho_{SP}(t) \otimes \rho_E(0)]] \ . \end{aligned} \tag{5.21}$$

Since we assume that the (initial) environmental state is thermal, $\rho_E(0)$ factorises: $\rho_E(0) = \rho_E^{pn}(0) \otimes \rho_E^{pt}(0)$.

5.3.2.1 Phonon bath correlations

For our phonon dissipator, the correlation functions are given by

$$\begin{aligned} C_{ii}^{pn}(\tau) &= \mathrm{Tr}_E^{pn}\left[\mathcal{B}_{\pm}^{\dagger}(\tau)\mathcal{B}_{\pm}(0)\rho_E^{pn}(0)\right] \\ &= \langle B\rangle^2(\mathrm{e}^{\phi(\tau)}-1)\ , \qquad (5.22) \\ C_{ij}^{pn}(\tau) &= \mathrm{Tr}_E^{pn}\left[\mathcal{B}_{\pm}^{\dagger}(\tau)\mathcal{B}_{\mp}(0)\rho_E^{pn}(0)\right] \\ &= \langle B\rangle^2(\mathrm{e}^{-\phi(\tau)}-1)\ , \qquad (5.23) \end{aligned}$$

where $i,j\in\{1,2\}$, $i\neq j$. The phonon dissipator can then be cast in the form

$$\gamma^{pn}(\omega')\mathcal{L}[\sigma_-]+\gamma^{pn}(-\omega')\mathcal{L}[\sigma_+]$$

$$-\gamma_{cd}^{pn}(\omega')\mathcal{L}_{cd}[\sigma_-]-\gamma_{cd}^{pn}(-\omega')\mathcal{L}_{cd}[\sigma_+]\ ,$$

where the emission and cross dephasing rates ($\gamma^{pn}(\pm\omega')$ and γ_{cd}^{pn}, respectively) are given by

$$\begin{aligned} \gamma^{pn}(\pm\omega') &= \frac{|\Omega_{cav}^{pn}|^2}{4}\int_{-\infty}^{\infty}\mathrm{d}\tau\ \mathrm{e}^{\pm i\omega'\tau}\left(\mathrm{e}^{\phi(\tau)}-1\right)\ , \\ \gamma_{cd}^{pn}(\omega') &= \frac{(\Omega_{cav}^{pn*})^2}{4}\int_{-\infty}^{\infty}\mathrm{d}\tau\ \cos(\omega'\tau)\left(1-\mathrm{e}^{-\phi(\tau)}\right)\ , \\ \gamma_{cd}^{pn}(-\omega') &= \frac{(\Omega_{cav}^{pn})^2}{4}\int_{-\infty}^{\infty}\mathrm{d}\tau\ \cos(\omega'\tau)\left(1-\mathrm{e}^{-\phi(\tau)}\right)\ , \end{aligned}$$

where $\phi(\tau)=\int_0^{\infty}\mathrm{d}\omega\frac{J_{pn}(\omega)}{\omega^2}[\coth(\beta\omega/2)\cos(\omega\tau)-i\sin(\omega\tau)]$. Our rates match the ones obtained by Roy-Choudhury *et al.* [9] in previous work[2].

5.3.2.2 Electromagnetic bath correlations

Having arrived at a 'Lindblad-like' phonon dissipator[3], we now consider the term yielding the modified spontaneous emission rate of the TLS near the cavity, as well as account for the frequency shift via a unitary renormalisation term. The correlation

[2]Ref. [9] introduces an additional, phenomenological, pure dephasing term, which we have not included in this paper.

[3]Note that we have not performed a full secularisation and our ME is therefore not strictly of Lindblad form.

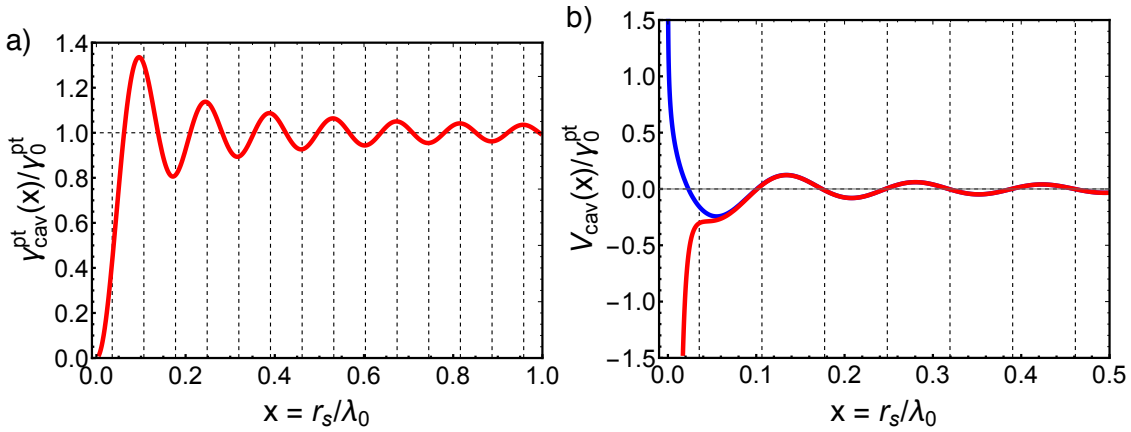

Figure 5.4: Spontaneous emission rate (a) and energy shift (b) for the half-sided cavity model (red), where we divided expressions (5.27) and (5.28) by the bare spontaneous emission rate in order to avoid dependence on its value. The blue energy shift curve denotes the energy shift obtained using a full QED approach [90], showing a distinctively different behaviour at smaller separations ($\lesssim 0.05\lambda_0$) when compared to the half-sided cavity and image approaches. The oscillations persist even at larger separations, of the order of the emission wavelength λ_0 for the spontaneous emission rate. As $x \to \infty$, the spontaneous emission rate tends to that of a bare emitter and the energy shift vanishes, as expected.

functions for this term are given by

$$\begin{aligned} & C^{pt}_{ij}(\tau) \\ &= \mathrm{Tr}_E \left[\left(B^{pt\dagger}_i(\tau) \otimes C^{\dagger}_i(\tau) \right) \left(B^{pt}_j(0) \otimes C_j(0) \right) \rho_E(0) \right] \ , \\ &= \mathrm{Tr}^{pn}_E \left[B^{pt\dagger}_i(\tau) B^{pt}_j(0) \rho^{pn}_E(0) \right] \mathrm{Tr}^{pt}_E \left[C^{\dagger}_i(\tau) C_j(0) \rho^{pt}_E(0) \right] \ , \end{aligned} \tag{5.24}$$

where $i, j \in \{1, 2\}$. After substituting for the bath operators, we make use of the the relations given by Eqns. (2.81) (assuming that $N(\omega) \approx 0, \ \forall \omega > 0$) [4], leading to a single non-vanishing correlation function $C^{pt}_{11}(\tau)$. Following Sec. 2.2.4, we then get

$$C^{pt}_{11}(\tau) = \frac{|\mathbf{d}|^2}{6\pi^2 \epsilon c^3} \int_0^\infty \mathrm{d}\nu \ \nu^3 [1 + \mathcal{F}_{cav}(q r_s)] \ , \tag{5.25}$$

where the term

$$\mathcal{F}_{cav}(x) = \frac{3}{2} \left(-\frac{\sin(2x)}{2x} - \frac{\cos(2x)}{(2x)^2} + \frac{\sin(2x)}{(2x)^3} \right) \ , \tag{5.26}$$

[4] Only (optical) photon modes with energies close to ω_0 are relevant, for which this approximation is typically justified under ambient conditions. However, the generalisation to a finite temperature photon bath is also straightforward.

describes the influence of the metal surface. After some tedious algebra [11], the spontaneous emission rate then evaluates to

$$\gamma_{cav}^{pt}(\omega') = (1 + \mathcal{F}_{cav}(q_0 r_s))\gamma_0^{pt}(\omega') \ , \tag{5.27}$$

where $\gamma_0^{pt}(\omega') = |\mathbf{d}|^2\omega'^3/3\pi\epsilon c^3$ is the bare spontaneous emission rate for an isolated TLS. The imaginary part of the correlation tensor has two components: the first term is the usual Lamb shift (whose expression is divergent unless one adopts a full QED approach based on a relativistic Hamiltonian and appropriate renormalisation [103]). The second term is the additional energy shift term and takes the form [104, 105, 11]

$$V_{cav} = \frac{1}{2}\mathcal{G}_{cav}(q_0 r_s)\gamma_0^{pt}(\omega') \ , \tag{5.28}$$

where the function $\mathcal{G}_{cav}$ is given by

$$\mathcal{G}_{cav}(x) = \frac{3}{2}\left(-\frac{\sin(2x)}{(2x)^2} - \frac{\cos(2x)}{(2x)^3} + \frac{\cos(2x)}{2x}\right) \ . \tag{5.29}$$

Overall, the transition frequency for the TLS in the polaron frame is now given by

$$\tilde{\omega}' = \omega' + V_{cav} \tag{5.30}$$

and the final polaron frame ME takes the following form in the Schrödinger picture:

$$\frac{\mathrm{d}}{\mathrm{d}t}\rho_{SP} = -\frac{i}{\hbar}[H'_{SP}, \rho_{SP}(t)] + D_{pn}(\rho_{SP}) + D_{pt}(\rho_{SP}) \ , \tag{5.31}$$

where $D_{pn}(\rho_{SP}) = \gamma^{pn}(\omega')\mathcal{L}[\sigma_-] + \gamma^{pn}(-\omega')\mathcal{L}[\sigma_+] - \gamma_{cd}^{pn}(\omega')\mathcal{L}_{cd}[\sigma_-] - \gamma_{cd}^{pn}(-\omega')\mathcal{L}_{cd}[\sigma_+]$ and $D_{pt}(\rho_{SP}) = \gamma_{cav}^{pt}(\omega')\mathcal{L}[\sigma_-]$. H'_{SP} is the system Hamiltonian in the polaron frame including the energy shift from Eq. (5.28).

In summary, Eqs. (5.27) and (5.28) capture how the presence of a metal surface (here treated as a perfect reflector) alters the spontaneous emission rate and the transition frequency of the TLS, respectively. Considering our results in the absence of phonons, we find full analytical agreement with the prior literature on the image dipole approach [11, 106], and except for very small separations, we also

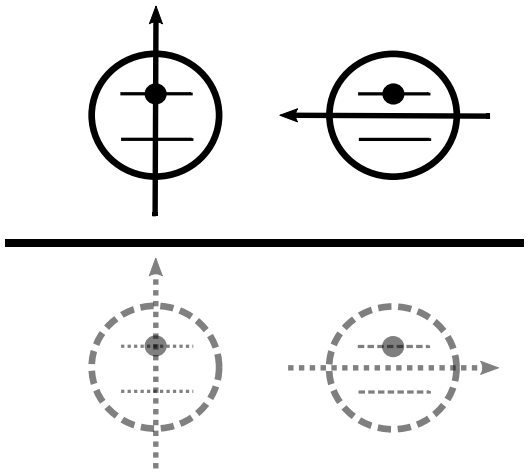

Figure 5.5: The two extreme orientations of the dipole close to a metal surface, with the left schematic showing the dipole perpendicular to the surface (resulting in the highest emission enhancement of in the limit $r_s \to 0$), and the parallel dipole-surface configuration shown on the right, leading to a suppressed emission rate in the same limit [5].

have excellent numerical agreement with the full QED approach [90], as well as field quantisation methods using the correct classical spatial modes [107]. We show this agreement in Fig. 5.4 as a function of the distance of the emitter to the surface. The dashed vertical lines at multiples of $1/8n$ (where n is the refractive index of the host material, taken to be GaAs in our case), taken from Eqns. (5.27) and (5.28), serve as a guide to the eye for the approximate frequency of oscillation, and demonstrate that multiple periods occur within a wavelength's separation of emitter to surface. In the limiting case $r_s \to \infty$, we have $V_{cav} \to 0$ and $\gamma_{cav}^{pt}(\omega') \to \gamma_0^{pt}(\omega')$, i.e. we recover the case of an isolated quantum dot as required.

5.4 Image Emitter Approach

Models involving emission from a combination of two identical TLS have been used extensively to study the modifications to the spontaneous emission rate of an emitter in the proximity of a dielectric or metal surface. After setting up the appropriate Hamiltonian, we shall once more derive a polaron frame ME. We then show that this ME is identical to the one derived using the half-sided cavity approach,

[5] For simplicity, we have shown the real and image TLSs in the same state. Later in this chapter, we will discuss how to properly symmetrize the system of real and image dipole to account for the additional selection rule.

provided we disregard certain terms in order to constrain the dynamics of our two emitter model to the 'right' subspace. After showing results for a single emitter, we shall then briefly discuss how this additional selection rule can be extended to N (real) identical TLSs close to the interface.

5.4.1 Setup

We focus on the case where the dipole is oriented parallel to the surface[6] (as is appropriate for a typical self-assembled quantum dot emitter), implying that the image dipole will be antiparallel [81, 104, 105, 90], as depicted in Fig. 5.5. In what follows, we shall once again take the *real* emitter to be situated at a distance $r_s > 0$ along the positive z-axis, with the dipole vector oriented in the positive x-direction. Hence, the corresponding *image* dipole is positioned at $z = -r_s$, with its dipole vector being parallel to the negative x-axis.

5.4.2 Hamiltonian

The Hamiltonian of the two driven TLS in a frame rotating with frequency ω_l is given by

$$H_S = \sum_{j=1}^{2} \delta \left|X_j\right\rangle \left\langle X_j\right| + \frac{\Omega_j^*}{2} \left|0_j\right\rangle \left\langle X_j\right| + \frac{\Omega_j}{2} \left|X_j\right\rangle \left\langle 0_j\right| \ , \tag{5.32}$$

where the subscript $j = 1, 2$ denotes the real and image TLS, respectively. In order to match the boundary conditions required for reflection, we model the classical driving field as two counter-propagating beams, with the secondary 'reflected' beam having a π phase shift with respect to the original beam. For simplicity, we model these as plane waves propagating along the z-axis and polarised in the x-direction. In phasor notation, these two waves can be written as

$$\begin{aligned} \mathbf{E}_1(\mathbf{r}) &= \mathbf{E}_{incident}(\mathbf{r}) = E_0 \mathrm{e}^{i\mathbf{q}_l \cdot \mathbf{r}} \hat{\mathbf{x}} \ , \\ \mathbf{E}_2(\mathbf{r}) &= \mathbf{E}_{reflected}(\mathbf{r}) = -E_0 \mathrm{e}^{-i\mathbf{q}_l \cdot \mathbf{r}} \hat{\mathbf{x}} \ , \end{aligned} \tag{5.33}$$

[6] We discuss modifications for the perpendicular case in Appendix A

giving rise to the following Rabi frequencies at the positions $\mathbf{r}_{1,2}$ of the two emitters:

$$\begin{aligned}\Omega_1 &= 2\mathbf{d}_1 \cdot (\mathbf{E}_1(\mathbf{r}_1) + \mathbf{E}_2(\mathbf{r}_1)) \ , \\ \Omega_2 &= 2\mathbf{d}_2 \cdot (\mathbf{E}_1(\mathbf{r}_2) + \mathbf{E}_2(\mathbf{r}_2)) \ .\end{aligned} \tag{5.34}$$

Since $\mathbf{r}_2 = -\mathbf{r}_1$ and $\mathbf{d}_2 = -\mathbf{d}_1$, we have $\Omega \coloneqq \Omega_1 = \Omega_2$.

We now turn to the wider electromagnetic environment (excluding the coherent driving field discussed above). The electric field operator can be written as in Eq. (5.9) but with the spatial mode functions now being replaced by the free-space functions

$$\mathbf{u}_{\mathbf{q}\lambda}(\mathbf{r}) = \sqrt{\frac{\omega_{\mathbf{q}\lambda}}{2\epsilon V}}\mathbf{e}_{\mathbf{q}\lambda}\mathrm{e}^{i\mathbf{q}r} \ . \tag{5.35}$$

The interaction Hamiltonian of the TLS with the photonic environment is then given by

$$\begin{aligned}H_I^{pt} =& H_I^{pt,1} + H_I^{pt,2} \\ =& -\sum_{j=1}^{2} \mathbf{d}_j \cdot \mathbf{E}(\mathbf{r}_j)(|0_j\rangle\langle X_j| + |X_j\rangle\langle 0_j|) \ .\end{aligned} \tag{5.36}$$

For the interaction with vibrational modes, we assume that both real and image TLS see the same phonon bath and possess perfectly correlated coupling constants $g_{\mathbf{k}}^{(1)} = g_{\mathbf{k}}^{(2)} \coloneqq g_{\mathbf{k}}$. This ensures the image system exactly follows the dynamics of the real dipole, as is required for matching the boundary condition of a perfectly reflecting interface. Thus, our relevant Hamiltonian reads

$$\begin{aligned}H_I^{pn} =& H_I^{pn,1} + H_I^{pn,2} \\ =& \sum_{j=1}^{2}\sum_{\mathbf{k}} |X_j\rangle\langle X_j| \, g_{\mathbf{k}}(b_{\mathbf{k}}^\dagger + b_{\mathbf{k}}) \ .\end{aligned} \tag{5.37}$$

Next, we move into the polaron frame with the transformation $\mathrm{e}^{S_1+S_2} = \mathrm{e}^{S_1}\mathrm{e}^{S_2}$,

obtaining the transformed Hamiltonians

$$H_{SP} = \sum_{j=1}^{2} \delta' \left|X_j\right\rangle \left\langle X_j\right| + \frac{\Omega^{pn*}}{2} \left|0_j\right\rangle \left\langle X_j\right| + \text{H.c.} \ , \tag{5.38}$$

$$\begin{aligned} H_{IP}^{pt,j} =& i \left|0_j\right\rangle \left\langle X_j\right| B_- \sum_{\mathbf{q},\lambda} \mathbf{d}_j \cdot \mathbf{u}^*_{\mathbf{q}\lambda}(\mathbf{r}_j) a^\dagger_{\mathbf{q}\lambda} \\ & -i \left|X_j\right\rangle \left\langle 0_j\right| B_+ \sum_{\mathbf{q},\lambda} \mathbf{d}_j \cdot \mathbf{u}_{\mathbf{q}\lambda}(\mathbf{r}_j) a_{\mathbf{q}\lambda} \ , \\ H_{IP}^{pn,j} =& \frac{\Omega^*}{2} \left|0_j\right\rangle \left\langle X_j\right| \mathcal{B}_- + \frac{\Omega}{2} \left|X_j\right\rangle \left\langle 0_j\right| \mathcal{B}_+ \ . \end{aligned} \tag{5.39}$$

As in Sec. 5.3, the latter two can easily be seen to be of the following generic form (with appropriate identifications for the A, B, C operators) which will enable straightforward use of the ME (3.118) from Ref. [1]:

$$H_{IP}^{pn,j} = \sum_{i=1}^{2} A_i^{pn,j} \otimes B_i^{pn,j} \ , \tag{5.40}$$

$$H_{IP}^{pt,j} = \sum_{i=1}^{2} A_i^{pt,j} \otimes B_i^{pt,j} \otimes C_i^j \ . \tag{5.41}$$

5.4.3 Master equation

The ME for our system can, once again, be written as

$$\begin{aligned} \frac{\mathrm{d}}{\mathrm{d}t}\rho_{SP}(t) =& \\ & - \int_0^\infty \mathrm{d}\tau \mathrm{Tr}_E^{pn}[H_{IP}^{pn}(t), [H_{IP}^{pn}(t-\tau), \rho_{SP}(t) \otimes \rho_E^{pn}(0)]] \\ & - \int_0^\infty \mathrm{d}\tau \mathrm{Tr}_E[H_{IP}^{pt}(t), [H_{IP}^{pt}(t-\tau), \rho_{SP}(t) \otimes \rho_E(0)]] \ , \end{aligned} \tag{5.42}$$

however, it now features a larger number of correlation functions due to the presence of the image emitter. Following the general procedure in Sec. 5.3.2, we shall analyse different contributions in turn to arrive at our final ME of the image emitter model.

5.4.3.1 Phonon dissipator

The correlation functions (including cross correlation terms between bath operators of the real and image system) result in the following phonon dissipator

$$
\begin{aligned}
D_{pn}(\rho_{SP}) = & \\
&\sum_{i,j=1}^{2} \gamma_{ji}^{pn}(\omega') \left(\sigma_-^j \rho_{SP}(t) \sigma_+^i - \frac{1}{2}\{\sigma_+^i \sigma_-^j, \rho_{SP}(t)\} \right) \\
&+ \sum_{i,j=1}^{2} \gamma_{ji}^{pn}(-\omega') \left(\sigma_+^j \rho_{SP}(t) \sigma_-^i - \frac{1}{2}\{\sigma_-^i \sigma_+^j, \rho_{SP}(t)\} \right) \\
&- \sum_{i,j=1}^{2} \gamma_{cd,ji}^{pn}(\omega') \left(\sigma_-^j \rho_{SP}(t) \sigma_-^i - \frac{1}{2}\{\sigma_-^i \sigma_-^j, \rho_{SP}(t)\} \right) \\
&- \sum_{i,j=1}^{2} \gamma_{cd,ji}^{pn}(-\omega') \left(\sigma_+^j \rho_{SP}(t) \sigma_+^i - \frac{1}{2}\{\sigma_+^i \sigma_+^j, \rho_{SP}(t)\} \right) \ ,
\end{aligned}
\tag{5.43}
$$

where the rates $\gamma_{ji}^{pn}(\pm\omega')$ and $\gamma_{cd,j}^{pn}$ are given by

$$
\begin{aligned}
\gamma_{ji}^{pn}(\pm\omega') &= \frac{|\Omega^{pn}|^2}{4} \int_{-\infty}^{\infty} \mathrm{d}\tau \ \mathrm{e}^{\pm i\omega'\tau} \left(\mathrm{e}^{\phi(\tau)} - 1 \right) \ , \\
\gamma_{cd,ji}^{pn}(\omega') &= \frac{(\Omega^{pn*})^2}{4} \int_{-\infty}^{\infty} \mathrm{d}\tau \ \cos(\omega' t) \left(1 - \mathrm{e}^{-\phi(\tau)} \right) \ , \\
\gamma_{cd,ji}^{pn}(-\omega') &= \frac{(\Omega^{pn})^2}{4} \int_{-\infty}^{\infty} \mathrm{d}\tau \ \cos(\omega' t) \left(1 - \mathrm{e}^{-\phi(\tau)} \right) \ .
\end{aligned}
$$

We shall return back to the phonon dissipator when discussing the ME equation in the symmetric-antisymmetric basis, which allows us to derive a model agreeing with the half-sided cavity approach.

5.4.3.2 Photon dissipator

We now turn our attention to the photon dissipator term from Eq. (5.42). After evaluating the correlation and cross-correlation functions, we obtain the usual expression for two emitters [11] in a shared electromagnetic environment,

$$
D_{pt}(\rho_{SP}) = \sum_{i,j=1}^{2} \gamma_{ji}^{pt} \left(\sigma_-^j \rho_{SP}(t) \sigma_+^i - \frac{1}{2}\{\sigma_+^i \sigma_-^j, \rho_{SP}(t)\} \right) \ , \tag{5.44}
$$

where the diagonal terms $\gamma_{22}^{pt}(\omega') = \gamma_{11}^{pt}(\omega') = \gamma_0^{pt}(\omega')$, whilst the off diagonal terms are given by $\gamma_{12}^{pt}(\omega') = \gamma_{21}^{pt}(\omega') = \mathcal{F}_{12}(q_0\Delta r)\gamma_0^{pt}(\omega')$ with $\Delta r = r_1 - r_2 = 2r_s$, and

$$\mathcal{F}_{12}(x) = \frac{3}{2}\left(-\frac{\sin(x)}{x} - \frac{\cos(x)}{x^2} + \frac{\sin(x)}{x^3}\right) . \tag{5.45}$$

This is the same function obtained for the half-sided cavity approach [cf. Eq. (5.26)]. The imaginary part of the correlation function yields the 'correction' term to the unitary part of the ME [11, 1, 104]: its diagonal contribution represents diagonal Lamb shift terms. Their small energetic shifts can be absorbed into the bare TLS transition frequency. We thus focus on the off-diagonal element which is of the form:

$$V_{12} = \frac{1}{2}\mathcal{G}_{12}(q\Delta r)\gamma_0^{pt}(\omega') , \tag{5.46}$$

where the function $\mathcal{G}_{12}$ is

$$\mathcal{G}_{12}(x) = \frac{3}{2}\left(-\frac{\sin(x)}{x^2} - \frac{\cos(x)}{x^3} + \frac{\cos(x)}{x}\right) . \tag{5.47}$$

Again, this corresponds to the same energy shift term we have previously encountered in Sec. 5.3.2.2. After diagonalising the Hamiltonian, the frequency of the symmetric excited to ground state transition (in the polaron frame) is then given by

$$\tilde{\omega}' = \omega' + V_{12} , \tag{5.48}$$

exactly matching the transition frequency Eq. (5.30) of the half-sided cavity model.

5.4.4 Effective TLS in the energy eigenbasis

As stated in the introduction, previous literature treating spontaneous emission from initially excited emitters considered the transition from the symmetrically excited to the ground state, as this choice yields matching results with other methods including the half-sided cavity approach [11, 81]. We follow this approach and adopt the basis $\{|e\rangle, |s\rangle, |a\rangle, |g\rangle\}$ with $|e\rangle = |X_1\rangle|X_2\rangle$, $|s\rangle = (|0_1\rangle|X_2\rangle + |X_1\rangle|0_2\rangle)/\sqrt{2}$, $|a\rangle = (|0_1\rangle|X_2\rangle - |X_1\rangle|0_2\rangle)/\sqrt{2}$ and $|g\rangle = |0_1\rangle|0_2\rangle$, see Fig. 5.6. In this basis, our

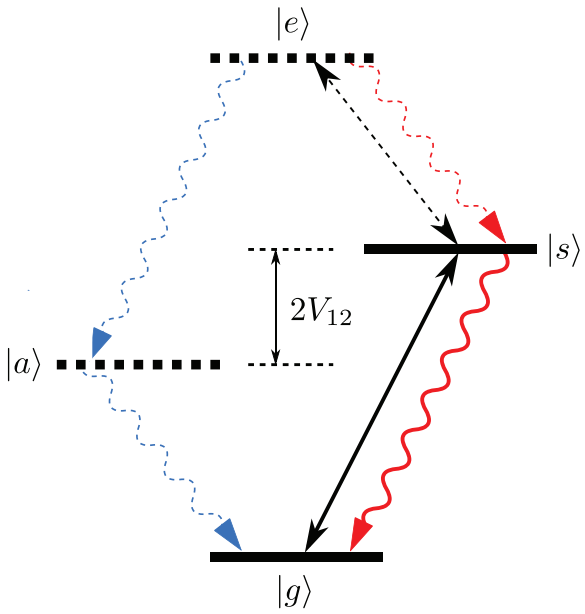

Figure 5.6: Energy level diagram for the two emitter system. The symmetric ($|s\rangle$) and antisymmetric ($|a\rangle$) levels are shifted up and down by V_{12}, respectively. The black arrows indicate the laser driving; the antisymmetric state is decoupled. Blue and red wavy lines indicate photon emission from the antisymmetric and symmetric channel, respectively. As discussed in the text, it is necessary to disable driving on the $|s\rangle \leftrightarrow |e\rangle$ transition (black dashed) to recover the effective two level-system $|g\rangle \leftrightarrow |s\rangle$.

Phonons: No	No	Yes	Yes
Mirror: No	Yes	No	Yes
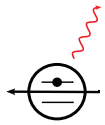	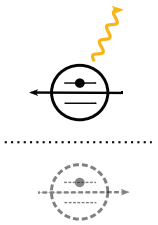	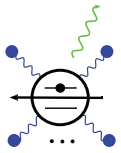	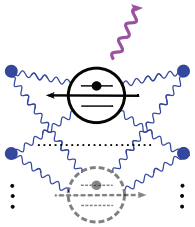
$\gamma_0 = \gamma_0^{pt}(\omega_0)$ $\omega = \omega_0$	$\gamma_0 = (1 + \mathcal{F}_{12}(q_0\Delta r))\gamma_0^{pt}(\omega_0)$ $\omega = \omega_0 + V_{12}$	$\gamma_0 = \gamma_0^{pt}(\omega')$ $\omega = \omega'$	$\gamma_0 = (1 + \mathcal{F}_{12}(q_0\Delta r))\gamma_0^{pt}(\omega')$ $\omega = \omega' + V_{12}$

Figure 5.7: Overview of the four scenarios for an optical dipole considered in this work. All cases have a schematic depiction accompanied by the corresponding spontaneous emission rates γ_0 and transition frequencies ω. Here, Δr is the separation between the real and image dipole, $\mathcal{F}_{12}(q_0\Delta r)$ and V_{12} are given by Eqns. (A.4) and (5.46), respectively, and ω_0 and ω' are the bare and polaron shifted frequencies, respectively. The blue 'masses on springs' (blue circles) denote the phonon bath. Note that the driving field is not shown here, as its presence or absence does not influence the relevant properties.

full polaron ME reads:

$$\frac{\mathrm{d}}{\mathrm{d}t}\rho_{SP}(t) = -\frac{i}{\hbar}[H'_{SP}, \rho_{SP}(t)] + D^s_{pn}(\rho_{SP}) + D^a_{pt}(\rho_{SP}) + D^s_{pt}(\rho_{SP}) \ , \tag{5.49}$$

where the dissipator terms are explicitly given in Appendix A. Here, H'_{SP} denotes the system diagonalised Hamiltonian [including the energy shift term Eq. (5.46)]. The ME photonic dissipator separates into a symmetric channel ($|g\rangle \leftrightarrow |s\rangle \leftrightarrow |e\rangle$) and an antisymmetric one ($|g\rangle \leftrightarrow |a\rangle \leftrightarrow |e\rangle$). Courtesy of the fully correlated phonon bath, phonons also only act in the symmetric channel.

Since $\Omega_1 = \Omega_2$, the symmetric channel Rabi frequency becomes $\Omega_{sg} \coloneqq (\Omega_1 + \Omega_2)/\sqrt{2} = \sqrt{2}\Omega = \Omega_{cav}$ and hence we obtain the same phonon rates as in the half-sided cavity approach[7]. Furthermore, the antisymmetric channel Rabi frequency $\Omega_a \coloneqq (\Omega_1 - \Omega_2)/\sqrt{2} = 0$, meaning that the laser field is completely decoupled from the antisymmetric state.

Consistency with the Green's function and half-sided cavity approach demands that we restrict the dynamics of our four-dimensional Hilbert space to the subspace spanned by the states $\{|g\rangle, |s\rangle\}$, i.e. the larger Hilbert space only served to let us calculate the correct properties of this single transition. Fully decoupling the antisymmetric singly and the doubly excited states from the dynamics is achieved by disabling the laser driving on the $|s\rangle \leftrightarrow |e\rangle$ transition. For finite temperature photon environments with $N(\omega) \neq 0$, we also need to remove dissipative photon absorption channels, by dropping the antisymmetric dissipator term $D^a_{pt}(\rho_{SP})$ from the ME and explicitly removing the dissipative $|s\rangle \leftrightarrow |e\rangle$ operator. This modification of the Hilbert space is justified by the additional selection rule that accompanies the image method, discussed further in Sec. 5.6.

The image approach can thus be reduced to an effective TLS model featuring the same Rabi frequency, spontaneous emission rate, and transition frequency as the half-sided cavity approach – i.e. displaying full equivalence between the two representations. In Fig. 5.7, we summarise the key results from the previous sections: We show the transition frequency and spontaneous emission rate for all four cases considered in this chapter alongside their schematic depictions. The driving term is not included as it has no direct influence on the properties of the optical dipole transition.

[7]The last equality holds due to the difference in density of modes appearing in the derivation of the Rabi frequency in both models. More specifically, the volume for the image approach is twice that in the half-sided cavity method

5.5 Resonance Fluorescence Spectrum

Having included the possibility of laser driving in our model, a natural application is to study the resonance fluorescence (RF) spectrum of a condensed matter TLS near a mirroring surface. We use the ME (5.49) (after discarding the anti-symmetric channel, as argued above) to calculate the spectral function, which is given by the Fourier transform of the (steady-state) first order correlation function $\lim_{t\to\infty}\langle \mathbf{E}^{(-)}(\mathbf{R},t)\mathbf{E}^{(+)}(\mathbf{R},t+\tau)\rangle$, where $\mathbf{E}^{(-)}(\mathbf{R},t)$ and $\mathbf{E}^{(+)}(\mathbf{R},t)$ are, respectively, the negative and positive components of the electric field operator evaluated at the position $\mathbf{R}$ of the detector [11]. These operators are related to the system operators $\sigma_- = |0\rangle\langle X|$ and $\sigma_+ = |X\rangle\langle 0|$, and hence, after applying the polaron transformation, the RF spectral function can be written as

$$S(\omega) \propto \int_{-\infty}^{\infty} \mathrm{d}\tau \mathrm{e}^{-i(\omega-\omega')\tau}\langle \sigma_+(\tau)B_+(\tau)\sigma_-(0)B_-(0)\rangle_s \ , \tag{5.50}$$

where we have exploited the temporal homogeneity of the stationary correlation function, and where the subscript 's' denotes the trace taken with respect the steady-state density matrix [1]. The correlation function appearing in Eq. (5.50) involves two timescales, the nanosecond timescale associated with the exciton lifetime, and the shorter picosecond phonon bath relaxation timescale, allowing us to separate the correlation function into the product $\langle \sigma_+(\tau)\sigma_-(0)\rangle_s\langle B_+(\tau)B_-(0)\rangle_s$ [108]. Substituting the expression for the phonon bath correlation function, we obtain the spectral function

$$S(\omega) \propto \langle B\rangle^2 \int_{-\infty}^{\infty} \mathrm{d}\tau \mathrm{e}^{-i(\omega-\omega')\tau}\mathrm{e}^{\phi(\tau)}\langle \sigma_+(\tau)\sigma_-(0)\rangle_s \ . \tag{5.51}$$

In Fig. 5.8, we show the incoherent part of the emission spectrum of our surface-modified system as well as that of a reference TLS (also subject to the same phonon environment). Following Ref. [65], we take the TLS's position relative to the surface as $r_s \sim 177$ nm. The reference TLS is driven with 'free space' Rabi frequency given by $\Omega^{pn} = 2\langle B\rangle \mathbf{d}\cdot\mathbf{E}_0$. As expected, the curves differ in the position of the Mollow sidebands and the width of the three peaks, since the former is determined by the effective Rabi frequency and the later depends on the emission rate, which both

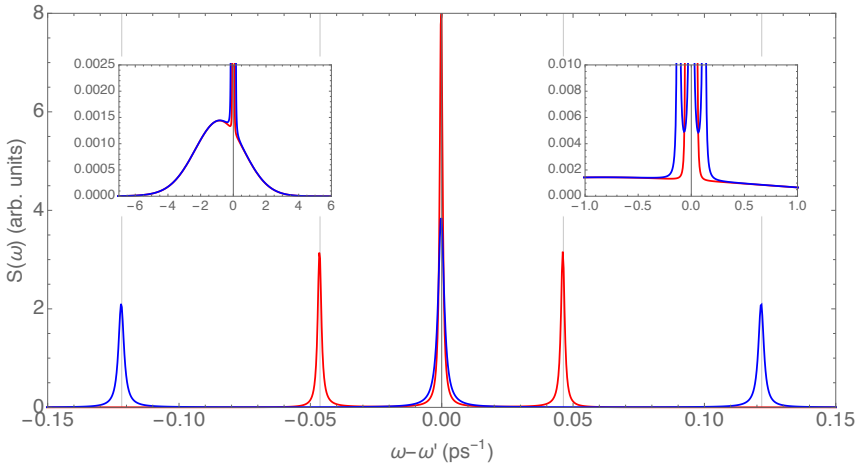

Figure 5.8: Incoherent component of the RF spectrum for a single TLS (blue) and the effective TLS incorporating surface-induced modifications (red).

undergo a change in the presence of a reflective surface. The two insets in Fig. 5.8 show the much broader phonon sideband, which receives $\sim$ 16% of the scattered photons for the chosen spectral density at a phonon temperature of T=10 K.

In Fig. 5.9, we plot the fraction of coherently scattered photons as a function of the renormalised effective Rabi frequency. This ratio is obtained numerically as the (integrated) coherent spectrum divided by the total integrated spectrum. There are two pairs of curves: one with and one without phonons. For the former, the finite area under the phonon sideband means that the coherent fraction does not go to unity even when driving far below saturation. The level at which this fraction plateaus is phonon coupling strength and temperature dependent [108]. By contrast, in the absence of phonons, almost all light is coherently scattered at weak enough driving. The close agreement between the two curves in each pair bears testament to the fact that the surface-modified emitter largely behaves like a bare emitter once the effective Rabi frequency has been corrected for (with the slight remaining discrepancy due to modifications of the natural lifetime). Indeed, plotting this ratio directly as a function of the laser driving field amplitude would reveal sizeable horizontal shifts between these two curves in each pair.

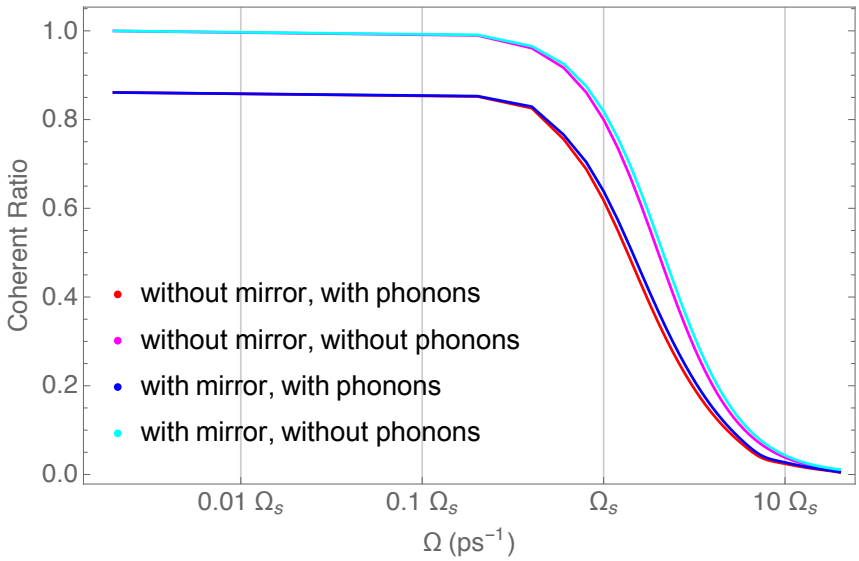

Figure 5.9: Ratio of coherent emission for all four cases (with/without mirror, with-/without the phonon environment) as a function of the (normalised) effective Rabi frequency. Ω_s denotes the saturation Rabi frequency for $\gamma_0^{pt} = 0.001$ ps^{-1}.

5.6 Extension to $N > 1$ TLSs

As mentioned in the introduction, having confirmed the agreement between the well-established half-sided cavity model and the image-dipole approach extended to solid-state emitters, we are able to extend our approach to $N > 1$ emitters by generalising the selection rule restricting us to the physical state space. For the $N = 1$ case, this meant constricting the space to the single excitation subspace which, in retrospect, is intuitive as the image-dipole is merely a mathematical construct to describe the effects of metal surface on the emitter's properties. Furthermore, the physical (connected) subspace one chooses in order to guarantee a physical picture must include the joint ground state, leaving only one subspace as an option for a dipole parallel to the surface, the $\{|g\rangle, |s\rangle\}$ subspace (keeping in mind the $|g\rangle \leftrightarrow |a\rangle$ and $|s\rangle \leftrightarrow |a\rangle$ transitions are dark due to $\Omega_1 = \Omega_2$ and identical vibrational couplings $g_{\mathbf{k}}^{(1)} = g_{\mathbf{k}}^{(2)}$, respectively).

Moving to the $N > 1$ then requires that we restrict our model to the N excitation subspace, in which the real dipole and its respective image can share together at most one excitation in a symmetrized fashion. We also require that the driving Rabi frequency and vibrational modes (and coupling strengths) for the image dipoles are the same as the corresponding real dipoles. In this section, we will use intensity

as a measure of superradiance for closely spaced sample of N emitters and show agreement between an isolated sample and an identical sample in the image-dipole approach once we take the sample-surface separation, r_s, to infinity. Furthermore, we show how the metal surface can either enhance, or reduce, the superradiant effect depending on r_s.

5.7 Setup

In analogy to Fig 5.5, a sample of N, identical, mutually parallel dipoles oriented perpendicular to the surface results in a series of corresponding N parallel image dipoles which would enhance the superradiant effect in the small separation limit (i.e. $r_s \to 0$). Recall, however, that the enhancement/reduction in intensity is also dependent on the value the surface-dipole separation r_s takes. This dependence can be seen for $N = 1$ in Fig. 5.4, where, despite the real and fictitious dipole being oriented opposite to each other, a non-zero finite value of surface-dipole separation may result in enhancement of the spontaneous emission rate.

In what follows, we assume that each of the N emitters is driven by a single classical field with Rabi frequency Ω and the emitters are coupled to individual vibrational environments. Whilst this is a specific case, our results can be easily extended to the case of non-identical Rabi frequencies and phonon couplings as these conditions do not affect the physicality of the model.

5.7.1 Hamiltonian and dissipative dynamics

In this section, we shall briefly discuss the Hamiltonian that captures the dynamics of the setup, as well as the corresponding master equation which is a modified extension of Sec. 2.2.4 and the results from the $N = 1$ case (with the additional the selection rule modified for $N > 1$ implemented). The modification made to the general $2N$-emitter (N real dipoles and corresponding images) master equation is, in fact, a truncation of the Hilbert space to the subspace containing the joint ground state, as discussed earlier, which is performed in the energy basis.

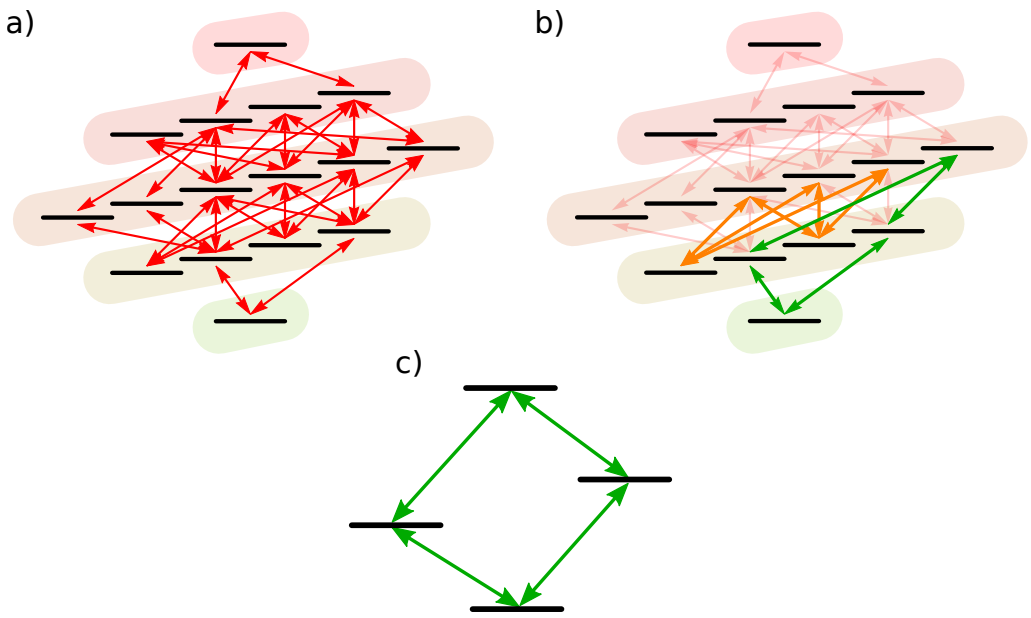

Figure 5.10: Schematic demonstrating the physical subspace search in the energy eigenbasis, in which the 2^N-dimensional subspace, capturing the surface-induced effects, is extracted from the full space of dimensions 2^{2N} (N real emitters along with their corresponding images). **a)** Full 2^{2N}-dimensional space, with the allowed optical transitions shown in red prior to the application of the selection rule. **b)** The operators acting on the full Hilbert space are modified in order to constrain the number of excitations shared by a real-image dipole pair to one. This results in connected subspaces (orange), with only one subspace containing the joint ground state (green). **c)** The Hilbert space is retracted to this connected subspace, resulting in a dimension reduction from 2^{2N} to 2^N. This routine is a generalisation of the effective TLS contraction for $N = 1$ discussed in Sec. 5.4.4. Schematic is shown for $N = 2$ real dipoles.

Our starting point is the full-space RWA Hamiltonian which is an extension of the $N = 1$ Hamiltonian, that is

$$
\begin{aligned}
H_S &= \sum_{j=1}^{N} \sum_{s\in\{r,i\}} \delta \left|X_j^s\right\rangle\left\langle X_j^s\right| + \frac{\Omega}{2}\left(\left|0_j^s\right\rangle\left\langle X_j^s\right| + \left|X_j^s\right\rangle\left\langle 0_j^s\right|\right) \ , \\
H_E^{pt} &= \sum_{\mathbf{q},\,\lambda} \nu_{\mathbf{q}} a_{\mathbf{q}\lambda}^{\dagger} a_{\mathbf{q}\lambda} \ , \\
H_E^{pn} &= \sum_{\mathbf{k}} \omega_{\mathbf{k}} b_{\mathbf{k}}^{\dagger} b_{\mathbf{k}} \ , \\
H_I^{pt} &= -\sum_{j=1}^{N} \sum_{s\in\{r,i\}} \mathbf{d}_j^s \cdot \mathbf{E}(\mathbf{r}_j^s)\left(\left|0_j^s\right\rangle\left\langle X_j^s\right| + \left|X_j^s\right\rangle\left\langle 0_j^s\right|\right) \ , \\
H_I^{pn} &= \sum_{j=1}^{N} \sum_{s\in\{r,i\}} \left|X_j^s\right\rangle\left\langle X_j^s\right| \sum_{\mathbf{k}} g_{\mathbf{k}}(b_{\mathbf{k}}^{\dagger} + b_{\mathbf{k}}) \ ,
\end{aligned}
\tag{5.52}
$$

where we separated the sum over the real-image dipole pairs and over the real and image dipoles, r and i denoting 'real' and 'image', respectively. Since we assume the TLSs are identical, $|\mathbf{d}_j^s| = |\mathbf{d}|$ and have set $\delta_j^s = \delta$, $\forall s, j$.

Having defined the Hamiltonian for our system, we search for the physical subspace which satisfies the selection rules and hence captures the surface-induced effects on the emitters. This search is computed numerically as follows: First we impose the condition that only N excitations are allowed, with an excitation shared between every real-image dipole pair, by modifying the raising and lowering operators for each real-image pair. Consider, for example, the raising operators for the j^{th} pair, given by

$$\begin{aligned}
\sigma_j^{+,r} &= \left|X_j^r\right\rangle \left\langle 0_j^r\right| = \left\{ \bigotimes_{k=1}^{j-1} \mathbb{I}_2 \otimes |X\rangle \langle 0| \otimes \bigotimes_{k=j+1}^{N} \mathbb{I}_2 \right\} \otimes \bigotimes_{k=1}^{N} \mathbb{I}_2 \ , \\
\sigma_j^{+,i} &= \left|X_j^i\right\rangle \left\langle 0_j^i\right| = \bigotimes_{k=1}^{N} \mathbb{I}_2 \otimes \left\{ \bigotimes_{k=1}^{j-1} \mathbb{I}_2 \otimes |X\rangle \langle 0| \otimes \bigotimes_{k=j+1}^{N} \mathbb{I}_2 \right\} \ ,
\end{aligned} \tag{5.53}$$

where $\mathbb{I}_2$ is the 2×2 density matrix. In order to limit the number of excitations shared by this dipole pair to one, we modify the above operators to

$$\begin{aligned}
\sigma_j^{+,r} &\to \left\{ \bigotimes_{k=1}^{j-1} \mathbb{I}_2 \otimes |X\rangle \langle 0| \otimes \bigotimes_{k=j+1}^{N} \mathbb{I}_2 \right\} \otimes \left\{ \bigotimes_{k=1}^{j-1} \mathbb{I}_2 \otimes |0\rangle \langle 0| \otimes \bigotimes_{k=j+1}^{N} \mathbb{I}_2 \right\} \ , \\
\sigma_j^{+,i} &\to \left\{ \bigotimes_{k=1}^{j-1} \mathbb{I}_2 \otimes |0\rangle \langle 0| \otimes \bigotimes_{k=j+1}^{N} \mathbb{I}_2 \right\} \otimes \left\{ \bigotimes_{k=1}^{j-1} \mathbb{I}_2 \otimes |X\rangle \langle 0| \otimes \bigotimes_{k=j+1}^{N} \mathbb{I}_2 \right\} \ ,
\end{aligned} \tag{5.54}$$

that is, we forbid excitation of the j^{th} real dipole if the image dipole is in the excited state and vice versa. After deriving the Hamiltonian Eq. (5.52) with the modified operators implementing this constraint, we move to the energy eigenbasis, where the optical driving terms in this basis indicate which transitions are allowed (similar to what we have done for the $N = 1$ case). Finally, by numerically searching through the subspaces, the space containing the joint ground state of the system is then identified. We are then able to contract the Hilbert space down to this allowed

subspace. This contraction enables us to reduce the number of allowed states in our space, reducing its dimensions from 2^{2N} to 2^N, as illustrated in Fig. 5.10 for $N = 2$. Thus, with this technique, the image-dipole approach does not suffer from the additional complexity linked to a higher-dimensional space. In what follows, unless otherwise stated, we shall be working in this contracted Hilbert space.

We then move to the polaron frame with respect to the transformation $U = \exp\left(\sum_{j=1}^{N}\sum_{s\in\{r,i\}} S_j^s\right) = \prod_{j=1}^{N}\prod_{s\in\{r,i\}}\exp\left(S_j^s\right)$, obtaining the polaron frame Hamiltonian terms:

$$\begin{aligned}
H_{SP} &= \sum_{j=1}^{N}\sum_{s\in\{r,i\}} \delta' \left|X_j^s\right\rangle\left\langle X_j^s\right| + \frac{\Omega^{pn}}{2}\left(\left|0_j^s\right\rangle\left\langle X_j^s\right| + \left|X_j^s\right\rangle\left\langle 0_j^s\right|\right) \ , \\
H_{IP}^{pt} &= i\sum_{j=1}^{N}\sum_{s\in\{r,i\}} \left|0_j^s\right\rangle\left\langle X_j^s\right| B_- \sum_{\mathbf{q},\lambda} \mathbf{d}_j\cdot\mathbf{u}_{\mathbf{q}\lambda}^*(\mathbf{r}_j)a_{\mathbf{q}\lambda}^\dagger + \text{H.c.} \ , \\
H_{IP}^{pn} &= \frac{\Omega}{2}\sum_{j=1}^{N}\sum_{s\in\{r,i\}} \left(\left|0_j^s\right\rangle\left\langle X_j^s\right| \mathcal{B}_- + \left|X_j^s\right\rangle\left\langle 0_j^s\right| \mathcal{B}_+\right) \ ,
\end{aligned} \tag{5.55}$$

which allows us to derive a Born–Markov master equation. Indeed, following the steps of Sec. 2.2.4 and Sec. 5.4, we arrive at a final master equation of the form

$$\frac{\mathrm{d}}{\mathrm{d}t}\rho_{SP} = -\frac{i}{\hbar}[H_{SP} + H_C, \rho_{SP}(t)] + D_{pn}(\rho_{SP}) + D_{pt}(\rho_{SP}) \ , \tag{5.56}$$

where, we recall, H_C is the Förster correction term given by

$$H_{C,ij} = (1-\delta_{ij})\frac{1}{2}\mathcal{G}(q_0 r_{ij})\gamma_0 \ , \tag{5.57}$$

with the function $\mathcal{G}(q_0 r_{ij})$ being the generalised form of Eq. (5.47) to any two dipoles (real or image). The phonon ($D_{pn}(\rho_{SP})$) and photon ($D_{pn}(\rho_{SP})$) dissipators are then given by

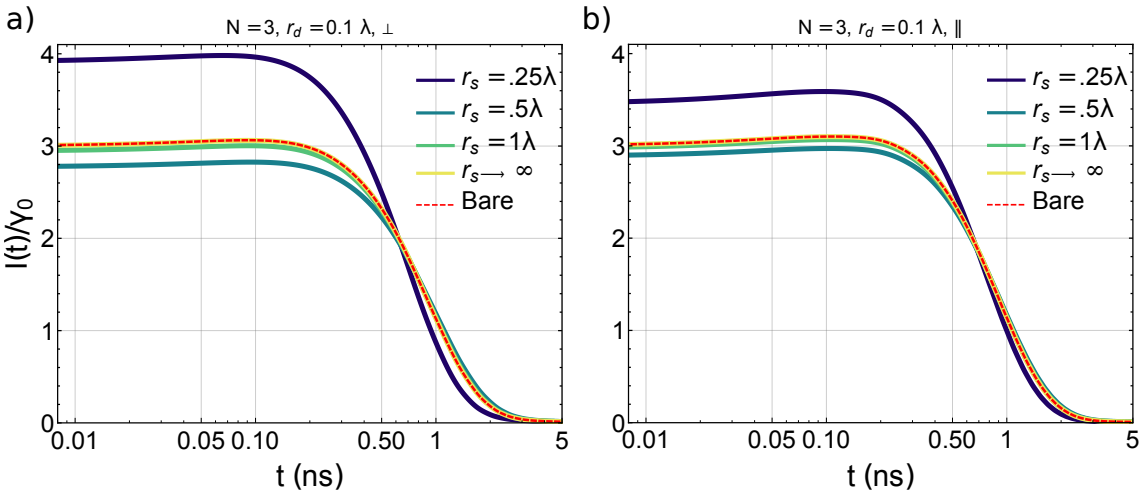

Figure 5.11: Intensity for three dipoles as the surface-dipole separation is increased, for dipoles oriented **a)** perpendicular and **b)** parallel to the surface. In both cases, the limit $r_s \to \infty$ matches the results obtained from having the same sample without surface.

$$
\begin{aligned}
D_{pn}(\rho_{SP}) = &\sum_{i,j=1}^{N} \sum_{s,k\in\{r,i\}} \gamma^{pn}_{j_k i_s}(\omega') \left(\sigma_-^{j_k} \rho_{SP}(t) \sigma_+^{i_s} - \frac{1}{2}\{\sigma_+^{i_s}\sigma_-^{j_k}, \rho_{SP}(t)\} \right) \\
&+ \sum_{i,j=1}^{N} \sum_{s,k\in\{r,i\}} \gamma^{pn}_{j_k i_s}(-\omega') \left(\sigma_+^{j_k} \rho_{SP}(t) \sigma_-^{i_s} - \frac{1}{2}\{\sigma_-^{i_s}\sigma_+^{j_k}, \rho_{SP}(t)\} \right) \\
&- \sum_{i,j=1}^{N} \sum_{s,k\in\{r,i\}} \gamma^{pn}_{cd,j_k i_s}(\omega') \left(\sigma_-^{j_k} \rho_{SP}(t) \sigma_-^{i_s} - \frac{1}{2}\{\sigma_-^{i_s}\sigma_-^{j_k}, \rho_{SP}(t)\} \right) \\
&- \sum_{i,j=1}^{N} \sum_{s,k\in\{r,i\}} \gamma^{pn}_{cd,j_k i_s}(-\omega') \left(\sigma_+^{j_k} \rho_{SP}(t) \sigma_+^{i_s} - \frac{1}{2}\{\sigma_+^{i_s}\sigma_+^{j_k}, \rho_{SP}(t)\} \right) ,
\end{aligned}
\tag{5.58}
$$

$$
D_{pt}(\rho_{SP}) = \sum_{i,j=1}^{N} \sum_{s,k\in\{r,i\}} \gamma^{pt}_{j_k i_s} \left(\sigma_-^{j_k} \rho_{SP}(t) \sigma_+^{i_s} - \frac{1}{2}\{\sigma_+^{i_s}\sigma_-^{j_k}, \rho_{SP}(t)\} \right) , \tag{5.59}
$$

where the definition of the various emission and absorption rates are the same as in Sec. 5.4.

5.7.2 Surface-modified intensity

As we have discussed in Sec. 2.3, the collective behaviour of a sample of emitters can be seen from the spontaneous emission intensity, namely the initial rise in inten-

sity, followed by the rapid decay (with a decay constant larger than the independent emission rate). Motivated by this, we study the intensity for a sample of quantum dots close to a metal surface, where we see how the proximity of the metal surface and the dipole orientations affect the superradiant behaviour of the sample. The intensity for this set up (in the image-dipole model) is given by the sum of the one-time first order correlation functions, weighted by the corresponding (normalised) optical rate, that is

$$I(t) = \frac{1}{\gamma_0} \sum_{i,j=1}^{N} \sum_{s,k\in\{r,i\}} \gamma^{pt}_{j_k i_s} \left\langle \sigma_+^{i_s}(t) \sigma_-^{j_k}(t) \right\rangle \tag{5.60}$$

and, in the limit of $r_s \to \infty$, we obtain the same intensity output of N emitters in the absence of a metal surface (Fig. 5.11)[8]. More importantly, however, is the smaller separation regime, where we see significant modifications of the emission intensity due to the presence of the surface. As expected, for small separations, we see an enhancement of the emission intensity of a dipole ensemble oriented perpendicular to the surface, both in the maximum intensity and the subsequent decay rate. For dipoles parallel to the surface, on the other hand, we observe suppressed intensity, being in the small r_s regime [16]. Furthermore, in Fig. 5.12 we show how the intensity varies for both dipole orientations in the limit of small and large real dipole separation, whereas in Fig. 5.13 we vary the surface-dipole separation. For all calculations, we limit our surface-dipole separations so as to remain in the regime of validity of the method of images (cf. Fig. 5.4b).

We also calculate the the second order coherence function $g^{(2)}(t,\tau)$, describing the instensity correlations, given by [11]:

$$\begin{aligned} g^{(2)}(t,\tau) =& \frac{\langle I(t) I(t+\tau) \rangle}{\langle I(t) \rangle \langle I(t+\tau) \rangle} \\ :=& \frac{G^{(2)}(t,\tau)}{G^{(1)}(t) G^{(1)}(t+\tau)} \ , \end{aligned} \tag{5.61}$$

where $G^{(1)}(t)$ is the first order coherence function, and the non-normalised coherence

[8] As an additional check to verify the validity of the subspace search algorithm, the integrated intensity was verified to be the same as for the bare emitters case.

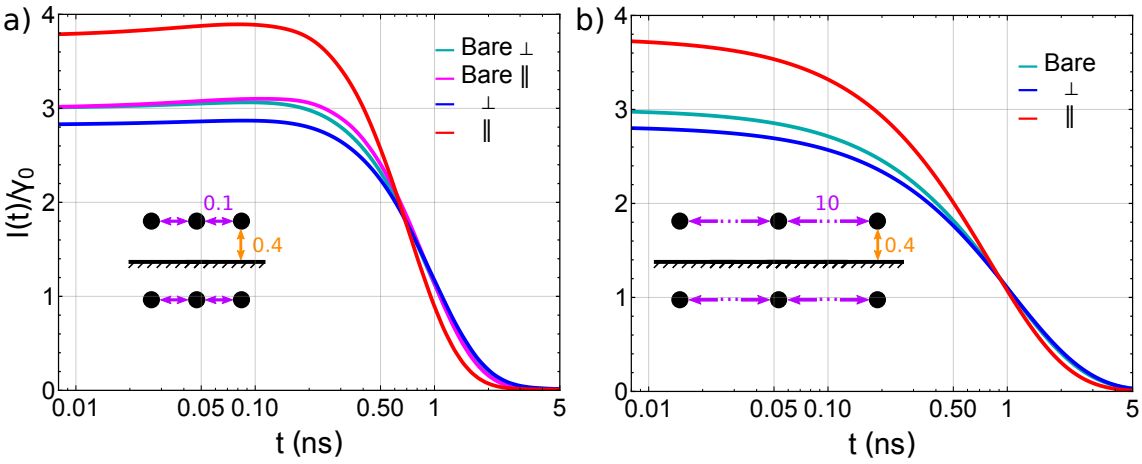

Figure 5.12: Intensity for three dipoles oriented parallel (red) and perpendicular (blue) to the the metal surface, with the magenta and cyan curves corresponding to the intensity of the same sample in the parallel and perpendicular configuration, respectively. **a)** Separation between real dipoles is small enough to observe superradiant behaviour which, at this separation, is enhanced (suppressed) if the dipoles are oriented parallel (perpendicular) to the surface. **b)** For larger values of r_d, the superradiant behaviour vanishes, and there is no distinction between the the two dipole orientations for the bare emitters case.

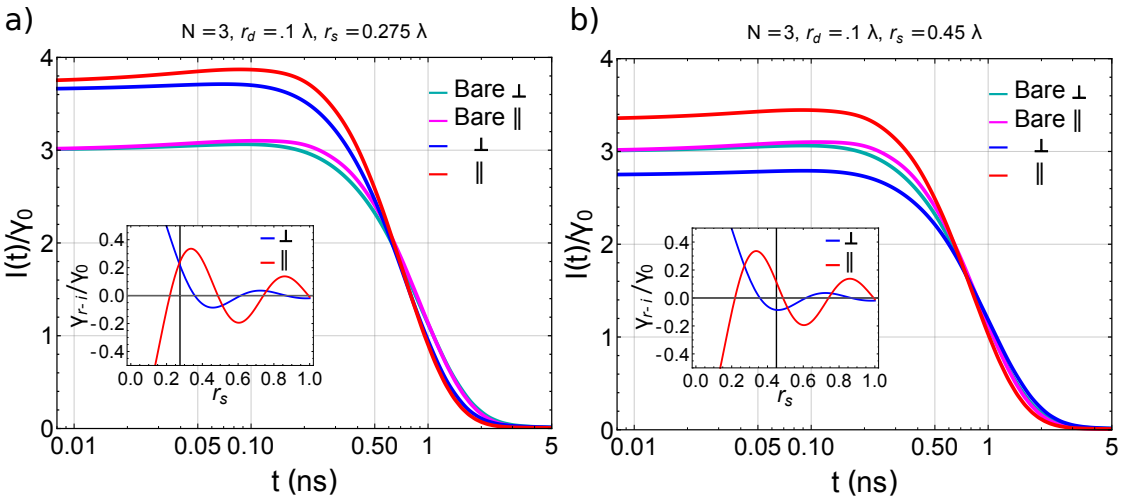

Figure 5.13: The separation of the sample from the surface may significantly modify the emission intensity of the former. **a)** For a dipole-surface separation $r_s = 0.275\lambda$, the two orientations presented here show enhanced superradiant behaviour. **b)** On the other hand, changing the separation to $r_s = 0.45\lambda$ leads to suppressed superradiance from the sample oriented perpendicular to the surface. The insets show the dipole-surface separation dependence of the (normalised) cross spontaneous emission rate for a real and image dipole.

function $G^{(2)}(t,\tau)$ is given by

$$G^{(2)}(t,\tau) = \sum_{i,j,m,n=1}^{N} \sum_{s,k,p,q\in\{r,i\}} \gamma^{pt}_{i_s n_q} \gamma^{pt}_{j_k m_p} \left\langle \sigma_+^{i_s}(t)\sigma_+^{j_k}(t+\tau)\sigma_-^{m_p}(t+\tau)\sigma_-^{n_q}(t)\right\rangle \ . \quad (5.62)$$

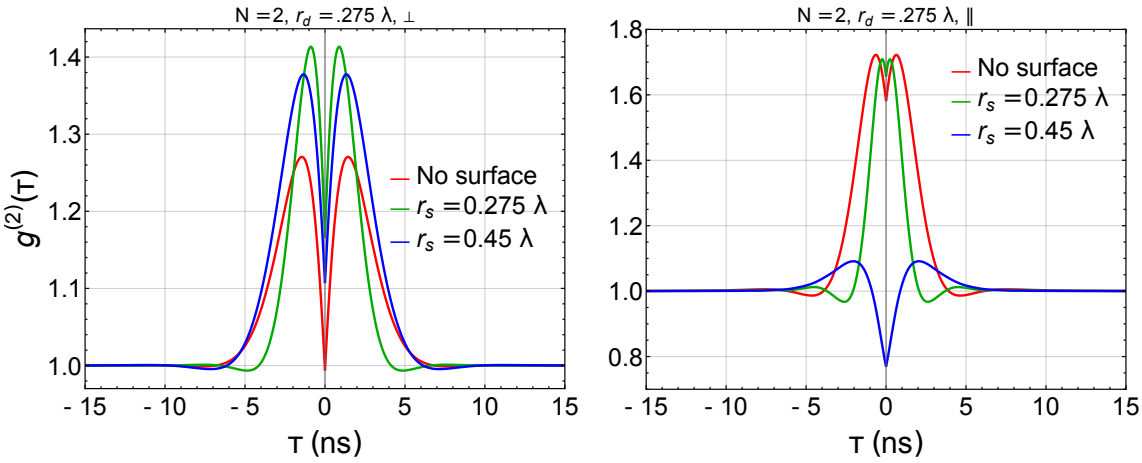

Figure 5.14: **a**) For a sample of two dipoles perpendicular to the surface, the two bunched peaks are enhanced for both surface-dipole separations chosen. **b**) For a sample of two dipoles parallel to the surface, on the other hand, the behaviour of the coherence function changes significantly when going from one separation to the other.

In Fig. 5.14, we show how $g^{(2)}(t,\tau)$ is modified with the presence of the metal surface for two dipoles oriented perpendicular and parallel to the surface, separated by $r_d = 0.1\lambda$. Once again, we see how a minor increment in separation can drastically affect the emission properties of the sample.

5.8 Conclusion

Improving the collection efficiency from solid state single photon sources can play an important role in making idealised theoretical proposals (such as the solid state based MBQC schemes discussed in Chapter 6) more feasible and experimentally realisable. In this chapter, we have extended the method of images – traditionally developed for capturing spontaneous emission in atomic ensembles near reflective interfaces – to the case of a driven solid-state emitter near a metal surface. We have developed two approaches: a half-sided cavity and image dipole, and shown that the latter agrees with the former, but only when additional selection rules are introduced to constrain the dynamics to the relevant subspace. Both our approaches agree with a Green's function treatment in the absence of a vibrational environment. By extending the polaron master equation to accomodate these selection rules, we find that the emitter can indeed still be described as an effective (phonon-dressed)

two-level system with appropriately modified properties, even in the presence of a phonon bath and for a driven system. Our calculated RF spectrum corroborates this observation.

We saw that, despite what earlier literature claims [24], the image-dipole method does not necessitate a larger Hilbert space once the correct subspace is identified, which is done numerically with almost no computational overhead. We submit that the method of images can more easily accommodate larger numbers of emitters near a surface (of varying separation to the surface), as the problem then straightforwardly maps onto the case of several optical dipoles in a shared (free space) electromagnetic environment – a problem which has been studied extensively, see, e.g., Ref. [11]. Finally, by extending the model to $N > 1$ emitters, we have shown that even in the trivial line geometry, an enhancement in the Dicke superradiance can be obtained [16, 109], depending on the orientation and separation of the dipoles from the interface. Future work shall characterise separations and orientations that could enhance the superradiant effect in both the emitted intensity and second order coherence [110]. The interaction of the emitters with the surface might also bring about collective effects other than superradiance, for example inspired by a recent proposal for engineering the quantum-enhanced absorption of light [19] or by harnessing sub-radiant collective states [17, 20].

Another interesting avenue for future work might be the study of charged quantum dots featuring excited trion states. In addition to the optical dipole, the image approach would then feature a separate electrostatic dipole formed by the trion state. To a first approximation, we would expect this second dipole to be static, meaning it would not radiate and only modify the spectrum via energetic shifts. However, one might speculate whether the Coulomb interaction of the three charges involved in the trion state could mediate oscillations in this dipole, making some radiative contribution to the overall spectrum conceivable.

Chapter 6

Frequency-encoded linear cluster states with coherent Raman photons

Having briefly discussed solid state emitters as single photon sources in Chapter 5, we now focus on an application of these nanostructures in the field of quantum computation. As discussed in Chapter 4, entangled multi-qubit states are an essential resource for quantum information and computation. Solid state emitters can mediate interactions between subsequently emitted photons via their spin, thus offering a route towards generating entangled multi-photon states. However, existing schemes typically rely on the excitation-relaxation of the emitter, resulting in single photons limited by the emitter's radiative lifetime, suffering from considerable practical limitations, for self-assembled quantum dots most notably the limited spin coherence time due to Overhauser magnetic field fluctuations. This effective magnetic field describes the averaged effects of the nuclear spin bath on the central electron spin. Thus, precessions of these nuclear spins causes this field to fluctuate with a characteristic timescale roughly given by the nuclear spin flipping rate. We here propose an alternative approach based on a spin-Λ system that overcomes the limitations of previous proposals. Studying the example of spin-flip Raman scattering of self-assembled quantum dots in Voigt geometry, we argue that weakly driven hole spins constitute a promising platform for the practical generation of frequency-

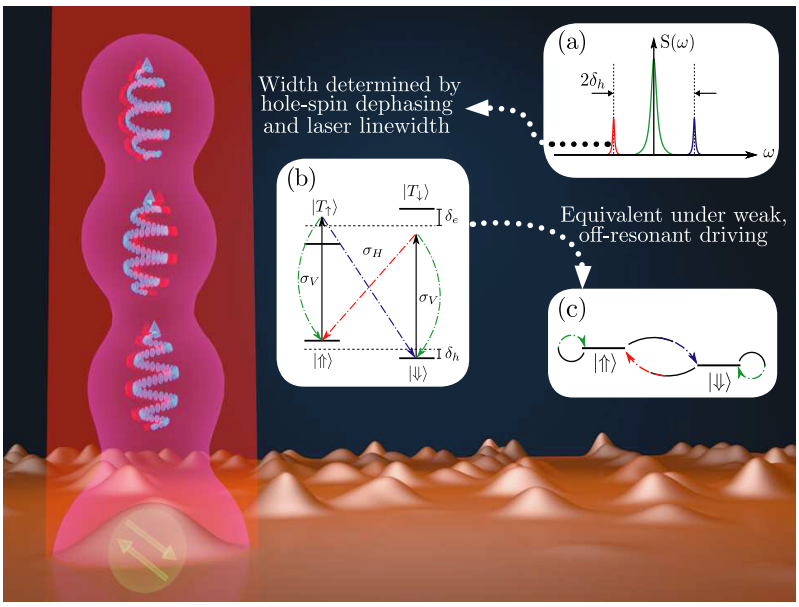

Figure 6.1: **Background**: artistic depiction of our protocol. **Inset a)**: Schematic of the emission spectrum showing the presence of the Raman sidebands. **Inset b)**: Schematic illustration of the scattering processes involving the two ground hole-spin states. The black arrows denote the laser driving on resonance with the unperturbed transitions (dashed lines), whereas the green, red and blue arrows denote the Rayleigh, red detuned and blue detuned events, respectively. **Inset c)**: Simple schematic of the scattering processes involved in the weak, detuned driving limit.

entangled photonic cluster states.

6.1 Motivation

Robust highly-entangled 'cluster' states are of paramount importance for measurement-based quantum computation [111, 47, 50, 112] (cf. Chapter 4). The experimental challenges of obtaining high-dimensional cluster states can be significantly reduced by probabilistically 'fusing' qubits from adjacent 1D linear cluster (LC) states [62, 54, 63], or 'glueing' together micro-clusters [64]. Several platforms for generating photonic LC states have been proposed, varying from condensed matter emitters such as quantum dots [53, 55, 56, 57, 54, 58] and crystal defects [59, 56] to parametric downconversion [60, 61], all presenting their own sets of advantages and challenges. Recently, a photonic LC of length two (LC_2) has been demonstrated experimentally, showing that the entanglement in this setup could persist for up to five consecutively emitted photons [58].

Whilst conceptually elegant and ostensibly deterministic, real-world imperfec-

tions pose significant barriers to the experimental realisation of protocols such as the ones introduced by Refs. [53, 113, 55, 114]. For the III-V platform, these include phonon-dephasing of excited states [115], modified selection rules as a consequence of hole mixing as well as a transverse (Voigt) component of the Overhauser field [116, 117, 118, 119], and limited spin lifetimes due to Overhauser field fluctuations [116, 120, 121, 122, 123]. Decoupling techniques [124, 125, 126, 127, 128, 129, 130] and control of the nuclear environment [131, 132, 123, 133] overcome the latter but provide no remedy for other error sources. Shortcomings of real quantum dots thus put a limit to the size of cluster state achievable and render genuinely deterministic operation impractical for the current experimental state-of-the-art.

In this chapter, we propose employing a weak (sub-saturation) continuous wave (c.w.) laser to drive the Zeeman-detuned transitions of a hole-spin for entangling the spin with the frequency of Raman scattered photon[1]. After discussing some of the imperfections in current solid state based schemes, we introduce our scheme and some theoretical results. We show how our setup overcomes some of the experimental barriers mentioned above: in particular, we shall see that our scheme is robust against fluctuations of the Overhauser field, and unaffected by heavy-hole (hh) light-hole (lh) mixing. This comes at the cost making the protocol probabilistic, however, we show that LC states of sufficient length to serve as building blocks for fusion [62] can be produced at high rates and fidelity based on current experimental capabilities. Furthermore, in Sec. 6.6, we show how our scheme can be extended and made deterministic. Finally, in Sec. 6.7, we analyse the robustness of 2D cluster states generated by probabilistically fusing linear cluster states together. Although we implement the scheme using hole spin transitions in self-assembled quantum dots, other quantum photonic platforms sharing a similar Λ-structure, including defects in wide-bandgap semiconductors [135, 136] and superconducting artificial atoms [137, 138, 139] can also serve as platforms for our scheme. Additional mathematical detail and extensions of the main protocol can be found in Appendix B Sec. B.3.

[1]The small Rabi energies entail that any dephasing due to the optical AC-Stark shift is negligible, although in principle AC-Stark shift tuning could be employed to significantly reduce the dephasing due to charge noise [134].

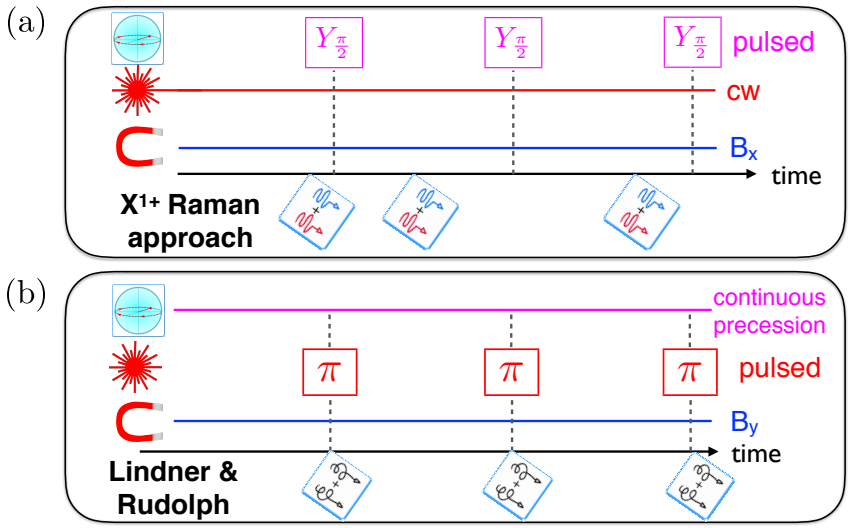

Figure 6.2: **a)** Schematic representation of our protocol. The spin precesses in a constant magnetic field in Voigt geometry. Driven weakly and off-resonantly, the hole-spin scatters Raman-detuned photons at random intervals. The timing between Y-pulses T_B should be chosen so as to maximise the probability of getting a single scattering event between the pulses. **b)** Schematic of the original Lindner and Rudolph proposal for comparison. Instead of a gated Y-rotation, an external field in Voigt geometry causes the spin to precess continuously, with optical π-pulses applied at the appropriate times to excite the emitter.

6.2 Model

We shall denote the (Zeeman) spin states of the heavy hole as $|\Uparrow\rangle$ and $|\Downarrow\rangle$ whereas the electron spin states are $|\uparrow\rangle$ and $|\downarrow\rangle$. In this notation, the positively charged X^{1+} transition $|\Uparrow\rangle \leftrightarrow |T_\uparrow\rangle = |\Uparrow\Downarrow,\uparrow\rangle$ couples to σ^- polarised light and $|\Downarrow\rangle \leftrightarrow |T_\downarrow\rangle = |\Uparrow\Downarrow,\downarrow\rangle$ to σ^+ light. In the presence of an external magnetic field in Voigt geometry (i.e. orthogonal to the optical axis), the otherwise dipole-forbidden diagonal Raman transitions are unlocked (see Fig. 6.1) [140]. As we shall see in Sec. 6.5.3, some complications arise due to a finite admixture of different hole state species. Nonetheless, this rich level structure and the additional selection rules make this system an attractive spin-photon qubit entangler [141, 142].

Wishing to exploit such Raman photons for LC generation we consider a self-assembled quantum dot in Voigt geometry, with the applied magnetic field B strong enough to dominate over nuclear Overhauser field fluctuations (see Sec. 6.5.1). The applied B-field (w.l.o.g. along the x-axis) then defines the basis of spin eigenstates. We also include a c.w. laser field that is resonant with the unperturbed transition of the QD (Fig. 6.1b). In a frame rotating with the laser frequency (after performing

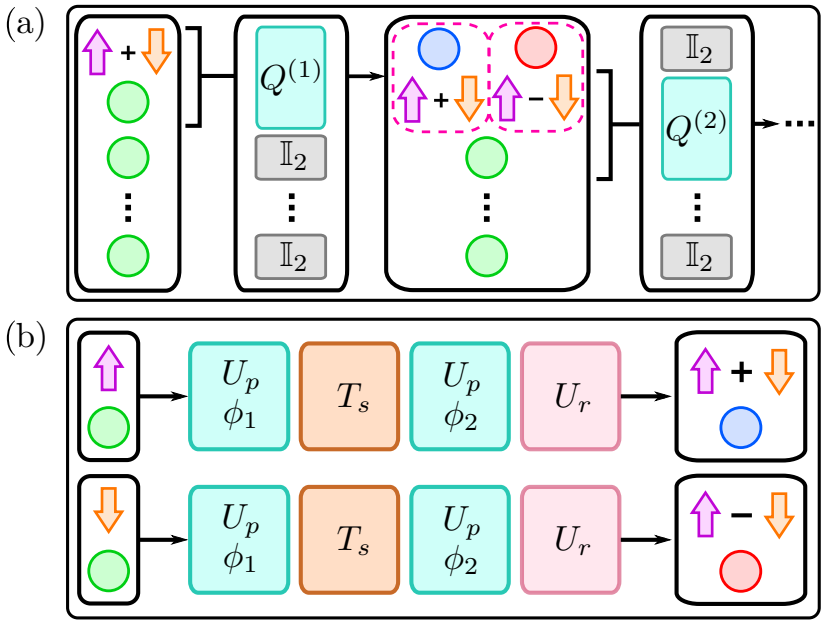

Figure 6.3: **a)**: Diagrammatic representation of the spin-photon entangling process for the first emitted photon. The initial spin state ($|\Uparrow\rangle + |\Downarrow\rangle$) and first laser photon to be scattered (upmost green circle) undergo a joint transformation $Q^{(1)}$, resulting either in a red or a blue-detuned Raman photon that is entangled with the hole spin. $Q^{(2)}$ includes the second Raman process and entangles the newly scattered with the previous photon. **b)**: Breakdown of the $Q^{(i)}$ operation through its action on spin basis states: the sequence of operations transforms includes two periods of free spin precession U_p, the Raman scattering process T_S, and a $\pi/2$ Y-rotation U_r. A full matrix representation of $Q^{(i)}$ is given in Appendix Sec. B.2.

the RWA), the QD Hamiltonian in the Zeeman basis reads

$$\begin{aligned} H =& \delta_h \left(|\Uparrow\rangle \langle\Uparrow| - |\Downarrow\rangle \langle\Downarrow| \right) + \delta_e \left(|T_\downarrow\rangle \langle T_\downarrow| - |T_\uparrow\rangle \langle T_\uparrow| \right) \\ & - \left(\frac{\Omega_H}{2} |T_\uparrow\rangle \langle\Downarrow| + \frac{\Omega_H}{2} |T_\downarrow\rangle \langle\Uparrow| + \frac{\Omega_V}{2} |T_\downarrow\rangle \langle\Downarrow| \right. \\ & \left. + \frac{\Omega_V}{2} |T_\uparrow\rangle \langle\Uparrow| + \text{H.c.} \right) , \end{aligned} \tag{6.1}$$

where $\delta_{e,h}$ are the electron and hole Zeeman splittings, respectively, $\Omega_{H/V}$ are the Rabi frequencies for the horizontally/vertically-polarised transitions, and H.c. denotes the Hermitian conjugate. We simulate the scattering events via Monte Carlo trajectories with jump operators for all allowed transitions, occurring with equal rates γ. This results in an effective (non-Hermitian) Hamiltonian $H_{eff} = H - \frac{i\hbar}{2}\gamma \sum_n C_n^\dagger C_n$, where the sum goes over the collapse operators [143, 144]. This non-unitary evolution of the system generates photons outside of the QD's Hilbert space, which build the LC states we are interested in. More specifically, each 'experi-

ment' is simulated as a quantum jump simulation, where an LC_n state is successfully measured if the correct n scattering events occur within the designated time-bins. The success rate is then calculated by averaging over the results.

6.3 Protocol

Fig. 6.1b shows that the emission of blue and red-detuned Raman spin-flip photons from a single quantum dot must alternate, provided that the scattering rate is faster than the hole spin-flip time. We build on this correlation between spin and photon colour to develop a protocol for generating an entangled LC state (filtering out Rayleigh scattered photons via their orthogonal polarisation). As an intrinsic drawback of Raman spin-flips, the time at which a photon is scattered is not known prior to its detection. In the following, we assume that there is exactly one Raman scattering event per time-bin T_B (albeit at a random time within the bin, see Fig. 6.2.). The overall probability and ways of circumventing this limitation[2] will be discussed later. Fig. 6.3 contains a diagrammatic representation of a successful run of our protocol. Let us trace the evolution of the joint spin-photon-state step by step: we start with the hole spin initialised in the superposition state $|\Uparrow\rangle + |\Downarrow\rangle$ (ignoring normalisation factors) and precessing at its Larmor frequency. Let the accumulated phase prior to the first scattering event be $\phi_1 = \delta_h \tau_1$ (denoted by the matrix $U_p(\phi_1)$ in Fig. 6.3), then a Raman spin flip (T_s in Fig. 6.3) evolves the state to

$$\mathrm{e}^{-i\frac{\phi_1}{2}} |\Uparrow\rangle + \mathrm{e}^{i\frac{\phi_1}{2}} |\Downarrow\rangle \rightarrow \mathrm{e}^{-i\frac{\phi_1}{2}} |\Downarrow B_1\rangle + \mathrm{e}^{i\frac{\phi_1}{2}} |\Uparrow R_1\rangle \ , \tag{6.2}$$

where the labels $B_1(R_1)$ inside the ket denote the first emitted blue (red) photon. A subsequent period of free precession $\tau_2 = T_B - \tau_1$ until the end of the time-bin T_B results in a phase $\phi_2 = \delta_h \tau_2$. We now apply a $\pi/2$ Y-rotation ($U_r = Y_{\frac{\pi}{2}}$ in Fig. 6.3), yielding the state

$$\mathrm{e}^{-i\frac{\chi_1}{2}} |\Uparrow B_1\rangle + \mathrm{e}^{-i\frac{\chi_1}{2}} |\Downarrow B_1\rangle + \mathrm{e}^{i\frac{\chi_1}{2}} |\Uparrow R_1\rangle - \mathrm{e}^{i\frac{\chi_1}{2}} |\Downarrow R_1\rangle \ , \tag{6.3}$$

[2]In practice, this assumption limits the size of the LCs that can be produced in this approach to less than ten.

where $\chi_1 \coloneqq \phi_1 - \phi_2$. The next Raman scattering event will have been preceded by another spin precession angle ϕ_3 resulting in

$$\begin{aligned} &\mathrm{e}^{-i\frac{\phi_3}{2}}\mathrm{e}^{-i\frac{\chi_1}{2}}\left|\Downarrow B_1B_2\right\rangle + \mathrm{e}^{i\frac{\phi_3}{2}}\mathrm{e}^{-i\frac{\chi_1}{2}}\left|\Uparrow B_1R_2\right\rangle \\ &+\mathrm{e}^{-i\frac{\phi_3}{2}}\mathrm{e}^{i\frac{\chi_1}{2}}\left|\Downarrow R_1B_2\right\rangle - \mathrm{e}^{i\frac{\phi_3}{2}}\mathrm{e}^{i\frac{\chi_1}{2}}\left|\Uparrow R_1R_2\right\rangle \ . \end{aligned} \tag{6.4}$$

The spin precesses by a further phase ϕ_4 before we apply the next $Y_{\frac{\pi}{2}}$ rotation, yielding

$$\begin{aligned} &\mathrm{e}^{-i\frac{\phi_3}{2}}\mathrm{e}^{i\frac{\phi_4}{2}}\mathrm{e}^{-i\frac{\chi_1}{2}}\left|\Downarrow B_1B_2\right\rangle + \mathrm{e}^{i\frac{\phi_3}{2}}\mathrm{e}^{-i\frac{\phi_4}{2}}\mathrm{e}^{-i\frac{\chi_1}{2}}\left|\Uparrow B_1R_2\right\rangle \\ &+\mathrm{e}^{-i\frac{\phi_3}{2}}\mathrm{e}^{i\frac{\phi_4}{2}}\mathrm{e}^{i\frac{\chi_1}{2}}\left|\Downarrow R_1B_2\right\rangle - \mathrm{e}^{i\frac{\phi_3}{2}}\mathrm{e}^{-i\frac{\phi_4}{2}}\mathrm{e}^{i\frac{\chi_1}{2}}\left|\Uparrow R_1R_2\right\rangle \\ \coloneqq &\mathrm{e}^{-i\frac{\chi_2}{2}}\mathrm{e}^{-i\frac{\chi_1}{2}}\left|\Downarrow B_1B_2\right\rangle + \mathrm{e}^{i\frac{\chi_2}{2}}\mathrm{e}^{-i\frac{\chi_1}{2}}\left|\Uparrow B_1R_2\right\rangle \\ &+\mathrm{e}^{-i\frac{\chi_2}{2}}\mathrm{e}^{i\frac{\chi_1}{2}}\left|\Downarrow R_1B_2\right\rangle - \mathrm{e}^{i\frac{\chi_2}{2}}\mathrm{e}^{i\frac{\chi_1}{2}}\left|\Uparrow R_1R_2\right\rangle \ . \end{aligned} \tag{6.5}$$

Let us stop at this point and, for clarity, consider the resulting state without its free precession phases

$$\left|\Downarrow B_1B_2\right\rangle + \left|\Uparrow B_1R_2\right\rangle + \left|\Downarrow R_1B_2\right\rangle - \left|\Uparrow R_1R_2\right\rangle \ . \tag{6.6}$$

Using the photon qubit encoding $|B_i\rangle = |1_i\rangle$, $|R_i\rangle = |0_i\rangle$, the state following the final $\mathrm{Y}_{\frac{\pi}{2}}$ rotation is given by

$$\begin{aligned} &\left|\Uparrow 1_1 1_2\right\rangle + \left|\Downarrow 1_1 1_2\right\rangle + \left|\Uparrow 1_1 0_2\right\rangle - \left|\Downarrow 1_1 0_2\right\rangle \\ &+\left|\Uparrow 0_1 1_2\right\rangle + \left|\Downarrow 0_1 1_2\right\rangle - \left|\Uparrow 0_1 0_2\right\rangle + \left|\Downarrow 0_1 0_2\right\rangle \ . \end{aligned} \tag{6.7}$$

In Appendix Sec. B.3, we show that, whether the spin is measured to be in the $|\Uparrow\rangle$ or $|\Downarrow\rangle$ state, the resulting photonic state indeed corresponds to LC_2, satisfying the conditions discussed in Chapter 4. Further, we show that the above protocol generalises trivially to the production of LC states of arbitrary length. Crucially, reintroducing the above precession phases keeps the state local-unitarily (LU) equivalent to LC_2. The phases become known post-measurement through the timestamps of the

detection clicks (i.e. photon arrival times), and in Chapter. 7, we discuss how state-of-the-art tomographic techniques can be modified to make allowances for them for a reconstruction of the LC state[3].

6.4 Results

We now analyse the quality and success probability of our protocol. We begin with the rate for Raman scattering events followed by the success probability of a string of n Raman photons with one per time-bin. Fig. 6.4a shows the Raman scattering rate and its dependence on both B and Ω_V. Comparison with numerical simulations shows that this rate is well-approximated by the transition probability obtained by treating the weak driving field perturbatively to second order (see Appendix Sec. B.1)

$$\gamma_{pert} = \frac{1}{8}\frac{\Omega_V^2 \gamma}{\Delta^2} \ , \tag{6.8}$$

provided $B \gtrsim 100$ mT and sub-saturation $\Omega_V \lesssim \gamma/\sqrt{2} = \Omega_{sat}$ (with γ being the spontaneous emission rate), where $\Delta = \delta_e + \delta_h$. We proceed to determine the optimal duration T_B (i.e. the free precession time between Y-rotations) for maximising the probability of obtaining a single Raman event per time bin. Adopting $B = 100$ mT, $\gamma = 1$ ns^{-1} and $\Omega_V = 0.2\ \Omega_{sat}$, we calculate the number of successful trials with one Raman photon per T_B interval (time interval between U_r rotations in Fig. 6.3) in n successive time-bins. Fig. 6.4c illustrates the results of Monte-Carlo simulations using the QuTiP package [143, 144] for $n = 1$ to 4 scattering events, suggesting that $T_B \approx 0.5\ \mu$s is close to optimal. We have the relation $P_s(n) = P_s(1)^n$ between the success probability for a single bin and that of n bins.

Apart from addressing the possibility of having no Raman events within a time-bin, we also need to account for the possibility of 'false-positives', i.e. detecting only one of multiple Raman events occurring in a single time-bin, due to a photon detection efficiency $\eta < 1$[4]. The probability of such n photon false positives, $P_{fp}(n)$,

[3]Time-stamping these photons does not impose any experimental challenges, as detector setups with ≈ 30 ps readily resolve these phases due to the precession time being of the order of $\sim$2 ns for an external field of 100 mT.

[4]We assume η is the probability of obtaining a detector click if a photon was produced by the

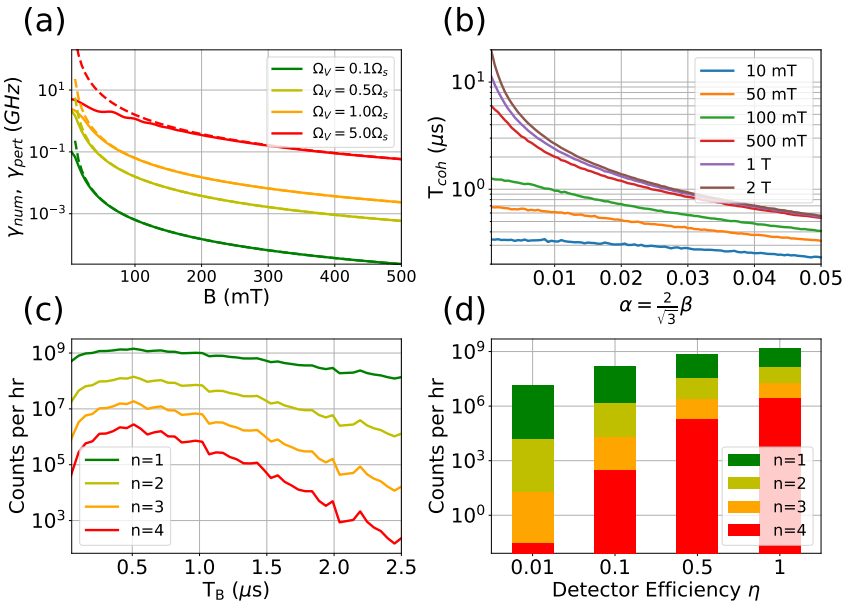

Figure 6.4: **a)**: Perturbative calculation γ_{pert} (dashed) and numerical value γ_{num} (solid) of the Raman scattering rate as a function of B for various driving strengths (from bottom to top: $\Omega_V = .1, .5, 1$, and 5 Ω_s). **b)**: Coherence time for the pseudospin initially prepared perpendicular to the applied external magnetic field with mixing factor $\alpha = \frac{2}{\sqrt{3}}\beta$ for various external field strengths. The Overhauser field was taken to have a spread of 14mT (from bottom to top: $B = .01, .05, .1, .5, 1$ and 2 T). **c)**: Number of successful n-photon correlations per hour against T_B, with $\eta = 1$ for the ideal scenario $B = 100$mT, $\Omega = 0.2\gamma/\sqrt{2}$, and $g_h^x = 0.1$ (from top to bottom: $n = 1, 2, 3$ and 4). **d)**: Success probabilities optimised for $T_B = 500$ ns [by minimising Eqn. (6.9)] against η, decreasing with increasing n.

is given by the simple relation:

$$\begin{aligned} P_{fp}(n) &= P_{nd}(n) \times P_d(1) \times P_s(n+1) \\ &= C_n^{n+1}(1-\eta)^n \times \eta \times P_s(n+1) \ , \end{aligned} \tag{6.9}$$

where C_n^{n+1} is the binomial coefficient, $P_d(n)$ $[P_{nd}(n)]$ denotes the probability of detecting [not detecting] n photons. We find that $T_B \approx 0.5$ μs remains optimal after taking this into account. Fig. 6.4d shows the rate of LC generation for $n = 1$ to 4 for different detector efficiencies.

To demonstrate the robustness of our protocol against nuclear environment fluctuations, we calculate the fidelity between the state obtained with and without Overhauser field (both for the the same set of precession phases determined by randomly chosen scattering times). For a pure hh, only the B_N^z Overhauser component

QD, i.e. it also includes any photon losses in the setup.)

perpendicular to the applied B-field affects the protocol [by randomly modifying direction and magnitude of the total B-field by $\arctan(B_N^z/B_{ext})$]. By contrast, a mixed hh–lh system suffers predominantly from the parallel B_N^x component, to an extent determined by the mixing factor α. This is also exemplified in a decreased spin coherence time from the ideal hh limit, as shown in Fig. 6.4b. Only considering this term, we can arrive at an analytical expression capturing the fidelity decay as a function of T_B.

Consider a single scattering event in which the spin precesses for a time $T_B^{(1)}$ prior to the scattering event and a subsequent precession time $T_B^{(2)}$ followed by a Y rotation marking the end of the run (such that $T_B^{(1)} + T_B^{(2)} = T_B$). In the presence of the B_N^x component, the rotation matrix $U_p(\phi)$ in (B.7) picks up a stochastic term $\omega_N t$, that is

$$U_p((\omega_B + \omega_N)t) = \begin{pmatrix} \mathrm{e}^{-i\frac{1}{2}(\omega_B+\omega_N)t} & 0 \\ 0 & \mathrm{e}^{i\frac{1}{2}(\omega_B+\omega_N)t} \end{pmatrix} \otimes \mathbb{I}_3^{\bigotimes_n} \ , \tag{6.10}$$

with $t = T_B^{(1)}$ or $T_B^{(2)}$, where we have written the precessed angle explicitly in terms of $\omega_B = g_h^x \mu_B B_{ext}/\hbar$ and the Overhauser stochastic frequency $\omega_N = g_h^x \mu_B B_N^x/\hbar$ (g_h^x being the x component of the anisotropic hole g-factor[5]).

The effect of this stochastic term can be seen in the trace fidelity between post Y rotation ideal photon state, and the more realistic case including the Overhauser field. The spin+photon states for the two cases, denoted by $S^{(1)}$ and $\tilde{S}^{(1)}$, respectively, are then given by

$$\begin{aligned} S^{(1)} =& \mathrm{e}^{-i\frac{1}{2}\omega_B \delta T_B} \left|\Uparrow B_1\right\rangle + \mathrm{e}^{-i\frac{1}{2}\omega_B \delta T_B} \left|\Downarrow B_1\right\rangle \\ &+ \mathrm{e}^{i\frac{1}{2}\omega_B \delta T_B} \left|\Uparrow R_1\right\rangle - \mathrm{e}^{i\frac{1}{2}\omega_B \delta T_B} \left|\Downarrow R_1\right\rangle \ , \end{aligned} \tag{6.11}$$

$$\begin{aligned} \tilde{S}^{(1)} =& \mathrm{e}^{-i\frac{1}{2}(\omega_B+\omega_N) \delta T_B} \left|\Uparrow B_1\right\rangle + \mathrm{e}^{-i\frac{1}{2}(\omega_B+\omega_N) \delta T_B} \left|\Downarrow B_1\right\rangle \\ &+ \mathrm{e}^{i\frac{1}{2}(\omega_B+\omega_N) \delta T_B} \left|\Uparrow R_1\right\rangle - \mathrm{e}^{i\frac{1}{2}(\omega_B+\omega_N) \delta T_B} \left|\Downarrow R_1\right\rangle \ , \end{aligned}$$

[5]The anisotropy in the hole g-factor is, in general, not the same as the effective anisotropy in the g-tensor for the hole Overhauser shift due to hh–lh mixing.

where $\delta T_B = T_B^{(1)} - T_B^{(2)} \in [-T_B, T_B]$ is a uniform random variable due to the fact that the spin precesses multiple times during T_B in the high external magnetic field. The final photon state, as discussed earlier, depends on the state the spin is measured in, so we shall denote the density matrices of the ideal and realistic cases by $\rho_+^{(1)}$ and $\xi_+^{(1)}$, respectively, if the spin is measured in the $|\Uparrow\rangle$ state, and similarly $\rho_-^{(1)}$ and $\xi_-^{(1)}$ for the $|\Downarrow\rangle$ result. The fidelity for a fixed value of B_N^x is then given by $\mathcal{F}^{(1)} = \mathrm{tr}(\rho_+^{(1)}\xi_+^{(1)}) = \mathrm{tr}(\rho_-^{(1)}\xi_-^{(1)}) = \cos^2(B_N^x \delta T_B/2)$.

Due to the stochastic nature of the Overhauser field, we need to ensemble-average $\mathcal{F}^{(1)}$ in order to get the true fidelity, that is $\bar{\mathcal{F}}^{(1)} = \left\langle \left\langle \mathrm{tr}(\rho_-^{(1)}\xi_-^{(1)}) \right\rangle_B \right\rangle_{\delta T} = \left\langle \left\langle \mathrm{tr}(\rho_+^{(1)}\xi_+^{(1)}) \right\rangle_B \right\rangle_{\delta T}$, where the Overhauser averaging $\langle\cdot\rangle_B$ and time averaging $\langle\cdot\rangle_{\delta T}$ are performed over a normal distribution with zero mean and finite standard deviation δB_N^x, and a uniform distribution over $[-T_B, T_B]$ [6]. In doing so, we get the averaged fidelity for a single scattering event in the presence of B_N^x given by

$$\bar{\mathcal{F}}^{(1)} = \frac{1}{2} + \frac{\sqrt{2\pi}}{4 T_B \delta B_N^x} \mathrm{erf}\left(\frac{T_B \delta B_N^x}{\sqrt{2}}\right) , \tag{6.12}$$

where $\bar{\mathcal{F}}^{(n)}$ denotes the average fidelity for a state of n scattered photons (written for $n = 1$ in Eq. (6.12) above), and δB_N^x is the fluctuation in B_N^x. For a single scattered photon, we obtain $\mathcal{F}_{av}^{(1)} \to 1/2$ for large T_B as expected. Not capturing decoherence due to B_N^z fluctuations, Eqn. (6.12) represents an upper bound on the maximally achievable fidelity in the case of finite hh-lh mixing. To fully account for the effects of the stochastically varying net B-field vector, we show numerically obtained[7] fidelity overlaps of desired vs the ensemble-average of realised LC_4 states in Fig. 6.5. In the presence of the Overhauser field with fluctuations ~ 14mT, near unit fidelity remains possible in the region with (moderately) strong $B \gtrsim 0.4$ T and relatively short $T_B \lesssim 0.25$ μs (Fig. 6.5a). Conversely, large LC generation rates demand 0.5 μs $\lesssim T_B \lesssim 1$ μs and $B \lesssim 0.1$ T (Fig. 6.5b), so that a trade-off situation arises. Encouragingly, there is a wide middle-ground where high fidelity operation is possible at respectable rates.

[6] The averages are performed independently due to the statistical independence of B_N^x and δT

[7] The numerical calculations were performed using the Overhauser ensemble-averaged matrix operations defined in Sec. B.2 of the Appendix.

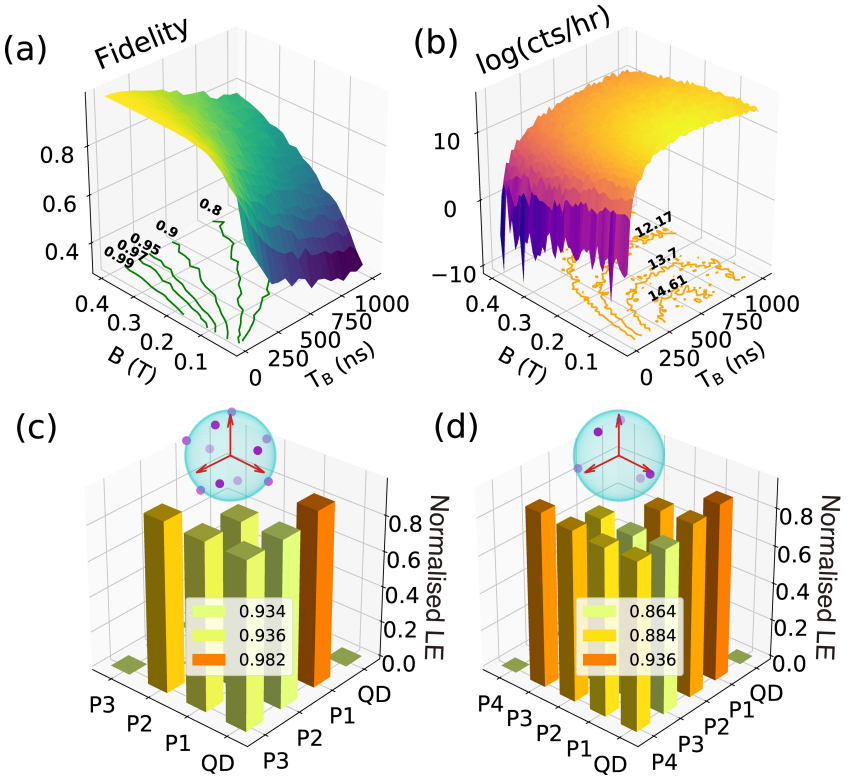

Figure 6.5: **a)** Fidelity of the LC_4 state in the presence of the Overhauser field against applied field magnitude and single time-bin duration for a mixed hh–lh spin state. Overhauser fluctuations were 14 mT [119], with $g_h^x = 0.1$, $\alpha = .01$ and a completely unpolarised spin bath. **b)** Natural logarithm of the success counts for a string of four photons. The overall detector efficiency was taken to be $\eta = 1$. The count rate increases with T_B until probability of multiple events in a single bin becomes significant. An increasing B-field decreases the count rate as predicted from Eqn. (6.8). **c) and d)** Normalised LE for between pairwise combinations of a spin and 3 (panel c) or 4 (panel d) scattered photons, respectively. Due to computational constraints, we limited ourselves to ten (panel c) and five (panel d) uniformly distributed basis states on the Bloch sphere (with projectors shown in relevant insets).

Another important figure of merit of our protocol is the localisable entanglement (LE) [145, 58] between any two qubits of the LC state (including the spin). The LE represents the maximum negativity of the reduced density matrix of two qubits of interest (indexed j and k), after all others have measured out projectively. Choosing the set of projectors $\mathcal{M} = \{P_i : 1 \leq i \leq n,\ i \notin \{j,k\}\}$ as our measurement defines an ensemble $\mathcal{E}_\mathcal{M} \coloneqq \{p_{\mathcal{M},s}, \rho^{j,k}_{\mathcal{M},s}\}$, where $p_{\mathcal{M},s}$ is the probability of obtaining the two-spin density matrix $\rho^{j,k}_{\mathcal{M},s}$ for the outcome $\{s\}$ having measured the remaining $N-2$ qubits. The LE is then defined as the maximum negativity after averaging over all

the outcomes for each measurement, that is

$$LE^{\mathcal{N}}_{j,k} = \max_{\mathcal{M}} \sum_{s} p_{\mathcal{M},s}\, \mathcal{N}(\rho^{j,k}_{\mathcal{M},s}) \ , \tag{6.13}$$

where $\mathcal{N}(\rho^{j,k}_{\mathcal{M},s})$ is the negativity of $\rho^{j,k}_{\mathcal{M},s}$. We choose a quasi-uniformly distributed basis on the Bloch sphere of each qubit (see points in insets of Fig. 6.5c,d). The computational unwieldiness of Eqn. (6.13) restricts the number of projectors, and we can only obtain a lower-bound of the true LE for $\mathrm{LC}_{3,4}$ (Fig. 6.5c,d). Within the variance of the sample over which the optimisation was performed, the LE falls off with qubit distance, but encouragingly it remains remarkably high overall, and is thus unlikely to be a limiting factor in the length of the LC that could be generated using this protocol.

6.5 Imperfections of QD-based protocols

Despite the encouraging results shown in the previous section, our scheme suffers from its inherent probabilistic nature. However, as we shall see in this section, unwanted environmental interactions mean that current deterministic solid state based schemes also suffer from probabilistic errors. The influential 2009 proposal by Lindner and Rudolph [53] offered an elegant and simple scheme which could be implemented using the circularly polarised degrees of freedom of a quantum dot. In essence, these imperfections effectively introduce limits to the size of achievable cluster states for those protocols, hence limiting the indefinite deterministic operation in the absence of further optimisations.

Indeed, despite its many attractive features for quantum metrology and quantum information [146, 120], the spin of an electron trapped in an epitaxial quantum dot suffers from rapid ensemble dephasing due to the hyperfine interaction with $\sim 10^4 - 10^6$ randomly fluctuating nuclear spins of the host material. This typically results in a loss of coherence on the order of nanoseconds [120, 121, 122, 119]. By contrast, the p-orbital-like wavefunction of hole spin states vanishes at the location of the nuclear spins, which suppresses the Fermi-contact interaction, leaving only the much weaker

dipole-dipole interaction as the main source of dephasing [147, 117, 148, 149]. Strain lifts the degeneracy of the $J = 3/2$ hole states, resulting in energetically split heavy ($J_z = \pm 3/2$) and light ($J_z = \pm 1/2$) holes; the former being closer to the valence band edge (see Fig. 6.1). Rashba or Dresselhaus spin-orbit coupling may be a limiting factor for the application of these hole spins in quantum information. This has been shown, both theoretically [150] and experimentally [151], to exacerbate the spin relaxation rate. However, we note that this spin-orbit coupling is still more detrimental to electron than hole spins [150].

6.5.1 Overhauser field limitations

The relatively short T_2^* time of the electron spin due to the fluctuating nuclear environment constitutes a severe shortcoming of real quantum dot spins, putting a limit on the order of a few nanoseconds on any experiment relying on the coherence of this system. For the Lindner and Rudolph protocol [53] one requires an external field of the order of $\sim$ 50mT along the Y direction in order to obtain a sufficient number of Y-gates for a multi photon $\mathrm{LC}_{4\geq n\geq 2}$ state within a few nanoseconds (assuming instantaneous excitation and radiative decay). Such an applied field, however, activates the previously dipole-forbidden transitions, degrading the correlations between the spin and emitted photons required for the LC state. Applying a strong field results in significant electron-spin precession between the pulsed excitation and spontaneous emission events, reducing the fidelity of the produced LC. By contrast, applying a weaker field limits the scalability of the protocol beyond a string of a couple of photons, as well as failing to screen the effects of the fluctuating Overhauser field. In short, the presence of the Overhauser field implies that the Lindner and Rudolph protocol would in practice need to be upgraded to incorporate dynamical decoupling and gated Y-rotations instead of relying on free spin precession.

One way to overcome some of these hurdles would be to adapt the Lindner and Rudolph protocol to a hole-spin system, having a longer dephasing time. However, due to the hole spins coupling weakly to external magnetic fields, the precession

time would be much longer, requiring stronger fields to implement the Y-rotations, hence resulting in the same issue discussed above; namely, the undesirable dipole-forbidden transitions becoming accessible. Hence, our scheme goes beyond a direct adaptation of the original Lindner and Rudolph scheme to the hole-spin platform, which would still suffer from most of the shortcomings of the original proposal.

Extending the promising dark exciton scheme [58] beyond a couple of photons presents similar experimental challenges: the finite radiative lifetime of the biexciton $\tau_{\mathrm{BiE}} \approx 0.33$ns entails that the spin precesses by a non-negligible random amount both in the dark exciton and biexciton states, and this limits the purity of the photon polarisation state. Furthermore, the dark exciton spin also suffers from environmental decoherence during its precession [58]. It should be noted, however, that the dark exciton scheme proposed in Ref. [58] could be optimised (for example, by using Purcell enhancement) to improve scalability.

The elegant recently proposed quantum dot scheme in Ref. [55] was designed to be robust against Overhauser fluctuations, provided the scattering events occur on a short enough timescale over which the Overhauser field can be assumed constant (so that only a global phase is gained in each trajectory). However, in this case an additional single photon source and high cooperativity is required, and any lifting of the selection rules (e.g. due to hole mixing, see below) will still impose practical limitations.

On the other hand, vanishing wavefunctions at the nuclear sites means that the Fermi-contact hyperfine term for the nuclear–hole spin interaction is effectively zero, leaving only the dipole-dipole interaction term as the dominant source of dephasing. For an idealised pure hh, this term is of Ising-nature, with just the ZZ component being present. In most epitaxially grown QDs, however, some degree of hh $|J; J_z\rangle = |3/2; \pm 3/2\rangle$ and lh $|J; J_z\rangle = |3/2; \pm 1/2\rangle$ mixing is always present [152, 117], breaking the Ising-like nature of the dipole-dipole term and introducing XX and YY terms in the Hamiltonian. This means that the eigenstates of the Hamiltonian are no longer given separately by the hh or lh states, but a linear combination of both (the consequences of this mixing in quantum dot-based LC protocols is further

discussed in Sec. 6.5.3). Without going into too much detail, the hyperfine coupling Hamiltonian for the hh–lh states is given by:

$$H_{hf}^{dd} = V \sum_j C_j |\Psi(\mathbf{R}_j)|^2 \left[\alpha(I_x^j S_x + I_y^j S_y) + I_z^j S_z\right] \tag{6.14}$$

where C_j are dipole-dipole hyperfine constants, V is the unit cell volume, and $\alpha = \frac{2}{\sqrt{3}}|\beta|$ is a parameter depending on the deformation potentials for the valence band, and the strain tensor [152, 117]. In the 'frozen-fluctuation' model [120], this results in an effective magnetic field with mean $\langle \mathbf{B}_N \rangle = (\langle B_N^x \rangle, \langle B_N^y \rangle, \langle B_N^z \rangle)$ (which, due to the finite size of the spin bath, is not necessarily zero), and a fluctuation $\delta\mathbf{B}_N = (\delta B_N^x, \delta B_N^y, \delta B_N^z)$ (which is the source of the spin's loss of coherence), and is assumed to follow normal statistics[117]:

$$\begin{aligned} P(\mathbf{B}_N) = &\left(\frac{1}{2\pi}\right)^{\frac{3}{2}} \frac{1}{\delta B_N^{\parallel 2} \delta B_N^{\perp}} \\ &\times \exp\left[-\frac{\Delta B_N^{x\,2}}{2\,\delta B_N^{\parallel 2}} - \frac{\Delta B_N^{y\,2}}{2\,\delta B_N^{\parallel 2}} - \frac{\Delta B_N^{z\,2}}{2\,\delta B_N^{\perp 2}}\right], \end{aligned} \tag{6.15}$$

where $\Delta B_N^i = B_N^i - \langle B_N^i \rangle$, $\delta B_N^{\perp} = \delta B_N^z$ and $\delta B_N^{\parallel} \coloneqq \delta B_N^x = \delta B_N^y = \alpha\, \delta B_N^{\perp}$. Experimentally, Overhauser field fluctuations of 10–30mT have been measured [122, 123], putting a lower-bound on the applied external field required to screen these fluctuations.

6.5.2 Shortcomings due to coupling to phonons

The solid-state environment further limits the deterministic nature of these protocols due to coupling to the phonon environment. Even in the limit of idealised instantaneous excitation pulses, a temperature-dependent fraction of the photons are inevitably emitted incoherently via the phonon sideband ($\sim 9\%$ at temperatures as low as $T = 4$K, increasing with temperature [108]). Emission into the phonon sideband thus adds a probabilistic element to all solid state based schemes, including

the one presented here. Whilst this is significantly detrimental to the deterministic schemes, our probabilistic scheme is not appreciably affected by this additional, smaller, probabilistic loss of photons. Furthermore, using frequency filters would allow us to filter out the unwanted photons scattered in the phonon sideband.

6.5.3 Effects of hole state mixing

Finally, we discuss how protocols using hole-spins in quantum dots fare against finite hh-lh mixing[8]. The first type of hh-lh mixing, due to anisotropy in the in-plane strain of the quantum dot, gives rise to the hh↑-lh↓ mixing, resulting in the hole eigenstates

$$\begin{aligned} |\Uparrow\rangle &= \frac{1}{\sqrt{1+|\beta_{ud}|^2}}(|3/2;+3/2\rangle + \beta_{ud}\,|3/2;-1/2\rangle)\ , \\ |\Downarrow\rangle &= \frac{1}{\sqrt{1+|\beta_{ud}|^2}}(|3/2;-3/2\rangle + \beta^*_{ud}\,|3/2;+1/2\rangle)\ , \end{aligned} \tag{6.16}$$

where, without giving its explicit form, β_{ud} is the in-plane strain-dependent mixing factor [117, 152]. This type of mixing primarily causes ellipticity of the dipole-allowed transitions which, for a hh system, would be driven by $\sigma^{\pm}$ polarized light. Hence this hh↑-lh↓ mixing does not induce the 'diagonal' dipole-forbidden transitions.

On the other hand, the hh↑-lh↑ mixing may allow transitions which would otherwise be forbidden for a hh system. The hole eigenstates solely due this type of mixing are given by:

$$\begin{aligned} |\Uparrow\rangle &= \frac{1}{\sqrt{1+|\beta_{uu}|^2}}(|3/2;+3/2\rangle + \beta_{uu}\,|3/2;+1/2\rangle)\ , \\ |\Downarrow\rangle &= \frac{1}{\sqrt{1+|\beta_{uu}|^2}}(|3/2;-3/2\rangle + \beta^*_{uu}\,|3/2;-1/2\rangle)\ , \end{aligned} \tag{6.17}$$

where β_{uu} is the hh↑-lh↑ admixture factor [117, 152]. From Eqns. (6.17), it can be immediately seen that the transitions, which are forbidden in Faraday geometry, are now allowed. For hole-spins, β_{uu} has been measured to be $\sim 8\%$, leading to

[8] Admixture of conduction band states even in the absence of a lh contribution may result in a non-Ising type hyperfine Hamiltonian for the hh system [152], however, this goes beyond the scope of this work

allowed-to-forbidden transition ratios of $|\beta_{uu}|^2/3 \approx 0.2\%$ [152], although this varies from one quantum dot to another. This means that even if the external field in the Lindner and Rudolph scheme is weak enough to preserve a pure Faraday geometry, dipole-forbidden transitions may still occur with some small, but finite probability, both for the original and the hole-spin variant of the Lindner and Rudolph protocol.

Similarly, in the dark exciton system z-polarised 'forbidden' transitions are also present due to hole sub-band mixing, although these transitions in this system are significantly weaker [153, 154]. In addition to hh-lh mixing, the dark exciton scheme also suffers from dark-bright exciton state mixing due to the breaking of the C_{2v} symmetry, although this effect is much weaker than the hh-lh mixing. Realistically, self-assembled QDs suffer from a reduction in symmetry during the growth process, causing a departure from the ideal C_{2v} symmetry. The resulting 'reduced' C_s symmetry leads to dark-bright exciton state couplings of two kinds; the first leads to finite z-polarised dipole transitions similar to the hh↑-lh↓ admixture in the bright exciton schemes, whilst the second gives rise to forbidden in-plane transitions, bearing similar repercussions as the hh↑-lh↑ mixing discussed above [153, 155], although to a much lesser extent.

We note that our approach does not suffer from modifications of the selection rules due to hole mixing: we already rely on the presence of off-diagonal transitions and slight changes to their rates will not make an appreciable difference.

6.6 Proposal for deterministic scheme using DQD

As discussed in the Sec 6.3, the main drawback of our protocol is the probabilistic nature of the photon scattering events due to the weak c.w. driving. With the aim of making our scheme more deterministic, we shall now discuss possible extensions of our cluster state protocol. Motivated by recent theoretical and experimental work, we propose extending our Raman protocol to a double quantum dot (DQD) system, where, depending on the relative strength of the exchange interaction and transition energy detuning between the two QDs, either joint measurements on the DQD system can be performed, whilst leaving the photon-entangling hole spin state

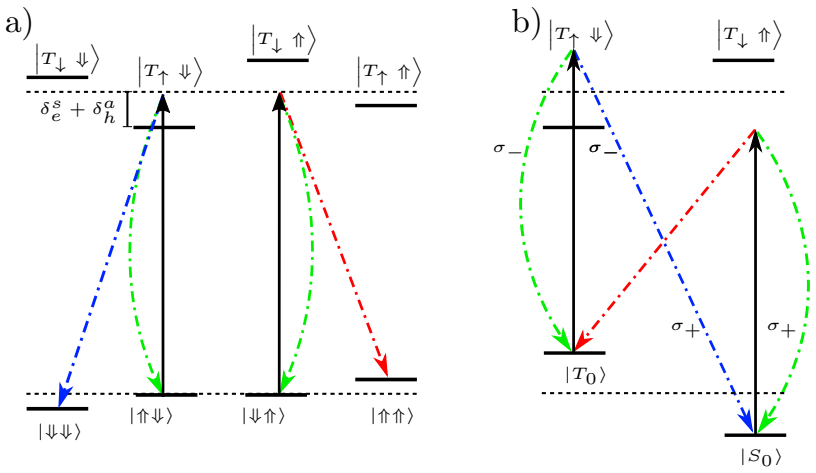

Figure 6.6: **a)** Extending the Raman spin-flip protocol to a DQD setup in Voigt geometry, where the two QDs are sufficiently detuned (relative to the exchange interaction), allowing the optical addressing of a single spin. **b)** An alternative setup in Faraday geometry [161], in which the initial state would be a superposition of S and T_0 states.

unaffected, or oscillations between joint states can be detected without collapsing the system joint state. In the following, we will discuss two possibilities of extending our protocol in such a way.

A)*Electrical control*: During the past few years, great progress has been made in synthesising and controlling quantum dot molecules, both in stacked [156, 157, 158] and lateral [159, 160] geometries. A Raman-spin flip DQD scheme was shown in Ref. [161], in which the external field is applied in Faraday geometry and the Raman spin-flips occur between the singlet S and triplet T_0 states of the system. Whilst this configuration would not allow screening of the dominant fluctuation component of the Overhauser field, such a setup would, in principle, allow a current measurement scheme to be applied and signal the Raman events. In fact, the standard singlet-triplet spin-blockade used in gated-DQDs [162] could be used to detect current drops, signalling the Raman event. This would require operation round the (1,0),(1,1),(2,0) triple-point at a negative bias, making use of the the additional charge state $S(2,0)$. Addressing and manipulation of these singlet and triplet states in optically-active DQDs have been recently been demonstrated for QD molecules [161, 163, 158, 164, 165], whereas the current transport measurements has been long understood for surface-defined QDs. This route would require a hybrid gated and optically-active device, which, although certainly challenging, might nonetheless present a feasible

route.

B) *Optical control*: A more attractive alternative to having a gated structure would be to have an all-optical non-invasive spin readout technique, provided by the rich energy level structure for these systems. In quantum dot molecules, this can be achieved by using the distributed trion state, with the ancilla spin being empty, whilst the host spin being singly-electron charged. The spin readout technique was demonstrated experimentally performing resonance fluorescence (RF) on the $|\downarrow_s, 0_a\rangle \leftrightarrow |\downarrow_s, \downarrow\Uparrow_a\rangle$ transition, which is decoupled from the main spin-flip transition [166]. This technique could be readily extended to hole spin systems with an analogous level structure. A similar setup was demonstrated experimentally in Ref. [167], where use of these cycling transitions was made to detect the flips of the host spin state. Both these setups would require individual addressing of the ancilla and host spin, meaning that the two QDs selected must be sufficiently relatively far-detuned, which could be achieved by tuning the bias voltage over the sample, decreasing the exchange energy splitting [163]. Alternatively, for samples with a much stronger singlet-triplet splitting, optical addressing of the joint states would be more feasible. In the singlet-triplet Raman scheme in Faraday geometry discussed in Ref. [161] (Fig. 6.6b), spin readout of the singlet state can be performed by using the decoupled cycling transition $T_+ \leftrightarrow R_{++}$ [164].

6.7 Robustness of 2D cluster state protocols and LC state fusing schemes

2D cluster states are a vital resource for universal quantum computation in the measurement-based paradigm, as we have seen in Chapter 4. Schemes extending the Lindner and Rudolph scheme for 2D cluster state generation have been proposed [113], in which it was shown that a pair of entangled QDs could be used to directly generate a 2D cluster state, reducing the required number of probabilistic fusion of LC state building blocks. Furthermore, it was recently shown that the requirement of two-qubit gates on the entangling emitters can be relaxed by a careful application

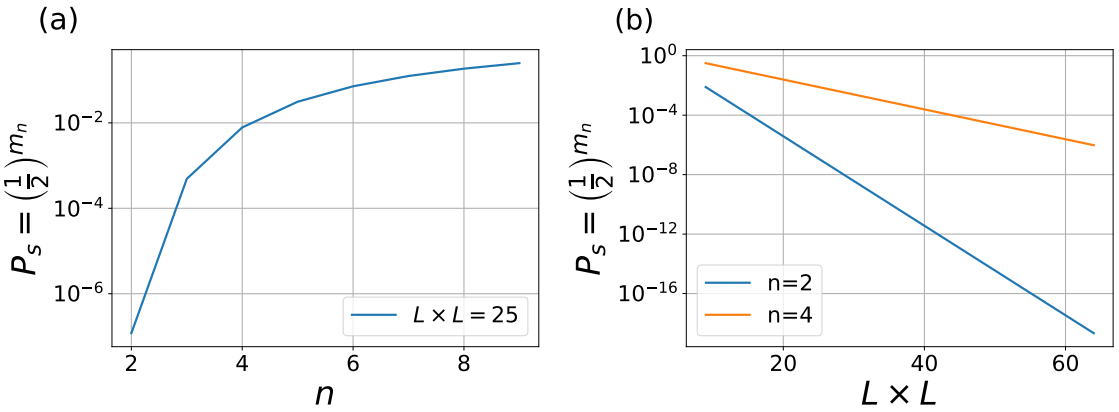

Figure 6.7: **a)** Success probability P_s of obtaining a 5×5 2D cluster state as a function of the length n of the input LC states to be fused. Going from LC_2 to LC_4 shows orders of magnitude improvement, underlining that having at least moderately sized LC states is essential for feasible 2D state growth. **b)** Success probability P_s against 2D cluster state size $L \times L$ for LC_2 (bottom, blue line) and LC_4 (top, orange line) 'building blocks', showing an increased improvement with size when going from one-dimensional states of size 2 to size 4.

of pulses and single-qubit gates on the emitters [114]. However, building on a similar setup and selection rules as the original Lindner and Rudolph protocol, we expect that the practical limitations discussed above will also limit the achievable size of photonic states that can be obtained with this protocol.

An alternative approach to generating a 2D cluster state is that of fusing LC states. We show that having high fidelity LC states of moderate length is essential for using one-dimensional states as building blocks. Consider a 2D cluster state of size $L \times L$. If we start with number of linear cluster states of size n, then the number of steps required to at least reach a 2D cluster state of size $L \times L$ is at least $m_n = \frac{L^2-n}{n-1}$: assuming that we have enough linear clusters to start with, each fusion process will (on average) increases the cluster size by $n(m_n+1)-m_n$ (noting that each fusion step leaves the fused qubit redundantly encoded with 2 photons in type II fusion, and disregarding the final layout of the 2D state for generality and simplicity). Clearly, we ignore the cases when $n > L^2$ as the probability saturates for $n = L^2$. We show how the probability scales for a 2D cluster state of size 5×5 as a function of the 'building block' size (i.e. the size of the initial cluster states) in Fig. 6.7a). This clearly demonstrates that the probability increases exponentially before saturating, showing a significant jump when going from linear cluster sizes of

2 to 4.

This increase in success probability is further emphasised when one considers increasing the 2D cluster state size. In Fig. 6.7b), we show how the difference in probability increases with increasing 2D state size $L \times L$. This approach assumes that upon failure, we have enough resources to replace the linear cluster state and try again. The results of this relatively naïve and basic analysis are further backed by an alternative approach presented in Ref. [168], in which Gross *et al.* fuse linear clusters by 'weaving' $n+1$ linear clusters of size n to form a cluster state of size $n \times n$. They show that as long as a careful choice of parameters is made, depending on the fusion success probability, then the cluster state can be prepared using $O(n^2)$ edges and the overall success probability approaches unity as n goes to infinity.

Besides having relatively longer linear states as building blocks, the fidelity of these states, indicative of quality, is also an important factor when considering scalability to higher dimensions [169, 170], as it will determine the 'percolation' or 'edge-bound' probability. Fortunately, our approach can deliver on both counts by producing LC_4 states with high fidelity at a respectable generation rate.

6.8 Conclusion

We have presented a novel scheme for generating frequency-encoded LC states, which could serve as a stepping stone towards measurement-based quantum computation. Unlike current rival schemes, our protocol is primarily sensitive to ground-state hole-spin and phonon dephasing, at the cost of being limited by its intrinsic probabilistic nature. Based on experimentally informed properties of real epitaxial quantum dots, we have shown that LC states of sufficient length and high fidelity for fusion into larger cluster states can nevertheless be produced at respectable rates. In turn, this facilitates type-II fusing into 2D cluster states [62, 170]. Our protocol takes full account of unmitigated Overhauser field fluctuations and is inherently impervious to hole-mixing induced modifications of the optical selection rules, but, like other approaches, it stands to gain from dynamic decoupling.

Whilst the probabilistic nature of the Raman scattering events limits our protocol

as described in the chapter to LC states of length $n < 10$, our approach can, in principle, be made deterministic, in the sense that the scattering events timestamps are known pre-measurement. The extensions for deterministic Raman cluster state generation make the Raman hole-spin emitter a viable, practical alternative in the quest for realising non-classical multi-photon states, and importantly one which can be straightforwardly implemented with current expertise and devices. Without these extensions to make the scheme deterministic, however, it is still possible to determine whether or not the resulting state is indeed an LC state up to the local phases. In Chapter 7, we discuss how to modify several quantum state tomographic techniques to account for random errors which are only known post-measurement. We show some preliminary results obtained when using one of these modified techniques to reconstruct our frequency-encoded linear cluster state in Appendix B.

Chapter 7

Coarse-graining in retrodictive quantum state tomography

Quantum state tomography (QST) is a foundational tool in quantum state characterisation. This technique relies on the combination of experimental and data-processing methods and, despite not being as efficient as entanglement witnesses in quantifying entanglement, it allows for full state characterisation. Despite the extensive library of techniques developed in the QST community, most methods rely heavily on the assumption of perfect measurements, which, combined with errors inherent to the reconstruction technique and its application, may lead to considerable reductions in the reconstruction accuracy. In this chapter, we propose to retrodict the quantum state of a system, existing prior to the application of random (but known post-measurement), allowing such errors to be separated and removed [171]. This idea of 'state retrodiction' can be applied to several physical scenarios, including the photonic cluster state generation presented in Chapter 6 (indeed, we provide the link between the abstract idea of state retrodiction and various physical applications in Appendix C). Applying this idea to various state-of-the-art QST techniques, we show that such a (relatively) minor correction can lead to improved reconstruction fidelities. Furthermore, we introduce the idea of 'coarse-graining' in order to significantly reduce the computational cost of reconstructing the state using retrodiction, for modest sacrifices in fidelity.

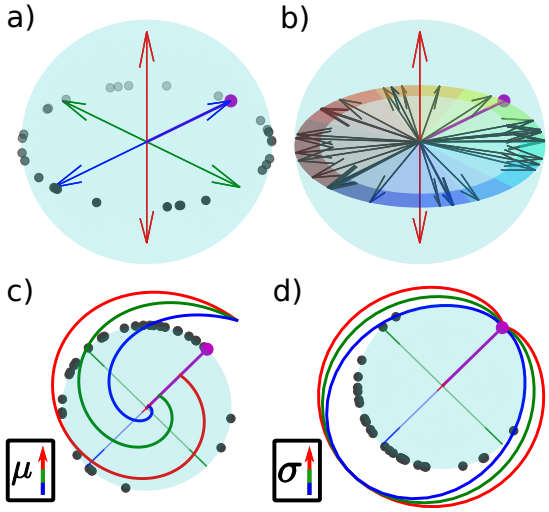

Figure 7.1: Bloch sphere representation of the problem in the context of a precessing qubit. **a)** In the Schrödinger picture, the state (purple) gains a random phase (dots) prior to every measurement, with the measurement bases given by the arrows (i.e. the state carries the time-dependency due to the random phases whilst the operators are fixed). **b)** In the Heisenberg picture, the state is static while the measurement operators are distributed randomly (i.e. the operators are time-dependent whilst the state is effectively time independent as the phases are inherited by the operators). The detector clicks can then be gathered in several bins on the Bloch sphere (coloured segments) to be used for coarse grained state reconstruction. Graphical depiction of **c)** exponentially distributed and **d)** normally distributed phases, for various distribution widths. The distributions are sketched in polar coordinates, with different colours indicating different widths, controlled by the distribution parameters μ and σ. Distributions are un-normalised to aid visual emphasis.

7.1 Motivation

Accurate quantum state reconstruction from finite data is undoubtedly a fundamental aspect of several quantum information and computation protocols, as it is one of the most complete characterisation approaches to various quantum systems such as atoms, molecules and engineered platforms such as quantum dots and NV centres. Despite joint efforts on both the experimental and data-processing fronts, QST still suffers from outstanding problems, such as measurement errors either due to mis-calibrated apparatuses or noisy detectors. Such errors can be either random or systematic, leading to lower reconstruction fidelity with respect to the true state.

Consider, for example, the highly active field of photonic cluster state generation, introduced in Chapters 4 and 6. An emitter, such as a quantum dot, spontaneously emits a photon at a random delay after being excited. We discussed the cluster state

generation scheme in detail in the Chapter 6; however, the essence of this process is the entanglement generated by spontaneous emission (or scattering) between the emitted (or scattered) photon and the emitter, as well as entanglement generated between subsequently emitted photons mediated by the emitter itself [172, 173, 58]. These schemes, which make use of the emitter to generate the entanglement resource required for MBQC, typically rely on the application of an external magnetic field orthogonal to the optical axis [172, 173, 58]. For an ideal scenario, the emitter's relaxation follows its excitation instantaneously, and thus does not suffer any precession between the two events. However, due to the emitter's non-zero lifetime τ_{d}, there is a non-zero delay between excitation and emission, during which the spin precesses at it's Larmor frequency ω_L. Thus, the emitter is no longer in the correct state for the protocol, but has suffered from a random precession angle which is then transferred to the emitted photon due the the entanglement between the two, and can only be detected by the experimenter *after* the photon is detected. Due to the unknown emission/scattering time, the standard spin echo technique would thus not be able to reverse this unwanted phase. The goal of retrodicting the quantum state of the emitter is then to essentially 'reverse' the effects of this additional phase on the joint emitter and photonic state (resulting in the state equivalent to having $\tau_{\mathrm{d}} \to 0$). As we shall see, this can be done by re-defining the measurement operators for the data-processing stem of tomography, using the additional post-measurement knowledge of the random phases.

More abstractly, this problem may be modelled by a semi-malevolent agent interfering in the experiment by applying random unitaries on the error-free photonic state ρ as $\rho \to U_\theta \rho U_\theta^\dagger$ (where we take $U_\theta \coloneqq \cos\left(\frac{\theta}{2}\right)\mathbb{I} + i\sin\left(\frac{\theta}{2}\right)\sigma_z$), which the experimenter only finds out after having made the measurements. Despite the inevitability of these errors, retrodicting the state is still possible during post-processing, thus eliminating the effects of these errors, allowing the identification and characterisation of other sources of errors which would have otherwise been masked by the non-retrodicted state.

We have already mentioned that this retrodiction can be performed by modifying

the measurement operators during the data-processing step. The link between state retrodiction and these new measurement operators can be obtained by moving from the Schrödinger to the Heisenberg picture. Indeed, since the success probability of a measurement operator M is given by $\mathrm{tr}(M[U_\theta \rho U_\theta^\dagger]) = \mathrm{tr}([U_\theta^\dagger M U_\theta]\rho)$, moving from one picture to the other allows us to define a new set of random measurement operators $\{M_\theta := U_\theta^\dagger M U_\theta\}$ which we use to reconstruct the retrodicted state ρ (Fig. 7.1). Clearly, a key requirement for this trick to work is knowledge of the effective measurement operators. Going back to the photonic cluster state generation example, these random phases can be easily calculated using, in principle, only three parameters: the arrival time of the photon τ_a, its time-of-flight to the detector τ_f, and the precession frequency ω_L. The first two parameters reveal the time the emitter spent precessing between excitation and relaxation, that is, $\tau_\mathrm{a} - \tau_\mathrm{f}$. The precession frequency can then be used to calculate the random phase accumulated during this time.

Due to the continuous nature of the distribution over the phase θ, the measurement record in the Heisenberg picture is sparse, as no effective measurement outcome will appear more than once, resulting in at most one click attributed to each outcome. This means that the more measurements we make, the higher the computational cost of processing the data using retrodiction, as more effective measurement operators M_θ are used for the reconstruction. We show, however, that our technique is successful despite of this feature, by equipping state-of-the-art tomographic techniques with this retrodictive modification and showing how we obtain high fidelity reconstructions of the density matrix. In order to overcome the sparsity condition inherent to retrodictive tomography, we discuss and implement a 'coarse-grained' approach, in which the data is sorted in the post-processing step into a finite number of discrete bins. Coarse-graining is not only a choice for the experimenter to reduce computation times, but can also be useful when only imperfect knowledge of the phases θ is available. Indeed, we find a drastic improvement in computational cost, at a small price in fidelity.

The Bayesian 'shot-by-shot' approach to tomography would be, intuitively, the

more natural approach to test the retrodictive technique on, as it makes use of prior information to update the current knowledge of the quantum state based on additional information gained as additional measurements are performed. Unfortunately, the coarse-grained approach we shall discuss in this chapter cannot be straightforwardly applied to the Bayesian scheme due to the latter's shot-by-shot' reconstruction approach. Thus, the latter will serve as benchmark for the Maximum Likelihood (ML) techniques which will follow.

7.2 Sparse and binned tomography

We define $p(\theta)$ as the distribution of random phases (supported on $[0, 2\pi)$), which determines how the effective measurement operators are distributed. This distribution depends on the physical scenario: in the example of frequency-encoded cluster-state generation in the hole-spin system in Chapter 6, when the precession time is much shorter than the emission time, $p(\theta) \approx 1/(2\pi)$. This is the extreme case in which the coherences of the reconstructed density matrix would be completely washed out using 'conventional' (that is, without making use of the phase knowledge) QST techniques. For the more general case of photon emission from spin-bearing emitters, however, the exponential distribution $p(\theta) \propto \mathrm{e}^{-\theta/\mu}$ (with the mean $\mu = \lambda^{-1}$, where λ is the rate parameter) is more adequate to describe the spread of operators. Other distributions may be similarly treated (making our work applicable to wide range of physical scenarios) although the measurement operators may then be clustered to a greater or lesser degree, affecting the accuracy of the retrodicted tomogram accordingly. In the discussion, we give the phase distribution and corresponding parameters for some quantum information and computation schemes. The normal distribution $p(\theta) \propto \mathrm{e}^{-\theta^2/2\sigma^2}$ (σ being the standard deviation) is considered in Section 7.5 [1], and for $\mu \to \infty$, we recover the uniform distribution limit, i.e. $p(\theta) \to 1/(2\pi)$.

In the Schrödinger picture, we fix the three measurement operators $|\uparrow\rangle\langle\uparrow|$, $|\downarrow\rangle\langle\downarrow|$

[1] It should be said however, that for most physical systems, the exponential distribution is a more appropriate distribution to describe emission times.

and $|\phi\rangle\langle\phi|$, where $\sqrt{2}|\phi\rangle = |\uparrow\rangle + e^{i\phi}|\downarrow\rangle$ and $\phi \in \{0, \pi\}$. Since emitted photons are measured independently, m-qubit states are generated by forming m-fold tensor products of all combinations of these projectors. By using the Heisenberg picture (as in the previous section), the tomographic protocol is equivalent to reconstructing some unknown state ρ with the following set of projective measurement operators

$$\mathcal{P} = \{|\uparrow\rangle\langle\uparrow|, |\downarrow\rangle\langle\downarrow|, \ M_{\theta_i} = U_{\theta_i}^{\dagger}|\phi\rangle\langle\phi|U_{\theta_i}\} \tag{7.1}$$

where $U_{\theta_i}^{\dagger}|\phi\rangle = |\phi + \theta_i\rangle$ for θ_i $(i = 1, ..., N/2)$ drawn from $p(\theta)$. Note that $U_{\theta_i}^{\dagger}|\updownarrow\rangle\langle\updownarrow|U_{\theta_i} = |\updownarrow\rangle\langle\updownarrow|$, and that the values of ϕ play less of a role as the spread of θ increases. Because $|\phi\rangle\langle\phi| + |\phi + \pi\rangle\langle\phi + \pi| = \mathbb{I}$, this set may be considered a Positive Operator Valued Measure (POVM) when normalised such that the sum of all operators is proportional to the identity.

We generated pseudo-tomographic data for a fixed ρ by drawing $N/2$ unique values of $\theta \in [0, 2\pi)$ from $p(\theta)$. We then simulate a single Bernoulli trial for each measurement operator, assigning the event to M_{θ_i} with probability $p_i = \mathrm{tr}(\rho M_{\theta_i})$, and to the orthogonal operator with the complementary probability. Similarly, the remaining $N/2$ Bernoulli trials are assigned to $|\uparrow\rangle\langle\uparrow|$ or $|\downarrow\rangle\langle\downarrow|$. The measurement record then consists of a set of $N/2 + 2$ distinct measurement operators, with multiplicities $n_i = 1$ (i.e. 'sparse') for the $N/2$ operators perpendicular to the axis about which the phases are accumulated (i.e. the 'precession' axis), whilst the pair of orthogonal operators parallel to the 'precession' axis have a joint multiplicity of $N/2$.

As discussed, we may also modify the measurement record by a process of coarse-graining or 'binning', resulting in a lower number $N_b < N/2$ of coarse-grained measurement operators perpendicular to the precession axis. Non-overlapping measurement bins are indexed by $j \in \{1, 2, ..., N_b\}$, and have multiplicities defined by

$$\tilde{n}_j = \sum_i n_i \mathrm{rect}\left(\frac{N_b\theta_i}{2\pi} - j + \frac{1}{2}\right) \ , \tag{7.2}$$

where $\mathrm{rect}(x) = 1$ if $|x| < \frac{1}{2}$ and 0 otherwise, i.e. we simply accumulate the events

according to the bin that they fall within, with the bins being intervals centred on $(2j-1)\frac{\pi}{N_b}$ and having width $2\pi/N_b$ (as shown graphically in Fig. 7.1). Each bin is assigned a measurement operator defined by:

$$M_{\tilde{\theta}_j} = U^{\dagger}_{\tilde{\theta}_j}|\phi\rangle\langle\phi|U_{\tilde{\theta}_j} \tag{7.3}$$

where the angle $\tilde{\theta}_j$ is the mean of the random angles in the j^{th} bin, that is

$$\tilde{\theta}_j = \frac{1}{\tilde{n}_j}\sum_i \theta_i \text{rect}\left(\frac{N_b\theta_i}{2\pi} - j + \frac{1}{2}\right) \ , \tag{7.4}$$

We should point out that other binning schemes are possible [174], however, we believe our coarse-graining scheme is fairly intuitive compared to other available binning techniques. We then run different reconstruction algorithms (to be introduced below) on the coarse-grained measurement record, to give a quantum state estimate or 'tomogram' ρ_{est}. The running time of the algorithm is noted, and the fidelity of the tomogram, given by $F(\rho_{est},\rho) = \text{tr}\sqrt{\sqrt{\rho}\rho_{est}\sqrt{\rho}}$, is computed. The infidelity is $1-F$, and is a measure of the distance between the true state and the retrodicted tomogram, and thus we use it as a figure of merit for our reconstructions. The procedure is then repeated for distinct, randomly generated (but full rank) ρ, and we collected statistics to summarise the performance on average.

Counter to intuition, using sparse tomography without any binning works remarkably well. However, algorithm running time tends to scale badly with N (since the calculation of the cost function and its gradient involves a contribution from each of the N distinct operators). As we shall see, the coarse-graining approach alleviates this problem significantly, with only modest fidelity sacrifices. The remainder of this chapter is dedicated to investigating the dependence of fidelity and run time on N_b, for different reconstruction algorithms. As $N_b, N \to \infty$, the sparse and coarse grained approaches are expected to give the same fidelities.

7.3 Non-adaptive Bayesian tomography

The Bayesian estimation approach has played an increasingly prominent role in state [175, 176, 177, 178, 179, 180] and parameter [181, 182, 183] estimation, and is still an ongoing theoretical and experimental research topic [184, 185, 186]. In this section, we shall be focussing on its application in quantum state estimation, whereas the topic of Chapter 8 shall be its role in parameter estimation. This approach offers numerous advantages over other techniques, such as use of online information available to the experimentalist after each measurement. Furthermore, Bayesian inference was also shown to be optimal with respect to any strictly proper scoring rule derived from Bregman distances [187, 184, 188] (near-optimal if the infidelity is used as a loss function instead [189]), with the ability to track fidelity bounds online [189] (allowing for feedback to minimise number of required measurements), as well as giving robust region estimates [190] and allowing for model selection/averaging. Thus, based on these advantages offered by the Bayesian approach, the latter shall be used as a benchmark for the other techniques discussed in this work.

Our implementation closely follows the approaches used in Refs. [185] and [191]. For a Bayesian update scheme, we start with an initial prior probability density $p(\rho)$ over a feasible state space (taken to be uninformed due to the absence of additional knowledge, resulting in a uniform prior). Choosing a uniform prior allows for the characterisation of dephased states, as the probability distribution extending to the interior of the Bloch sphere (cf. Fig 7.2). After obtaining a new measurement datum D, the posterior distribution $p(\rho|D)$ is then built using the likelihood function $\mathcal{L}(\rho; D)$ as

$$p(\rho|D) \propto \mathcal{L}(\rho; D)p(\rho) \ . \tag{7.5}$$

Typically, Bayesian tomography schemes would then make use of the narrower posterior and additional criteria (for example, Shannon information [191]) to infer the next optimal measurement setting [191, 185]. However, when considering a finite lifetime for the emitter, any measurement basis prediction would be futile for the next measurement due to the random phase gained known only post-detection. Although we do not make use of any criteria to track the narrowing of the sample, one

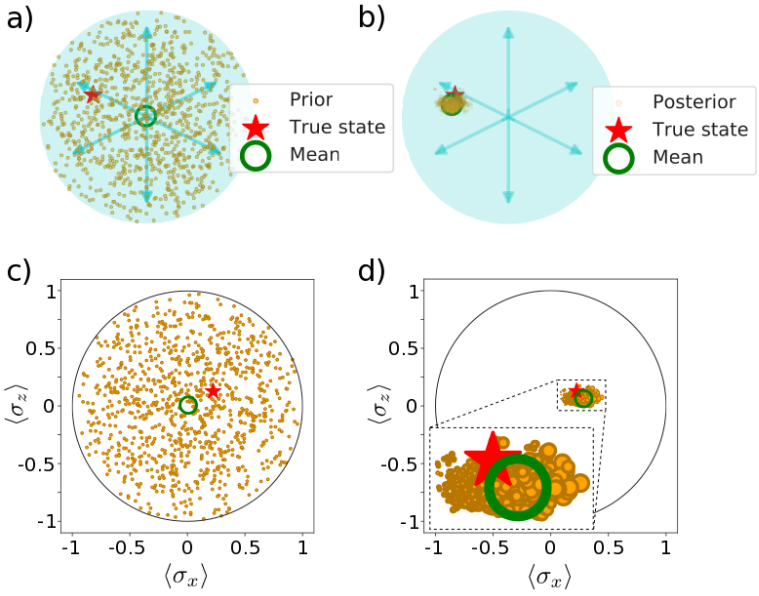

Figure 7.2: **a)** Initial uninformed prior (orange), with the mean of the distribution shown in green, and the true state to be reconstructed in red. **b)** Final posterior (orange) after 2000 measurements, where the marker size indicates the relative particle weights. **c)** and **d)** show the $[\langle\sigma_x\rangle, \langle\sigma_z\rangle]$ projection of the prior and posterior, respectively, as a visual aid. As more measurements are performed, most of the original particle weights drop to zero, requiring resampling for a more accurate prediction without requiring an excessive number of particles to begin with.

could still use the covariance of the the narrowed posterior, in this case, to indicate when a sufficiently precise estimate has been found.

Despite the simple form of Eq. 7.5, the analytical evaluation of the posterior is seldom feasible, and hence the latter is typically replaced with an approximation. To this end, several Markov Chain Monte Carlo techniques (MCMC) have been adopted in previous literature, including the Metropolis-Hastings algorithm [184]. However, these MCMC techniques tend to be computationally expensive, with decreasing acceptance probabilities at each sampling step, leading to more samples being discarded as additional data is obtained. Furthermore, these methods require the assumption of a normal posterior, which is not always the case in state tomography. The Sequential Monte Carlo technique (SMC) [192, 193], on the other hand, only requires the computation of a single term of the likelihood to update the weights of the approximate distribution with each measurement [191]. In this approach, adopting the notation in Ref. [191], the posterior after the i^{th} measurement is approximated by a number P of randomly sampled particles, $\{\rho_p\}$, and their

corresponding weights $\{w_p^{(i)}\}$ as

$$p(\rho|\{D_i\}) \approx \sum_{p=1}^{P} w_p^{(i)} \delta(\rho - \rho_p) \ . \tag{7.6}$$

Suppose our current (prior) knowledge is given by the dataset $\{D_i\} = \{\alpha_j : \ 1 \leq j \leq i, \ \alpha_j \in \mathcal{P}\}$, where the set $\mathcal{P}$ is defined in Eq. 7.1. If the next projection phase is θ_{i+1}, (that is, $\alpha_{i+1} = M_{\theta_{i+1}}$), then, following Ref. [191] and using Bayes' rule (Eq. 7.5), we can write the approximation for the next posterior as

$$\begin{aligned} p(\rho|\{D_{i+1}\}) &= p(\rho|\{D_i\} \cup \{M_{\theta_{i+1}}\}) \\ &\approx \sum_{p=1}^{P} \frac{\mathbb{P}(M_{\theta_{i+1}}|\rho_p) w_p^{(i)}}{\sum_{q=1}^{P} \mathbb{P}(M_{\theta_{i+1}}|\rho_q) w_q^{(i)}} \delta(\rho - \rho_p) \\ &\coloneqq \sum_{p=1}^{P} w_p^{(i+1)} \delta(\rho - \rho_p) \ , \end{aligned} \tag{7.7}$$

where $\mathbb{P}(M_{\theta_{i+1}}|\rho_p) = \mathrm{Tr}(M_{\theta_{i+1}}\rho_p)$. In our numerical simulations, we perform the first $N/2$ measurements along the z-axis (that is, using projection operators $\{|\uparrow\rangle\langle\uparrow|, |\downarrow\rangle\langle\downarrow|\}$), followed by the remaining $N/2$ measurements in the equatorial plane of the Bloch sphere. As more measurements are performed, narrowing the particle distribution, most of the weights drop to zero as more points in the chosen sample become less likely estimates for actual state ρ of the system. This can be remedied by resampling using the new posterior distribution [191]. Finally, the Bayes estimator ρ_{est} can be extracted from the mean of the final posterior approximation. In Fig. 7.2 we show the above steps graphically, emphasising the use of resampling to obtain an accurate posterior.

We numerically benchmarked the Bayesian technique, using a uniform prior and samples being drawn from a Ginibre ensemble (random matrices with normally distributed entries), and subsequently multiplied by their corresponding Hermitian conjugates to give positive matrices. Finally, these are normalised to unit trace [143, 144]. An example is shown in Fig. 7.2. and further results are summarised in Fig. 7.3. As the data follow a skewed distribution due to the fidelity being capped by

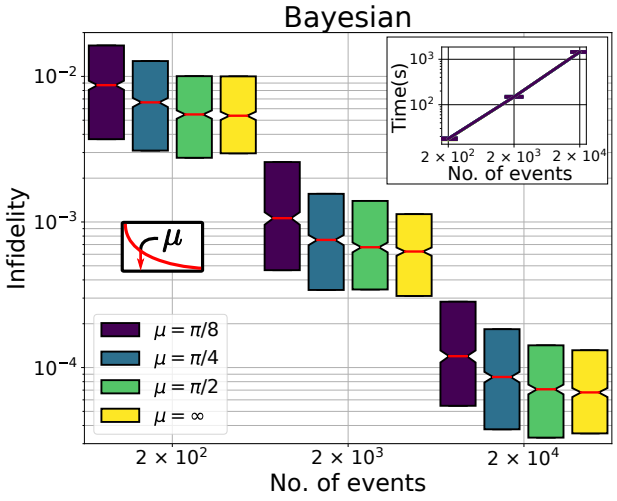

Figure 7.3: First and third quartile box plots for full rank, single qubit reconstruction using the non-adaptive Bayesian approach, with exponentially distributed measurement operators, averaged over 1000 trials using 1000 particles for sampling. The performance improves with increasing rate parameter $\mu = \lambda^{-1}$. Unless otherwise stated, all box plot error bars will display first and third quartiles. Otherwise, error bars used correspond to one sigma uncertainty. **Inset:** Algorithm running times for the Bayesian approach. For all values of μ, the computation time scales linearly with number of measurement repetitions (or, equivalently, the number of operators used for the reconstruction) due to the sparse nature of our Bayesian reconstruction, having each measurement outcome assigned an effective measurement operator M_θ.

unity, the use of box plots was preferred over the standard approach of mean and error bars, which would only be appropriate for symmetrically-distributed data. More specifically, as the fidelity is upper-bounded by unity, the probability distribution obtained after we perform several realisations of the tomographic reconstruction is truncated at 1 and thus symmetric error bars are inadequate. Despite the fact that we cannot decide which measurement to perform next, our random basis measurement can be seen to give a good convergence after 2000 measurements with 1000 particles.

7.4 Maximum Likelihood Estimation

A common, alternative, approach to state estimation is producing a tomogram ρ_{est} which maximises the likelihood function. Naive approaches may result in an invalid tomogram (obtaining, for example, negative eigenvalues using gradient descent without projection), meaning that the search for the best fit to the data should

then be constrained to the allowed state space of trace-one positive semidefinite matrices [194, 195, 196]). Previously (in the Bayesian method) this was ensured by choosing a prior distribution supported only in the allowed state space. Here, the prior is not modelled, but we consider two alternative approaches: the constraints are implemented 1) by a non-linear parametrization of the density matrix and 2) periodically in the course of an iterative gradient descent procedure, allowing for temporary violations [197, 198, 196]. Given a density matrix ρ, the likelihood function to be maximised has the form

$$\mathcal{L}(\rho) \propto \prod_{j=1}^{N_b} p_j^{n_j} \ , \tag{7.8}$$

with equality holding up to an irrelevant proportionality constant. For sparse tomography, the product would be over N exponentiated probabilities p_j, with each n_j taking a binary value of either 0 or 1. The above function essentially describes the joint probability of observing the j^{th} outcomes, each with probability p_j and frequency n_j. Due to the monotonicity of the logarithm, maximising the likelihood function is identical to minimising the negative of its logarithm [which we refer to as the cost function $\mathcal{C}(\rho)$], given by

$$\mathcal{C}(\rho) \coloneqq -\log \mathcal{L}(\rho) = -\sum_{j=1}^{N_b} n_j \log(p_j) \ , \tag{7.9}$$

where we took the normalising constant to identity. Recall that the sparse tomography limit is recovered when $N_b = N$ and $n_j = 1$. In the limit of a large number of detections per measurement, the probability of obtaining the j^{th} measurement can be approximated by a Gaussian distribution [199, 200], with the estimated number of detections for the j^{th} measurement given by $\bar{n}_j = N p_j$. Since this approximation clearly fails for the sparse case due to the binary nature of the n_j's, we do not make it.

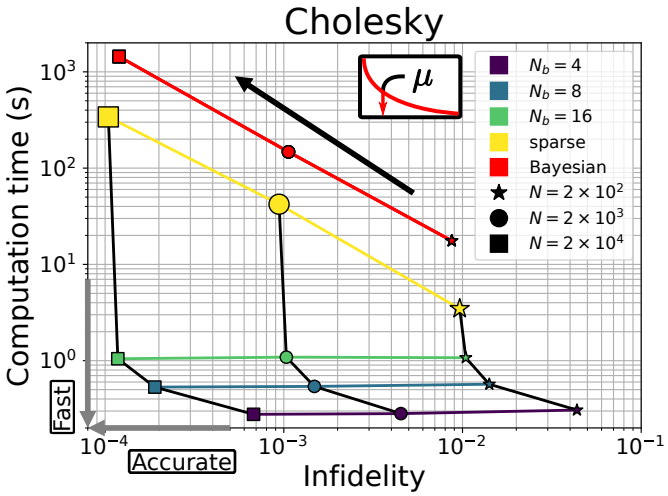

Figure 7.4: Full rank, single qubit reconstruction using the Cholesky decomposition method, averaged over 1000 trials. The random phases were sampled from an exponential distribution with $\mu = \pi/8$. As expected the coarse grained approach returns slightly higher infidelities (shown on the x-axis). The algorithm running times (y-axis) for the sparse approach scales linearly with number of measurement repetitions. On the other hand, the computation times for the binned approach, within error bars, remain the same with increased repetitions, as the number of projective operators used for binned reconstruction is fixed to N_b, regardless of the number of repetitions N. The results from the Bayesian method are also shown for comparison. While the Bayesian approach offers higher fidelity estimates for lower measurement numbers N (star), the infidelity is higher compared to the sparse Cholesky for higher N, and the corresponding computation time heavily offsets any advantages gained in fidelity by the Bayesian approach. The black arrow indicates the direction of the trend as the number of measurement events increases; infidelity decreasing at the expense of higher computation time, whilst the grey arrows on the axes point towards the ideal region of low infidelity and computation time.

7.4.1 Cholesky factorisation

In this section we implement a Cholesky-like decomposition of the density matrix in order to minimise Eq. 7.9 [199, 200, 201], allowing us to use Python's SciPy least-squares solver on a 1D array [2] One can easily show that any qubit density matrix ρ allows for a decomposition of the form

$$\rho = T^\dagger T / \mathrm{Tr}[T^\dagger T] \ , \tag{7.10}$$

[2]More formally, this least-squares solver uses the Trust Region Reflective technique (involving searching along directions reflected from the trust region bounds).

where T is the lower triangular matrix given by

$$T(\mathbf{t}) = \begin{pmatrix} t_1 & 0 \\ t_3 + it_4 & t_2 \end{pmatrix} , \tag{7.11}$$

with $\mathbf{t} = (t_1, t_2, t_3, t_4)$ being the array over which the minimisation search is performed. In particular, we can use this decomposition to calculate $\bar{n}_j \propto p_j = \mathrm{Tr}\left[|\phi + \theta_j\rangle \langle \phi + \theta_j| T^\dagger T\right] / \mathrm{Tr}[T^\dagger T]$. Generalising this parametrisation to m qubits, we get

$$T(\mathbf{t}) = \begin{pmatrix} t_1 & 0 & ... & 0 \\ t_{2^m+1} + it_{2^m+2} & t_2 & ... & 0 \\ ... & ... & ... & 0 \\ t_{4^m-1} + it_{4^m} & t_{4^m-3} + it_{4^m-2} & ... & t_{2^m} \end{pmatrix} , \tag{7.12}$$

and hence the search needs to be done over a real array of length 4^m.

Having formulated a decomposition guaranteeing a valid density matrix, the problem can be recast to a least-squares minimisation problem [199, 200] in order to find the minimum of the negative log likelihood, as the latter may be written down as

$$\mathcal{C}(\rho) = \sum_{i=1}^{N} [f_i(\mathbf{t})]^2 , \tag{7.13}$$

where, for the general case of a multinomial probability distribution, we get using Eq. 7.9

$$\begin{aligned} f_j(\mathbf{t}) &= \sqrt{n_j \log(p_j)} && (7.14) \\ &= \sqrt{n_j} \left(\log\{\mathrm{Tr}\left[|\phi_j\rangle \langle \phi_j| T^\dagger(\mathbf{t}) T(\mathbf{t})\right]\} \right. && (7.15) \\ &\quad \left. - \log\{\mathrm{Tr}\left[T^\dagger(\mathbf{t}) T(\mathbf{t})\right]\} \right)^{\frac{1}{2}} . && (7.16) \end{aligned}$$

This optimization problem was shown to have a single global solution, despite having several local minima [201], meaning that all local minimizers lead to the same solution minimizing the negative log likelihood.

In Fig. 7.4 we show the results for single qubit reconstruction. As expected, the fidelity of the reconstructed density matrix increases with number of Bloch sphere

partitions. This is also the case for a two-qubit reconstruction, as we show in C.1.

7.4.2 Projected gradient descent

Gradient descent algorithms rely on following the path of steepest descent of the cost function, in this case Eq. 7.9, starting from a well chosen initial estimate. If left unconstrained in the convex space of $d \times d$ matrices (where d is the Hilbert space dimension), the resulting estimate ρ_{est} might lie outside the convex subspace of unit-trace, positive semidefinite matrices, leading to an unphysical estimate. Hence, projection back to the physical subspace, minimising distance as measured through of a matrix norm (such as projection of the spectrum onto the unit simplex [201, 197, 198]) is employed, giving rise to projected gradient descent (PGD) algorithms. Iterating this process leads to a convergence of the cost function to a minimum within any tolerance. A unique solution satisfying the appropriate constraints and minimising the cost function is then guaranteed as long as the latter is a continuously differentiable convex function of the density matrix. Eq. 7.9 is convex but not continuously differentiable, but this tends to not pose a problem in practice, as discussed in Ref. [196]. Choosing the projection of ρ to be of its spectrum onto the unit simplex (which we refer to as $\mathcal{P}_S$), the PGD algorithm update can be written as

$$\rho_k = \mathcal{P}_S[\rho_{k-1} - \nabla\mathcal{C}(\rho_{k-1})] \ . \tag{7.17}$$

As is commonplace, we supplement the PGD algorithm with a backtracking line search (PGDB) based on the Armijo–Goldstein condition to loosely optimise the maximum step size for each descent iteration [201, 197, 198]. The estimate at the k^{th} PGDB iteration can thus be written as

$$\rho_k = (1-\alpha)\rho_{k-1} + \alpha\ \mathcal{P}_S[\rho_{k-1} - \nabla\mathcal{C}(\rho_{k-1})] \ , \tag{7.18}$$

where $\alpha \in [0, 1]$ is the line search parameter to be roughly optimised at each step. We assess the impact of binning on the PGDB algorithm, Fig. 7.5a showing the

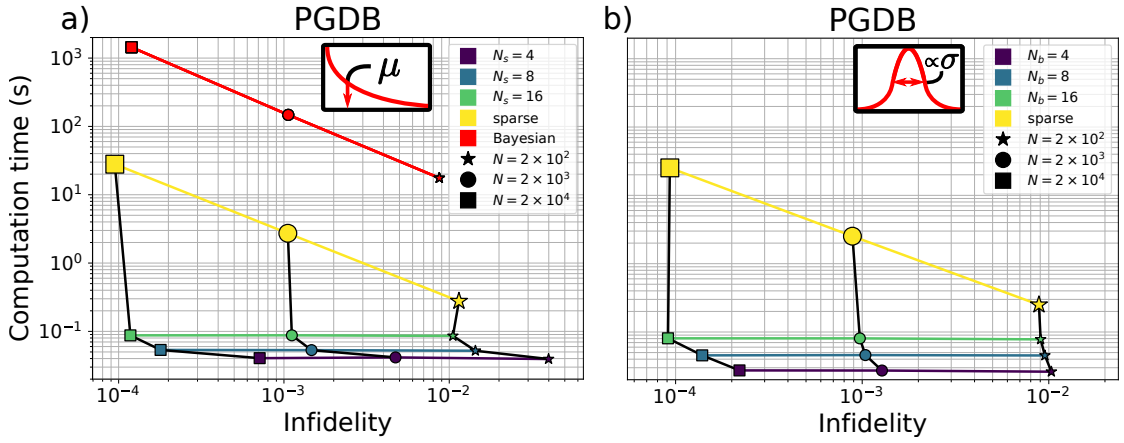

Figure 7.5: Full rank, single qubit reconstruction using gradient descent, averaged over 1000 trials. **a)** The random phases were sampled from an exponential distribution with $\mu = \pi/8$. The results follow a similar behaviour as the Cholesky method, except that the PGDB algorithm (for the given exit criteria in C.2) shows lower computation times both for the sorted and binned approaches. For comparison, we also show the Bayesian result for the exponentially distributed phases. **b)** The random phases were sampled from a normal distribution with standard deviation $\sigma = \pi/8$. For lower N, going from $N_b = 4$ to $N_b = 8$ or from $N_b = 16$ to sparse tomography does not reduce the infidelity as significantly as when increasing the number of bins from 8 to 16.

trade-off between computation time and fidelity for $\mu = \pi/8$. Fig. 7.5b, on the other hand shows the relation between computation time and infidelity for various number of bins N_b and events N for normally distributed phases, showing a similar trend to the exponentially spread phases.

As expected, within standard deviation error, the binned approach gives slightly lower fidelities than the sparse one (see Fig. 7.6). This difference, however, is well justified when considering the significant reduction in computation time shown in Fig. 7.5a and Fig. 7.6b. The trends in Fig. 7.5a, both for computation time and infidelity, are similar to those shown in Fig. 7.4 for the Cholesky method. However, our numerical simulations clearly show lower reconstruction times achieved using the PDGB technique. In Fig. 7.7, we show how the infidelity varies with increasing mean μ for various values of the bin number N_b.

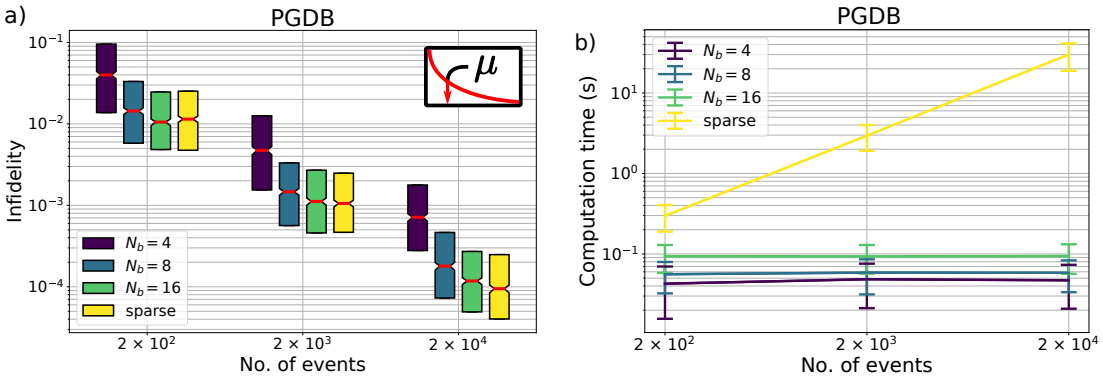

Figure 7.6: a) Full rank, single qubit reconstruction using gradient descent, averaged over 1000 trials. The random phases were sampled from an exponential distribution with $\mu = \pi/8$. As expected the coarse grained approach returns slightly higher infidelities. b) Algorithm running times for the unsorted, and coarse grained approaches. The unsorted approach scales linearly with number of measurement repetitions. The coarse grained approaches, within the standard deviation, do not scale with increased repetitions as the number of projective operators used for reconstruction is the same for all repetition numbers.

7.5 Condition numbers

Using a single basis for reconstruction along the plane of precession, we see that the higher the spread of the distribution, the higher the fidelity one expects, as the effective rotated bases sample larger portions of the Bloch plane, thus having more measurements spread out across the entirety of the Bloch sphere. For lower spreads, on the other hand, the additional phase knowledge does not contribute considerably, and hence incomplete Pauli tomography (in which only x- and z- basis measurements are performed) is recovered. This can be seen in Fig. 7.8, showing the behaviour of the condition number $\kappa(A)$ of the measurement matrix A for increasing N, where A is given by

$$A = \begin{pmatrix} \mathrm{vec}(M_{\theta_1})^T \\ \vdots \\ \mathrm{vec}(M_{\theta_{N/2+2}})^T \end{pmatrix}, \tag{7.19}$$

where the projectors $\hat{\Pi}_i$ make up the set $\mathcal{P}$ in Eq. 7.1 [202, 198]. The condition number decreases significantly with increasing standard deviation of the distribution, meaning that sampling distributions with larger spreads results in a better conditioned measurement matrix.

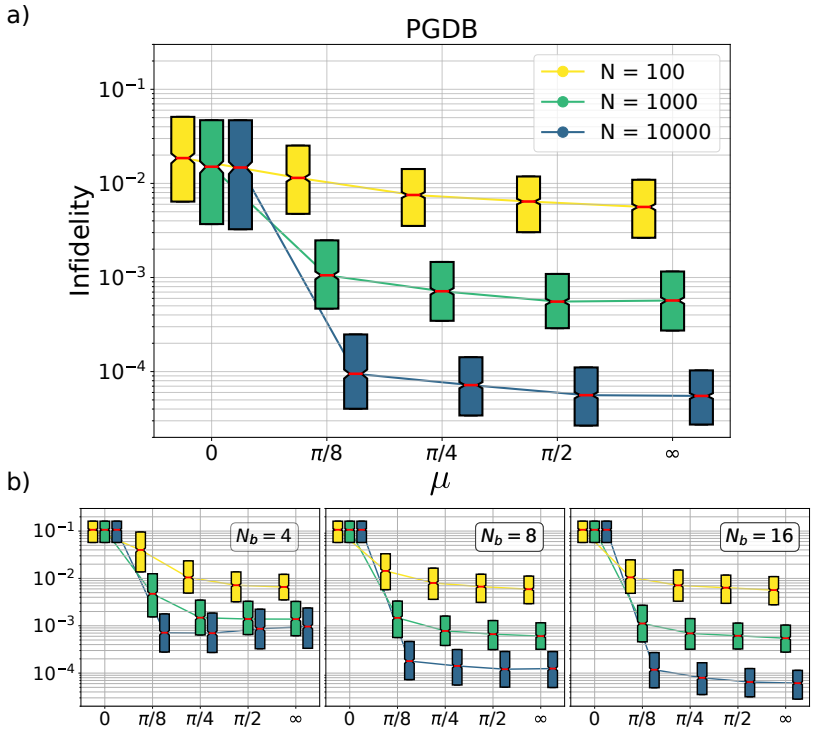

Figure 7.7: **a)** Full rank, sparse single qubit reconstruction infidelities for phases sampled from exponential distribution with various values of μ and experiment repetitions N. **b)** Infidelities for various segment numbers N_b. In both **a)** and **b)**, averages were performed over 1000 trials.

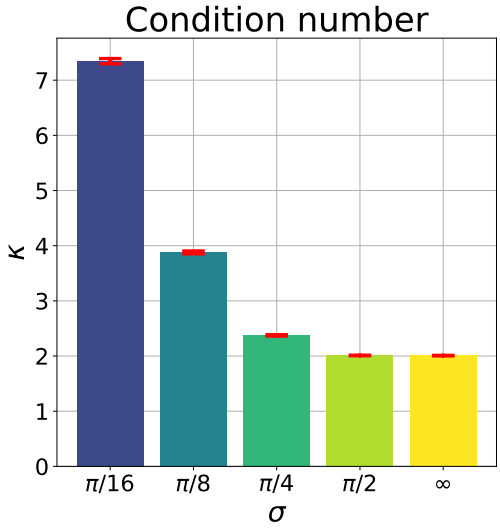

Figure 7.8: Sparse tomography condition number (shown above for $N = 2 \times 10^4$) decreases (improves) as the standard deviation of the normally distributed phases (σ) increases. The red bars indicate one sigma uncertainty. When σ is high, we recover the limit of many measurements distributed evenly around the equator of the Bloch sphere. In this situation, we obtain the same condition number, $\kappa(A) = 2$, as in the case of complete Pauli measurements [202].

7.6 Discussion

Quantum state tomography is still an active area of experimental and theoretical research, allowing the reconstruction of quantum states from finite experimental data. In this chapter, we implemented several QST algorithms in the presence of phase errors which are only known after the system is measured. We showed, with a simple modification, how the unaffected state may be retrodicted using the additional knowledge of the photon's arrival time t_a. Furthermore, we demonstrated that, at a small cost in fidelity, the reconstruction time can be significantly decreased. Having discussed these modifications for abstract phase distributions, we now make a connection between dimensionless parameters used in our work to characterise these random phase distributions, and the physical parameters involved in some recent quantum information processing and computation protocols. In Table 7.1, we give the phase distributions that can be applied to various quantum computation and information schemes, along with the relevant parameters used to calculate their effective mean μ. For all distributions shown, μ is given by $\mu = \frac{\omega}{2\pi}\frac{1}{\gamma}$, where ω and γ are parameters to be defined shortly.

For the last four schemes in Table 7.1, ω denotes the emitter's precession frequency, whereas for the Barrett and Kok protocol [56], ω represents the local phase picked up by one of the two spins which spends additional time in the excited state. For a typical GaAs quantum dot with excitonic energy ~ 1.35 eV, this leads to an excitonic frequency of $\omega \approx 3.265 \times 10^5$ GHz. Assuming a similar setup is used for the Lim *et al.* scheme [203], we arrive at a similar phase distribution. On the other hand, for the first four schemes, γ represents the decay rate of the emitter due to spontaneous emission, whereas for the Scerri *et al.* scheme [173] (which makes use of photon-scattering), $1/\gamma$ is the loosely-optimised time between Y-rotations during which the emitter probabilistically scatters a photon. For the Lindner and Rudolph scheme [172], μ was calculated using parameters which give an error rate of 0.2%, whereas for the Denning *et al.* scheme [55], the mean was calculated based on values suggested for high Q-factor cavities.

All data in this work was generated and visualised using Python and QuTiP

Protocol	$\boldsymbol{\omega/2\pi}$ (GHz)	$\mathbf{1/\gamma}$ (ns)	$\mathbf{p(\theta)}$	$\boldsymbol{\mu}$
Barrett and Kok [56]	3×10^5	0.100	QU	$\to \infty$
Lim *et al.* [203]	3×10^5	0.100	QU	$\to \infty$
Lindner and Rudolph [172]	0.105	0.100	E	0.011
Schwartz *et al.* [58]	0.200	0.330	E	0.066
Denning *et al.* [55]	0.955	0.167	E	0.159
Scerri *et al.* [173]	0.420	500	QU	$\to \infty$

Table 7.1: Table showing the phase distributions for various state-of-the-art protocols, where QU and E stand for 'quasi-uniform' and 'exponential', respectively. The mean varies from protocol to protocol, with some schemes having quasi-uniform phase distributions. For the latter, we expect retrodiction to significantly improve the reconstruction fidelity.

package [143, 144].

Chapter 8

Adaptive Bayesian spin bath narrowing

After having introduced the Bayesian approach in the context of quantum state estimation in Chapter 7, we now focus on another application of this formalism: extending the coherence time of solid state spins, which would have several interesting applications such as improved spin magnetometry. Single spin sensors are able to give highly sensitive measurements of external magnetic fields with nanometre-scale spatial resolution [204, 205], allowing for high-resolution mapping of magnetic field textures in condensed matter and atomic nanostructures. In a solid state nanostructure such as a diamond NV centre, the dilute nuclear environment is the main cause of decoherence of the central spin, ultimately putting a cap on how sensitive these devices can be. In this chapter, we investigate how the back-action of performing Ramsey measurements on the central spin affects the latter's nuclear environment. We apply the Bayesian scheme to estimate the state of the spin bath and find that the resulting distribution of possible fields due to these surrounding spins narrows down, considerably enhancing the T_2^* time of the central spin, which we define as the time it takes for the Ramsey signal to decay to $\sim 37\%$ its original value due to electron–nuclear spin bath interactions. We benchmark the adaptive strategy with non-adaptive techniques, finding a considerable improvement over the narrowing limit of the non-adaptive strategies.

8.1 Motivation

Several fields in quantum technology, such as metrology and information, rely on the capability to preserve the coherence of quantum states. Due to the rich fluctuating solid state environment surrounding most of these platforms (discussed in Chapter 3), coherence is only preserved during a finite timescale dictated by the fluctuations in the spin environment of the central spin. An obvious, intuitive, way to combat this decoherence would be to minimise these environmental fluctuations by isolating the central spin from its environment by developing higher purity materials for platforms such as NV centres. Unfortunately, this technique is limited by experimental resources and may not always be an option. Techniques to mitigate errors resulting from this decoherence, such as quantum error correction methods, can preserve the quantum state of the system. However, quantum error correction adds a significant overhead due to the additional qubits required. On the other hand, pulse sequences such as dynamical decoupling can efficiently separate the qubit from its environment at specific times during its evolution. The latter poses obvious problems when the qubit is required on-demand and not at pre-determined intervals.

Recently, parameter estimation techniques have been adopted in an attempt to solve this this problem from a different angle: By applying fast measurements on the central spin, information about the state of the surrounding spin bath can be gained, resulting in a partial projection of the latter to a particular state, hence reducing the effects of decoherence. This technique has been shown to increase the T_2^* time for quantum dots with large, many-body environments in an experiment by the Yacoby group [206]. For these systems, the interaction with the spin bath environments can be treated as a semi-classical time-varying magnetic field due to the size of the spin bath.

NV centres, on the other hand, have dilute nuclear environments, unlike GaAs quantum dots. Recent work has shown that by applying controlled pulse sequences to the NV centre, a small ensemble of nuclear spins from its environment can be sensed [207, 208, 209] and controlled [210, 211], making the NV centre and its sur-

rounding nuclear spins a good candidate system for a quantum register. Would parameter estimation techniques for spin bath partial projection work for NV centres or other solid state nanostructures with dilute environments? We show that, indeed, enhancing the T_2^* time using these partial-projection schemes works even for dilute environments. Unlike the large environment of a quantum dot, this dilute spin bath can be characterised by a tractable quantum state. By estimating the hyperfine coupling between the electron spin and the surrounding nuclei, one can infer the probability of the nuclear spin bath to be in a particular joint state. Thus, with every measurement performed on the central spin, additional information about its environment is gained, narrowing down this state probability distribution, and hence reducing the fluctuations on the electron spin, resulting in a longer coherence time. In contrast to dynamical decoupling sequences, the improved coherence is maintained, until the intrinsic quantum evolution of the environment quantum states broadens the set of possible coupling strengths. Compared to similar experiments performed on a semi-classical bath, by narrowing the bath distribution and increasing the coherence time, the need for very fast, continuous measurements on the bath can be relaxed.

In this chapter, we discuss and implement the Bayesian parameter estimation scheme [181, 182, 183], and use the measurement back-action to narrow the bath state uncertainty. We present some preliminary results benchmarking two variations of this technique, more specifically, by showing coherence time improvements for every algorithm. Whilst the techniques studied here can be applied for more general systems with dilute environments, we focus on the electronic spin of a negatively charged nitrogen-vacancy (NV^-) centre in diamond, coupled to a bath of ^{13}C nuclear spins.

8.2 Model

NV^- centre defects in diamond, as discussed in Chapter 3, host an $S = 1$ electronic spin that can be optically initialized and read-out. For simplicity, we assume the experiments are carried out at cryogenic temperatures, where fast initialization

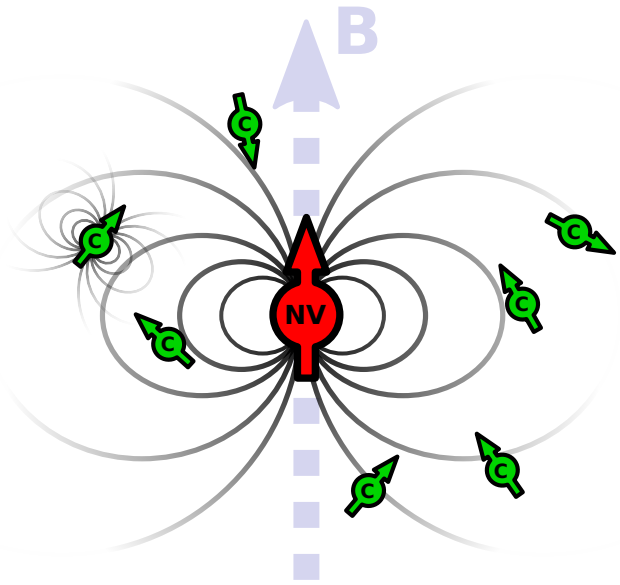

Figure 8.1: NV centre (red) in an external magnetic field (blue arrow) interacting with surrounding ^{13}C nuclear spins (green) via the hyperfine field. The nuclear spins are also coupled to each other (to a weaker extent) via the dipole-dipole interaction

and single-shot read-out of the electronic spin can be performed with high fidelity ($> 95\%$). We also assume that the concentration of electronic impurities (substitutional nitrogen) is sufficiently low that the main cause of decoherence is due to the hyperfine interaction with the surrounding ^{13}C nuclear spins. The natural abundance of this isotope in diamond is $\sim 1.1\%$, but can be as low as $\sim 0.01\%$ for isotropically modified diamond samples.

Following Refs. [212, 213], the Hamiltonian of our system can be written as:

$$H = H_{cs} + H_b + H^{int}_{cs-b} \ , \tag{8.1}$$

where H_{cs}, H_b and H^{int}_{cs-b} are the central spin (in our case the NV$^-$ electron spin) and spin bath Hamiltonians, and the interaction Hamiltonian of the defect and bath, respectively. In the presence of an external magnetic field $\mathbf{B} = (B_x, B_y, B_z)$,

the individual Hamiltonian components can be written as

$$\begin{aligned} H_{cs} &= DS_z^2 + \gamma_e \mathbf{B}\cdot\mathbf{S} \ ; \\ H_b &= \gamma_N \sum_n \mathbf{B}\cdot\mathbf{I}_n + \sum_{n<m} \mathbf{I}_n \cdot \mathbb{C}_{nm} \cdot \mathbf{I}_m \ , \\ H_{cs-b}^{int} &= \sum_n \mathbf{S}\cdot\mathbb{A}_n\cdot\mathbf{I}_n \ , \end{aligned} \tag{8.2}$$

where D is the electron spin zero-field splitting, γ_e and γ_N are the electron and nuclear gyromagnetic ratios, respectively, $\mathbf{S}$ and $\mathbf{I}_n$ are the spin vectors for the electron and n^{th} nuclear spin, respectively, $\mathbb{A}_n$ is the hyperfine tensor of the n^{th} spin, while $\mathbb{C}_{nm}$ is the coupling tensor between nuclei n and m. Assuming the external field and NV^- centre axis are aligned along the z-axis, we denote the Zeeman split states by $\{|\mu\rangle\,;\ \mu = -1, 0, 1\}$. Moving to a rotating frame with respect to the electron $\mu = 0 \leftrightarrow 1$ transition, we recover the Hamiltonian

$$\begin{aligned} H &= \sum_{\mu=0}^{1} |\mu\rangle\langle\mu| \otimes H_\mu \ ; \\ H_\mu &= \sum_n \mathbf{\Omega}_n^{(\mu)}\cdot\mathbf{I}_n + \sum_{nm} \mathbf{I}_n\cdot\mathbb{C}_{nm}^{(\mu)}\cdot\mathbf{I}_m \ , \end{aligned} \tag{8.3}$$

where $\mathbf{\Omega}_n^{(\mu)} = \gamma_N\mathbf{B} + \mu\mathbf{A}_n$ [$\mathbf{A}_n = (A_n^{zx}, A_n^{zy}, A_n^{zz})$ now denoting the hyperfine vector] is the effective Larmor vector for the n^{th} nuclear spin, and the form of $\mathbb{C}_{nm}^{(\mu)}$ can be found in Appendix D. We have also made the secular approximation, allowing the discarding of the zero-field splitting term.

8.3 Ramsey measurements

In this section we will discuss how the Bayesian scheme is applied to the Ramsey measurements. The standard Ramsey pulse sequence is given by $\frac{\pi}{2} - \tau - \frac{\pi}{2}$, where the first pulse rotates the electron spin from the initial $|0\rangle$ state to the superposition $\frac{1}{\sqrt{2}}(|0\rangle + |1\rangle)$. No longer in an eigenstate of the external field, the spin precesses for a given time τ, after which the second pulse rotates the spin by a further $\pi/2$ on the Bloch sphere. The resulting evolution can be written as $U(\tau) = R_x\left(\frac{\pi}{2}\right) U_f(\tau) R_x\left(\frac{\pi}{2}\right)$,

where $U_f(\tau)$ denotes the (unitary) free evolution, and $R_j(\phi)$ represents rotation by an angle ϕ about the j-axis, $j \in \{x, y, z\}$. Tracing out the nuclear bath component of the density matrix would give a free induction decay (FID) signal, which can be used to infer the probability of finding the central spin in the $|0\rangle$ state.

Due to the interaction with several nuclear spins, the central spin loses coherence, as this interaction effectively causes the net magnetic field felt by the central spin to fluctuate. However, due to the back-action of the central spin measurement on the surrounding nuclear environment, the result from each Ramsey measurement gives partial information on projection of the hyperfine field along the magnetic field axis (in our case, the z-axis), thus narrowing the uncertainty in the bath state with each measurement. In turn, as knowledge of the spin bath state increases, the fluctuations in the magnetic field felt by the central spin diminish, thus increasing the T_2^* time of the latter.

However, an underlying problem of the standard Ramsey sequence with fixed measurement times is the trade-off between sensitivity to changes in the signal, which for our setup consists of the z component of the hyperfine field, and measurement range. If we repeat the sequence for a total time T, with each measurement time being τ, our uncertainty of the signal decreases as $1/(2\pi\sqrt{\tau T})$ [183]. Increasing the measurement time then clearly increases the maximum sensitivity with which we can detect the signal. However, due to the surrounding nuclear spin bath, the longest measurement time τ_{max} is capped off by the natural timescale over which decoherence plays a significant role, that is, $\tau_{max} \sim T_2^*$.

Naively performing Ramsey experiments sequentially with fixed measurement parameters is thus not optimal for a number of reasons, as we shall further discuss in the next section. The Bayesian optimisation scheme aims to use the data obtained after each measurement in order to infer what the free precession time $\tau \lesssim T_2^*$ and measurement angle ϕ of the next sequence should be in order to narrow down the spin bath distribution. In the next two sections, we shall discuss two variants of the Bayesian scheme, differing in the parameters that are adaptively changed.

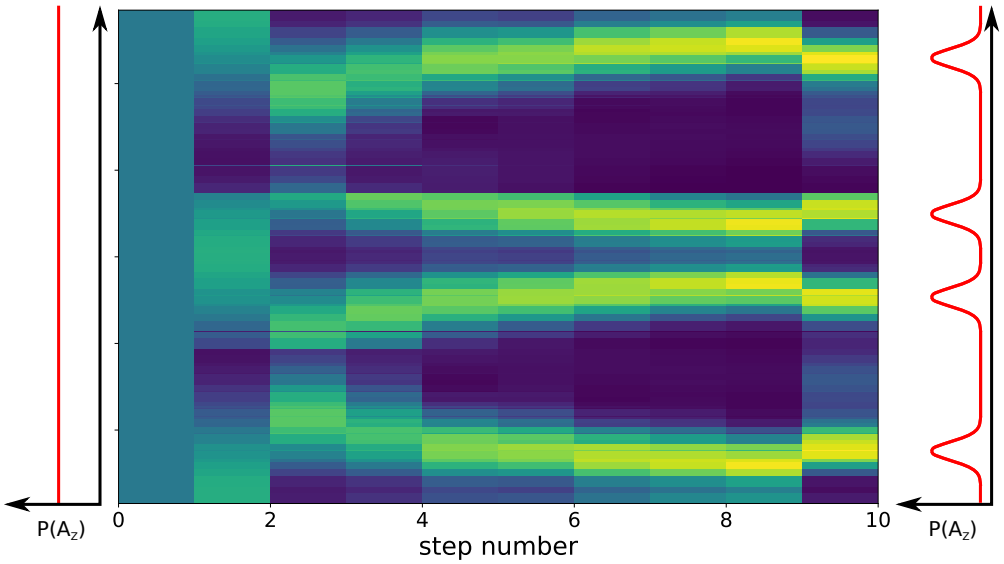

Figure 8.2: One of the caveats of naively applying Ramsey measurements with fixed parameters is that, despite significant narrowing of the initial probability distribution $P(A_z)$, the final distribution might be multimodal, leading to result ambiguity. The red curves shown above are graphical depictions of the initial and final probability distributions at steps 0 and 10, respectively, of the middle figure showing the probability distribution over 10 Ramsey sequences. The simulation above was done for a 7 nuclear spin bath and a magnetic field $B_z = 1\text{T}$.

8.4 Partially adaptive Bayesian scheme

As mentioned in the previous section, the electron spin measurement back-action infers additional knowledge with each measurement sequence. The main advantage of using a Bayesian scheme is that, with each measurement, we can extract the optimal measurement parameters for the next sequence, allowing us to decrease the total estimation time required to reach the T_2 limit (after which the nuclear spin flip-flops become the main cause of electron spin decoherence).

The protocol consists of adaptively changing the measurement angle ϕ, whilst the measurement time for the k^{th} step is set to be $\tau_k = 2^k\tau_0$, where τ_0 is the smallest measurement time. Initially, the spin bath distribution $P(A_z) = \{\text{Tr}(|A_z^i\rangle\langle A_z^i|\,\rho_0) : 1 \leq i \leq 2^N\}$ (where ρ_0 is the initial spin bath density matrix, $|A_z^j\rangle$ is the j^{th} joint spin bath eigenstate, with eigenvalue A_z^j and N is the number of nuclear spins in the environment) is assumed to be uniform, that is to say, the nuclear spin bath is in the thermal state $\rho_0 = 2^{-N}\mathbb{I}_N$. The goal is to then partially project the spin bath state, narrowing the state probability distribution of the bath. Given the estimated probability distribution at the m^{th} step $P(A_z|\mu_1, ..., \mu_m)$, the distribution for the

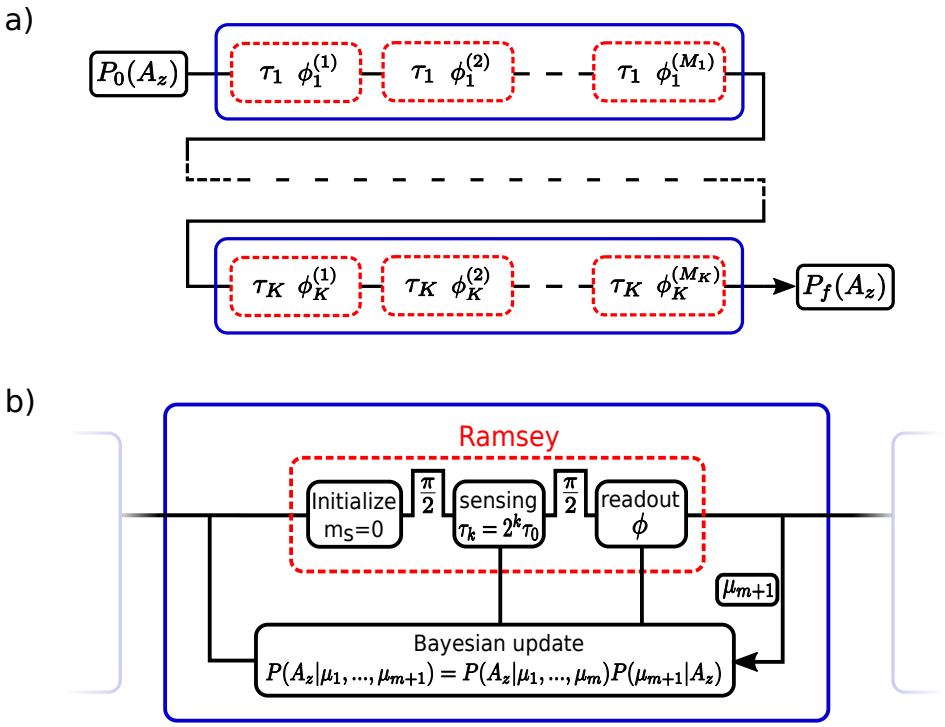

Figure 8.3: Schematic for the Bayesian adaptive scheme **a)** The scheme consists of K sequences (blue boxes), with the k^{th} sequence repeated M_k times. For each measurement (red dashed box) in the sequence, we fix the measurement time τ_k, with k either increasing monotonically for the phase adaptive scheme, or optimised for each sequence in the fully adaptive scheme. The measurement angle is optimised for each individual measurement. **b)** Details of the k^{th} sequence, showing the Ramsey measurement with the optimised parameters.

$m+1^{\text{th}}$ step can be found using Bayes' theorem

$$P(A_z|\mu_1,...,\mu_{m+1}) = P(A_z|\mu_1,...,\mu_m)P(\mu_{m+1}|A_z)\ , \tag{8.4}$$

where μ_l is the Ramsey result of the l^{th} estimation step (i.e. $\mu_l \in \{0,1\}$), and, from Refs. [181, 183], the conditional probability $P(\mu_{m+1}|A_z)$ in the presence of environmental decoherence is given by

$$\begin{aligned} P(\mu_{m+1}=0|A_z) &= \frac{1+f_0-f_1}{2} \\ &\quad + \frac{f_0+f_1-1}{2} e^{-(\tau/T_2^*)^2}\cos(2\pi A_z\tau+\phi) \\ P(\mu_{m+1}=1|A_z) &= 1 - P(\mu_{m+1}=0|A_z)\ , \end{aligned} \tag{8.5}$$

where f_0 and f_1 are the readout fidelities for the two possible outcomes $\mu_{m+1}=0$, and $\mu_{m+1}=1$, respectively [183]. Having defined the update rule for our distribu-

tion, we can now identify another problem with the naive Ramsey approach: As can be seen from Fig. 8.2, naively applying Ramsey measurement sequences with fixed phase ϕ and measurement time may lead to ambiguities in the measured signal [183] despite narrowing the distribution to some extent.

Previous work dealing with estimating periodic, classical signals f_B [181, 182, 183] expressed the probability distribution $P(f_B)$ in Fourier space due to the periodicity of the signal. In our case, measurements involving multiple values of τ_0 result in a periodic distribution with a Gaussian envelope, due to the limited range of possible net magnetic field strengths sensed by the central spin due to the surrounding environment. Thus, we can also represent our probability distribution $P(A_z)$ in Fourier space as

$$P(A_z) = \sum_j p_j \mathrm{e}^{i2\pi j A_z \tau_0} \ , \tag{8.6}$$

where the coefficients p_j are determined by the previous measurement results [181]. The estimate A_z^{est} of the actual signal A_z can then be easily quantified by a single Fourier coefficient, that is

$$A_z^{est} = \frac{1}{2\pi\tau_0} \arg \left\langle \mathrm{e}^{i2\pi A_z \tau_0} \right\rangle = \frac{1}{2\pi\tau_0} \arg |p_{-1}| \ , \tag{8.7}$$

where the last equality is a direct result of the Fourier representation of $P(A_z)$.

The use of the standard definition of variance may be problematic for estimating a periodic signal, for example, when considering the initial distribution. If we start from a completely uniform prior, we would expect infinite variance, which is clearly not the case as we are limiting our search to a finite region in frequency space. A more adequate variance measure can be obtained by modifying the Holevo variance V_H [214], giving

$$\begin{aligned} V_H &= \left\langle \cos[2\pi(A_z - A_z^{est})\tau_0] \right\rangle^{-2} - 1 \\ &= (2\pi|p_1|)^{-2} - 1 \ . \end{aligned} \tag{8.8}$$

Previous work using non-adaptive strategies involved optimising the measurement angle ϕ in order to maximise $|p_1|$ (which can be shown to be equivalent to minimis-

ing Eq. (8.8)) and performing measurements with decreasing measurement times $2^k\tau_0, 2^{k-1}\tau_0, ..., \tau_0$. Whilst we still use the modified Holevo variance to find the optimal measurement angle, our non-adaptive scheme reverses the order of measurements, as the T_2^* time is extended with each measurement, thus allowing longer measurement times before decoherence sets in. Using the Fourier representation, it can be shown that the optimal phase ϕ_k for the k^{th} sequence can be found by maximising the absolute value of the Fourier coefficient $|p_{-t_k}|$, where $t_k\tau_0 = 2^k\tau_0$ is the (fixed) measurement time for this sequence. In Ref. [181] the authors showed that, with monotonically decreasing measurement times, the k^{th} optimal readout angle is given by $\phi_k = \frac{1}{2}\arg(p_{-2^{K-k}})$.

The minimum uncertainty that is achievable with this partially adaptive approach would be obtained during the longest measurement time of $2^K\tau_0$, giving an uncertainty of $\sigma_{min} \sim 2^{-K}\tau_0^{-1}$. This however, cannot be achieved by having a single repetition for each sequence. Following Refs. [215, 182], we implement $M_k = G + kF$ repetitions for the k^{th} Ramsey sequence, where F and G are integers, the latter being the number of repetitions of the shortest measurement sequence. Thus the total sensing time T is simply given by $T = \sum_{k=0}^{K} M_k 2^k\tau_0 = G(2^{K+1}-1)+F(2^{K+1}-K-2)$. Due to the reversed order of the measurements (that is, increasing instead of decreasing in length), we suggest updating the phase for the m^{th} measurement of the k^{th} sequence based on the recent work done in Ref. [183]:

$$\phi_k^{(m)} = \frac{1}{2}\arg(p_{-2^m}) \ . \tag{8.9}$$

We additionally include a conditional phase of $\pi/2$ when the subsequent electron spin measurement result differs, in order to differentiate more rapidly between additional peaks that appear in the multimodal probability distribution (cf. Fig. 8.2).

8.5 Fully adaptive Bayesian strategy

The algorithm discussed in the previous section makes use of the adaptive phase for each measurement. However, the measurement time increases exponentially with

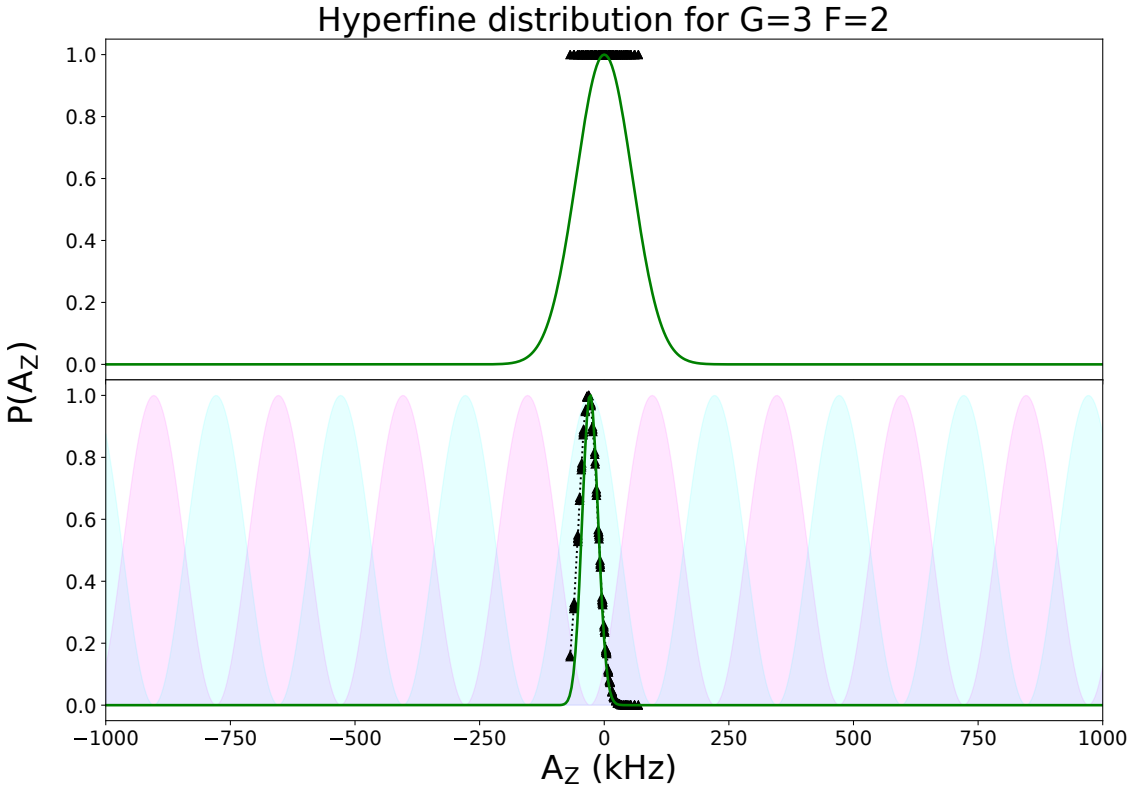

Figure 8.4: Probability distribution $P(A_z)$ for a 7 nuclear spins with an applied magnetic field $B_z = 1$T before and after 20 Ramsey sequences with $G = 3$ and $F = 2$. The green curve is the Bayesian distribution, whereas the discrete distribution in black is the distribution simulated directly from the Hamiltonian dynamics. The initial estimate is taken to be a normal distribution of width $\sim \tau_0^{-1}$. The conditional probabilities $P(\mu|A_z)$ for $\mu = 0$ and $\mu = 1$ are shown in magenta and cyan, respectively.

each set of M_k repetitions. Whilst this approach may seem intuitive as the sensitivity increases relatively quickly, the T_2^* of the central spin during the measurements quickly puts a limit on the performance of this scheme. More precisely, as soon as the inequality $2^k\tau_0 > T^*_{2,k}$ holds (that is, the measurement time surpasses T_2^* at the k^{th} sequence), the protocol has to be terminated as decoherence effects will play an increasingly significant role in the electron–bath dynamics.

We thus suggest using an alternative, fully-adaptive scheme, whereby the parameter k, determining the measurement time for the k^{th} sequence, is also optimised. We implement this optimisation based on the current value of the coherence time, $T^*_{2,k-1}$[1]; more specifically, we choose $k = k_{opt}$ so as to saturate the current (improved)

[1]In an experiment without access to $T^*_{2,k-1}$, the width of the bath probability distribution may be used instead as an alternative measure of the coherence time.

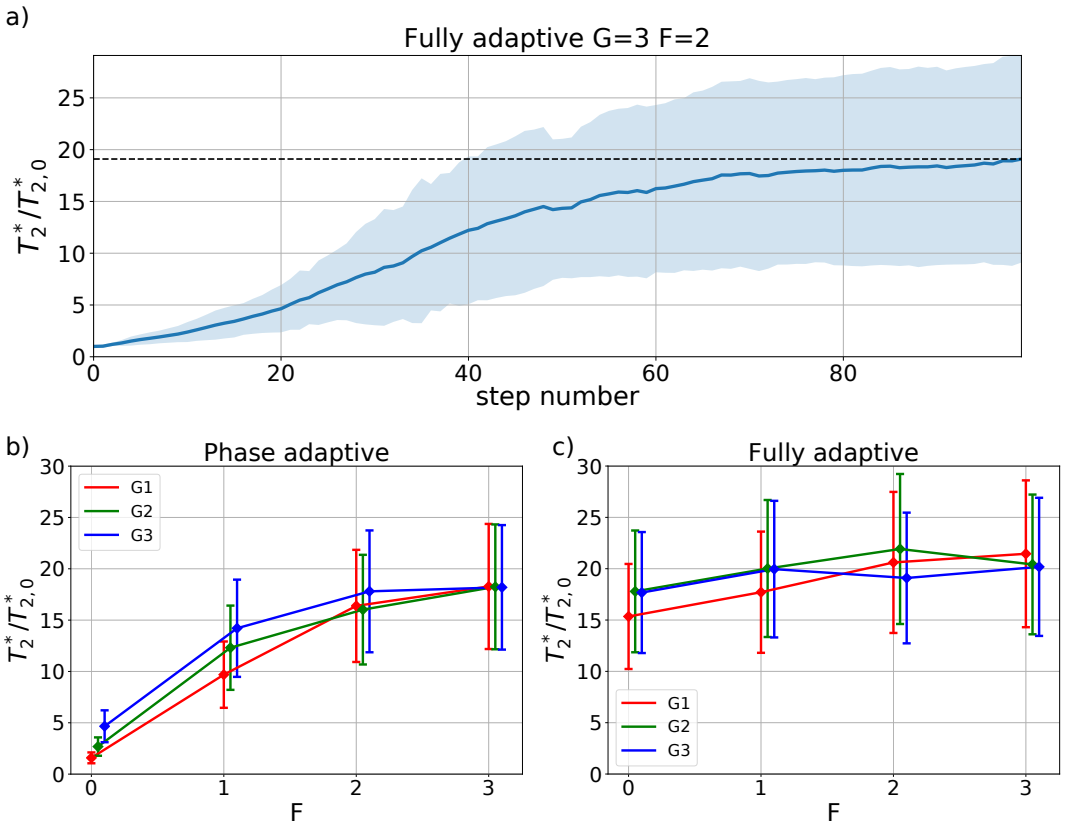

Figure 8.5: **a)** Narrowing factor averaged over 100 trials for three different spin baths using $G = 3$ and $F = 2$. The light shaded region is the standard deviation at each step. **b-c)** Final averaged narrowing factor for the **b)** phase-adaptive and **c)** fully adaptive scheme for various values of the two integer parameters G and F. For all cases considered, a bath of 7 spins was simulated for measurement outcomes, with an applied magnetic field $B_z = 1\text{T}$.

coherence time $T^*_{2,k-1}$:

$$k_{opt} = \left\lfloor \log_2 \left(\frac{T^*_{2,k-1}}{\tau_0} \right) \right\rfloor \ , \tag{8.10}$$

where $\lfloor \cdot \rfloor$ denotes the closest smallest integer, so that $2^k_{opt}\tau_0 \leq T^*_{2,k}$. In Fig. 8.4, we give an example of how our scheme narrows the initial spin bath distribution over 20 Ramsey sequences.

In Fig. 8.5, we compare this fully adaptive scheme to the phase adaptive scheme. The phase-adaptive scheme performs worse for lower values of the parameter F for every value of G, whereas the performance fully-adaptive scheme is relatively constant over all values of the two integer parameters (within error bars), with the narrowing factor $T_2^*/T_{2,0}^*$ being as high as the factor obtained using the phase-adaptive scheme for the optimal value $F = 3$. It should be noted, however, that the error bars for the phase-adaptive scheme are narrower, most likely due to the deter-

ministic, monotonically increasing, measurement times, as opposed to the sequence of optimised k values used for the fully-adaptive scheme, which is different for each realisation of the experiment.

8.6 Conclusion

In this chapter, we have studied the Bayesian adaptive sensing algorithm which, in recent work, has been shown to reach the quantum limit of parameter estimation [181]. We apply this algorithm, with some minor modifications, to gain information about the dilute nuclear environment of a solid state nanostructure (an example of which would be an NV^- centre), in the presence of a known, external magnetic field. We have shown that, in turn, this information reduces the magnetic field fluctuations felt by the central spin, as the state of the surrounding nuclear ensemble is partially projected and steered toward a particular state, resulting in a considerably extended coherence time T_2^*. Whilst focussing on the specific environment of NV^- centres, these results can be straightforwardly extended to other systems having sparse nuclear spin environments.

Several interesting avenues can be pursued in the future, having established the efficacy of the Bayesian scheme. Suppose, for example, that the experimenter has performed an experiment using spin after the narrowing scheme has been applied, what would the time window be before the spin bath diffuses back to a thermal state, and would we then be able to narrow the state distribution back? After $\sim T_2$, we would expect the spin bath to have undergone significant diffusion, but more work needs to be done to investigate the second question. The Bayesian scheme should also allow us to track the spin bath distribution during this diffusion, as long as the T^2 is known (for example, by performing a spin echo experiment). Tracking the distribution would then indicate to the experimenter when the next round of the narrowing protocol should be applied in order to combat this diffusion. Yet another interesting application of the narrowing scheme would be engineering interesting spin bath states. The full control over the measurement times and readout angle means that it is possible, in principle, to 'guide' the state into several pos-

sible states by choosing, instead of optimising, the measurement time and phase, thereby projecting the distribution onto the desired state which may show different entanglement properties and other interesting features.

Chapter 9

Summary and future work

In this thesis, we investigated a few applications of solid state nanostructures in fields such as quantum metrology, information and computation. Whilst we have mainly focussed on self-assembled quantum dots, we also investigated a potential application of the negatively charged NV centre in Chapter 8, the results of which can be extended to other crystal defect structures sharing similar properties. Using the polaron formalism, we accurately modelled the interaction between these structures and their solid state environments, and showed that, despite the detrimental effects such interactions may have, our proposed applications still shows promising results.

After having introduced the mathematical formalism, focussing mostly on the master equation framework, we discussed how a quantum dot can be improved as a single photon source in Chapter 5. By using the 'image dipole' method originally developed for atomic systems, we studied how the presence of the metal surface affects the dynamics of a self-assembled quantum dot. We then showed how superradiant behaviour of a sample of such emitters can be enhanced, or suppressed, depending on the sample's orientation and position from the surface. Further work can be done to investigate optimal dipole orientations and separations in order to improve the enhanced superradiant behaviour, or perhaps investigate other collective phenomena such as superabsorption.

Having introduced quantum dots as single photon sources, we then discussed an application of these solid state emitters in the field of quantum computation. More specifically, we developed a new cluster state generation protocol using the hole-

spin in a quantum dot as a Raman photon generator and entangler. We showed that our scheme, making use of both the coherence properties of hole-spins and weak continuous wave driving, overcomes some experimental challenges faced by rival solid state-based schemes. Despite being an inherently probabilistic scheme, we suggested an extension of our protocol in order to deterministically generate linear cluster states. Furthermore, we proposed a simple modification that can be applied to several state-of the-art quantum state tomography techniques, discussed in Chapter 7, in order to reconstruct the linear cluster state without the random measurement phases.

In Chapter 7, we studied this modification for state tomography which allows for quantum state reconstruction in the presence of random, but known post-measurement, errors. In order to reduce the additional computational cost introduced by the retrodicted techniques, we proposed a coarse-grained approach, resulting in a significant reduction of this computation overhead at a modest price in fidelity. Finally, we linked this technique to several state-of-the-art quantum information protocols using solid state emitters.

Having introduced the Bayesian formalism in the context of state tomography in Chapter 7 as one of the techniques used, we applied the Bayesian framework to the field of quantum metrology in Chapter 8. More precisely we extended the Bayesian adaptive scheme, which typically entails using solid state spins for sensing unknown magnetic fields, to estimate the interaction between an NV^- centre electron and its dilute environment of ^{13}C nuclei. We showed how, by performing Ramsey measurements adaptively on the central spin, information can be gained on the state of the spin bath, reducing the uncertainty in our estimate, thus increasing the NV^- spin coherence time. In the near future, we shall be pursuing a number of avenues building on this work, including using this modified adaptive strategy to steer the spin bath into more exotic states, and to track the state of the bath in the presence of nuclear spin diffusion.

Appendix A

Appendix: Image Dipole Eigenbasis Dissipators

The dissipators of Sec. 5.4.4 are given by

$$
\begin{aligned}
&D^{s}_{pn}(\rho_{SP}) \\
&= 2\gamma^{pn}(\omega')\Big[(S_{se}+S_{gs})\rho_{SP}(t)(S_{es}+S_{sg}) \\
&- \frac{1}{2}\{(S_{ee}+S_{ss}),\rho_{SP}(t)\}\Big] \\
&+ 2\gamma^{pn}(-\omega')\Big[(S_{es}+S_{sg})\rho_{SP}(t)(S_{se}+S_{gs}) \\
&- \frac{1}{2}\{(S_{gg}+S_{ss}),\rho_{SP}(t)\}\Big] \\
&- 2\gamma^{pn}_{cd}(\omega')(S_{se}+S_{gs})\rho_{SP}(t)(S_{se}+S_{gs}) \\
&- 2\gamma^{pn}_{cd}(-\omega')(S_{es}+S_{sg})\rho_{SP}(t)(S_{es}+S_{sg}) \ ,
\end{aligned}
\tag{A.1}
$$

$$
\begin{aligned}
&D^{a}_{pt}(\rho_{SP}) \\
&= 2\gamma^{pt}(\omega')\Big[(S_{se}+S_{gs})\rho_{SP}(t)(S_{es}+S_{sg}) \\
&- \frac{1}{2}\{(S_{ee}+S_{ss}),\rho_{SP}(t)\}\Big] \\
&+ 2\gamma^{pt}(-\omega')\Big[(S_{es}+S_{sg})\rho_{SP}(t)(S_{se}+S_{gs}) \\
&- \frac{1}{2}\{(S_{gg}+S_{ss}),\rho_{SP}(t)\}\Big]
\end{aligned}
\tag{A.2}
$$

$$
\begin{aligned}
&D^{s}_{pt}(\rho_{SP}) \\
&= 2\gamma^{pt}(\omega')\Big[(S_{se}+S_{gs})\rho_{SP}(t)(S_{es}+S_{sg}) \\
&- \frac{1}{2}\{(S_{ee}+S_{ss}),\rho_{SP}(t)\}\Big] \\
&+ 2\gamma^{pt}(-\omega')\Big[(S_{es}+S_{sg})\rho_{SP}(t)(S_{se}+S_{gs}) \\
&- \frac{1}{2}\{(S_{gg}+S_{ss}),\rho_{SP}(t)\}\Big] \ ,
\end{aligned}
\tag{A.3}
$$

with $S_{ij} = |i\rangle\langle j| \ ; i,j \in \{g,a,s,e\}$; $|g\rangle$, $|a\rangle$, $|s\rangle$ and $|e\rangle$ being the doubly ground, antisymmetric, symmetric and doubly excited state of our joint system, respectively.

A.1 SE rate and cross Lamb shift terms for dipole perpendicular to the surface

In the case of a dipole perpendicular to the surface, expressions for the cross Lamb shift term and SE rate similar to the ones used in section 5.4 can be derived from first principles as well, arriving at the expressions

$$
\mathcal{F}_{12}(q\Delta r) = 3\left(-\frac{\cos(q\Delta r)}{(q\Delta r)^2} + \frac{\sin(q\Delta r)}{(q\Delta r)^3}\right) \ , \tag{A.4}
$$

and

$$
\mathcal{G}_{12}(q\Delta r) = -3\left(\frac{\sin(q\Delta r)}{(q\Delta r)^2} + \frac{\cos(q\Delta r)}{(q\Delta r)^3}\right) \ , \tag{A.5}
$$

instead of the ones used in section 5.4.

Appendix B

Appendix: Frequency-encoded cluster state details

B.1 Second-order perturbation rate

It can be easily shown that, after moving to a rotating frame with respect to the unperturbed transition frequency, the amplitude of the Raman-flip transition $|\Downarrow\rangle \rightarrow |\Uparrow\rangle$ is given by

$$\begin{aligned}\mathcal{T}_{\Downarrow\rightarrow\Uparrow} =& \frac{\langle\Uparrow;\omega_R|\, H_I\, |T_\downarrow;0\rangle\, \langle T_\downarrow;0|\, H_I\, |\Downarrow;\omega_{Ray}\rangle}{\hbar\Delta_1^{(1)}} \\ &+ \frac{\langle\Uparrow;\omega_{Ray}|\, H_I\, |T_\uparrow;0\rangle\, \langle T_\uparrow;0|\, H_I\, |\Downarrow;\omega_B\rangle}{\hbar\Delta_2^{(1)}}\ ,\end{aligned} \tag{B.1}$$

where $\Delta_1^{(1)} = \delta_h + \delta_e$, $\Delta_2^{(1)} = \delta_h - \delta_e$, H_I is the light-matter interaction Hamiltonian (in this case between the spin and c.w. laser field), and ω_R, ω_B and ω_{Ray} are the red-, blue-detuned and Rayleigh scattered photon frequencies, respectively. The first term in Eqn. (B.1) gives the amplitude of a red Raman photon event: the system, initially in the $|\Downarrow\rangle$ state, scatters a σ^V photon, after which the final state is given by $|\Uparrow;H\rangle$ (that is, the system in the $|\Uparrow\rangle$ state and a red-detuned Raman photon (σ^H polarised) is scattered). Similarly, the $|\Uparrow\rangle \rightarrow |\Downarrow\rangle$ transition giving rise to the blue-detuned photon scattering event occurs with amplitude

$$\begin{aligned}\mathcal{T}_{\Uparrow\to\Downarrow} =& \frac{\langle\Downarrow;\omega_B|\, H_I\,|T_\uparrow;0\rangle\,\langle T_\uparrow;0|\, H_I\,|\Uparrow;\omega_{Ray}\rangle}{\hbar\Delta_1^{(2)}} \\ &+\frac{\langle\Downarrow;\omega_{Ray}|\, H_I\,|T_\downarrow;0\rangle\,\langle T_\downarrow;0|\, H_I\,|\Uparrow;\omega_R\rangle}{\hbar\Delta_2^{(2)}}\ ,\end{aligned} \tag{B.2}$$

where $\Delta_1^{(2)} = -\delta_h - \delta_e$, $\Delta_2^{(2)} = -\delta_h + \delta_e$.

The second term in each of the transition amplitudes does not contribute to the Raman processes, and vanish as the driving field can only drive vertically-polarised transitions. After performing the necessary solid angle integrals, we arrive at the scattering rate given by Eqn. (6.8) in the main text.

B.2 Matrix operations

Consider a single scattering process that can be described by the action of the product of matrices:

$$\begin{aligned}|\Uparrow\rangle\,|Ray_k\rangle \to& \,\mathrm{e}^{-i\frac{\phi_1^{(k)}}{2}}\mathrm{e}^{i\frac{\phi_2^{(k)}}{2}}\,(|\Uparrow\rangle + |\Downarrow\rangle)\,|B_k\rangle \\ =&U_rU_p(\phi_2^{(k)})T_s^{(k)}U_p(\phi_1^{(k)})\,|\Uparrow\rangle\,|Ray_k\rangle \\ =&Q^{(k)}\,|\Uparrow\rangle\,|Ray_k\rangle\ ,\end{aligned}$$

$$\begin{aligned}|\Downarrow\rangle\,|Ray_k\rangle \to& \,\mathrm{e}^{i\frac{\phi_1^{(k)}}{2}}\mathrm{e}^{-i\frac{\phi_2^{(k)}}{2}}\,(|\Uparrow\rangle - |\Downarrow\rangle)\,|R_k\rangle \\ =&U_rU_p(\phi_2^{(k)})T_s^{(k)}U_p(\phi_1^{(k)})\,|\Downarrow\rangle\,|Ray_k\rangle \\ =&Q^{(k)}\,|\Downarrow\rangle\,|Ray_k\rangle\ ,\end{aligned} \tag{B.3}$$

where $U_p(\phi_{1,2}^{(k)})$ is the free spin precession transformation before ($\phi_1^{(k)}$) and after ($\phi_2^{(k)}$) the k^{th} scattering event (prior to the $\mathrm{Y}_{\frac{\pi}{2}}$ rotation), with the resulting matrix of events being $Q^{(k)} \coloneqq U_rU_p(\phi_2^{(k)})T_s^{(k)}U_p(\phi_1^{(k)})$. The scattering matrix $T_s^{(k)}$ is given by

$$T_s^{(k)} = \left(\begin{array}{c|c} 0 & T_R^{(k)} \\ \hline T_B^{(k)} & 0 \end{array}\right) \ , \tag{B.4}$$

with $T_R^{(k)}$ and $T_B^{(k)}$ written in the basis $\{|B_k\rangle, |R_k\rangle, |Ray_k\rangle\}$, which simultaneously flips the spin state $|\Uparrow\rangle \leftrightarrow |\Downarrow\rangle$, and applies the local transformations

$$\begin{aligned} T_B^{(k)} &: |Ray_k\rangle \mapsto |B_k\rangle \\ T_R^{(k)} &: |Ray_k\rangle \mapsto |R_k\rangle \ , \end{aligned} \tag{B.5}$$

where we have omitted the unaffected photon states for brevity. Hence $T_B^{(k)}$ and $T_R^{(k)}$ take the form:

$$\begin{aligned} T_R^{(k)} &= \mathbb{I}_3^{\otimes_{k-1}} \otimes \begin{pmatrix} 0 & 0 & 0 \\ 0 & 0 & 1 \\ 0 & 0 & 0 \end{pmatrix} \otimes \mathbb{I}_3^{\otimes_{n-k}} \\ T_B^{(k)} &= \mathbb{I}_3^{\otimes_{k-1}} \otimes \begin{pmatrix} 0 & 0 & 1 \\ 0 & 0 & 0 \\ 0 & 0 & 0 \end{pmatrix} \otimes \mathbb{I}_3^{\otimes_{n-k}} \ , \end{aligned} \tag{B.6}$$

and U_r and $U_p(\phi)$ are simply given by given by

$$\begin{aligned} U_r &= \exp\left(i\frac{\pi}{4}\sigma_y\right) \otimes \mathbb{I}_3^{\otimes_n} \\ U_p(\phi) &= \begin{pmatrix} \mathrm{e}^{-i\frac{\phi}{2}} & 0 \\ 0 & \mathrm{e}^{i\frac{\phi}{2}} \end{pmatrix} \otimes \mathbb{I}_3^{\otimes_n} \ , \end{aligned} \tag{B.7}$$

where the first matrices act on the spin state and have been written in the $\{|\Uparrow\rangle, |\Downarrow\rangle\}$ basis. Unfortunately, the matrix product describing n-photon scattering events becomes unwieldy with increasing n. In Appendix Sec. B.3, however, we show that

this protocol does indeed generalise to a LC_n state, up to free precession phases.

B.3 Generalisation to n-photons

B.3.1 Preliminary lemmas

In this section, we will show that the general form of the n-photon state $S^{(n)}$ obtained using our protocol can be written recursively (where we have suppressed the ket representation for these states for ease of notation). In fact,

Lemma B.3.1. *$\forall n \in \mathbb{N}$, the n-photon state $S^{(n)}$ can be decomposed into the recursive relations*

$$\begin{aligned} S_+^{(n)} &= S_+^{(n-1)} |1_n\rangle + S_-^{(n-1)} |0_n\rangle \ , \\ S_-^{(n)} &= S_+^{(n-1)} |1_n\rangle - S_-^{(n-1)} |0_n\rangle \ , \end{aligned} \tag{B.8}$$

depending whether the spin is measured to be in the $|\Uparrow\rangle$ or $|\Downarrow\rangle$ state, respectively.

Proof. We will, w.l.o.g., ignore the spin precession, although the proof is the same for the general case:

Basis case: For $j = 1$, $S_+^{(1)} = |1_1\rangle + |0_1\rangle$ and $S_-^{(1)} = |1_1\rangle - |0_1\rangle$. After the next scattering event, we get

$$\begin{aligned} S_+^{(2)} &= |1_1 1_2\rangle + |1_1 0_2\rangle + |0_1 1_2\rangle - |0_1 0_2\rangle \\ &= (|1_1\rangle + |0_1\rangle)\,|1_2\rangle + (|1_1\rangle - |0_1\rangle)\,|0_2\rangle \\ &= S_+^{(1)} |1_2\rangle + S_-^{(1)} |0_2\rangle \ . \end{aligned} \tag{B.9}$$

Similarly,

$$\begin{aligned} S_-^{(2)} &= |1_1 1_2\rangle - |1_1 0_2\rangle + |0_1 1_2\rangle + |0_1 0_2\rangle \\ &= (|1_1\rangle + |0_1\rangle)\,|1_2\rangle - (|1_1\rangle - |0_1\rangle)\,|0_2\rangle \\ &= S_+^{(1)}\,|1_2\rangle - S_-^{(1)}\,|0_2\rangle \ . \end{aligned} \tag{B.10}$$

Induction step: Assume statement holds for $j = n$, and consider the $(n+1)^{\text{th}}$ scattering event:

$$\begin{aligned} S_+^{(n+1)} &= U_r T_{scat}^{(n+1)}(|\Uparrow\rangle\, S_+^{(n)} + |\Downarrow\rangle\, S_-^{(n)})\,|Ray_{n+1}\rangle \\ &= (|\Uparrow\rangle + |\Downarrow\rangle) S_+^{(n)}\,|1_{n+1}\rangle + (|\Uparrow\rangle - |\Downarrow\rangle) S_-^{(n)}\,|0_{n+1}\rangle \\ &= |\Uparrow\rangle\,(S_+^{(n)}\,|1_{n+1}\rangle + S_-^{(n)}\,|0_{n+1}\rangle) \\ &\quad + |\Downarrow\rangle\,(S_+^{(n)}\,|1_{n+1}\rangle - S_-^{(n)}\,|0_{n+1}\rangle)\ . \end{aligned} \tag{B.11}$$

Therefore $S_+^{(n+1)} = S_+^{(n)}\,|1_{n+1}\rangle + S_-^{(n)}\,|0_{n+1}\rangle$ and $S_-^{(n+1)} = S_+^{(n)}\,|1_{n+1}\rangle - S_-^{(n)}\,|0_{n+1}\rangle$, so the statement holds $\forall n \in \mathbb{N}$. □

It is then easy to see that we also have that

Lemma B.3.2.

$$\sigma_z^{(n)} S_\pm^{(n)} = -S_\mp^{(n)} \quad \forall n \in \mathbb{N}\ , \tag{B.12}$$

which we shall use to prove that the n-photon state we generate is indeed a linear cluster state.

B.3.2 Equivalence to LC$_n$ states

In order to show that the $S_\pm^{(n)}$ states are indeed LC$_n$s, we have to show that they both satisfy the set of eigenvalue equations

$$K_n^{(a)} S_\pm^{(n)} = (-1)^{k_\pm^{(a)}} S_\pm^{(n)}\ , \tag{B.13}$$

with

$$K_n^{(a)} = \sigma_x^{(a)} \bigotimes_{b \in N(a)} \sigma_z^{(b)} \ , \tag{B.14}$$

where $1 \leq a \leq n$, $N(a)$ is the set of direct neighbours of photon a along the state, and $k_{\pm}^{(a)} \in \{0, 1\}$, depending on the particular realisation of LC_n. The subscript on the operator K denotes the state tensor-length of K, and hence the length of the state it acts upon. In fact we shall show the following statement

Theorem B.3.3. *The n-photon $S^{(n)}$ state satisfies the set of LC_n-eigenvalue equations for*

$$\begin{aligned} k_+^{(a)} &= \begin{cases} 1, & \text{if } a \in \{1, n\} \\ 0, & \text{if } 1 < a < n \end{cases} \\ k_-^{(a)} &= \begin{cases} 1, & \text{if } a = 1 \\ 0, & \text{if } 1 < a \leq n \end{cases} \end{aligned} \tag{B.15}$$

Proof. The proof follows, once again, by induction, as well as the use of Lemma B.3.1

Basis case: For $j = 2$, .

$$\begin{aligned} S_+^{(2)} &= (|1_1\rangle + |0_2\rangle)\,|1_n\rangle + (|1_1\rangle - |0_1\rangle)\,|0_2\rangle \ , \\ S_+^{(2)} &= (|1_1\rangle + |0_2\rangle)\,|1_n\rangle - (|1_1\rangle - |0_1\rangle)\,|0_2\rangle \ , \end{aligned} \tag{B.16}$$

and the statement holds when applying $\sigma_x^{(1)} \otimes \sigma_z^{(2)}$ and $\sigma_z^{(1)} \otimes \sigma_x^{(2)}$.

Induction step: Suppose the statement holds for $j = n$, and consider $S_+^{(n+1)} = S_+^{(n)}\,|1_{n+1}\rangle + S_-^{(n)}\,|0_{n+1}\rangle$.Then

If $a = 1$:

$$\begin{aligned} K_{n+1}^{(a)} S_{+}^{(n+1)} &= (K_n^{(a)} \otimes \mathbb{I}_2)(S_{+}^{(n)} |1_{n+1}\rangle + S_{-}^{(n)} |0_{n+1}\rangle) \\ &= (-1)^{k_{+}^{(1)}} S_{+}^{(n)} |1_{n+1}\rangle + (-1)^{k_{-}^{(1)}} S_{-}^{(n)} |0_{n+1}\rangle \\ &= -(S_{+}^{(n)} |1_{n+1}\rangle + S_{-}^{(n)} |0_{n+1}\rangle) \\ &= -S_{+}^{(n+1)} \ , \end{aligned} \tag{B.17}$$

with $\mathbb{I}_2$ being the 2×2 identity matrix. The penultimate step holds due the induction hypothesis. Similarly, for $S_{-}^{(n+1)}$,

$$\begin{aligned} K_{n+1}^{(a)} S_{-}^{(n+1)} &= (K_n^{(a)} \otimes \mathbb{I}_2)(S_{+}^{(n)} |1_{n+1}\rangle - S_{-}^{(n)} |0_{n+1}\rangle) \\ &= (-1)^{k_{+}^{(1)}} S_{-}^{(n)} |1_{n+1}\rangle - (-1)^{k_{-}^{(1)}} S_{-}^{(n)} |0_{n+1}\rangle \\ &= -(S_{+}^{(n)} |1_{n+1}\rangle - S_{-}^{(n)} |0_{n+1}\rangle) \\ &= -S_{-}^{(n+1)} \ . \end{aligned} \tag{B.18}$$

If $1 < a < n$:

$$\begin{aligned} K_{n+1}^{(a)} S_{+}^{(n+1)} &= (K_n^{(a)} \otimes \mathbb{I}_2)(S_{+}^{(n)} |1_{n+1}\rangle + S_{-}^{(n)} |0_{n+1}\rangle) \\ &= (-1)^{k_{+}^{(a)}} S_{+}^{(n)} |1_{n+1}\rangle + (-1)^{k_{-}^{(a)}} S_{-}^{(n)} |0_{n+1}\rangle \\ &= S_{+}^{(n)} |1_{n+1}\rangle + S_{-}^{(n)} |0_{n+1}\rangle \\ &= S_{+}^{(n+1)} \ , \end{aligned} \tag{B.19}$$

$$\begin{aligned} K_{n+1}^{(a)} S_{-}^{(n+1)} &= (K_n^{(a)} \otimes \mathbb{I}_2)(S_{+}^{(n)} |1_{n+1}\rangle - S_{-}^{(n)} |0_{n+1}\rangle) \\ &= (-1)^{k_{+}^{(a)}} S_{-}^{(n)} |1_{n+1}\rangle - (-1)^{k_{-}^{(a)}} S_{-}^{(n)} |0_{n+1}\rangle \\ &= S_{+}^{(n)} |1_{n+1}\rangle - S_{-}^{(n)} |0_{n+1}\rangle \\ &= S_{-}^{(n+1)} \ . \end{aligned} \tag{B.20}$$

If $a = n$:

$$\begin{aligned} K_{n+1}^{(a)} S_{+}^{(n+1)} &= (K_n^{(a)} \otimes \sigma_z^{(n+1)})(S_{+}^{(n)} |1_{n+1}\rangle + S_{-}^{(n)} |0_{n+1}\rangle) \\ &= -(-1)^{k_{+}^{(n)}} S_{+}^{(n)} |1_{n+1}\rangle + (-1)^{k_{-}^{(n)}} S_{-}^{(n)} |0_{n+1}\rangle \\ &= S_{+}^{(n)} |1_{n+1}\rangle + S_{-}^{(n)} |0_{n+1}\rangle \\ &= S_{+}^{(n+1)} , \end{aligned} \tag{B.21}$$

$$\begin{aligned} K_{n+1}^{(a)} S_{-}^{(n+1)} &= (K_n^{(a)} \otimes \sigma_z^{(n+1)})(S_{+}^{(n)} |1_{n+1}\rangle - S_{-}^{(n)} |0_{n+1}\rangle) \\ &= -(-1)^{k_{+}^{(n)}} S_{-}^{(n)} |1_{n+1}\rangle - (-1)^{k_{-}^{(n)}} S_{-}^{(n)} |0_{n+1}\rangle \\ &= S_{+}^{(n)} |1_{n+1}\rangle - S_{-}^{(n)} |0_{n+1}\rangle \\ &= S_{-}^{(n+1)} . \end{aligned} \tag{B.22}$$

For the $a = n+1$ case, we shall make use of Lemma B.3.2. The operator $K_{n+1}^{(n+1)}$ can be decomposed as $\mathbb{I}_2^{\otimes_{n-1}} \otimes \sigma_z^{(n)} \otimes \sigma_x^{(n+1)}$, and hence we get that

If $a = n+1$:

$$\begin{aligned} K_{n+1}^{(a)} S_{+}^{(n+1)} &= -S_{-}^{(n)} |0_{n+1}\rangle - S_{+}^{(n)} |1_{n+1}\rangle \\ &= -S_{+}^{(n+1)} , \end{aligned} \tag{B.23}$$

$$\begin{aligned} K_{n+1}^{(a)} S_{-}^{(n+1)} &= -S_{-}^{(n)} |0_{n+1}\rangle + S_{+}^{(n)} |1_{n+1}\rangle \\ &= S_{-}^{(n+1)} . \end{aligned} \tag{B.24}$$

Therefore, the states $S_{\pm}^{(n)}$ satisfy the eigenvalue conditions (B.13) for the set of parameters (B.15), meaning that the the state obtained by our protocol is an LC_n state. □

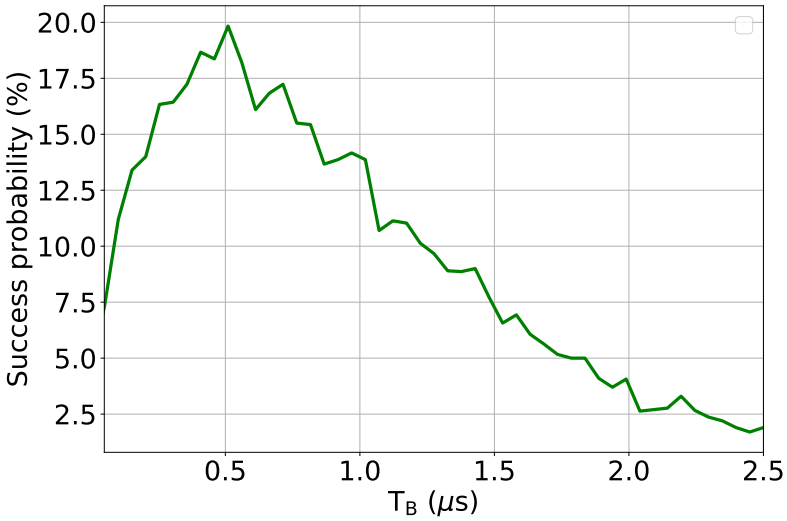

Figure B.1: Success probability of scattering a single Raman photon using a c.w. source against time-bin length T_B. At an optimised time-bin length $T_B \approx 0.5\mu$s, the probability can be as high as 20%, before it drops once more due to the probabilities of getting multiple photons in a single time-bin.

B.4 Pulsed scheme limitations

As mentioned earlier, the main limitation of our scheme is the unknown time-of-arrival of the photons due to the c.w. source. An obvious solution might be using a pulsed source for the photons. Despite addressing the issue of the photons' unknown phases, such a protocol would still not be deterministic, as there is still a 50% probability that a Rayleigh scattering event, instead of a spin-flipping Raman one, occurs. Whilst this is still a considerable improvement over the $\sim 20\%$ we get for an optimised time-bin length (Fig. B.1), this pulsed-excitation scheme would not benefit from the advantages of sub-saturation driving; mainly the photon linewidth limited only by the hole spin coherence and laser linewidth, and be susceptible to phonon dephasing. Hence, the opportunity to create longer LCs with less probabilistic phase uncertainty comes at the price of lower quality LC states, which we argue is paramount for reliably constructing 2D cluster states required for quantum computation using probabilistic fusion gates.

Appendix C

Appendix: Retrodictive tomography: Extension to two qubits and algorithm pseudocodes

C.1 Two-qubit results

Fig C.1 and Fig C.2 show the effect of particle filter sample sizes on a Bayesian two-qubit reconstruction, and the performance of the Cholesky method for a two-qubit reconstruction, respectively.

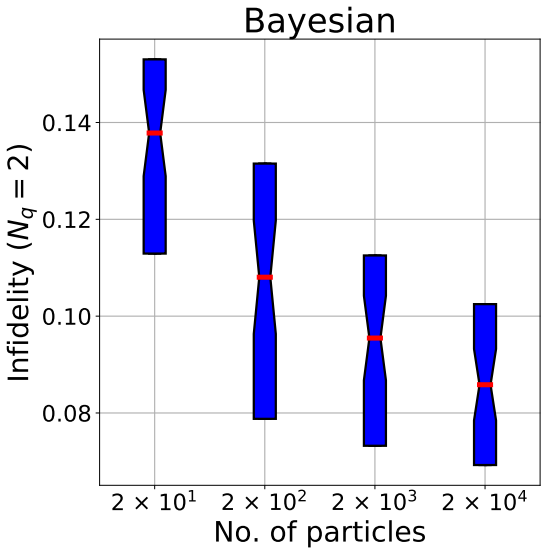

Figure C.1: Bayesian reconstruction of random two-qubit state against particle filter sample sizes, averaged over 50 trials. In each case the number of measurements was taken to be $N = 100$ due to the computation time taken for higher sample sizes.

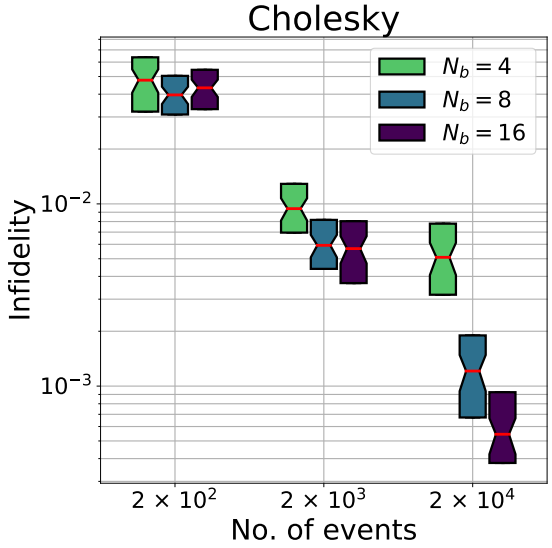

Figure C.2: Full rank two-qubit reconstruction infidelity using the Cholesky method results for 4,8 and 16 segments, with increasing number of measurements and averaged over 50 trials.

C.2 Pseudocodes

In this section we present the pseudocodes for the PGDB algorithm, and some subroutines used for the Bayesian approach taken from [188].

Algorithm 1 PGDB

$k = 0$, $\mu_{k=0} = 1$

Initial estimate $\rho_{k=0} \in \mathcal{S}$.

Given $\delta = 10^{-4}$, $\gamma = 10^{-3}$, $\mu_{min} = 10^{-4}$, $\mu_{max} = 10^{4}$

while $\sum_{i=1}^{20} |\mathcal{C}(\rho_i) - \mathcal{C}(\rho_{i-1})| > \delta$ **do**

    Calculate probability estimates

    Calculate log likelihood $\mathcal{C}(\rho_k) = -\sum_i n_i \log(p_i)$

    Calculate gradient $\nabla\mathcal{C}(\rho_k) = -\sum_i (n_i/p_i) \left|\phi_i\right\rangle \left\langle\phi_i\right|$

    $D_k = \mathcal{P}_S(\rho_k - \mu_k^{-1}\nabla\mathcal{C}) - \rho_k$

    $\tilde{\mathcal{C}}(\rho_k) = \mathcal{C}(\rho_k) + \gamma \mathrm{Tr}[D_k \mathcal{C}(\rho_k)]$

    Initialise line search parameter $\alpha = 1$

    while $\mathcal{C}(\rho_k + \alpha D_k) > \tilde{\mathcal{C}}(\rho_k)$ **do**

        $\alpha = \alpha/2$

        $\tilde{\mathcal{C}}(\rho_k) = \mathcal{C}(\rho_k) + \gamma\alpha \mathrm{Tr}[D_k \mathcal{C}(\rho_k)]$

    end while

    $\rho_{k+1} = \rho_k + \alpha D_k$

    $\mu_{k+1} = \min\{\max\{\frac{\langle \rho_k - \rho_{k-1}, \nabla\mathcal{C}(\rho_k) - \nabla\mathcal{C}(\rho_{k-1})\rangle}{\|\rho_k - \rho_{k-1}\|^2}, \mu_{min}\}, \mu_{max}\}$ ▷ Update scale factor for step in gradient direction [197]

    $k = k + 1$

end while

return $\rho_{end} = \mathcal{P}_S(\rho_{k+1})$

Algorithm 2 SMC update algorithm

Initial distribution for particle positions $\{\mathbf{x}_j\}$ and weights $\{w_j\}$ ▷ Chosen to be both uniform
for $i \in \text{range}(N)$ **do**
    New datum $D_i = \{\alpha_i, \mu_i\}$ is measured
    for $j \in \text{range}(n_{part})$ **do**
        $w_j = w_j P(\{\alpha_i, \mu_i\}|\mathbf{x}_j)$
    end for
    Renormalise $\{w_j\}$
end for

Algorithm 3 SMC resampling algorithm

function RESAMPLE($\{\mathbf{x}_j\}, \{w_j\}$, a)
    $\boldsymbol{\mu} = \text{MEAN}(\{\mathbf{x}_j\}, \{w_j\})$ ▷ Weighted mean of $\{\mathbf{x}_j\}$
    $h = \sqrt{1 - a^2}$
    $\boldsymbol{\Sigma} = \text{COV}(\{\mathbf{x}_j\}, \{w_j\})$ ▷ Find covariance
    for $i \in \text{range}(n_{part})$ **do**
        Select particle $\mathbf{x}_j$ with probability w_j
        $\boldsymbol{\mu}_i = a\mathbf{x}_j + (1 - a)\boldsymbol{\mu}$ ▷ Mean for new particle location
        Pick $\mathbf{x}'_i$ randomly from $\mathcal{N}(\boldsymbol{\mu}_i, \boldsymbol{\Sigma})$ ▷ Draw new, shifted, particle
        $w'_i = n_{part}^{-1}$ ▷ Reset weights to uniform
    end for
return $\{\mathbf{x}'_j\}, \{w'_j\}$
end function

Algorithm 3 can then be added to Algorithm 2, conditioned on the value of the effective sample size $n_{eff} = 1/\sum_i w_i$. If n_{eff} is less than some threshold value (taken to be 0.5 [188]), then the distribution is resampled. Details on the MEAN and COV functions can be found in Ref. [188]

Appendix D

Appendix: Bayesian spin bath narrowing: Rotating frame Hamiltonian

D.1 Secular approximation correction

In making the secular approximation for high fields, the components of the hyperfine fields from ^{13}C orthogonal to the NV axis can be treated perturbatively in order to account for them. Following Refs. [216, 212], with the magnetic field parallel to the z-axis, we get an effective nuclear-nuclear spin coupling given by

$$\mathbb{C}_{nm}^{eff} = \mathbb{C}_{nm} + \delta\mathbb{C}_{nm}^{(m_s)} \ , \tag{D.1}$$

where

$$\delta\mathbb{C}_{nm}^{(m_s)} = -\frac{D(\gamma_N/\gamma_e)^2}{2-3m_s}\delta\mathbf{g}_n^T \cdot \delta\mathbf{g}_m \ ; \tag{D.2}$$

$$\delta\mathbf{g}_n = \frac{(2-3m_s)\gamma_e}{D\gamma_n}\begin{pmatrix} A_n^{xx} & A_n^{xy} & A_n^{xz} \\ A_n^{yx} & A_n^{yy} & A_n^{yz} \\ 0 & 0 & 0 \end{pmatrix} \ . \tag{D.3}$$

Bibliography

[1] H. Breuer and F. Petruccione, *The Theory of Open Quantum Systems*. OUP Oxford, 2007.

[2] G. Mahan, *Many-Particle Physics*. Physics of Solids and Liquids, Springer, 2000.

[3] A. Nazir and D. P. S. McCutcheon, "Modelling exciton–phonon interactions in optically driven quantum dots," *Journal of Physics: Condensed Matter*, vol. 28, p. 103002, Feb. 2016.

[4] A. J. Ramsay, A. V. Gopal, E. M. Gauger, A. Nazir, B. W. Lovett, A. M. Fox, and M. S. Skolnick, "Damping of exciton Rabi rotations by acoustic phonons in optically excited InGaAs/GaAs quantum dots," *Phys. Rev. Lett.*, vol. 104, p. 017402, Jan. 2010.

[5] A. J. Ramsay, T. M. Godden, S. J. Boyle, E. M. Gauger, A. Nazir, B. W. Lovett, A. M. Fox, and M. S. Skolnick, "Phonon-induced Rabi-frequency renormalization of optically driven single InGaAs/GaAs quantum dots," *Phys. Rev. Lett.*, vol. 105, p. 177402, Oct. 2010.

[6] D. P. S. McCutcheon and A. Nazir, "Quantum dot Rabi rotations beyond the weak exciton-phonon coupling regime," *New Journal of Physics*, vol. 12, p. 113042, Nov. 2010.

[7] C. Roy-Choudhury and S. Hughes, "Phonon-dressed Mollow triplet in the regime of cavity quantum electrodynamics: Excitation-induced dephasing and nonperturbative cavity feeding effects," *Phys. Rev. Lett.*, vol. 106, p. 247403, Jun. 2011.

[8] K. Roy-Choudhury and S. Hughes, "Quantum theory of the emission spectrum from quantum dots coupled to structured photonic reservoirs and acoustic phonons," *Phys. Rev. B*, vol. 92, p. 205406, Nov. 2015.

[9] K. Roy-Choudhury and S. Hughes, "Theory of phonon-modified quantum dot photoluminescence intensity in structured photonic reservoirs," *Opt. Lett.*, vol. 40, pp. 1838–1841, Apr. 2015.

[10] A. Ulhaq, S. Weiler, C. Roy, S. M. Ulrich, M. Jetter, S. Hughes, and P. Michler, "Detuning-dependent Mollow triplet of a coherently-driven single quantum dot," *Opt. Express*, vol. 21, pp. 4382–4395, Feb. 2013.

[11] Z. Ficek and S. Swain, *Quantum Interference and Coherence: Theory and Experiments*. Springer Series in Optical Sciences, Springer, 2005.

[12] A. J. Ramsay, A. V. Gopal, E. M. Gauger, A. Nazir, B. W. Lovett, A. M. Fox, and M. S. Skolnick, "Damping of exciton Rabi rotations by acoustic phonons in optically excited InGaAs/GaAs quantum dots," *Phys. Rev. Lett.*, vol. 104, p. 017402, Jan. 2010.

[13] R. H. Dicke, "Coherence in spontaneous radiation processes," *Phys. Rev.*, vol. 93, pp. 99–110, Jan. 1954.

[14] M. Gross and S. Haroche, "Superradiance: An essay on the theory of collective spontaneous emission," *Physics Reports*, vol. 93, no. 5, pp. 301 – 396, 1982.

[15] M. Babiker, "Super-radiance near conducting and plasma surfaces," *Journal of Physics A: Mathematical and General*, vol. 9, pp. 799–813, May 1976.

[16] J. J. Choquette, K.-P. Marzlin, and B. C. Sanders, "Superradiance, subradiance, and suppressed superradiance of dipoles near a metal interface," *Phys. Rev. A*, vol. 82, p. 023827, Aug. 2010.

[17] M. O. Scully, "Single photon subradiance: Quantum control of spontaneous emission and ultrafast readout," *Phys. Rev. Lett.*, vol. 115, p. 243602, Dec. 2015.

[18] J. Kim, D. Yang, S.-h. Oh, and K. An, "Coherent single-atom superradiance," *Science*, vol. 359, pp. 662–666, Feb. 2018.

[19] K. D. B. Higgins, S. C. Benjamin, T. M. Stace, G. J. Milburn, B. W. Lovett, and E. M. Gauger, "Superabsorption of light via quantum engineering," *Nat. Comms.*, vol. 5, Aug. 2014.

[20] K. D. B. Higgins, B. W. Lovett, and E. M. Gauger, "Quantum-enhanced capture of photons using optical ratchet states," *The Journal of Physical Chemistry C*, vol. 121, no. 38, pp. 20714–20719, 2017.

[21] W. M. Brown and E. M. Gauger, "Light-harvesting with guide-slide superabsorbing condensed-matter nanostructures," *arXiv:1803.08036*, Mar. 2018.

[22] D. M. Rouse, E. M. Gauger, and B. W. Lovett, "Optimal power generation using dark states in dimers strongly coupled to their environment," *arXiv:1901.11527*, Jan. 2019.

[23] G. V. Varada and G. S. Agarwal, "Two-photon resonance induced by the dipole-dipole interaction," *Phys. Rev. A*, vol. 45, pp. 6721–6729, May 1992.

[24] D. Scerri, T. S. Santana, B. D. Gerardot, and E. M. Gauger, "Method of images applied to driven solid-state emitters," *Phys. Rev. B*, vol. 95, p. 165403, Apr. 2017.

[25] D. P. S. McCutcheon and A. Nazir, "Coherent and incoherent dynamics in excitonic energy transfer: Correlated fluctuations and off-resonance effects," *Phys. Rev. B*, vol. 83, p. 165101, Apr. 2011.

[26] T. Hammerschmidt, *Growth simulations of InAs/GaAs quantum dots*. PhD thesis, Technische Universität Berlin Berlin, 2006.

[27] J. R. Schaibley, A. P. Burgers, G. A. McCracken, D. G. Steel, A. S. Bracker, D. Gammon, and L. J. Sham, "Direct detection of time-resolved Rabi oscillations in a single quantum dot via resonance fluorescence," *Phys. Rev. B*, vol. 87, p. 115311, Mar. 2013.

[28] B. Lounis, H. Bechtel, D. Gerion, P. Alivisatos, and W. Moerner, "Photon antibunching in single CdSe/ZnS quantum dot fluorescence," *Chemical Physics Letters*, vol. 329, no. 56, pp. 399 – 404, 2000.

[29] M. L. Cohen and T. K. Bergstresser, "Band structures and pseudopotential form factors for fourteen semiconductors of the diamond and Zinc-blende structures," *Phys. Rev.*, vol. 141, pp. 789–796, Jan. 1966.

[30] P. Hohenberg and W. Kohn, "Inhomogeneous electron gas," *Phys. Rev.*, vol. 136, pp. B864–B871, Nov. 1964.

[31] M. Schaffry, E. M. Gauger, J. J. L. Morton, and S. C. Benjamin, "Proposed spin amplification for magnetic sensors employing crystal defects," *Phys. Rev. Lett.*, vol. 107, p. 207210, Nov. 2011.

[32] N. Zhao, J.-L. Hu, S.-W. Ho, J. T. K. Wan, and R. B. Liu, "Atomic-scale magnetometry of distant nuclear spin clusters via nitrogen-vacancy spin in diamond," *Nat. Nano.*, vol. 6, p. 242, Feb. 2011.

[33] P. Maletinsky, S. Hong, M. S. Grinolds, B. Hausmann, M. D. Lukin, R. L. Walsworth, M. Loncar, and A. Yacoby, "A robust scanning diamond sensor for nanoscale imaging with single nitrogen-vacancy centres," *Nat. Nano.*, vol. 7, p. 320, Apr. 2012.

[34] B. Hensen, H. Bernien, A. E. Dreau, A. Reiserer, N. Kalb, M. S. Blok, J. Ruitenberg, R. F. L. Vermeulen, R. N. Schouten, C. Abellan, W. Amaya, V. Pruneri, M. W. Mitchell, M. Markham, D. J. Twitchen, D. Elkouss, S. Wehner, T. H. Taminiau, and R. Hanson, "Loophole-free bell inequality violation using electron spins separated by 1.3 kilometres," *Nature*, vol. 526, pp. 682–686, Oct. 2015.

[35] L. Rondin, J.-P. Tetienne, T. Hingant, J.-F. Roch, P. Maletinsky, and V. Jacques, "Magnetometry with nitrogen-vacancy defects in diamond," *Reports on Progress in Physics*, vol. 77, p. 056503, May 2014.

[36] F. Dolde, I. Jakobi, B. Naydenov, N. Zhao, S. Pezzagna, C. Trautmann, J. Meijer, P. Neumann, F. Jelezko, and J. Wrachtrup, "Room-temperature entanglement between single defect spins in diamond," *Nat. Phys.*, vol. 9, pp. 139–143, Mar. 2013.

[37] C. Schreyvogel, V. Polyakov, R. Wunderlich, J. Meijer, and C. E. Nebel, "Active charge state control of single NV centres in diamond by in-plane Al-Schottky junctions," *Sci. Rep.*, vol. 5, p. 12160, Jul. 2015.

[38] P. Tamarat, N. B. Manson, J. P. Harrison, R. L. McMurtrie, A. Nizovtsev, C. Santori, R. G. Beausoleil, P. Neumann, T. Gaebel, F. Jelezko, P. Hemmer, and J. Wrachtrup, "Spin-flip and spin-conserving optical transitions of the nitrogen-vacancy centre in diamond," *New Journal of Physics*, vol. 10, no. 4, p. 045004, 2008.

[39] A. Haque and S. Sumaiya, "An overview on the formation and processing of nitrogen-vacancy photonic centers in diamond by ion implantation," *Journal of Manufacturing and Materials Processing*, vol. 1, p. 6, Aug. 2017.

[40] A. Gupta, L. Hacquebard, and L. Childress, "Efficient signal processing for time-resolved fluorescence detection of nitrogen-vacancy spins in diamond," *J. Opt. Soc. Am. B*, vol. 33, pp. B28–B34, Mar. 2016.

[41] F. Jelezko, T. Gaebel, I. Popa, A. Gruber, and J. Wrachtrup, "Observation of coherent oscillations in a single electron spin," *Phys. Rev. Lett.*, vol. 92, p. 076401, Feb. 2004.

[42] D. Deutsch and R. Penrose, "Quantum theory, the Church-Turing principle and the universal quantum computer," *Proceedings of the Royal Society of London. A. Mathematical and Physical Sciences*, vol. 400, no. 1818, pp. 97–117, 1985.

[43] D. E. Deutsch and R. Penrose, "Quantum computational networks," *Proceedings of the Royal Society of London. A. Mathematical and Physical Sciences*, vol. 425, no. 1868, pp. 73–90, 1989.

[44] C. A. Pérez-Delgado and P. Kok, "Quantum computers: Definition and implementations," *Phys. Rev. A*, vol. 83, p. 012303, Jan. 2011.

[45] M. Hebenstreit, D. Alsina, J. I. Latorre, and B. Kraus, "Compressed quantum computation using a remote five-qubit quantum computer," *Phys. Rev. A*, vol. 95, p. 052339, May 2017.

[46] S. Johri, D. S. Steiger, and M. Troyer, "Entanglement spectroscopy on a quantum computer," *Phys. Rev. B*, vol. 96, p. 195136, Nov. 2017.

[47] R. Raussendorf and H. J. Briegel, "A one-way quantum computer," *Phys. Rev. Lett.*, vol. 86, pp. 5188–5191, May 2001.

[48] R. Raussendorf and H. J. Briegel, "Computational model underlying the one-way quantum computer," *Quantum Info. Comput.*, vol. 2, pp. 443–486, Oct. 2002.

[49] R. Raussendorf, D. E. Browne, and H. J. Briegel, "Measurement-based quantum computation on cluster states," *Phys. Rev. A*, vol. 68, p. 022312, Aug. 2003.

[50] R. Raussendorf, J. Harrington, and K. Goyal, "Topological fault-tolerance in cluster state quantum computation," *New Journal of Physics*, vol. 9, no. 6, p. 199, 2007.

[51] A. Barenco, C. H. Bennett, R. Cleve, D. P. DiVincenzo, N. Margolus, P. Shor, T. Sleator, J. A. Smolin, and H. Weinfurter, "Elementary gates for quantum computation," *Phys. Rev. A*, vol. 52, pp. 3457–3467, Nov. 1995.

[52] E. Farhi, J. Goldstone, S. Gutmann, J. Lapan, A. Lundgren, and D. Preda, "A quantum adiabatic evolution algorithm applied to random instances of an NP-complete problem," *Science*, vol. 292, pp. 472–475, Apr. 2001.

[53] N. H. Lindner and T. Rudolph, "Proposal for pulsed on-demand sources of photonic cluster state strings," *Phys. Rev. Lett.*, vol. 103, p. 113602, Sep. 2009.

[54] D. A. Herrera-Martí, A. G. Fowler, D. Jennings, and T. Rudolph, "Photonic implementation for the topological cluster-state quantum computer," *Phys. Rev. A*, vol. 82, p. 032332, Sep. 2010.

[55] E. V. Denning, J. Iles-Smith, D. P. S. McCutcheon, and J. Mørk, "Protocol for generating multiphoton entangled states from quantum dots in the presence of nuclear spin fluctuations," *Phys. Rev. A*, vol. 96, p. 062329, Dec. 2017.

[56] S. D. Barrett and P. Kok, "Efficient high-fidelity quantum computation using matter qubits and linear optics," *Phys. Rev. A*, vol. 71, p. 060310, Jun. 2005.

[57] Z.-R. Lin, G.-P. Guo, T. Tu, F.-Y. Zhu, and G.-C. Guo, "Generation of quantum-dot cluster states with a superconducting transmission line resonator," *Phys. Rev. Lett.*, vol. 101, p. 230501, Dec. 2008.

[58] I. Schwartz, D. Cogan, E. R. Schmidgall, Y. Don, L. Gantz, O. Kenneth, N. H. Lindner, and D. Gershoni, "Deterministic generation of a cluster state of entangled photons," *Science*, Oct. 2016.

[59] S. E. Economou and P. Dev, "Spin-photon entanglement interfaces in silicon carbide defect centers," *Nanotechnology*, vol. 27, no. 50, p. 504001, 2016.

[60] G. Vallone, E. Pomarico, P. Mataloni, F. De Martini, and V. Berardi, "Realization and characterization of a two-photon four-qubit linear cluster state," *Phys. Rev. Lett.*, vol. 98, p. 180502, May 2007.

[61] X. Zou and W. Mathis, "Generating a four-photon polarization-entangled cluster state," *Phys. Rev. A*, vol. 71, p. 032308, Mar. 2005.

[62] D. E. Browne and T. Rudolph, "Resource-efficient linear optical quantum computation," *Phys. Rev. Lett.*, vol. 95, p. 010501, Jun. 2005.

[63] Y. Weinstein, "Fusing imperfect photonic cluster states," *Journal of Modern Optics*, vol. 58, no. 14, pp. 1285–1291, 2011.

[64] M. A. Nielsen, "Optical quantum computation using cluster states," *Phys. Rev. Lett.*, vol. 93, p. 040503, Jul. 2004.

[65] Y. Ma, P. E. Kremer, and B. D. Gerardot, "Efficient photon extraction from a quantum dot in a broad-band planar cavity antenna," *Journal of Applied Physics*, vol. 115, no. 2, 2014.

[66] T. Santana, *Resonance Fluorescence of Self-assembled Quantum Dots*. Heriot-Watt University, 2016.

[67] S. Fischbach, A. Kaganskiy, E. B. Y. Tauscher, F. Gericke, A. Thoma, R. Schmidt, A. Strittmatter, T. Heindel, S. Rodt, and S. Reitzenstein, "Efficient single-photon source based on a deterministically fabricated single quantum dot - microstructure with backside gold mirror," *Appl. Phys. Lett.*, vol. 111, no. 1, p. 011106, 2017.

[68] E. Knill, R. Laflamme, and G. J. Milburn, "A scheme for efficient quantum computation with linear optics," *Nature*, vol. 409, pp. 46–52, Jan. 2001.

[69] W. Qin and F. Nori, "Controllable single-photon transport between remote coupled-cavity arrays," *Phys. Rev. A*, vol. 93, p. 032337, Mar. 2016.

[70] Y. Wang, Y. Zhang, Q. Zhang, B. Zou, and U. Schwingenschlogl, "Dynamics of single photon transport in a one-dimensional waveguide two-point coupled with a Jaynes-Cummings system," *Scientific Reports*, vol. 6, pp. 33867 EP –, Sep. 2016. Article.

[71] X. Zang and C. Jiang, "Single-photon transport properties in a one-dimensional resonator waveguide coupled to a whispering-gallery resonator," *Journal of Physics B: Atomic, Molecular and Optical Physics*, vol. 43, no. 21, p. 215501, 2010.

[72] P. R. Dolan, G. M. Hughes, F. Grazioso, B. R. Patton, and J. M. Smith, "Femtoliter tunable optical cavity arrays," *Opt. Lett.*, vol. 35, pp. 3556–3558, Nov. 2010.

[73] L. Greuter, S. Starosielec, A. V. Kuhlmann, and R. J. Warburton, "Towards high-cooperativity strong coupling of a quantum dot in a tunable microcavity," *Phys. Rev. B*, vol. 92, p. 045302, Jul. 2015.

[74] J. Miguel-Sánchez, A. Reinhard, E. Togan, T. Volz, A. Imamoglu, B. Besga, J. Reichel, and J. Estève, "Cavity quantum electrodynamics with charge-controlled quantum dots coupled to a fiber Fabry-Pérot cavity," *New Journal of Physics*, vol. 15, no. 4, p. 045002, 2013.

[75] E. Hwang, I. I. Smolyaninov, and C. C. Davis, "Surface plasmon polariton enhanced fluorescence from quantum dots on nanostructured metal surfaces," *Nano Letters*, vol. 10, no. 3, pp. 813–820, 2010. PMID: 20112921.

[76] A. Neogi and H. Morkoç, "Resonant surface plasmon-induced modification of photoluminescence from GaN/AlN quantum dots," *Nanotechnology*, vol. 15, no. 9, p. 1252, 2004.

[77] Y. Fu, J. Zhang, and J. R. Lakowicz, "Silver-enhanced fluorescence emission of single quantum dot nanocomposites," *Chem. Commun.*, pp. 313–315, 2009.

[78] K. Drexhage, "Influence of a dielectric interface on fluorescence decay time," *Journal of Luminescence*, vol. 1, pp. 693 – 701, 1970.

[79] R. R. Chance, A. Prock, and R. Silbey, "Frequency shifts of an electric-dipole transition near a partially reflecting surface," *Phys. Rev. A*, vol. 12, pp. 1448–1452, Oct. 1975.

[80] H. Morawitz, "Self-coupling of a two-level system by a mirror," *Physical Review*, vol. 187, no. 5, pp. 1792–1796, 1969.

[81] M. Al-Amri and M. Babiker, "Quantum correlations across a metallic screen," *Phys. Rev. A*, vol. 67, p. 043820, Apr. 2003.

[82] C. Bennett, M. Babiker, and J. Kirk, "Spontaneous emission and cooperative effects near a thin metallic film," *Journal of Modern Optics*, vol. 49, no. 1-2, pp. 269–284, 2002.

[83] P. Milonni and P. Knight, "Spontaneous emission between mirrors," *Optics Communications*, vol. 9, no. 2, pp. 119 – 122, 1973.

[84] C. Ropp, Z. Cummins, S. Nah, J. T. Fourkas, B. Shapiro, and E. Waks, "Nanoscale probing of image dipole interactions in a metallic nanostructure," *Nat. Comms.*, vol. 6, p. 6558, 2015.

[85] W. Niu, L. A. Ibbotson, D. Leipold, E. Runge, G. V. Prakash, and J. J. Baumberg, "Image excitons and plasmon-exciton strong coupling in two-dimensional perovskite semiconductors," *Phys. Rev. B*, vol. 91, p. 161303, Apr. 2015.

[86] D. Zhang, Y.-C. Wu, M. Yang, X. Liu, C. Coileáin, M. Abid, M. Abid, J.-J. Wang, I. Shvets, H. Xu, B. S. Chun, H. Liu, and H.-C. Wu, "Surface enhanced Raman scattering of monolayer MX_2 with metallic nano particles," *Scientific Reports*, vol. 6, p. 30320, Jul. 2016.

[87] I.-C. Hoi, A. F. Kockum, L. Tornberg, A. Pourkabirian, G. Johansson, P. Delsing, and C. M. Wilson, "Probing the quantum vacuum with an artificial atom in front of a mirror," *Nat. Phys.*, vol. 11, p. 1045, Sep. 2015.

[88] K. Koshino and Y. Nakamura, "Control of the radiative level shift and linewidth of a superconducting artificial atom through a variable boundary condition," *New Journal of Physics*, vol. 14, no. 4, p. 043005, 2012.

[89] J. D. Jackson, *Classical electrodynamics*. New York, NY: Wiley, 3rd ed., 1999.

[90] G. S. Agarwal, "Quantum electrodynamics in the presence of dielectrics and conductors. IV. general theory for spontaneous emission in finite geometries," *Phys. Rev. A*, vol. 12, pp. 1475–1497, Oct. 1975.

[91] S. M. Barnett, N. Harris, and J. J. Baumberg, "Molecules in the mirror: how SERS backgrounds arise from the quantum method of images," *Phys. Chem. Chem. Phys.*, vol. 16, pp. 6544–6549, 2014.

[92] W. Barnes, "Fluorescence near interfaces: The role of photonic mode density," *Journal of Modern Optics*, vol. 45, no. 4, pp. 661–699, 1998.

[93] K. C. Liu and T. F. George, "Spontaneous emission by two atoms with different resonance frequencies near a metal surface," *Phys. Rev. B*, vol. 32, pp. 3622–3633, Sep. 1985.

[94] C.-r. Fu and C.-d. Gong, "Resonance fluorescence of two adatoms near a metal surface," *Phys. Rev. A*, vol. 40, pp. 207–214, Jul. 1989.

[95] L. Novotny and B. Hecht, *Principles of Nano-Optics*. Cambridge University Press, 2006.

[96] I. Prigogine and S. Rice, *Advances in Chemical Physics*. No. v. 74 in Advances in Chemical Physics, Wiley, 2009.

[97] S. M. Barnett and R. Loudon, "Sum rule for modified spontaneous emission rates," *Phys. Rev. Lett.*, vol. 77, pp. 2444–2446, Sep. 1996.

[98] S. M. Barnett and R. Loudon, "Sum rule for environmentally modified spontaneous emission rates," *Quantum and Semiclassical Optics: Journal of the European Optical Society Part B*, vol. 10, pp. 591–599, Aug. 1998.

[99] R. J. Ram, D. I. Babid, Y. A. York, and J. E. Bowers, "Spontaneous emission in microcavities with distributed mirrors," *IEEE Journal of Quantum Electronics*, vol. 31, pp. 399–410, Feb. 1995.

[100] A. Krügel, V. Axt, T. Kuhn, P. Machnikowski, and A. Vagov, "The role of acoustic phonons for Rabi oscillations in semiconductor quantum dots," *Applied Physics B*, vol. 81, no. 7, pp. 897–904, 2005.

[101] P. Machnikowski and L. Jacak, "Resonant nature of phonon-induced damping of Rabi oscillations in quantum dots," *Phys. Rev. B*, vol. 69, p. 193302, May 2004.

[102] F. De Martini, M. Marrocco, P. Mataloni, L. Crescentini, and R. Loudon, "Spontaneous emission in the optical microscopic cavity," *Phys. Rev. A*, vol. 43, pp. 2480–2497, Mar. 1991.

[103] C. Gardiner and P. Zoller, *Quantum noise: a handbook of Markovian and non-Markovian quantum stochastic methods with applications to quantum optics*, vol. 56. Springer Science & Business Media, 2004.

[104] G. S. Agarwal, *Quantum Optics*. Berlin, Heidelberg: Springer Berlin Heidelberg, 1974.

[105] G. V. Varada and G. S. Agarwal, "Two-photon resonance induced by the dipole-dipole interaction," *Phys. Rev. A*, vol. 45, pp. 6721–6729, May 1992.

[106] P. Milonni, *The Quantum Vacuum: An Introduction to Quantum Electrodynamics*. Academic Press, 1994.

[107] H. Khosravi and R. Loudon, "Vacuum field fluctuations and spontaneous emission in the vicinity of a dielectric surface," *Proceedings of the Royal Society of London A: Mathematical, Physical and Engineering Sciences*, vol. 433, no. 1888, pp. 337–352, 1991.

[108] J. Iles-Smith, D. P. S. McCutcheon, J. Mørk, and A. Nazir, "Limits to coherent scattering and photon coalescence from solid-state quantum emitters," *Phys. Rev. B*, vol. 95, p. 201305, May 2017.

[109] W. Abdussalam and P. Machnikowski, "Superradiance and enhanced luminescence from ensembles of a few self-assembled quantum dots," *Phys. Rev. B*, vol. 90, p. 125307, Sep. 2014.

[110] J.-H. Kim, S. Aghaeimeibodi, C. J. K. Richardson, R. P. Leavitt, and E. Waks, "Super-radiant emission from quantum dots in a nanophotonic waveguide," *Nano Letters*, vol. 18, pp. 4734–4740, Jul. 2018.

[111] H. J. Briegel and R. Raussendorf, "Persistent entanglement in arrays of interacting particles," *Phys. Rev. Lett.*, vol. 86, pp. 910–913, Jan. 2001.

[112] J. L. O'Brien, A. Furusawa, and J. Vuckovic, "Photonic quantum technologies," *Nat. Photon.*, vol. 3, pp. 687–695, Dec. 2009.

[113] S. E. Economou, N. Lindner, and T. Rudolph, "Optically generated 2-dimensional photonic cluster state from coupled quantum dots," *Phys. Rev. Lett.*, vol. 105, p. 093601, Aug. 2010.

[114] M. Gimeno-Segovia, T. Rudolph, and S. E. Economou, "Deterministic generation of large-scale entangled photonic cluster state from interacting solid state emitters," vol. arXiv:1801.02599, Jan. 2018.

[115] J. Iles-Smith, D. P. S. McCutcheon, A. Nazir, and J. Mørk, "Phonon scattering inhibits simultaneous near-unity efficiency and indistinguishability in semiconductor single-photon sources," *Nat. Photon.*, vol. 11, p. 521, Jul. 2017.

[116] A. V. Khaetskii, D. Loss, and L. Glazman, "Electron spin decoherence in quantum dots due to interaction with nuclei," *Phys. Rev. Lett.*, vol. 88, p. 186802, Apr. 2002.

[117] C. Testelin, F. Bernardot, B. Eble, and M. Chamarro, "Hole-spin dephasing time associated with hyperfine interaction in quantum dots," *Phys. Rev. B*, vol. 79, p. 195440, May 2009.

[118] J. Hansom, C. H. H. Schulte, C. Le Gall, C. Matthiesen, E. Clarke, M. Hugues, J. M. Taylor, and M. Atatüre, "Environment-assisted quantum control of a solid-state spin via coherent dark states," *Nat. Phys.*, vol. 10, pp. 725–730, Sep. 2014.

[119] R. N. E. Malein, T. S. Santana, J. M. Zajac, A. C. Dada, E. M. Gauger, P. M. Petroff, J. Y. Lim, J. D. Song, and B. D. Gerardot, "Screening nuclear field fluctuations in quantum dots for indistinguishable photon generation," *Phys. Rev. Lett.*, vol. 116, p. 257401, Jun. 2016.

[120] I. A. Merkulov, A. L. Efros, and M. Rosen, "Electron spin relaxation by nuclei in semiconductor quantum dots," *Phys. Rev. B*, vol. 65, p. 205309, Apr. 2002.

[121] P. Braun, X. Marie, L. Lombez, B. Urbaszek, T. Amand, P. Renucci, V. K. Kalevich, K. V. Kavokin, O. Krebs, P. Voisin, and Y. Masumoto, "Direct

observation of the electron spin relaxation induced by nuclei in quantum dots," *Phys. Rev. Lett.*, vol. 94, p. 116601, Mar. 2005.

[122] E. Chekhovich, M. Makhonin, A. Tartakovskii, A. Yacoby, H. Bluhm, K. Nowack, and L. Vandersypen, "Nuclear spin effects in semiconductor quantum dots," *Nat. Mater.*, vol. 12, p. 494, May 2013.

[123] B. Urbaszek, X. Marie, T. Amand, O. Krebs, P. Voisin, P. Maletinsky, A. Högele, and A. Imamoğlu, "Nuclear spin physics in quantum dots: An optical investigation," *Rev. Mod. Phys.*, vol. 85, pp. 79–133, Jan. 2013.

[124] L. Viola, E. Knill, and S. Lloyd, "Dynamical decoupling of open quantum systems," *Phys. Rev. Lett.*, vol. 82, pp. 2417–2421, Mar. 1999.

[125] W. M. Witzel and S. Das Sarma, "Concatenated dynamical decoupling in a solid-state spin bath," *Phys. Rev. B*, vol. 76, p. 241303, Dec. 2007.

[126] W. Zhang, V. V. Dobrovitski, L. F. Santos, L. Viola, and B. N. Harmon, "Dynamical control of electron spin coherence in a quantum dot: A theoretical study," *Phys. Rev. B*, vol. 75, p. 201302, May 2007.

[127] G. S. Uhrig, "Keeping a quantum bit alive by optimized π-pulse sequences," *Phys. Rev. Lett.*, vol. 98, p. 100504, Mar. 2007.

[128] G. S. Uhrig, "Exact results on dynamical decoupling by pulses in quantum information processes," *New Journal of Physics*, vol. 10, no. 8, p. 083024, 2008.

[129] H. Bluhm, S. Foletti, I. Neder, M. Rudner, D. Mahalu, V. Umansky, and A. Yacoby, "Dephasing time of GaAs electron-spin qubits coupled to a nuclear bath exceeding 200μs," *Nat. Phys.*, vol. 7, pp. 109–113, Dec. 2010.

[130] R. Stockill, C. Le Gall, C. Matthiesen, L. Huthmacher, E. Clarke, M. Hugues, and M. Atatüre, "Quantum dot spin coherence governed by a strained nuclear environment," *Nat. Comms.*, vol. 7, p. 12745, Sep. 2016.

[131] B. Eble, O. Krebs, A. Lemaître, K. Kowalik, A. Kudelski, P. Voisin, B. Urbaszek, X. Marie, and T. Amand, "Dynamic nuclear polarization of a single charge-tunable InAs/GaAs quantum dot," *Phys. Rev. B*, vol. 74, p. 081306, Aug. 2006.

[132] J. R. Petta, J. M. Taylor, A. C. Johnson, A. Yacoby, M. D. Lukin, C. M. Marcus, M. P. Hanson, and A. C. Gossard, "Dynamic nuclear polarization with single electron spins," *Phys. Rev. Lett.*, vol. 100, p. 067601, Feb. 2008.

[133] G. Éthier-Majcher, D. Gangloff, R. Stockill, E. Clarke, M. Hugues, C. Le Gall, and M. Atatüre, "Improving a solid-state qubit through an engineered mesoscopic environment," *Phys. Rev. Lett.*, vol. 119, p. 130503, Sep. 2017.

[134] A. J. Ramsay, "Passive stabilization of a hole spin qubit using the optical Stark effect," *Phys. Rev. B*, vol. 93, p. 075303, Feb. 2016.

[135] J. N. Becker, J. Görlitz, C. Arend, M. Markham, and C. Becher, "Ultrafast all-optical coherent control of single silicon vacancy colour centres in diamond," *Nat. Comms.*, vol. 7, p. 13512, Nov. 2016.

[136] C. G. Yale, B. B. Buckley, D. J. Christle, G. Burkard, F. J. Heremans, L. C. Bassett, and D. D. Awschalom, "All-optical control of a solid-state spin using coherent dark states," *Proceedings of the National Academy of Sciences*, vol. 110, no. 19, pp. 7595–7600, 2013.

[137] S. Novikov, T. Sweeney, J. E. Robinson, S. P. Premaratne, B. Suri, F. C. Wellstood, and B. S. Palmer, "Raman coherence in a circuit quantum electrodynamics lambda system," *Nat. Phys.*, vol. 12, p. 75, Nov. 2015.

[138] Q.-C. Liu, T.-F. Li, X.-Q. Luo, H. Zhao, W. Xiong, Y.-S. Zhang, Z. Chen, J. S. Liu, W. Chen, F. Nori, J. S. Tsai, and J. Q. You, "Method for identifying electromagnetically induced transparency in a tunable circuit quantum electrodynamics system," *Phys. Rev. A*, vol. 93, p. 053838, May 2016.

[139] S. P. Premaratne, F. C. Wellstood, and B. S. Palmer, "Characterization of coherent population-trapped states in a circuit-QED Λ system," *Phys. Rev. A*, vol. 96, p. 043858, Oct. 2017.

[140] C. Emary, X. Xu, D. G. Steel, S. Saikin, and L. J. Sham, "Fast initialization of the spin state of an electron in a quantum dot in the Voigt configuration," *Phys. Rev. Lett.*, vol. 98, p. 047401, Jan. 2007.

[141] A. Delteil, Z. Sun, W.-b. Gao, E. Togan, S. Faelt, and A. Imamoğlu, "Generation of heralded entanglement between distant hole spins," *Nat. Phys.*, vol. 12, p. 218, Dec. 2015.

[142] R. Stockill, M. J. Stanley, L. Huthmacher, E. Clarke, M. Hugues, A. J. Miller, C. Matthiesen, C. Le Gall, and M. Atatüre, "Phase-tuned entangled state generation between distant spin qubits," *Phys. Rev. Lett.*, vol. 119, p. 010503, Jul. 2017.

[143] J. Johansson, P. Nation, and F. Nori, "QuTiP: An open-source Python framework for the dynamics of open quantum systems," *Computer Physics Communications*, vol. 183, no. 8, pp. 1760 – 1772, 2012.

[144] J. Johansson, P. Nation, and F. Nori, "QuTiP 2: A Python framework for the dynamics of open quantum systems," *Computer Physics Communications*, vol. 184, no. 4, pp. 1234 – 1240, 2013.

[145] M. Popp, F. Verstraete, M. A. Martín-Delgado, and J. I. Cirac, "Localizable entanglement," *Phys. Rev. A*, vol. 71, p. 042306, Apr. 2005.

[146] D. Loss and D. P. DiVincenzo, "Quantum computation with quantum dots," *Phys. Rev. A*, vol. 57, pp. 120–126, Jan. 1998.

[147] J. Fischer, W. A. Coish, D. V. Bulaev, and D. Loss, "Spin decoherence of a heavy hole coupled to nuclear spins in a quantum dot," *Phys. Rev. B*, vol. 78, p. 155329, Oct. 2008.

[148] E. A. Chekhovich, A. B. Krysa, M. S. Skolnick, and A. I. Tartakovskii, "Direct measurement of the hole-nuclear spin interaction in single InP/GaInP quantum dots using photoluminescence spectroscopy," *Phys. Rev. Lett.*, vol. 106, p. 027402, Jan. 2011.

[149] P. Fallahi, S. T. Yılmaz, and A. Imamoğlu, "Measurement of a heavy-hole hyperfine interaction in InGaAs quantum dots using resonance fluorescence," *Phys. Rev. Lett.*, vol. 105, p. 257402, Dec. 2010.

[150] D. V. Bulaev and D. Loss, "Spin relaxation and decoherence of holes in quantum dots," *Phys. Rev. Lett.*, vol. 95, p. 076805, Aug. 2005.

[151] K. De Greve, P. L. McMahon, D. Press, T. D. Ladd, D. Bisping, C. Schneider, M. Kamp, L. Worschech, S. Höfling, A. Forchel, and Y. Yamamoto, "Ultrafast coherent control and suppressed nuclear feedback of a single quantum dot hole qubit," *Nat. Phys.*, vol. 7, p. 872, Aug. 2011.

[152] J. H. Prechtel, A. V. Kuhlmann, J. Houel, A. Ludwig, S. R. Valentin, A. D. Wieck, and R. J. Warburton, "Decoupling a hole spin qubit from the nuclear spins," *Nat. Mater.*, vol. 15, pp. 981–986, Sep. 2016.

[153] M. Zieliński, Y. Don, and D. Gershoni, "Atomistic theory of dark excitons in self-assembled quantum dots of reduced symmetry," *Phys. Rev. B*, vol. 91, p. 085403, Feb. 2015.

[154] M. A. Dupertuis, K. F. Karlsson, D. Y. Oberli, E. Pelucchi, A. Rudra, P. O. Holtz, and E. Kapon, "Symmetries and the polarized optical spectra of exciton complexes in quantum dots," *Phys. Rev. Lett.*, vol. 107, p. 127403, Sep. 2011.

[155] Y. Don, M. Zielinski, and D. Gershoni, "The Optical Activity of the Dark Exciton," vol. arXiv:1601.05530, Jan. 2016.

[156] E. A. Stinaff, M. Scheibner, A. S. Bracker, I. V. Ponomarev, V. L. Korenev, M. E. Ware, M. F. Doty, T. L. Reinecke, and D. Gammon, "Optical signatures of coupled quantum dots," *Science*, vol. 311, pp. 636–639, Feb. 2006.

[157] H. J. Krenner, M. Sabathil, E. C. Clark, A. Kress, D. Schuh, M. Bichler, G. Abstreiter, and J. J. Finley, "Direct observation of controlled coupling in an individual quantum dot molecule," *Phys. Rev. Lett.*, vol. 94, p. 057402, Feb. 2005.

[158] D. Kim, S. G. Carter, A. Greilich, A. S. Bracker, and D. Gammon, "Ultrafast optical control of entanglement between two quantum-dot spins," *Nat. Phys.*, vol. 7, pp. 223–229, Mar. 2011.

[159] R. Songmuang, S. Kiravittaya, and O. G. Schmidt, "Formation of lateral quantum dot molecules around self-assembled nanoholes," *Appl. Phys. Lett.*, vol. 82, no. 17, pp. 2892–2894, 2003.

[160] L. Wang, A. Rastelli, S. Kiravittaya, P. Atkinson, F. Ding, C. C. Bof Bufon, C. Hermannstaedter, M. Witzany, G. J. Beirne, P. Michler, and O. G. Schmidt, "Towards deterministically controlled InGaAs/GaAs lateral quantum dot molecules," *New Journal of Physics*, vol. 10, no. 4, p. 045010, 2008.

[161] P. M. Vora, A. S. Bracker, S. G. Carter, T. M. Sweeney, M. Kim, C. S. Kim, L. Yang, P. G. Brereton, S. E. Economou, and D. Gammon, "Spin-cavity interactions between a quantum dot molecule and a photonic crystal cavity," *Nat. Comms.*, vol. 6, Jul. 2015.

[162] N. Shaji, C. B. Simmons, M. Thalakulam, L. J. Klein, H. Qin, H. Luo, D. E. Savage, M. G. Lagally, A. J. Rimberg, R. Joynt, M. Friesen, R. H. Blick, S. N. Coppersmith, and M. A. Eriksson, "Spin blockade and lifetime-enhanced transport in a few-electron Si/SiGe double quantum dot," *Nat. Phys.*, vol. 4, p. 540, Jun. 2008.

[163] A. Greilich, S. G. Carter, D. Kim, A. S. Bracker, and D. Gammon, "Optical control of one and two hole spins in interacting quantum dots," *Nat. Photon.*, vol. 5, pp. 702–708, Nov. 2011.

[164] K. M. Weiss, J. M. Elzerman, Y. L. Delley, J. Miguel-Sanchez, and A. Imamoğlu, "Coherent two-electron spin qubits in an optically active pair

of coupled InGaAs quantum dots," *Phys. Rev. Lett.*, vol. 109, p. 107401, Sep. 2012.

[165] J. M. Elzerman, K. M. Weiss, J. Miguel-Sanchez, and A. Imamoğlu, "Optical amplification using Raman transitions between spin-singlet and spin-triplet states of a pair of coupled InGaAs quantum dots," *Phys. Rev. Lett.*, vol. 107, p. 017401, Jun. 2011.

[166] A. N. Vamivakas, C.-Y. Lu, C. Matthiesen, Y. Zhao, S. Fält, A. Badolato, and M. Atatüre, "Observation of spin-dependent quantum jumps via quantum dot resonance fluorescence," *Nature*, vol. 467, p. 297, Sep. 2010.

[167] D. Kim, S. E. Economou, i. m. c. C. Bădescu, M. Scheibner, A. S. Bracker, M. Bashkansky, T. L. Reinecke, and D. Gammon, "Optical spin initialization and nondestructive measurement in a quantum dot molecule," *Phys. Rev. Lett.*, vol. 101, p. 236804, Dec. 2008.

[168] D. Gross, K. Kieling, and J. Eisert, "Potential and limits to cluster-state quantum computing using probabilistic gates," *Phys. Rev. A*, vol. 74, p. 042343, Oct. 2006.

[169] M. Gimeno-Segovia, P. Shadbolt, D. E. Browne, and T. Rudolph, "From three-photon Greenberger-Horne-Zeilinger states to ballistic universal quantum computation," *Phys. Rev. Lett.*, vol. 115, p. 020502, Jul. 2015.

[170] S. Morley-Short, S. Bartolucci, M. Gimeno-Segovia, P. Shadbolt, H. Cable, and T. Rudolph, "Physical-depth architectural requirements for generating universal photonic cluster states," *Quantum Science and Technology*, vol. 3, no. 1, p. 015005, 2018.

[171] D. Scerri, E. M. Gauger, and G. C. Knee, "Coarse-graining in retrodictive quantum state tomography," *Journal of Physics Communications*, 2019.

[172] N. H. Lindner and T. Rudolph, "Proposal for pulsed on-demand sources of photonic cluster state strings," *Phys. Rev. Lett.*, vol. 103, p. 113602, Sep. 2009.

[173] D. Scerri, R. N. E. Malein, B. D. Gerardot, and E. M. Gauger, "Frequency-encoded linear cluster states with coherent Raman photons," *Phys. Rev. A*, vol. 98, p. 022318, Aug. 2018.

[174] J. L. E. Silva, S. Glancy, and H. M. Vasconcelos, "Quadrature histograms in maximum-likelihood quantum state tomography," *Phys. Rev. A*, vol. 98, p. 022325, Aug. 2018.

[175] K. Jones, "Principles of quantum inference," *Annals of Physics*, vol. 207, no. 1, pp. 140 – 170, 1991.

[176] K. R. W. Jones, "Quantum limits to information about states for finite dimensional Hilbert space," *Journal of Physics A: Mathematical and General*, vol. 24, no. 1, p. 121, 1991.

[177] P. B. Slater, "Quantum coin-tossing in a Bayesian Jeffreys framework," *Physics Letters A*, vol. 206, no. 1, pp. 66 – 72, 1995.

[178] R. Derka, V. Bužek, G. Adam, and P. L. Knight, "From quantum Bayesian inference to quantum tomography," *arXiv:quant-ph/9701029*, Jan. 1997.

[179] V. Bužek, R. Derka, G. Adam, and P. Knight, "Reconstruction of Quantum States of Spin Systems: From Quantum Bayesian Inference to Quantum Tomography," *Annals of Physics*, vol. 266, no. 2, pp. 454 – 496, 1998.

[180] R. Schack, T. A. Brun, and C. M. Caves, "Quantum Bayes rule," *Phys. Rev. A*, vol. 64, p. 014305, Jun. 2001.

[181] P. Cappellaro, "Spin-bath narrowing with adaptive parameter estimation," *Phys. Rev. A*, vol. 85, p. 030301, Mar. 2012.

[182] C. Bonato, M. S. Blok, H. T. Dinani, D. W. Berry, M. L. Markham, D. J. Twitchen, and R. Hanson, "Optimized quantum sensing with a single electron spin using real-time adaptive measurements," *Nat. Nano.*, vol. 11, pp. 247–252, Nov. 2015.

[183] C. Bonato and D. W. Berry, "Adaptive tracking of a time-varying field with a quantum sensor," *Phys. Rev. A*, vol. 95, p. 052348, May 2017.

[184] R. Blume-Kohout, "Optimal, reliable estimation of quantum states," *New Journal of Physics*, vol. 12, no. 4, p. 043034, 2010.

[185] C. Granade, J. Combes, and D. G. Cory, "Practical Bayesian tomography," *New Journal of Physics*, vol. 18, no. 3, p. 033024, 2016.

[186] G. I. Struchalin, I. A. Pogorelov, S. S. Straupe, K. S. Kravtsov, I. V. Radchenko, and S. P. Kulik, "Experimental adaptive quantum tomography of two-qubit states," *Phys. Rev. A*, vol. 93, p. 012103, Jan. 2016.

[187] R. Blume-Kohout and P. Hayden, "Accurate quantum state estimation via "Keeping the experimentalist honest"," *arXiv:quant-ph/0603116*, Mar. 2006.

[188] C. E. Granade, C. Ferrie, N. Wiebe, and D. G. Cory, "Robust online Hamiltonian learning," *New Journal of Physics*, vol. 14, no. 10, p. 103013, 2012.

[189] R. Kueng and C. Ferrie, "Near-optimal quantum tomography: estimators and bounds," *New Journal of Physics*, vol. 17, p. 123013, Dec. 2015.

[190] C. Ferrie, "High posterior density ellipsoids of quantum states," *New Journal of Physics*, vol. 16, no. 2, p. 023006, 2014.

[191] F. Huszár and N. M. T. Houlsby, "Adaptive Bayesian quantum tomography," *Phys. Rev. A*, vol. 85, p. 052120, May 2012.

[192] J. S. Liu and R. Chen, "Sequential Monte Carlo methods for dynamic systems," *Journal of the American Statistical Association*, vol. 93, no. 443, pp. 1032–1044, 1998.

[193] J. Liu and M. West, "Combined parameter and state estimation in simulation-based filtering," in *Sequential Monte Carlo Methods in Practice* (D. Freitas and N. Gordon, eds.), Springer-Verlag, New York, 2001.

[194] M. S. Kaznady and D. F. V. James, "Numerical strategies for quantum tomography: Alternatives to full optimization," *Phys. Rev. A*, vol. 79, p. 022109, Feb. 2009.

[195] Y. S. Teo, *Introduction to Quantum-State Estimation*. World Scientific Publishing Co, 2016.

[196] G. C. Knee, E. Bolduc, J. Leach, and E. M. Gauger, "Maximum-likelihood quantum process tomography via projected gradient descent," *arXiv:1803.10062*, Mar. 2018.

[197] D. Gonçalves, M. Gomes-Ruggiero, and C. Lavor, "A projected gradient method for optimization over density matrices," *Optimization Methods and Software*, vol. 31, no. 2, pp. 328–341, 2016.

[198] E. Bolduc, G. C. Knee, E. M. Gauger, and J. Leach, "Projected gradient descent algorithms for quantum state tomography," *NPJ Quantum Information*, vol. 3, no. 1, p. 44, 2017.

[199] D. F. V. James, P. G. Kwiat, W. J. Munro, and A. G. White, "Measurement of qubits," *Phys. Rev. A*, vol. 64, p. 052312, Oct. 2001.

[200] J. Altepeter, E. Jeffrey, and P. Kwiat, "Photonic state tomography," vol. 52 of *Advances In Atomic, Molecular, and Optical Physics*, pp. 105 – 159, Academic Press, 2005.

[201] D. S. Gonçalves, M. A. Gomes-Ruggiero, C. Lavor, O. Jiménez Farías, and P. H. Souto Ribeiro, "Local solutions of Maximum Likelihood Estimation in Quantum State Tomography," *arXiv:1103.3682*, Mar. 2011.

[202] A. Miranowicz, K. Bartkiewicz, J. Peřina, M. Koashi, N. Imoto, and F. Nori, "Optimal two-qubit tomography based on local and global measurements: Maximal robustness against errors as described by condition numbers," *Phys. Rev. A*, vol. 90, p. 062123, Dec. 2014.

[203] Y. L. Lim, A. Beige, and L. C. Kwek, "Repeat-until-success linear optics distributed quantum computing," *Phys. Rev. Lett.*, vol. 95, p. 030505, Jul. 2005.

[204] J. M. Taylor, P. Cappellaro, L. Childress, L. Jiang, D. Budker, P. R. Hemmer, A. Yacoby, R. Walsworth, and M. D. Lukin, "High-sensitivity diamond magnetometer with nanoscale resolution," *Nat. Phys.*, vol. 4, p. 810, Sep. 2008.

[205] A. Ajoy, U. Bissbort, M. D. Lukin, R. L. Walsworth, and P. Cappellaro, "Atomic-scale nuclear spin imaging using quantum-assisted sensors in diamond," *Phys. Rev. X*, vol. 5, p. 011001, Jan. 2015.

[206] M. D. Shulman, S. P. Harvey, J. M. Nichol, S. D. Bartlett, A. C. Doherty, V. Umansky, and A. Yacoby, "Suppressing qubit dephasing using real-time hamiltonian estimation," *Nat. Comms.*, vol. 5, p. 5156, Oct. 2014.

[207] P. Neumann, J. Beck, M. Steiner, F. Rempp, H. Fedder, P. R. Hemmer, J. Wrachtrup, and F. Jelezko, "Single-shot readout of a single nuclear spin," *Science*, vol. 329, pp. 542–544, Jul. 2010.

[208] L. Robledo, L. Childress, H. Bernien, B. Hensen, P. F. A. Alkemade, and R. Hanson, "High-fidelity projective read-out of a solid-state spin quantum register," *Nature*, vol. 477, p. 574, Sep. 2011.

[209] N. Zhao, J. Honert, B. Schmid, M. Klas, J. Isoya, M. Markham, D. Twitchen, F. Jelezko, R.-B. Liu, H. Fedder, and J. Wrachtrup, "Sensing single remote nuclear spins," *Nat. Nano.*, vol. 7, p. 657, Sep. 2012.

[210] T. H. Taminiau, J. J. T. Wagenaar, T. van der Sar, F. Jelezko, V. V. Dobrovitski, and R. Hanson, "Detection and control of individual nuclear spins using a weakly coupled electron spin," *Phys. Rev. Lett.*, vol. 109, p. 137602, Sep. 2012.

[211] T. Unden, N. Tomek, T. Weggler, F. Frank, P. London, J. Zopes, C. Degen, N. Raatz, J. Meijer, H. Watanabe, K. M. Itoh, M. B. Plenio, B. Naydenov,

and F. Jelezko, "Coherent control of solid state nuclear spin nano-ensembles," *npj Quantum Information*, vol. 4, no. 1, p. 39, 2018.

[212] J. R. Maze, J. M. Taylor, and M. D. Lukin, "Electron spin decoherence of single nitrogen-vacancy defects in diamond," *Phys. Rev. B*, vol. 78, p. 094303, Sep. 2008.

[213] J. R. Maze, A. Dréau, V. Waselowski, H. Duarte, J.-F. Roch, and V. Jacques, "Free induction decay of single spins in diamond," *New Journal of Physics*, vol. 14, p. 103041, Oct. 2012.

[214] A. S. Holevo, "Covariant measurements and imprimitivity systems," *Lecture Notes in Mathematics, Berlin Springer Verlag*, vol. 1055, p. 153, 1984.

[215] B. L. Higgins, D. W. Berry, S. D. Bartlett, M. W. Mitchell, H. M. Wiseman, and G. J. Pryde, "Demonstrating Heisenberg-limited unambiguous phase estimation without adaptive measurements," *New Journal of Physics*, vol. 11, p. 073023, Jul. 2009.

[216] L. Childress, M. V. Gurudev Dutt, J. M. Taylor, A. S. Zibrov, F. Jelezko, J. Wrachtrup, P. R. Hemmer, and M. D. Lukin, "Coherent dynamics of coupled electron and nuclear spin qubits in diamond," *Science*, vol. 314, pp. 281–285, Oct. 2006.